Exploring Aromaticity and Antiaromaticity Using Magnetic Shielding Calculations

James Edward Cummings MSci (Hons)

PhD Thesis

University of York

Chemistry

September, 2025

Abstract

This thesis investigates aromaticity and antiaromaticity using magnetic shielding, with a particular focus on extending the conclusions that can be drawn from nucleus-independent chemical shifts (NICS) by using three-dimensional isotropic magnetic shielding volume data to visualise magnetic shielding with isosurfaces. In particular, the extent of aromatic reversal upon excitation from the ground to the lowest triplet excited state is explored for a range of molecular systems.

Through the case study of thiophene and its condensed forms, it is demonstrated that excited-state aromaticity is highly sensitive to geometry, with isomers of condensed heterocycles experiencing significantly different levels of aromaticity reduction upon excitation, while a select few show true Baird-type aromaticity reversals. Condensed macrocycles show a variety of behaviours when excited from the ground to the lowest energy triplet state: the degree of aromatic reversal in heterocirculenes is highly dependent on ring strain, and any changes in aromaticity are relatively modest; aromaticity in norcorrole is dominated by large π networks, so the molecule experiences a significant aromatic reversal upon excitation.

Significant contributions include the proposal of novel structures, such as sulfinfinitenes, and the examination of boron clusters, where σ-aromaticity dominates magnetic shielding over π-aromaticity. Additionally, deshielding in the T_1 state of ethyne highlights that the central deshielded region in antiaromatic molecules is not solely due to electron delocalisation. Model chemistry dependence is highlighted, with varying computational methods yielding different results, emphasising the need for chemical intuition alongside computational insights. The study of annulenes reveals that excited-state and geometry-dependent effects must be carefully considered, particularly when charged systems are involved.

Ultimately, this work reinforces the complexity of aromaticity as a continuum, rather than a binary property, and suggests that magnetic shielding can provide a robust tool for investigating electronic structure, provided it is paired with a comprehensive chemical understanding.

Contents

Contents

List of Figures

List of Tables

Acknowledgements

A PhD requires years of study leading up to it, so I would like to thank all of my school and A-level teachers for all of their efforts to equip me with the knowledge required to progress to the next level in my educational journey. A special thanks must go to my MSci supervisor, Michael Peach, without whom I would never have embarked on a PhD to begin with. Michael was somebody who really put his students first; prioritising lecturing and caring for students, which is rare in university environments, as they are often more focused on research. I should also mention my current PhD supervisor in this section for his guidance and expertise.

Outside of academics, I have had the privilege to interact with two incredible groups of people during my PhD. Despite many of them being younger than me, they have all been so incredibly kind, nurturing and supportive, and often it has felt like they have taken more of a parental role than anything else. It has honestly been very heartwarming how nice these groups have been. When I have nothing to offer them in return, they just selflessly help me. Between the two groups, I have had so many firsts. As an extremely sheltered person who was very focused on their studies, I did not believe many of the things these two groups have done for me would be possible. Small things that others did with friends when they were 12, I did not do until reaching 25. I will always be grateful for how much they have facilitated my development and helped me feel like a normal person. In the past three years, I learnt far more outside the PhD than within it.

The first group is the University of York Gymnastics Society. These insanely talented individuals have shown such patience to me as a complete beginner. In between them jumping up, flipping and twisting three times before they land back on the ground, they have been so friendly and encouraging to me. An exceptional mention must go to our two-time president, Liv. Not in a metaphorical sense, but the club would have literally ceased in her first year without her. She has taken it from strength to strength, increasing the active membership tenfold. I would not have had the wonderful environment to both exercise and meet all of the other incredible people without her.

The gymnasts Beth, Charlotte, Lauren and Robyn have been particularly caring, giving me many lifts to training and always showing me warmth and acceptance. They have all made an environment that I have felt comfortable in and encouraged me to take part in as much as possible. Niccolò, Elizabeth and James have been amazing coaches; despite paying to train themselves, they have put so much time and effort into helping me develop new skills in a friendly way. Even after I accidentally punched one of them in the face in training, I was still shown so much understanding and friendship. There are three main components to life: physical, mental and social ability. All of these people excel in every single area, which makes their empathy towards somebody like me who struggles so much in every one of these areas even more moving. They are also so perfect and talented in every area that I honestly view them as superheroes and gods, as I constantly remind them. Those listed and so many more have ensured I have not broken my neck trying something new; have always been excited to go to training up to five times a week, and they have pushed me safely out of my comfort zone to develop as a person. I have transitioned from being practically non-verbal to not taking a breath whilst speaking. From saying about 50 words a week to missing the social community of gymnastics so much in the summer holidays that I got a part-time job. My transition is a real testament to how wonderful this group has been.

This leads me onto my second group: the Sainsbury's crew. I have been so excited for every weekend, getting to socialise and speak with them all. I have always found it bizarre that I got paid to be there. I would do it for free. I loved socialising with them so much whilst completing tasks, as we talked about life and bantered together. I have found it magical.

I owe so much to Ella. With her support, encouragement and mentorship, I can finally act the way I act with family around other people. I did not think this was possible. To feel so much social energy that I have spent so many hours on the phone with her would have been completely alien to the pre-York version of myself. The conversations are always so easy and engaging. Being her wingman and going through great lengths to get her into a relationship with Ewen has been incredible and has left me with so many funny stories. It means so much to me that they have allowed me to help and watch their love blossom together.

Elliot has been so nice to me, guiding me through so many situations and offering advice that I really trust. I have enjoyed stalking him home after every shift, speaking at him really fast with no breaks like a five-year-old telling their parent about their day at school. Elliot has taught me so much about the world, showing me so much patience as he explains topics which I have been completely clueless. Frances has been so lovely and fiercely protective, creating a really safe, open and affectionate environment. I do not think she will ever truly understand the wave of euphoria that passes over colleagues when we find out she is leading the shift or how special she makes everybody feel. Grace has a wonderful energy lighting up any room she is in, with her constant beaming smile, she never fails to be bubbly and excitable. By contrast, she also shocks me with her wisdom despite her young age. Thank you to so many others, including Bernie, Shirely and Chris, for making each shift so enjoyable.

During my PhD, I have also enjoyed being a graduate teaching assistant. I have found it rewarding to help others, after the incredible support that both the gymnasts and Sainsbury's crew have so selflessly provided for me. I always find that, despite my best efforts, everybody is able to help me far more than I am able to help them. Since I can never pay back all the kindness others have shown me directly, helping students has really meant a lot to me, leading me to desire to be a secondary school teacher after this PhD is over.

Finally, I need to thank my family. Those who have gone far beyond any academic accolade that one can get. My little sisters, Summer and Mae, have always inspired me to act in the way which I would advise them to. Just being there has meant that I have always tried to set a good example for them. My older brother, Chris, has been the closest person to me and my only friend for most of my life. I am grateful that he made so much time for me growing up, as it must have been annoying having a little kid wanting to be with you every second of the day. I treasure the plethora of obscure references that only we share.

Then there are my parents. The bedrock of my very being. I want to thank them for their unwavering support, truly having no vested interests other than my happiness and well-being. Thank them for being exceptional parents my entire life, and doing everything that children can never thank their parents for enough, like changing my nappies, providing me with all the essentials and putting up with my teenage mood swings. My father was the perfect example of a gentleman, never needing to tell me to behave a certain way, instead he led by example. I am honoured to have had such a stellar role model to base my fundamental character on. My mother spent so much time helping all of her children succeed. Explaining to babies the name of every single object must have been mind numbing. She is somebody whom I can turn to for every problem and know she will care, and we can have a good chat. Although they never put any pressure on me, trying to make my parents proud has always been high on the list of objectives. I know that my character is far more important to them, but surprising them with a PhD will hopefully make them even prouder. Without the motivation of the surprise, I do not believe I would have completed my studies at York.

Despite all my academic frustrations during this PhD, I am so glad and grateful to have met all the incredible people during the past three years. I am certain that I will look back on this time as the apex of my life. With many experiences and memories that I will truly never forget, those in my life have meant that I have never felt more complete, fulfilled and like I matter. Thank you all so, so much.

Thank you.

Declaration

The research contained within this thesis was carried out between October, 2022 and March, 2025 in the Department of Chemistry at the University of York. To the best of my knowledge, except where reference is made to other authors within, this research is original and my own.

This thesis contains four pieces of work that have been previously published in four different journals, each as a primary or secondary author alongside my Supervisor Peter Karadakov. Namely,

- The study of fused thiophene rings was published in Chemistry – A European Journal
- The study of thiophene was published in ChemPhysChem
- The study of Sulfinfinitenes was published in Chemical Communications
- The study of Norcorrole was published in Physical Chemistry Chemical Physics

In addition, the work on Annulenes has been presented and discussed at three conferences:

- Magnetically Induced Molecular Currents (MAGIC) Conference, Frauenwörth Germany
- Annual Northern Universities Meeting On Chemical Physics (ANUMOCP) Conference, Durham
- Chemistry@York Research Conference, York

James Edward Cummings

1 Introduction

What is chemistry? The quantum mechanics of valence electrons in interacting atoms. Typically, this involves nuclei sharing their valence electrons to achieve full outer shells. The electronic wavefunctions combine to reduce the energy of the system. Chemists refer to this sharing of electrons as a bond. Electrons can be completely donated from one atom to another to form ions, but more commonly, electrons interact with both atoms, with two electrons between two nuclei considered a single bond; four electrons between two nuclei are known as a double bond, and six electrons between two nuclei are considered a triple bond. The electrons in these bonds are localised to the vicinity of the nuclei donating them. Some atoms, known as transition metals, can delocalise their electrons, allowing electrons to travel between all nuclei in the structure. But what happens when neither of these concepts of a bond can explain the bonding within a molecule? When electrons are delocalised, but only in a small region amongst a small number of atoms?

This problem is generally considered to start almost exactly two centuries ago, in 1825, when Michael Faraday discovered benzene, the archetype for aromaticity. It took another forty years for Kekulé to suggest his theory of 'single' and 'double' alternating bonds in a carbon ring, which is referred to as a Kekulé structure. Despite disagreeing with more modern studies, this was an incredible achievement as it was over thirty years before J. J. Thomson discovered the electron in 1897, so the idea of a bond was not even defined or understood at the time.

The term aromaticity has always been linked to benzene and, despite a controversial definition, is often considered as a property of 'benzene-like' molecules. To non-chemists, the term aromatic is used to describe 'odours' and in chemistry the early scientists of the 1800s used the term to refer to compounds with volatile odours, isolated from vegetable oils,[3] as well as to distinguish these compounds from aliphatic (nonaromatic) fatty compounds,[4] which were known to be carbon compounds.[5] From the mid-1800s, the "aromatic" term was used to define benzenoid compounds for around a century.[4] Whereas, due to their less-defined aromatic characters, non-benzenoids and heterocyclic aromatics were excluded from being described as "aromatic". In the modern day, the International Union of Pure and Applied Chemistry

(IUPAC) defines aromatic as ‘in the traditional sense, having a chemistry typified by benzene’,[6] which is not inherently useful. A more useful definition would be ‘an energy stabilisation due to electron delocalisation in a closed circuit within a molecule’. From this definition, it is easy to identify that antiaromatic molecules also have electron delocalisation, but this delocalisation causes an energy destabilisation. It also propagates the concept that molecules are not either aromatic or nonaromatic, but aromaticity is a spectrum, ranging from stabilised aromatic molecules, to traditionally conjugated nonaromatic molecules, to destabilised antiaromatic molecules. Despite using this definition, there is not a unanimously accepted way to either quantify or compare aromaticity between molecules, and numerous approaches have attempted to quantify or qualify aromaticity. Before exploring the ideas proposed in Section 1.4, we need to understand the theoretical background to aromaticity and the rationale behind the rules that govern them. In order to that, we must first explore basic photophysics concepts.

1.1 Photophysics

Electrons occupy energy levels within atoms and molecules. The lowest energy structure is always desired by the molecule, so the lowest energy levels are occupied first. The lowest energy structure is known as the ground state, and usually consists of a singlet wavefunction, i.e. a wavefunction with paired antiparallel spins. The highest energy electrons can also be configured to have parallel spins, often after excitation, which promotes an electron to a higher energy level. To achieve the excitation, a specific photon is absorbed by the molecule corresponding to the energy difference between the two energy levels.

Figure 1 is a simplified Jablonski diagram, giving a brief overview of the processes discussed in this work. The relative energy levels, E, of molecules are shown. Where the electronic wavefunction is evaluated at a different structure from the optimised state, the electronic state is given first, with the geometry used given after a double dash (//). The left side of the diagram differs from the right, with the $S_0//T_1$ state being of lower (left) or higher (right) energy than the optimised T_1 state. The energy ordering of these levels will differ according to the specific molecule concerned.

From the ground state, a molecule can be excited by a photon (with energy, $E = hf$, where h is the Planck constant and f is the frequency) to the lowest energy triplet state. This is shown by **1** on the diagram and represents a vertical excitation. After the excitation, the geometry will adjust through a process of relaxation **2** to the lowest energy structure for the triplet wavefunction. The energy difference between the optimised ground state and the optimised triplet state is an adiabatic excitation ($\mathbf{x} = \mathbf{1} - \mathbf{2}$). For most molecules in this thesis, the T_1 wavefunction is evaluated at its respective optimised T_1 geometry. This is because the $T_1//S_0$ geometry is short lived and relaxation occurs in a short timeframe. In some instances, a comparison between the magnetic shielding between $T_1//S_0$ and T_1 is presented and discussed. As will be explored, the geometry changes lead to very different results. Depending on the specific molecule, an emission of a photon to return to a singlet state (left side of Figure 1), or absorption of a photon (right side of Figure 1) may be required, as indicated by **3** on both diagrams, respectively. A further relaxation would be required to return to the ground state geometry **4**.

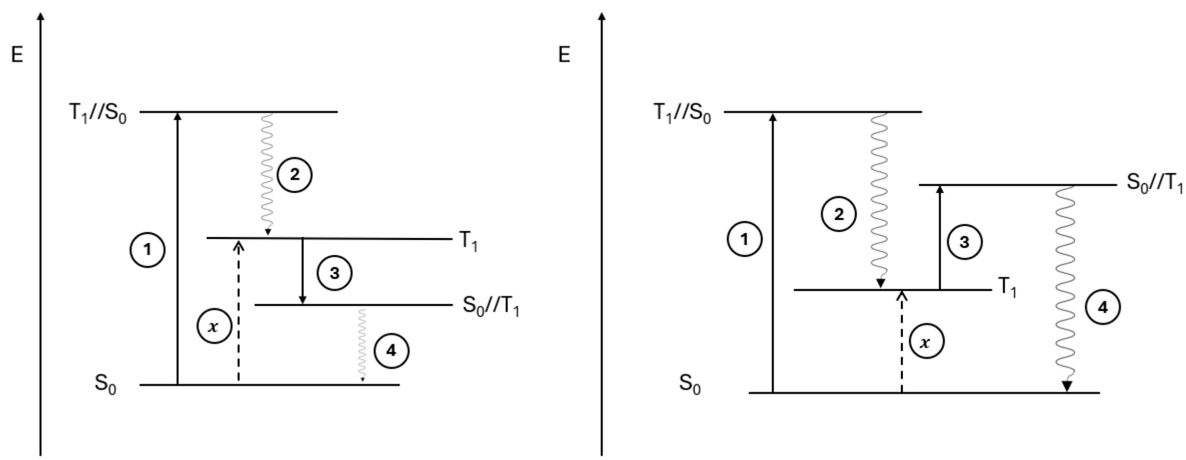

Figure 1: A simplified Jablonski diagram detailing the difference between vertical and adiabatic excitations. See text for further details.

1.2 Hückel's and Baird's Aromaticity Rules

While Hückel's rule has long served as the foundational criterion for predicting aromaticity in the singlet ground state (S_0) of monocyclic conjugated systems, a contrasting behaviour emerges in the lowest triplet excited state (T_1). This inversion is captured by Baird's rule[7], which posits that planar monocyclic systems with $4n$ π-electrons are aromatic in the triplet state, whereas those with $4n+2$ π-electrons are antiaromatic. This subsection provides the rationale for these rules using examples from Hückel molecular orbital (HMO) theory and explores the energetic and orbital consequences that underpin these aromaticity reversals.

1.2.1 Hückel Orbital Energies

Under the HMO approximation, the π-molecular orbitals of an annulene (regular cyclic polyene with N atoms) are constructed by diagonalising a simplified Hamiltonian matrix for the carbon 2p atomic orbitals (AOs) from the conjugated system that accounts only for nearest-neighbour interactions.

The resulting HMO energies are given by:

$$E_k = \alpha + 2\beta \cos\left(\frac{2\pi k}{N}\right), k = 0, 1, 2, .., N - 1 \tag{1}$$

where α is the Coulomb integral (the energy of a carbon 2p AO), β is the resonance integral between neighbouring carbon AOs (typically negative), and N is the number of 2p AOs (or carbon atoms). Each HMO can accommodate two electrons with opposite spins.

The total π-electron energy in the ground state is obtained by summing the energies ϵ_k of the HMOs multiplied by the respective occupation numbers n_k (2, 1 or 0):

$$E_\pi = \sum_{k=0}^{N-1} n_k \epsilon_k. \tag{2}$$

The lowest-energy HMO is non-degenerate, and so is the highest-energy HMO if N is an even number; all other HMOs appear in degenerate pairs.

1.2.2 Aromaticity in the Ground State

In the electronic ground state, electrons fill the HMOs according to the *aufbau* principle. For cyclic conjugated systems with $4n + 2$ π-electrons, this results in a completely filled set of bonding HMOs, thereby maximising delocalisation and minimising electronic repulsion. Benzene, with six π-electrons, exemplifies this behaviour.

The filled bonding orbitals of benzene have energies $\alpha + 2\beta$ (non-degenerate) and $\alpha + \beta$ (doubly degenerate) and so:

$$E_\pi(\text{benzene } \mathrm{S_0}) = 2(\alpha + 2\beta) + 4(\alpha + \beta) = 6\alpha + 8\beta \tag{3}$$

The HMO delocalisation energy of benzene is given by the difference between E_π(benzene S_0) and the combined HMO energies of three double bonds (ethene molecules):

$$\Delta E_{\text{deloc}} = [6\alpha + 8\beta] - 3[2\alpha + 2\beta] = 2\beta. \tag{4}$$

This negative HMO delocalisation energy is an indication of aromatic stabilisation.

In contrast, in a $4n$ system like cyclobutadiene (4 π-electrons) the degenerate pair of HMOs with energy α are singly occupied and with parallel spins (according to Hund's rule). This suggests, incorrectly, that the ground electronic states of $4n$ systems are triplet. The HMO delocalisation energy of cyclobutadiene (the difference between the energy of its π electrons and the combined energies of two double bonds) is given by:

$$\Delta E_{\text{deloc}} = [2(\alpha + 2\beta) + 2(\alpha)] - 4[\alpha + \beta] = 0, \tag{5}$$

which indicates that the ground electronic state of this molecule is not stabilised by its π electrons.

A $D_{4\text{h}} \rightarrow D_{2\text{h}}$ symmetry reduction through a Jahn–Teller distortion from a square to a rectangular geometry removes the degeneracy of the highest occupied MO (HOMO) and leads to a lower-energy geometry with alternating 'single' and 'double' bonds with a singlet ground electronic state. If we introduce separate resonance integrals for the 'single' and 'double' bonds, β_s and β_d, respectively, the HMO energies for rectangular cyclobutadiene become (in order of increasing energies):

$$\varepsilon_{1,4} = \alpha \pm (\beta_d + \beta_s), \quad \varepsilon_{2,3} = \alpha \pm (\beta_d - \beta_s). \tag{6}$$

The HMO delocalisation energy of rectangular cyclobutadiene,

$$\Delta E_{\text{deloc}} = 2(\alpha + \beta_d + \beta_s) + 2(\alpha + \beta_d - \beta_s) - 2(2\alpha + 2\beta) = 4(\beta_d - \beta), \tag{7}$$

is still small, indicating a low level of π-electron stabilisation. The absence or near absence of HMO delocalisation energy in the electronic ground state of cyclobutadiene has been attributed traditionally to the antiaromatic character of this molecule. However, it has been suggested that the high energy of cyclobutadiene is not due primarily to 'antiaromaticity', but rather to angle strain, torsional strain, and Pauli repulsion between the parallel carbon–carbon 'double' bonds.[8]

It should be noted that more advanced calculations show that the ground state of square cyclobutadiene is an open-shell singlet. Clearly, HMO theory explains the ground state aromaticity of $4n + 2$ annulenes well, but it is not equally convincing in the explanation of the ground state antiaromaticity of rings with $4n$ π electrons; other aromaticity criteria, especially magnetic ones, usually do a much better job.

1.2.3 Aromaticity in the Lowest Triplet State

Upon vertical excitation to the lowest triplet state, a single electron is promoted from the HOMO to the lowest unoccupied MO (LUMO), leaving both orbitals singly occupied by electrons with parallel spins. In benzene, this means that one electron is excited from the degenerate bonding HOMO ($\alpha + \beta$) to the degenerate antibonding LUMO ($\alpha - \beta$), and we have:

$$E_\pi(\text{benzene T}_1) = 2(\alpha + 2\beta) + 3(\alpha + \beta) + (\alpha - \beta) = 6\alpha + 6\beta. \tag{8}$$

The corresponding HMO delocalisation energy is thus zero, which, in analogy to the HMO picture of the electronic ground state of cyclobutadiene, indicates that the T_1 state of benzene is not stabilised by its π electrons and could be considered as antiaromatic.

In the case of cyclobutadiene we need to look at the rectangular geometry because, as mentioned earlier, HMO theory incorrectly claims that the electronic ground state of square cyclobutadiene is triplet. Similarly to the analysis of the T_1 state of benzene, we obtain:

$$E_\pi(D_{2h}\ \text{CBD T}_1) = 2(\alpha + \beta_d + \beta_s) + (\alpha + \beta_d - \beta_s) + (\alpha - \beta_d + \beta_s) = 4\alpha + 2\beta_d + 2\beta_s. \tag{9}$$

The corresponding HMO delocalisation energy,

$$\Delta E_{\text{deloc}} = 2(\beta_d + \beta_s) - 4\beta, \tag{10}$$

is very small and could even be positive. Thus, simple HMO theory does not explain why cyclobutadiene becomes aromatic in its T_1 state.

Baird's treatment of the aromaticity reversals in the T_1 states of $4n + 2$ and $4n$ annulenes makes use of a more in-depth treatment based on Dewar's perturbation molecular orbital (PMO) theory.[9] While this treatment is theoretically sound, it is qualitative; if one wishes to quantify the changes in aromaticity between S_0 and T_1, it is more appropriate to apply other aromaticity criteria, for example, magnetic ones.

1.3 Computational Methods

In order to computationally investigate aromaticity, the different electronic structure methods, approximations and model refinements used in computational chemistry in general need to outlined.

1.3.1 HF and DFT

Hartree–Fock (HF) theory describes electron–electron interactions for one electron moving in the average field created by other electrons but fails for many-electron systems as electrons attempt to avoid each other—lowering electron–electron repulsion, causing a stabilisation and hence lower total energy E than predicted by HF theory. Density functional theory (DFT)[10–12] uses functionals of electron density to approximate the effects of electron correlation. In the absence of external perturbations, the Kohn–Sham (KS) formalism[10] decomposes E as

$$E = T_{\mathrm{s}} + E_{\mathrm{nn}} + E_{\mathrm{ne}} + E_{\mathrm{J}} + E_{\mathrm{xc}} \tag{11}$$

where T_{s} is the kinetic energy of the KS non-interacting system, E_{nn} is the nuclear–nuclear repulsion energy, E_{ne} is the nuclear–electron attraction energy, E_{J} is the classical Coulombic electron–electron repulsion energy and E_{xc} is the exchange–correlation energy functional (XCF). The first four terms are straightforward to calculate, but the fifth is unknown, so it must be approximated. Most XCFs are semi-empirical, with their parameters fitted to best match exact calculations or experimental values.

Density functional theory (DFT) utilises exchange correlation functionals (XCFs) of electron density to approximate electron correlation.[13] Generalised gradient approximations[14] (GGAs), such as BLYP, contains no HF exchange, E_{xx}, but were quickly found to overestimate the amount of electron correlation, hence hybrid-GGAs, including B3LYP were created by incorporating a fixed 20% E_{xx}. Increasing the percentage of E_{xx} is (in some respects) synonymous with reducing the amount of non-dynamic electron correlation. The exchange correlation energy of B3LYP $E_{\mathrm{xc}}^{\mathrm{B3LYP}}$ is defined as:

$$E_{\mathrm{xc}}^{\mathrm{B3LYP}} = (1-a)E_{\mathrm{x}}^{\mathrm{LSDA}} + aE_{\mathrm{x}}^{\mathrm{HF}} + b\Delta E_{\mathrm{x}}^{\mathrm{B88x}} + (1-c)E_{\mathrm{c}}^{\mathrm{VWN}} + cE_{\mathrm{c}}^{\mathrm{LYP}} \tag{12}$$

where $E_{\mathrm{x}}^{\mathrm{LSDA}}$, $E_{\mathrm{x}}^{\mathrm{HF}}$ and $\Delta E_{\mathrm{x}}^{\mathrm{B88x}}$ are energy contributions to the exchange interaction from the local spin density approximation (LSDA), Hartree–Fock and B88 exchange[15] components respectively. $E_{\mathrm{c}}^{\mathrm{VWN}}$ and $E_{\mathrm{c}}^{\mathrm{LYP}}$ are Vosko–Wilk–Nusair (VWN)[16] and Lee–Yang–Parr (LYP)[17] correlation functionals. Their individual contributions to B3LYP are determined by the coefficients a, b and c which have values 0.20, 0.72 and 0.81, respectively. There are many DFT methods, but B3LYP is the main method used in this thesis, due to its ubiquity across computational chemistry and ability to describe systems adequately when paired with a reasonably sized basis set. Other DFT functionals are formulated in a similar way.

1.3.2 Many-Body Perturbation Theory

Many-body perturbation theory (MBPT) can be understood as a sequence of refinements applied to the simpler Hartree-Fock (HF) method. This approach aims to incorporate the effects of electron correlation. A widely employed approximation within MBPT is Møller-Plesset second-order (MP2) perturbation theory.[18] This method starts with the unperturbed HF approximation as the zeroth-order description and subsequently introduces small corrections at the first and second order using the MBPT framework.

To begin, the many-electron Hamiltonian operator, $\hat{H}$, is modified according to:

$$\hat{H} = \hat{H}_0 + \lambda\hat{V} \tag{13}$$

where λ represents a small perturbation parameter, $\hat{V}$ is the perturbation operator, and

$$\hat{H}_0 = \sum_i \hat{f}_i \tag{14}$$

with $\hat{f}_i$ being the Fock operator. Consequently, the original Schrödinger equation,

$$\hat{H}\psi = E\psi \tag{15}$$

where E denotes the system's energy, transforms into:

$$(\hat{H}_0 + \lambda\hat{V})\psi_i = E_i\psi_i \tag{16}$$

Given the small magnitude of λ, both the perturbed wavefunction and energy can be expressed as power series. In these series, the initial term corresponds to the zeroth-order contribution, the second term to the first-order correction, and the third to the second-order correction, and so forth. Notably, the zeroth-order wavefunction is identical to the HF wavefunction, implying that the zeroth-order energy contribution is the sum of the individual orbital energies:

$$E^{(0)} = \sum_{i=1}^{N} \epsilon_i \tag{17}$$

The first-order energy correction is simply the difference between the HF energy and the zeroth-order energy:

$$E^{(1)} = E_{HF} - \sum_{i=1}^{N} \epsilon_i \tag{18}$$

This first-order correction is known as MP1. However, achieving an improvement over the original HF energy necessitates at least the MP2 energy correction. The second-order correction is given by:

$$E^{(2)} = \sum_i \sum_{j>i} \sum_p \sum_{q>p} \frac{(\langle\psi_p\psi_q|\psi_i\psi_j\rangle - \langle\psi_p\psi_q|\psi_j\psi_i\rangle)^2}{\epsilon_i + \epsilon_j - \epsilon_p - \epsilon_q} \tag{19}$$

where the indices p and q refer to virtual orbitals, and i and j refer to occupied orbitals. The total MP2 energy is then obtained by summing $E^{(0)}$, $E^{(1)}$, and $E^{(2)}$, which simplifies to the sum of the HF energy and $E^{(2)}$.

1.3.3 CASSCF

The complete active space self-consistent field (CASSCF) method,[19–22] is a type of multi-configurational self-consistent field (MCSCF) method. The MCSCF method produces reliable results for states of different spin multiplicities and for bond rearrangement processes during chemical reactions. The CASSCF procedure involves dividing orbitals into three subspaces: an inactive space has doubly occupied orbitals, an active space which contains the orbitals that contribute most to the system's multireference character, and a set of unoccupied virtual orbitals. The idea is that the first and last of these subspaces do not require the same rigorous approach as the active space, since these orbitals are less likely to change energy ordering. The active space in CASSCF includes all possible electron arrangements (configurations or configuration state functions, CSFs) for n electrons distributed among m orbitals, CASSCF(n,m). One can select which orbitals comprise the active space, minimising the number of CSFs by correlating the orbitals in the active space only. This decision is not always clear-cut, and calculation with a less accurate method is still often required first, such as Hartree-Fock (HF), so one can inspect the orbitals and identify which ones require a multiconfigurational treatment. If the wrong selection is made, the results are very poor.

The orbitals in the active space are usually π electrons, and the most straightforward example would be benzene treated with a CASSCF(6,6) wavefunction. 36 σ electrons populate 18 doubly occupied σ orbitals forming the inactive space. These orbitals can be optimised or can be kept "frozen" during the CASSCF calculation. The 6 π electrons would be selected for the active space, and the starting guess for the 6 π orbitals in this space can be provided by three occupied and three virtual π orbitals from a preliminary HF calculation. The ground state benzene CASSCF(6,6) wavefunction includes 175 singlet CSFs. Extending this method to larger and fused rings takes significant computational time. Current computational resources suggest that CASSCF(20,20) is approaching the limit of what is achievable,[23] due to the exponential cost of increasing the active space. The majority of the work in this thesis is based on the systematic modification of molecules, and as some sections will demonstrate, the importance of a consistent model chemistry for determining the relative aromaticities should not be understated. Hence, CASSCF is not used significantly in any new calculations presented in this thesis, but results are close to previous calculations using CASSCF should be a strong indication that the methods utilised in this thesis are valid.

1.3.4 Basis Sets

Basis sets are comprised of basis functions used to represent the electronic wave function of a molecule, essentially acting as building blocks to create molecular orbitals by combining them in linear combinations; these functions are typically centred on individual atoms and resemble atomic orbitals. The better the description, the better the results, but the longer the calculations will take. Due to their computational efficiency, Gaussian functions are used to describe orbitals. A primitive Gaussian function takes the form:

$$G_{nlm}(r,\theta,\psi) = N_n r^{n-1} e^{-\alpha r^2} Y_l^m(\theta,\psi) \tag{20}$$

where n is the principal quantum number, N is the normalising constant, r is electron-nuclear separation and α is an exponential parameter. Together $r^{n-1}e^{-\alpha r^2}$ is the radial part and $Y_l^m(\theta,\psi)$ is the angular part of the wavefunction. Gaussian-type functions fail to describe the correct radial dependence near the nucleus (being flat rather than steep) and at large radial distances (decaying too rapidly) in the same way which more computationally expensive Slater-type functions can, whose dependence is $e^{-\alpha r}$ instead of $e^{-\alpha r^2}$. To achieve better behaviour, linear combinations of the primitive Gaussians are formed to approximate the radial part of a Slater-type orbital. This linear combination is not optimised further in the energy variational calculation, but fixed and considered as a single function. The linear combination of primitive Gaussian functions is called a contracted Gaussian function. Generally, the more primitives a contracted basis function has, the better the description it will provide.

Table 1: The primitives (round brackets) and contractions (square brackets) in the triple-ζ basis sets used in this work.

Row	**def2-TZVP**	**6-311++G(d,p)**	**6-311++G(2d,2p)**
First row	(5s,1p) → [3s,1p]	(6s,1p) → [4s,1p]	(6s,2p) → [4s,2p]
Second row	(11s,6p,2d,1f) → [5s,3p,2d,1f]	(12s,6p,1d) → [5s,4p,1d]	(12s,6p,2d) → [5s,4p,2d]
Third row	(14s,9p,3d,1f) → [5s,5p,2d,1f]	(14s,10p,1d) → [7s,6p,1d]	(14s,10p,2d) → [7s,6p,2d]

In this thesis, def2-TZVP is used for geometry optimisations, and either 6-311++G(d,p) or 6-311++G(2d,2p) are used for magnetic shielding calculations, depending on the size of the molecule in question, and which other molecules comparisons need to be made. All three are valence triple-ζ basis sets, meaning each valence orbital will be represented by three contracted basis functions. The two popular modifications to basis sets are generally adding polarisation or diffuse functions. The former is included to help describe how an atom's electron density polarises in molecules, so it is important for modelling chemical bonding because bonds are often polarised. Hence, this is a greater factor for geometry optimisations to get the shape of the molecule correct, whilst shielding is not as dependent on polarisability. Polarised basis functions describe an orbital with a higher angular momentum quantum number than required to contain all electrons. As can be seen from Table 1, def2-TZVP contains more polarisation functions than the Pople basis sets and hence is better for geometry optimisations. Diffuse functions are extended Gaussian basis functions with a smaller exponent, allowing greater flexibility in the atomic orbitals in regions far from the nuclei, allowing for a better description of long-range properties. Magnetic shielding is not typically long-range, however, as we encounter larger and more unique molecules at sub-optimal geometries, we can generate large shieldings, so it is advisable to have this description. Not only are these basis sets sufficient for meaningful calculations, but these basis sets have been the most commonly used by the predecessors of this research, and hence are also a good choice for direct comparisons to other molecules.

1.3.5 Model Chemistry Refinements

In quantum chemical calculations, the accuracy of computed geometries, energies, and response properties depends not only on the choice of functional and basis set, but also on how strictly the calculations are converged and how well-known physical effects are treated. Density functional theory calculations are particularly sensitive to numerical thresholds, dispersion effects, and response-property convergence. Consequently, several non-default computational settings were required to ensure that all results presented in this thesis are both physically meaningful and numerically robust.

A fundamental requirement of any geometry optimisation is that the resulting structure corresponds to a true local minimum on the potential energy surface rather than a saddle point or transition state. Geometry optimisations alone cannot guarantee this, as they provide no information about the curvature of the potential energy surface at the stationary point. To address this limitation, a vibrational analysis is necessary to confirm the absence of imaginary frequencies. In addition, vibrational calculations provide zero-point energies and thermal corrections, which are essential for meaningful comparisons of relative energies and thermodynamic quantities. To satisfy these requirements, all optimised structures were followed by an analytic harmonic frequency calculation, implemented in GAUSSIAN using the 'Freq' keyword.

Beyond verifying the nature of the stationary point, reliable downstream property calculations—such as NMR shieldings or excited-state analyses—require geometries that are converged to a higher standard than the default optimisation criteria. Loose convergence thresholds can leave residual forces on the nuclei, leading to small but systematic geometric errors that propagate into calculated energies and response properties. This issue is particularly important when interpreting small energy differences or subtle magnetic effects. To minimise such artefacts and ensure highly converged structures, stricter optimisation thresholds were imposed by employing the 'Opt(VeryTight)' keyword, which enforces tighter limits on both maximum and root-mean-square forces and displacements.

Another significant source of error in conventional DFT calculations arises from the inadequate description of long-range dispersion (van der Waals) interactions. Hybrid functionals such as B3LYP do not inherently capture these effects, which can lead to systematic errors in molecular geometries, relative energies, and conformational preferences. This deficiency is especially relevant for systems where weak noncovalent interactions, intramolecular contacts, or extended π-systems play an important role. To correct for this missing physics, an empirical dispersion correction was included in all geometry optimisations. This was achieved using Grimme's D3 dispersion model with Becke–Johnson damping, activated in GAUSSIAN via the 'EmpiricalDispersion=GD3BJ' keyword.[24]

Together, the use of tighter optimisation thresholds, explicit vibrational verification of minima, and dispersion corrections establishes a geometry optimisation protocol that is both numerically rigorous and physically realistic. All molecules in this thesis were therefore optimised at the B3LYP/def2-TZVP level with Opt(VeryTight), Freq, and EmpiricalDispersion=GD3BJ applied consistently.

Magnetic shielding calculations are particularly sensitive to numerical noise, incomplete SCF convergence, and instabilities in the electronic response to external perturbations. As shielding tensors are second-order response properties, even small inaccuracies in the underlying electron density or its magnetic response can lead to significant errors in the final values. For this reason, additional measures were required to ensure numerical stability and reproducibility.

One important source of numerical error in DFT-based magnetic shielding calculations is the finite numerical integration grid used to evaluate exchange–correlation contributions. Inadequate grid density can introduce integration artefacts, especially for systems with delocalised electron densities or heavier atoms, leading to inconsistent or non-smooth shielding tensors. To mitigate this issue and reduce numerical noise, a very dense integration grid was employed throughout. In GAUSSIAN, this was implemented using the 'Int(Grid=SuperFine)' keyword.

Accurate magnetic shielding calculations also require a highly converged self-consistent field solution. Since shielding tensors depend directly on the quality of the electronic ground state, residual SCF errors can propagate into the response calculation and compromise the reliability of the results. Default SCF convergence thresholds are often sufficient for total energies but may be inadequate for sensitive magnetic properties. To ensure that the electron density was converged to a level appropriate for response calculations, stricter SCF convergence criteria were enforced using the 'SCF(Tight)' keyword.

Finally, the solution of the coupled-perturbed Hartree–Fock (or Kohn–Sham) equations plays a central role in determining magnetic response properties. When multiple perturbations are treated simultaneously, numerical instabilities or convergence difficulties can arise, particularly in larger or electronically delicate systems. Separating the treatment of individual magnetic perturbations can improve stability and reduce cross-coupling errors in the response equations. For this reason, the magnetic shielding calculations in this thesis employed a separated solution of the coupled-perturbed equations, implemented in GAUSSIAN via the 'CPHF(Separate)' keyword. Although computationally more demanding, this approach improves convergence robustness and enhances the reliability of the resulting shielding tensors.

In combination, the use of a superfine integration grid, tight SCF convergence, and a separated CPHF treatment constitutes a deliberate strategy to maximise the numerical accuracy of all magnetic shielding calculations presented in this thesis. These settings are particularly important when small differences in shielding values between closely related systems are interpreted, as is the case throughout this work.

1.4 Aromaticity Criteria

A topic as important as aromaticity has many interpretations, and each scientist has different arguments for the best method to research the phenomenon, based on their own experience and which aspect of aromaticity they place the most emphasis on, whether it be the energy stabilisation, electron delocalisation or the equalisation of bond lengths. Figure 2 is a non-exhaustive representation of some of the popular methods to assess the level of aromaticity in given systems. Comparing and fully understanding all of these methods would be the scope of an entire academic career.

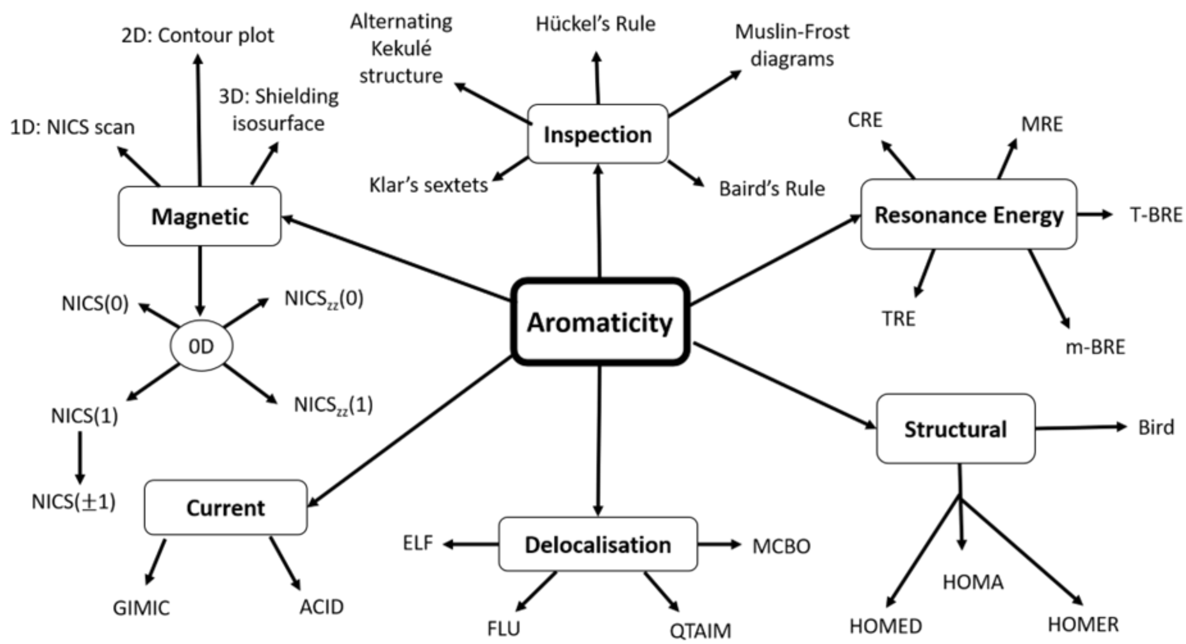

Figure 2: Some of the commonly utilised metrics to assess or quantify aromaticity, grouped according to their theoretical foundations.

Due to the links with nuclear magnetic resonance (NMR) experimental results, magnetic shielding is of great interest to scientists as it offers the only criteria that can be linked to experiment. Additionally, through the Biot-Savart law, it can be shown that current and magnetic studies should provide identical results. Yet magnetic shielding, in particular three-dimensional isosurfaces, have not historically been investigated in depth, with very few candidate molecules studied. Hence, the motivation for a magnetic shielding study is enormous and forms the focus of this thesis. The methods and concepts underpinning magnetic shielding are mainly discussed in the following subsections. For comparison, some structural indices were also calculated, so these will be briefly explained first.

1.4.1 HOMA

Whilst magnetic criteria are the focus of this research, reference to other indices is often useful. The simplest aromaticity indices are geometrical, comparing the geometry (typically bond lengths) to reference values from highly aromatic systems. The most popular of these is arguably the Harmonic oscillator measure of aromaticity (HOMA). All that is required are the atomic coordinates of the optimised geometry, and in milliseconds, these geometry indexes are outputted. HOMA is usually reported as

$$\text{HOMA} = 1 - \sum_i \frac{\alpha_{i,j}}{N}(R_{i.j} - R_{\text{O}})^2 \tag{21}$$

where N is the total number of atoms in the ring, j is the atom next to atom i; α is a pre-calculated constant given by the inverse of the average of the squares of the deviation of single and double bonds from R_{ref}:

$$\alpha = \frac{2}{(R_{\text{s}} - R_{\text{O}})^2 + (R_{\text{d}} - R_{\text{O}})^2} \tag{22}$$

with R_{s} and R_{d} are the experimental bond lengths of single and double bonds, respectively, whilst R_{ref} is defined as

$$R_{\text{O}} = \frac{R_s + wR_d}{1 + w} \tag{23}$$

where w is the ratio of force constants of double (k_{d}) and single (k_{s}) bonds:

$$w = \frac{k_{\text{d}}}{k_{\text{s}}} \tag{24}$$

so is often set equal to 2.0 (although not always, $w = 4.2$ for the boron–nitrogen bond). R_{O} is the average separation between double and single bonds of the constituent atoms, weighted according to the force constants, as can be seen from substituting equation (4) into (3) and rearranging:

$$R_{\text{O}} = \frac{k_s R_s + k_d R_d}{k_s + k_d} \tag{25}$$

Due to its fast computation and correlation with other aromaticity measures, HOMA is a popular aromaticity measure. However, for some condensed polycyclic structures (including those studied in this thesis), the measure fails. This is partly due to an underlying assumption that all aromatic rings will have a similar geometry in larger molecules, which is not always the case, as rings get forced to connect with other groups and may lose planarity.

HOMA is strongly dependent on the reference parameters selected, so there have been numerous attempts to modify the parameters for specific systems including: HOMAc[25] where the parameters were determined using both aromatic and antiaromatic reference structures instead of the nonaromatic structures used in the standard parameterisation; Harmonic Oscillator Model of Electron delocalisation (HOMED)[26] an extension of HOMA for rings with an uneven number of bonds; Harmonic Oscillator Model of Excited-state aRomaticity (HOMER)[27] index reparametrised the R_O values for molecules in the T_1 state, and HOMA optimised for cations and conjugated radicals.[28] Some of these are briefly discussed for comparison in this thesis, but are not the main focus of the research. Values of these geometric indices were computed using Multiwfn.[29]

1.4.2 Magnetic Criteria

Magnetic criteria are closely related to those based on current and arise from similar equations, which can be directly linked through Maxwell's equations. Studies using ring currents include the popular Gauge including magnetically induced current (GIMIC) method,[30] which provides a good insight into aromaticity, bonding and electron delocalisation. This thesis focuses on magnetic criteria, which have the advantage of also calculating magnetic shielding for nuclei, which can be compared to experimental measurements. This is because the theory originates from nuclear magnetic resonance (NMR) theory, where the magnetic field at nucleus J deviates from the applied field $\mathbf{B}_0$ due to the shielding of electrons. Assuming nuclei are translationally stationary with respect to the static external magnetic field,[31] Ramsey's theory[32] dictates nuclear magnetic moments, μ, of molecules (in a non-degenerate ground state) may be considered classical vectors because their dynamics are significantly slower than those of electrons.[33] Electron clouds adiabatically follow rotating nuclear moments and at each moment in time, ground state electrons correspond to instantaneous orientations of nuclear moments. Consequently, similar to nuclear positions and applied magnetic fields B, components of μ may be considered external parameters in the electronic Born–Oppenheimer Hamiltonian.[33] The ground state energy $E(\mu, B)$ can be expanded in a Taylor series as a function of μ and B, involving the magnetic shielding tensor, σ:

$$E(\mu, B) = E_0 + \sum_{\alpha\beta} B_\alpha \sigma_{\alpha\beta} \mu_\beta + \text{higher order terms} \tag{26}$$

where E_0 is the molecular energy with neither an applied magnetic field nor nuclear moments. Assuming E_0 is a non-degenerate eigenvalue of a time-even Hamiltonian energy removes odd degree terms.[33] The equation also only considers one magnetic nucleus when, in reality, each nucleus will have its own shielding tensor. This can be expanded to energy $E(\mu_1, \mu_2, ..., B)$ to account for all nuclear moments. The second term equation 26 is simply the Zeeman interaction between μ and the induced field $-B \cdot \sigma$. Through perturbation theory, equation 26 can be used to determine σ and experimentally verified using

$$\mathbf{B}_J = (\mathbf{I} - \sigma_J)\mathbf{B}_0 \tag{27}$$

In NMR, the magnetic shielding tensor σ at a given nucleus is a 3×3 matrix with components in the $\alpha\beta$ direction (where both α and β are either x, y or z directions) is given by

$$\sigma_{\alpha\beta} = \frac{\partial^2 E}{\partial \mu_\alpha \partial B_\beta} \tag{28}$$

Theoretically, a similar approach can be taken at points which are not nuclei, with μ and B arbitrary, since, regardless of whether a nucleus is present or not, the differential is evaluated at zero. Whilst this 'off-nucleus' shielding does not directly measure the degree of aromaticity and measures absolute magnetic shielding, it provides important indirect descriptions of the electronic structure between the nuclei.

In line with previous work on magnetic shielding and ring currents in triplet systems (see, for example, refs. 34 and 35), the UB3LYP-GIAO magnetic properties of the T_1 states of compounds computed in this thesis include the contributions arising from the perturbation to the Kohn-Sham orbitals only. The omission of the large terms associated with the interaction of the electronic spin angular momentum and the magnetic field[36,37] means that the reported numbers will exhibit considerable differences from experimental measurements when and if such measurements become available. The advantage of the approach adopted here is that the values reported for triplet states can be compared directly to those for singlet states.

1.4.3 NICS

The magnetic shielding at a single point is known as nuclear-independent chemical shifts (NICS).[38,39]

$$\sigma_{\text{iso}}(\mathbf{r}) = \tfrac{1}{3}[\sigma_{xx}(\mathbf{r}) + \sigma_{yy}(\mathbf{r}) + \sigma_{zz}(\mathbf{r})] \tag{29}$$

For structures containing rings, the point is usually chosen as the geometrical centre of the explicit members of that ring, determined by averaging the atomic coordinates, denoted as NICS(0).[40] There is concern that the σ-bonding orbitals may influence the results, so sometimes a value 1 Å above the planar ring, since π-bonding electrons typically have a significant probably of being further away from the nucleus, whilst σ-orbitals extend out of the plane negligibly. If the ring is not planar, then the NICS(1) value will vary on either side of the plane, hence this is replaced with NICS($\pm$1). This requires some consideration, as

NICS inside a bowl-shaped structure will have contributions from multiple rings, whilst outside the 'bowl' will not. Additionally, the argument for NICS(1) over NICS(0) is not a straightforward one, as no atomic orbitals exist in bonding and many are sp^2 hybrids. Nevertheless, having a simple single number to compare between molecules is very useful and computationally far faster than performing multiple calculations, so NICS indices are used for nearly every molecule in this work.

1.4.4 One-Dimensional Scans

To partially overcome the arbitrary nature of selecting a single point in the NICS calculations, NICS scans produce one-dimensional plots of NICS values, typically in a line perpendicular to the molecular plane. The drawback is that these calculations will take far longer than single-point NICS and lose quantitative comparison. The scans do not often alter the conclusions which can be drawn from the quicker NICS(0) and NICS($\pm$1) calculations. Figure 3 is a NICS scan of benzene, perpendicular to the molecular plane and passing through the molecular centre. NICS scans can be useful since there is nothing intrinsically significant about the centre of the ring, or 1 Å above it, so this accounts for more possibilities and allows an identification of the most shielded region, for example, at 0.8 Å above the molecular plane for benzene.

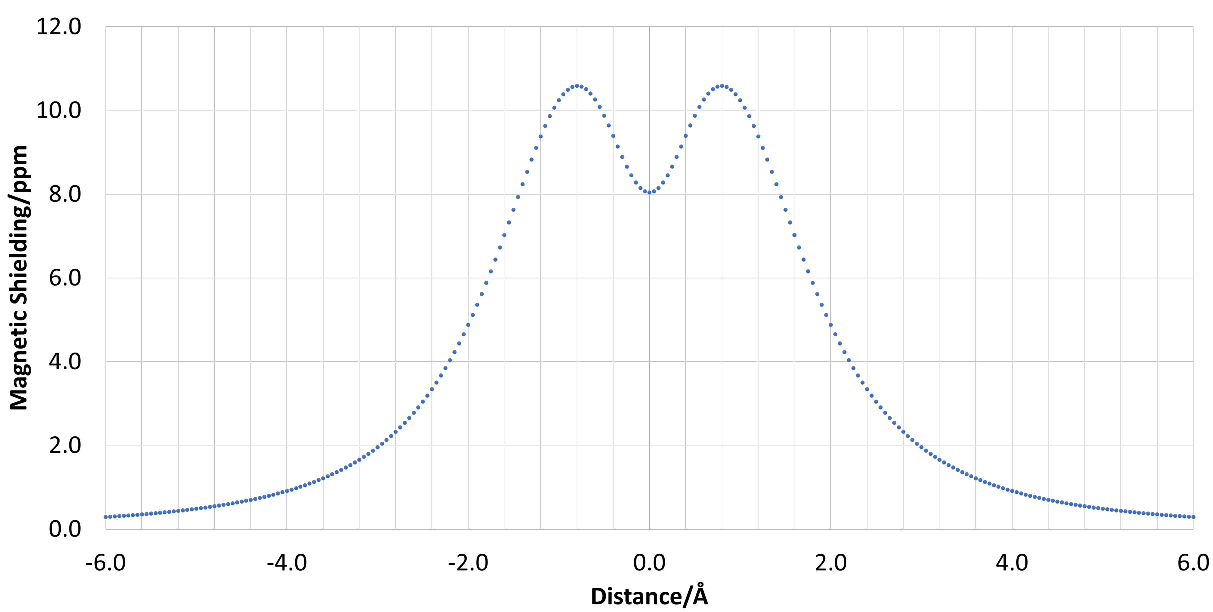

Figure 3: The magnetic shielding along a scan coordinate perpendicular to the molecular plane of benzene passing through the molecular centre.

1.4.5 Two-Dimensional Scans

Calculating NICS values across an entire plane provides rich detail of the bonding across the entire molecule. Unlike NICS scans, the plane usually contains the molecule instead of scanning perpendicular to it. Contour plots enables a range of chemical shift values to be easily displayed on a single plot, unlike a three-dimensional approach. Figure 4 of both benzene and cyclobutadiene published by Karadakov and Horner,[1] demonstrates the stronger shielded regions around bonds in aromatic molecules compared to antiaromatic molecules and the central deshielded region in antiaromatic molecules. The drawback of the method is that only one plane is viewed at a time, losing any information about the third dimension. If one is concerned about σ-bonding influencing the assessment of aromaticity, a parallel plane can be set 1 Å above the molecular plane for the contour plot. Contour plots were favoured by Karadakov, Horner and Al-Yassiri,[41,42] but as the variety of molecules studied with magnetic shielding continues to expand, the molecules of interest can often be very non-planar, particularly for relaxed triplet state geometries for molecules which were planar in their ground state. Additionally, compounds with many fused rings can have rings lying in different planes, meaning selecting an appropriate plane is near impossible. Hence, this thesis transitions away from two-dimensional NICS contour plots to three-dimensional NICS isosurfaces.

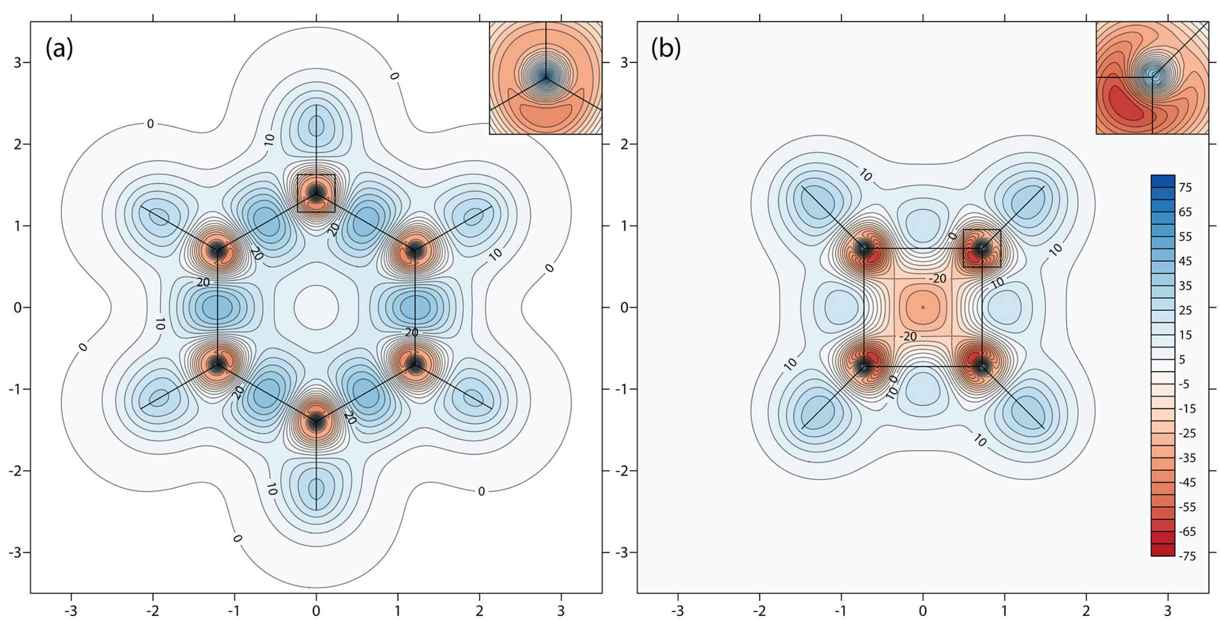

Figure 4: Examples[1] of the 2D isotropic shielding maps for benzene (a) and cyclobutadiene (b) calculated at CASSCF(6,6)-GIAO/6-311++G(d,p) and CASSCF-(4,4)GIAO/6-311++G(d,p), respectively. (The above shielding contours are used here with permission.)

1.4.6 Three-Dimensional Scans and Isovalue Surfaces

NICS values calculated around the entire volume encompassing the molecule ensure no information is omitted. NICS calculations were first carried out across three-dimensional lattices with the resulting values plotted as isochemical shielding surfaces (ICSSs) by Kleinpeter and co-workers in 2001.[43] Consideration as to the best chemical shift to view the surface is required. They used (and continue to use[44]) quite small chemical shift thresholds, with shielding investigated at 5 ppm or lower, and deshielding at just −0.5 ppm. Karadakov and co-workers have typically used larger chemical shifts, at either 12 or 16 ppm for both shielding and deshielding and just a single chemical shift threshold in order to better focus on aromaticity and produce more intuitive plots. It could be argued that one of the slight drawbacks of this method is that only one chemical shift (and all values above it) can be viewed on any one plot without it becoming confusing for more complex molecules with multiple fused rings. Additionally, some features (such as deshielding around nuclei with valence 2p electrons) can be difficult to identify through a transparent shielding isosurface. By adjusting the transparency of the negative (orange) and positive (blue) isosurfaces, this problem may be minimised. An example of 3D magnetic shielding in Figure 5 shows the archetype aromatic and antiaromatic molecules benzene and cyclobutadiene, respectively.

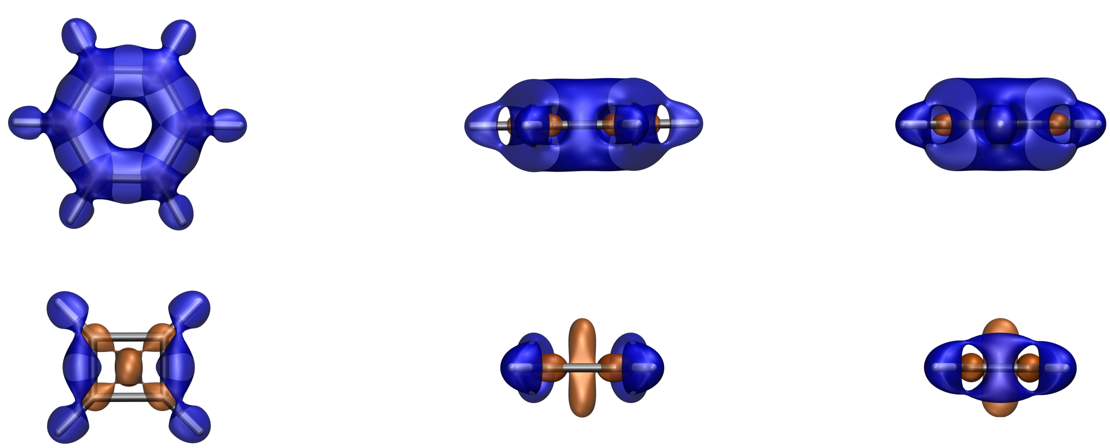

Figure 5: The magnetic shielding ($\sigma_{\text{iso}}(\mathbf{r})$) around benzene (top) and cyclobutadiene (bottom) with $+16$ ppm (blue) and -16 ppm (orange).

The volume data required to construct S_0 isotropic shielding isosurfaces in this thesis was primarily obtained through RB3LYP-GIAO/6-311++G(d,p) calculations at the RB3LYP-D3(BJ)/def2-TZVP optimised geometry of each molecule investigated. The volume data needed for T_1 isotropic shielding isosurfaces were primarily obtained in a similar way, using UB3LYP-GIAO/6-311++G(d,p) calculations at UB3LYP-D3(BJ)/def2-TZVP geometries. In all volume data calculations, $\sigma_{\text{iso}}(\mathbf{r})$ was evaluated on regular three-dimensional grids of points with a spacing of 0.1 Å. To reduce computational effort, shielding tensors were calculated at the symmetry-unique points (using Abelian symmetry only) and then data was replicated via symmetry to create a complete grid. To enable visualisation, all $\sigma_{\text{iso}}(\mathbf{r})$ values from the RB3LYP-GIAO/6-311++G(d,p) and UB3LYP-GIAO/6-311++G(d,p) calculations for each molecule were assembled in GAUSSIAN[45] cube files and isosurfaces visualised in VMD.[46] The main exception to this, is the work on annulenes, in which a larger basis set of 6-311++(2d,2p) was used instead of 6-311++G(d,p) for shielding calculations and grids of points were spaced by 0.05 Å. Any other differences are highlighted in the relevant sections.

1.5 Chemical Shift Threshold

Rigorously, $\sigma_{\text{iso}}(\mathbf{r})$ can be decomposed into the direct sum of diamagnetic and paramagnetic components.[47] The results in this thesis refer to the net combination of these influences. The diamagnetic contribution is typically positive, manifests as shielding, and is highly dependent on the total electron density. Conversely, the paramagnetic contribution is typically negative, manifests as deshielding, and depends on the perturbability of the wavefunction by an external magnetic field. Comparisons between moving from benzene to cyclobutadiene have previously revealed that decreases in the positive diamagnetic term appear to be as crucial as the parallel increase in the magnitudes of the respective negative paramagnetic contributions.[47] Throughout this thesis, shielding is represented in blue and deshielding in orange. Thus, to a lay reader, they can interpret the blue regions as areas where electrons are present and 'happy' so form nice stable bonds and orange regions as where the electrons are 'unhappy' and don't want to be there.

The exemption to this small ovoid deshielded regions inside which $\sigma_{\text{iso}}(\mathbf{r})$ becomes negative around some carbon nuclei. These regions are more noticeable in the $\sigma_{\text{iso}}(\mathbf{r})$ isosurface plots for states in which the C–C and C–H bonds are less shielded, but are present in most aromatic systems, albeit obscured by greater shielding above and below the molecular plane. In highly antiaromatic molecules, these are often connected to, or encompassed by, the deshielded region expanding from the centre. Similar deshielded 'halos' around sp^2 and sp-hybridised carbon atoms and other sp^2 hybridised first main row atoms have been observed previously in conjugated rings,[1,48,49] as well as in open-chain conjugated molecules such as ethene, ethyne and *s-trans*-1,3-butadiene.[50,51] As is shown in this thesis, these deshielded ovoids are not present in sp^3 hybridised carbons, such as those in ethane. Hence, the presence of deshielded 'halos' around the carbon atoms in $\sigma_{\text{iso}}(\mathbf{r})$ isosurface plots reported in this thesis suggests that the hybridisation states of these atoms are close to sp^2. The close to sp^2 hybridisation states of the carbon atoms suggests that referring to the Kohn–Sham orbitals in the non-planar annulenes examined in this thesis as (almost) σ and π orbitals can be viewed as a reasonable approximation; this approximation is also supported by comparisons between the shapes of these orbitals. Hence, these regions do not require rigorous discussion in most cases; they do not indicate instability and are only used to aid identification of sp^2 hybridised atoms.

Something that is of great interest in conferences and discussions with members of the scientific community is the selection of the chemical shift threshold for creating the shielding plots. This is the value for which values of a magnitude greater than or equal to the threshold will be visible in the shielding plot. Kleinpeter originally used quite low thresholds, but it is proposed this may not be optimal or intuitive for our purpose of identifying bonding. Each molecule will vary, so the exact thresholds at which certain features of the isosurface plots are no longer visible and are not overly important, and this section suggests some of the more general trends.

1.5.1 The Nonaromatic Case: C_5H_{10}

The discussion shielding starts with the nonaromatic case of C_5H_{10}. As can be seen from Figure 6, low chemical shift thresholds of 2 and 4 ppm create a completely shielded molecule, with no shielding hole at the molecular centre. It should be noted that even at these low values, there are no deshielded (negative $\sigma_{iso}(\mathbf{r})$) regions. At 8 ppm, a shielding hole appears in the centre of the molecule. As the threshold increases, so does the size of the shielding hole. For an intuitive picture of bonding, shielding should be along the bonds. As the threshold increases to 18 ppm, the shape of the molecule begins to become apparent in the shielding absence, and by 24 ppm, the absence of shielding takes the shape of a pentagonal prism and is easily distinguishable from the cylindrical one at lower thresholds.

At the same time, there are these internal ovoid absences in shielding around the carbon nuclei, which first appear around 12 ppm. By 28 ppm, the ovoid non-shielded regions extend to the surface. At 32 ppm and beyond, shielding is localised around bonds and not nuclei. Switching from 40 to 44 ppm, shielding changes from localisation along C–H and C–C bonds, to just C–C bonds. By 52 ppm, no surface is visible, although this could just be from the thickness of the bond representation.

The diamagnetic term dominates for stable molecules, hence shielding in simple terms can be used to indicate favourable bonding. This is often localised between two atoms, and in such a case, represents a single bond. In a simple molecule, the electron has no preference for which side of the bond it is situated on, so the $\sigma_{\text{iso}}(\mathbf{r})$ at a particular threshold will create a cylindrical shape around the bond. In a cyclical system, comprised of single bonds, these shieldings superimpose, which typically creates an absence in shielding in the $\sigma_{\text{iso}}(\mathbf{r})$ isosurface plots. Provided there is not a destabilising effect (i. e. an antiaromatic molecule), combinations of double and single bonds will yield a similar shielding picture.

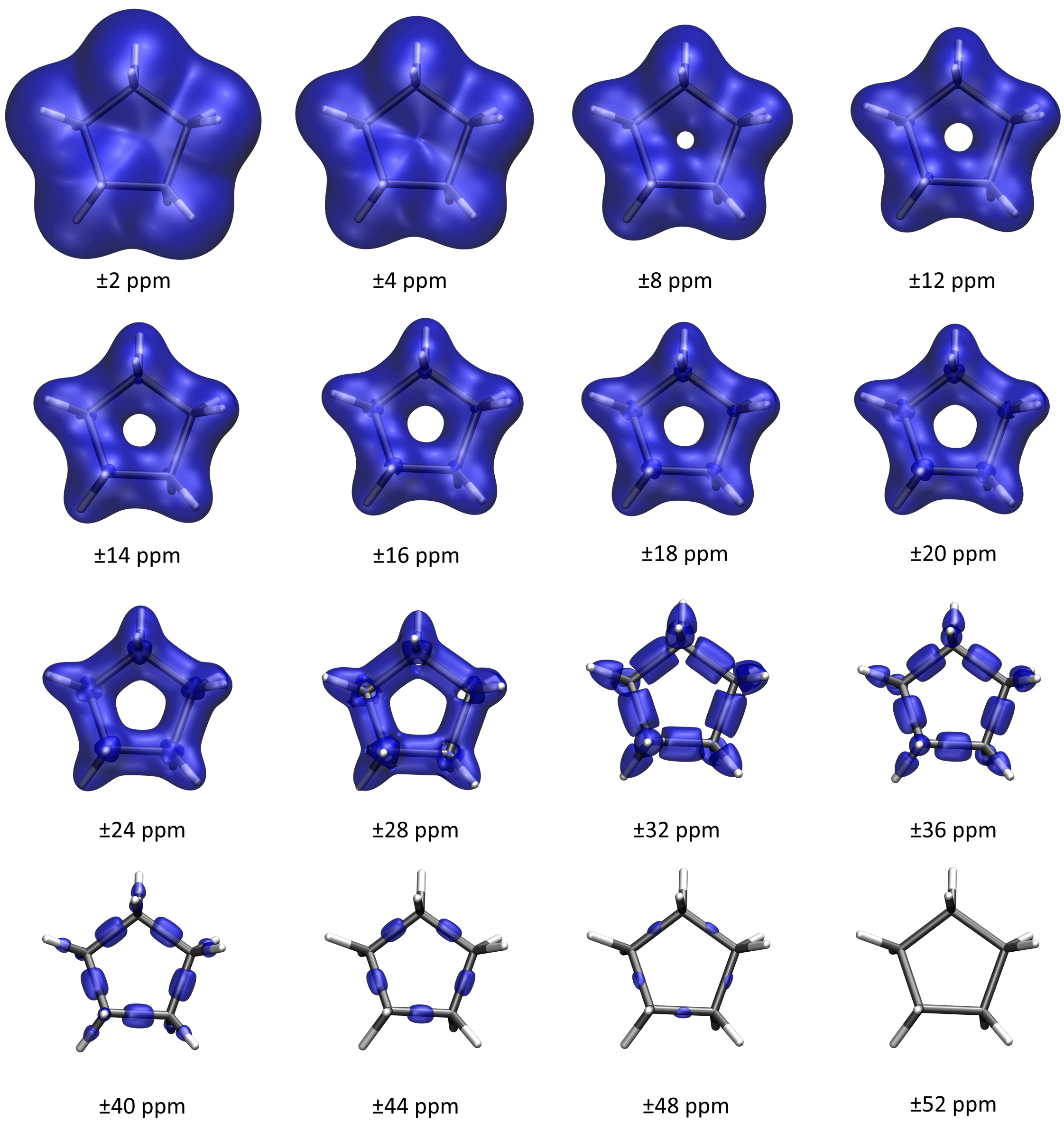

Figure 6: The magnetic shielding ($\sigma_{\text{iso}}(\mathbf{r})$) around C_5H_{10} at a range of chemical shift thresholds.

There are two types of nonaromatic systems, the first of which (shown in Figure 6) is a saturated ring, which by definition has no delocalised π-electron system. The second type, more ubiquitous in this thesis, involves a ring containing a π-system, but does not have a favourable (aromatic) or unfavourable (antiaromatic) effect on the bonding. This type of nonaromaticity is identifiable through shielding plots containing little shielding, as shielding (aromaticity) is approximately balanced with deshielding (antiaromaticity). These plots look similar to C_5H_{10} at ±28 ppm, but at the lower chemical shift threshold of ±16 ppm.

1.5.2 The Aromatic Case: C_6H_6

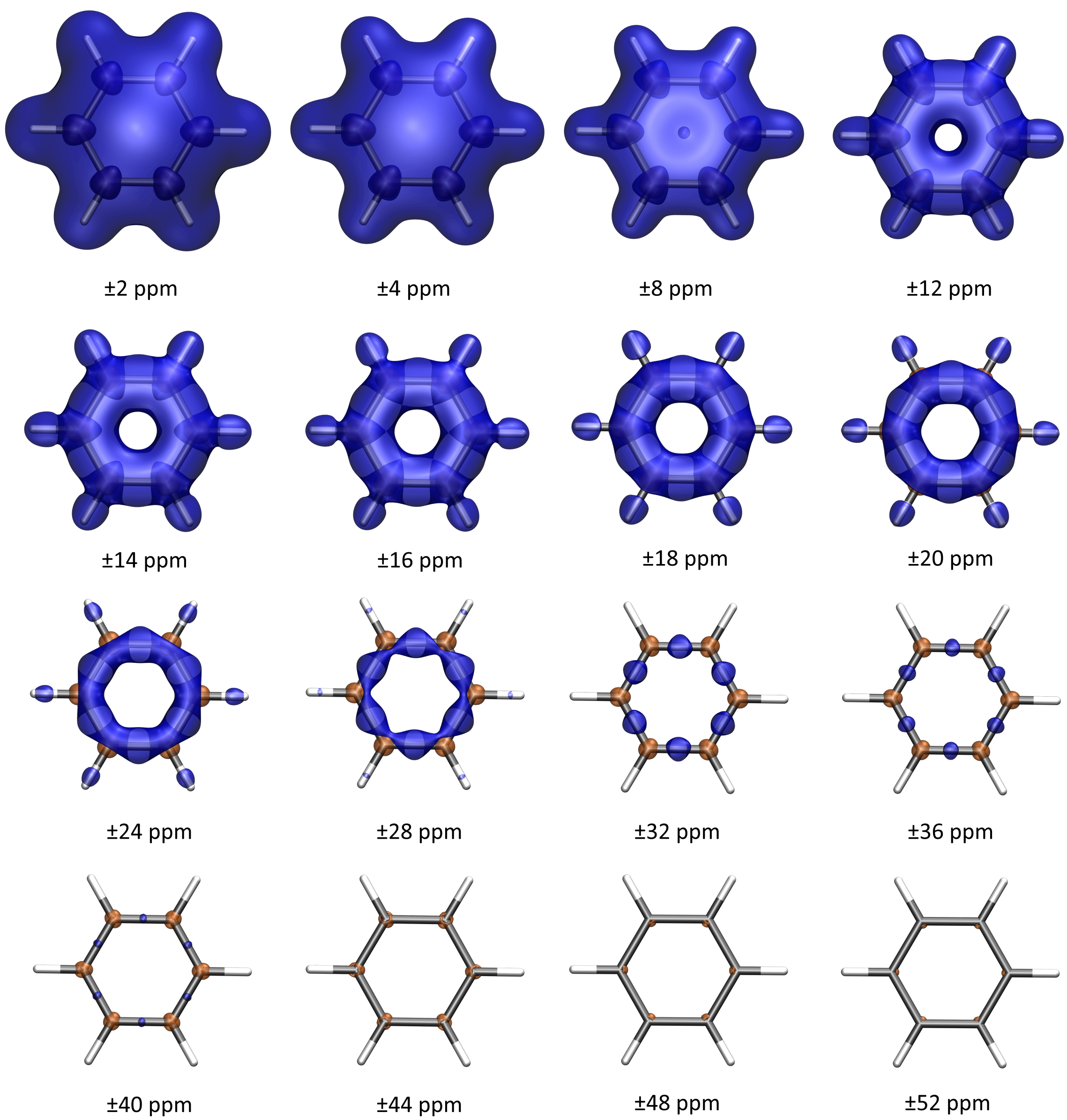

Figure 7: The magnetic shielding ($\sigma_{\text{iso}}(\mathbf{r})$) around C_6H_6 at a range of chemical shift thresholds.

For benzene, at ±2 ppm, the shielding encompasses the whole molecule, just as in the nonaromatic case. However, the surface is smoother, due to the structure now being planar. Unlike C_5H_{10}, there are not only nonshielded ovoids around carbon nuclei (which did not appear until higher thresholds), but there are deshielded regions around them. It is not understood why this is the case; however, has been observed for sp^2 hybridised atoms and is often used as an indicator for non-planar structures having close to sp^2 hybridised orbitals. At ± 8 ppm, there is an ovoid desheilded region at the centre of the ring, which would be expected from the NICS(0) value of -7.6 ppm. There is a cylindrical absence of shielding from ± 12 to ± 16 ppm at the centre of the ring. By ± 18 ppm and ± 20 ppm, the shielding hole takes the shape of the molecule, in this case a hexagonal prism. At these thresholds, the C–H bonds become non-shielded. Increasing the threshold further to ± 24 ppm, shielding is reduced further along C–H bonds, with the external ovoids no longer encompassed by a shielding region on the outside of the ring. The shielding continues along the entire ring, yet is localised around C–C bonds far more. This is further exemplified by the ± 28 ppm, as the shielding absence closer resembles a six-pointed star than a hexagon. Beyond ± 32 ppm, the shielding is localised to the C–C bonds. By ± 44 ppm, no shielding is visible and the deshielded ovoids become significantly reduced in size, and by ± 44 ppm, this is barely visible.

In an aromatic system, the electrons are shared by more than two centres in π systems, so it makes sense to use a chemical shift threshold which, when viewed from above the plane, there is a circular absence of shielding, instead of a polygonal-shaped one. Since shielding is three-dimensional, aromatic rings have a characteristic 'doughnut'-shaped $\sigma_{\text{iso}}(\mathbf{r})$, and the presence of such a shape is synonymous with aromaticity. The threshold set for visualising the shielding (at $\pm$ 16 ppm throughout this thesis) is useful for displaying this character. Comparisons between the nonaromatic and aromatic systems suggest that the shielding is only useful to determine aromaticity when information about the molecule is already known, such as if it contains a π-system. The relative contributions from paramagnetic and diamagnetic components to the shielding tensor are similar for both. The significance of magnetic shielding is its ability to distinguish aromatic and antiaromatic systems for systems known to delocalised electrons.

1.5.3 The Antiaromatic Case: C_4H_4

For cyclobutadiene, shielding is located outside of the molecule, with a large deshielded region within it. At ± 2 and ± 4 ppm, the shielding around the C–C bonds is similar along what would be traditionally thought of as single and double bonds. At ± 8 ppm, the C–C single bonds are far less shielded than the C=C double bonds and by ± 12 ppm, the shielding does not extend along single entire C–C bonds, with just small shielded regions, which disappear by the ± 16 ppm isosurface. There is quite a major shift in the isosurfaces appearance from ± 16 to ± 18 ppm. At ± 18 ppm, the shielding long 'double bonds' does not connect to the hydrogen shielding and the deshielded region in the centre no longer connects the sp^2 hybridised carbon nuclei' deshielded ovoids. The C=C bond shielding and central deshielded region continue to get smaller in volume as the threshold increases, with no deshielded central region at ±28 ppm, and the C=C bond shielding disappears by the time we reach the ±40 ppm threshold. Only the deshielded ovoids around the carbon nuclei remain, until around ±80 ppm. This is far larger than ±52 ppm of benzene.

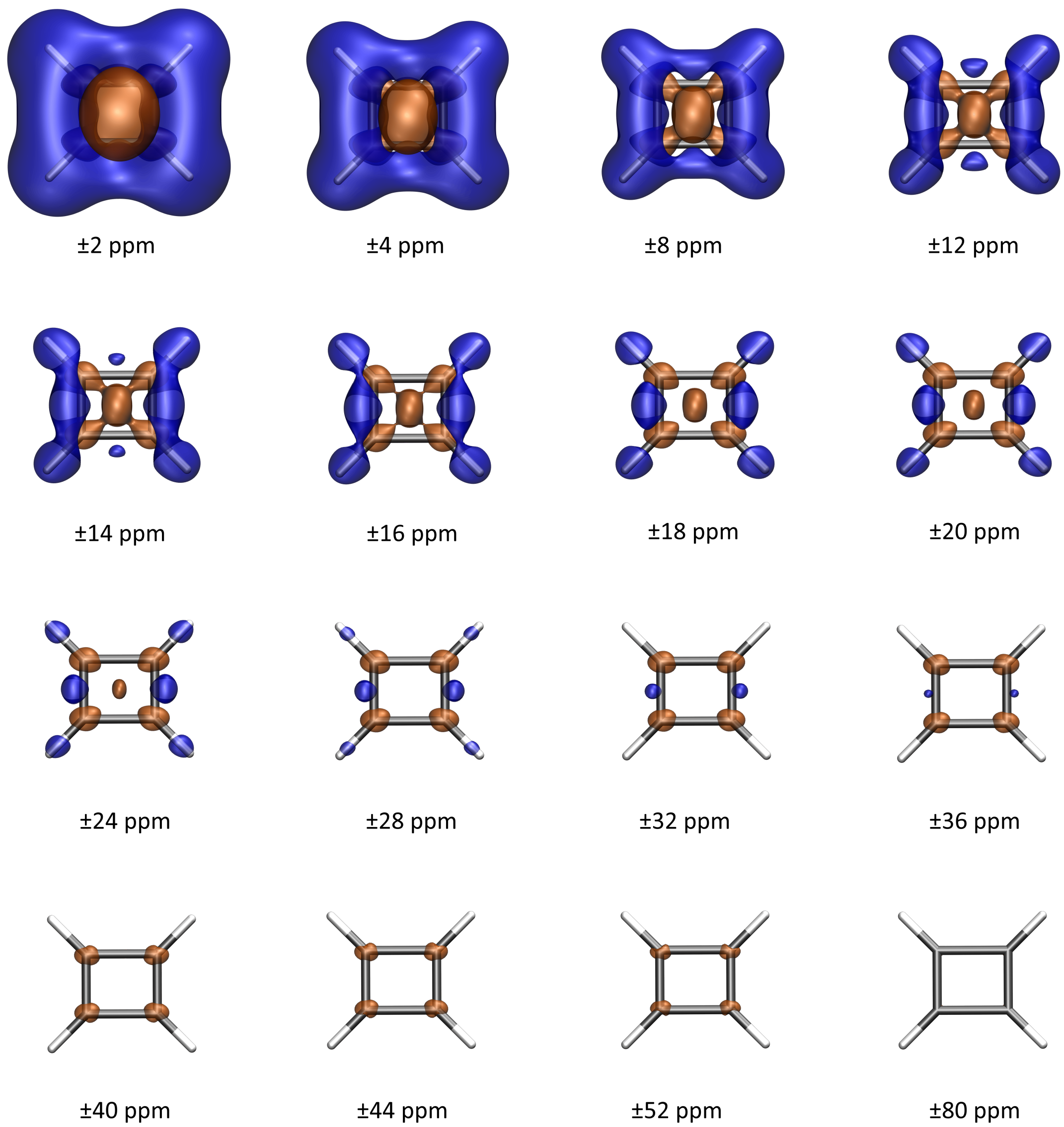

Figure 8: The magnetic shielding ($\sigma_{\mathrm{iso}}(\mathbf{r})$) around C_4H_4 at a range of chemical shift thresholds.

Large regions of deshielding traditionally signify a destabilisation. In cyclical systems, this deshielded region extends from the molecular centre as π-electrons, most likely responsible for the destabilisation, are present here, whilst the stabilising σ bonds are not. Given high enough antiaromaticity, the shielding is excluded from the centre and extends beyond the perimeter of the carbon ring. The electrons in the π system are often those in the highest occupied orbitals, so are those most likely to be excited in the lowest triplet state. Hence, a ground state aromatic system is expected to become antiaromatic upon excitation (Baird's rule), and an S_0 antiaromatic system should be aromatic upon excitation to the T_1 state. Geometry relaxations can mitigate the destabilisation, so both shielding changes for vertical excitations (de-excitations) and after adiabatic relaxations have been measured.

These three examples suggest that at lower chemical shift thresholds ($\sigma_{iso}(\mathbf{r})$<|12| ppm) the abundance of shielding makes it difficult to identify key features in the bonding. At high thresholds ($\sigma_{iso}(\mathbf{r})$>|20| ppm), there is a lack of shielding, particularly along C–H bonds, which is counterintuitive to our ideas of bonding. Hence, to allow some flexibility, ±16 ppm was chosen in the centre of this range for the majority of this work, to allow reasonable comparisons between similar molecules and identify changes in bonding.

1.5.4 Overview

This thesis first examines the aromatic molecule thiophene by comparing vertical and adiabatic excitations and higher excited states. This chapter comes first as it focuses on one small, well-behaved molecule in greater detail than the plethora of molecules covered later in the thesis. The next chapter leads to an examination of condensed thiophene rings and a comparison between the ground state and adiabatic excitations to the T_1 state. In particular, the question of whether aromaticity can explain the optimal number of condensed thiophene rings in heterocirculenes (specifically 'Sulflowers') is discussed. This study motivated the next chapter whereby new molecules, sulfinfinitenes, are supposed by fusing sulflowers together. Subsequently, the next question addressed is whether or not replacing the heteroatom is in a fused system affects aromaticity? For this investigation, the heteroatom is switched from sulfur to oxygen by studying furans and oxiflowers. The nature of excited state aromaticity reversals in norcorrole, naturally builds on from these studies in the following chapter, as a heterocyclic system with competing aromatic and antiaromatic macrocycles. A novel use of magnetic shielding to explore the σ aromaticity in boron clusters is quite unique, so it forms the penultimate main chapter as a distinct discussion from the other work presented before and after this investigation. A brief chapter on vertically exciting, relaxing and de-exciting ethane, ethene and ethyne sets the stage in terms of discussion and methodology for the large final chapter where annulenes are explored. Despite arguably being the simplest set of aromatic and antiaromatic molecules, the findings in the chapter are perhaps the most unexpected and important discoveries of this thesis. Hence, the findings and resultant ramifications are discussed last.

2 Focus on Thiophene

2.1 Introduction

Condensed thiophenes have already been discussed in detail in the subsequent chapter. However, thiophene itself is an interesting molecule and this chapter is an opportunity to explore higher excited states, in particular, the T_2 state. Comparisons can be drawn between the vertical and adiabatic excitations to the T_1 and T_2 states, with a larger focus on how slight changes to the model chemistry affect geometry and magnetic properties.

According to Baird's rule, the familiar Hückel $4n + 2$ and $4n$ rules for electronic ground state (S_0) aromaticity in cyclic conjugated hydrocarbons are reversed in the lowest triplet $\pi\pi^*$ state (usually T_1): Rings with $4n$ π electrons attain aromatic character, whereas those with $4n + 2$ π electrons gain antiaromatic character. Similar aromaticity reversals occur between S_0 and the lowest singlet $\pi\pi^*$ excited state (usually S_1).[48,52–54] Other low-lying electronic states of cyclic conjugated hydrocarbons exhibit magnetic properties, such as nucleus-independent chemical shifts (NICS)[38,55,56] and off-nucleus isotropic magnetic shielding ($\sigma_{\text{iso}}(\mathbf{r})$), that suggest aromaticity or antiaromaticity. State-optimised CASSCF-GIAO calculations have revealed "strongly aromatic" vertical S_2 states in benzene, regular octagonal cyclooctatetraene, naphthalene, and anthracene. These calculations show substantially more negative NICS values compared to the S_0 state. While the interiors of the carbon framework are well-shielded, the carbon–hydrogen bonds exhibit reduced shielding compared to the S_0 states.

Currently, state-optimised CASSCF-GIAO is the only available method to calculate magnetic shielding tensors for singlet excited states, and these findings lack alternative theoretical confirmation. Also, there are no reports of similar "strongly aromatic" triplet states. Notably, state-optimised full π space CASSCF-GIAO calculations on anthracene predict a "strongly aromatic" vertical S_1 state ($1\ {}^1B_{2u}$), while the lowest singlet antiaromatic state is S_2 ($1\ {}^1B_{3u}$).[57] The aromaticities of vertical S_1 and S_2 states of higher acenes are expected to follow the pattern observed in anthracene.

Most research on excited state aromaticity and antiaromaticity focuses on the T_1 state, which is computationally easier to access than the S_1 state through UDFT calculations. While TD-DFT and TDA-DFT calculate excitation energies and optimise excited state geometries, there are currently no codes for calculating magnetic shielding tensors using these methods.

This chapter investigates aromaticity reversals between the S_0, T_1, and T_2 states of thiophene. DFT, UDFT, TD-DFT, and TDA-DFT are employed to calculate excitation energies and optimise geometries, while DFT-GIAO and UDFT-GIAO calculate magnetic shielding tensors for all states. The study shows that thiophene, which is aromatic in its S_0 state, becomes antiaromatic in its vertical T_1 state and reverts to aromatic in its vertical T_2 state. Geometry optimisations of the antiaromatic vertical T_1 state and the 'strongly aromatic' vertical T_2 state leads to non-planar geometries with reduced antiaromaticity and enhanced aromaticity, respectively. The magnetic properties of the 'strongly aromatic' low-lying vertical singlet excited states are also exhibited by low-lying vertical triplet excited states. This suggests that these properties are not a computational artefact but characterize states with increased shielding activity within the ring interiors, leading to very negative NICS values. However, these negative NICS values alone do not necessarily indicate higher aromatic stabilisation than aromatic S_0 states. While changes in NICS signs identify excited state aromaticity reversals, comparing NICS magnitudes across electronic states with the same sign may not reliably reflect relative aromaticity.

The S_0 ($1\ ^1A_1$) geometry of thiophene (C_{2v} symmetry) was optimised using B3LYP-D3(BJ) with the def2-TZVP and def2-TZVPPD basis sets. The def2-TZVPPD basis sets were obtained from the Basis Set Exchange.[58] The initial guesses for Kohn-Sham orbitals in triplet UB3LYP/6-311++G(d,p) and UB3LYP/6-311++G(2d,2p) calculations at the S_0 B3LYP-D3(BJ)/def2-TZVP geometry had different symmetries, leading to convergence to different vertical triplet states. Similar behaviour was observed at the S_0 B3LYP-D3(BJ)/def2-TZVPPD geometry. Using appropriate initial guesses allowed convergence to the desired vertical T_1 and T_2 states. Vertical excitation energies ($S_0 \rightarrow T_1$ and $S_0 \rightarrow T_2$) were calculated using UB3LYP, TD-B3LYP, and TDA-B3LYP with the def2-TZVP and def2-TZVPPD basis sets. The geometries of the T_1 and T_2 states were optimised using UB3LYP-D3(BJ) and TDA-B3LYP-D3(BJ) with both basis sets.

Magnetic properties of triplet states were computed using UB3LYP-GIAO, including only contributions arising from the perturbation to Kohn-Sham orbitals. HOMA calculations were performed using Multiwfn[29] with default parameterisation. NICS values and volume data for the isotropic shielding isosurfaces were obtained using B3LYP-GIAO/6-311++G(2d,2p) and UB3LYP-GIAO/6-311++G(2d,2p) calculations at the optimised geometries. Shielding tensors were calculated on regular 0.05 Å spaced three-dimensional grids.

2.2 Results and Discussion

The atom numbering scheme used for comparing bond lengths generated from various model chemistries is shown in Figure 9.

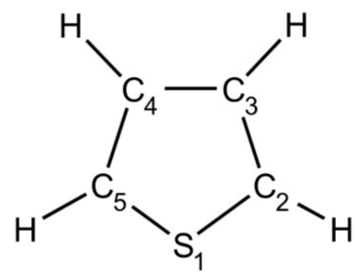

Figure 9: Atom numbering scheme for thiophene.

The optimised S_0 geometries of thiophene, obtained using B3LYP-D3(BJ) with def2-TZVP[a] and def2-TZVPPD[b] basis sets, agree well with those from high-level coupled-cluster calculation with single, double, and perturbative triple excitations in the cc-pCV5Z basis set (CCSD(T)/cc-pCV5Z),[56] and from a precise semi-experimental equilibrium structure (SE).[56,59] The carbon-sulfur bond length shows a slight overestimation by B3LYP-D3(BJ) of almost 0.01 Å, but all other parameters, including bond angles, agree well (see Table 2).

Table 2: Geometric parameters for S_0 thiophene using various computational methods; bond lengths in Å and angles in degrees; see Figure 9 for atom numbering scheme. The DFT method was B3LYP-D3(BJ) with basis sets def2-TZVP[a] and def2-TZVPPD[b]. See text for further details.

	RDFT[a]	RDFT[b]	CCSD(T)	SE
$R(S_1–C_2)$	1.718	1.718	1.709	1.710
$R(C_2–C_3)$	1.365	1.365	1.366	1.366
$R(C_3–C_4)$	1.422	1.422	1.422	1.422
$R(C_2–H)$	1.077	1.077	1.076	1.077
$R(C_3–H)$	1.080	1.080	1.079	1.079
$\angle(C_2–S_1–C_5)$	91.9	91.9	92.1	92.0
$\angle(S_1–C_2–C_3)$	111.5	111.5	111.6	111.6
$\angle(S_1–C_2–H)$	120.3	120.3	120.3	120.1
$\angle(C_2–C_3–H)$	123.4	123.4	123.4	123.4

The geometric parameters in T_1 thiophene change very little between the def2-TZVP and def2-TZVPD basis sets. Applying the TDA results in a slight change: the C_2–C_3 bond shortens and the C_3–C_4 bond lengthens by around 0.004 Å each. The dihedral $\angle(S_1–C_2–C_3)$ contracts by approximately 1° in both basis sets. A full comparison of both the T_1 and T_2 structural parameters is shown in Table 3. Greater variation is observed in the T_2 structural parameters between the def2-TZVP and def2-TZVPD basis sets. The largest is the $\angle(C_2–C_3–H)$ dihedral angle, varying by up to 0.9° between basis sets. Application of the TDA typically increases non-planarity in the T_2 geometry. The reduction in planarity (the S_0 dihedral angles are all 180°) intuitively suggests a loss of aromatic character.

The structural parameters show a reduction in symmetry from C_{2v} in S_0 to C_s in T_1 and T_2 states, accompanied by ring puckering and out-of-plane bending of hydrogen atoms. Changes in carbon–carbon bond alternation patterns are observed between S_0 and T_1 geometries, while the T_2 geometry exhibits a pattern similar to S_0 with longer carbon–carbon bonds. These observations suggest potential aromaticity reversals between S_0 and T_1, and between T_1 and T_2, with T_2 resembling the S_0 state.

Table 3: Geometric parameters for T_1 and T_2 thiophene. Bond lengths in Å and angles in degrees. The DFT method was B3LYP-D3(BJ) with a basis set of ^{a}def2-TZVP and ^{b}def2-TZVPPD.

	T_1				T_2			
	UDFT^a	UDFT^b	TDA^a	TDA^b	UDFT^a	UDFT^b	TDA^a	TDA^b
$R(S_1–C_2)$	1.771	1.771	1.770	1.770	1.768	1.766	1.771	1.769
$R(C_2–C_3)$	1.463	1.463	1.459	1.458	1.401	1.401	1.398	1.398
$R(C_3–C_4)$	1.343	1.343	1.348	1.348	1.434	1.435	1.438	1.439
$R(C_2–H)$	1.082	1.081	1.081	1.080	1.077	1.076	1.077	1.076
$R(C_3–H)$	1.081	1.080	1.080	1.080	1.081	1.080	1.081	1.080
$\angle(C_2–S_1–C_5)$	89.6	89.5	89.4	89.3	93.6	93.5	93.3	93.3
$\angle(S_1–C_2–C_3)$	111.1	111.1	111.5	111.6	105.6	105.6	105.6	105.5
$\angle(S_1–C_2–H)$	120.1	120.2	120.2	120.3	117.9	118.0	117.9	118.1
$\angle(C_2–C_3–H)$	121.8	121.8	121.9	121.9	123.1	123.2	123.2	123.3
$\angle(S_1–C_1–C_2–C_3)$	9.2	9.3	8.2	8.4	17.6	17.9	18.0	18.3
$\angle(C_4–C_3–C_2–H)$	−146.7	−147.3	−150.4	−151.2	162.0	162.8	162.1	163.0
$\angle(C_5–C_4–C_3–H)$	−178.9	−178.8	−178.8	−178.7	−178.4	−178.3	−178.6	−178.5

Given the significant structural changes, it is appropriate to examine geometric aromaticity indices such as HOMA for further insight. HOMA values (Table 4) confirm the expectation that the aromaticity in S_0 state becomes nonaromatic in T_1, and a return to aromaticity in T_2 state, albeit far less pronounced than in S_0. The small differences in HOMA values between geometries optimised with different basis sets and methods highlight their similarity.

Table 4: HOMA values for the S_0, T_1 and T_2 geometries of thiophene optimised using the def2-TZVP and def2-TZVPPD basis sets.

State	def2-TZVP	def2-TZVPPD
S_0 B3LYP-D3(BJ)	0.822	0.821
T_1 UB3LYP-D3(BJ)	−0.022	−0.014
T_1 TDA-B3LYP-D3(BJ)	0.077	0.084
T_2 UB3LYP-D3(BJ)	0.559	0.570
T_2 TDA-B3LYP-D3(BJ)	0.526	0.538

Table 5 presents vertical excitation energies ($S_0 \rightarrow T_1$ and $S_0 \rightarrow T_2$) calculated using UB3LYP, TD-B3LYP, and TDA-B3LYP with the def2-TZVPPD basis set. TDA-B3LYP results show better agreement with experimental band maxima compared to TD-B3LYP. Both UB3LYP and TDA-B3LYP provide accurate $S_0 \rightarrow T_1$ and $S_0 \rightarrow T_2$ excitation energies, comparable to CASSCF and PT_2F estimates.[60] The nature of vertical T_1 and T_2 states, dominated by specific orbital excitations, is consistent with previous findings and expectations for five-membered heterocycles.

Table 5: Vertical excitation energies (in eV) of thiophene to the T_1 ($1\,^3B_2$) and T_2 ($1\,^3A_1$) states.

Method	T_1	T_2
UB3LYP[a]	3.86	4.57
TD B3LYP[a]	3.56	4.45
TDA B3LYP[a]	3.82	4.53
DFT/MRCI[61]	3.53	4.35
CASSCF[60]	3.83	4.90
PT_2F[60]	3.75	4.50
Exp. band maximum	3.7[62], 3.75[63,64], 3.74[65]	4.6[62], 4.62[63–65]

Table 6 presents NICS values and isotropic nuclear shieldings for S_0, T_1, and T_2 states. NICS values support conclusions from shielding variations. However, the magnitude of $\sigma_{\text{iso}}(\mathbf{r})$ can change significantly near NICS positions, highlighting the limitations of NICS as a quantitative measure, especially for non-planar rings.

Table 6: NICS values and isotropic nuclear shieldings for the symmetry-unique nuclei in the S_0, T_1, and T_2 electronic states of thiophene (in ppm). The NICS(+1) values correspond to positions above the ring (Figure 10).

State	NICS(0)	NICS(±1)	$\sigma_{\text{iso}}(^{33}\mathrm{S})$	$\sigma_{\text{iso}}(^{13}\mathrm{C})$	Atom	$\sigma_{\text{iso}}(^{1}\mathrm{H})$
S_0	−12.5	−10.0	231.3	50.3	(C2)	24.3
				53.0	(C3)	24.5
$T_1//S_0$	31.1	27.3	320.3	80.0	(C2)	28.7
				36.2	(C3)	26.9
T_1	5.4	4.8	309.5	69.6	(C2)	26.9
		5.8		47.8	(C3)	25.7
$T_2//S_0$	−18.0	−19.2	−158.3	136.1	(C2)	27.3
				50.7	(C3)	23.3
T_2	−31.4	−23.5	−190.4	115.8	(C2)	24.9
		−36.1		50.4	(C3)	22.8

Nuclear shieldings ($\sigma_{\text{iso}}(^{33}\text{S})$, $\sigma_{\text{iso}}(^{13}\text{C})$, and $\sigma_{\text{iso}}(^{1}\text{H})$) vary considerably between the different states. The S_0 values agree with previous DFT calculations.[66] Proton shieldings increase in the antiaromatic vertical T_1 state compared to S_0 and decrease as antiaromaticity is reduced in the optimised T_1 geometry. A decrease in proton shieldings is observed in the aromatic vertical T_2 state compared to the vertical T_1 state, further decreasing in the optimised T_2 geometry, reflecting the increase in aromaticity.

Figure 10 provides further information through contour plots in vertical symmetry planes. The contour plot emphasises the strong shielding in the T_2 state, even at the S_0 geometry. Whilst the S_0 shielding has greater shielding around the sulfur atom, the shielding perpendicular to the molecular plane passing through the molecular centre is greater in the $T_2//S_0$ state. The shielding is then enhanced significantly as the geometry is relaxed in the T_2 state. Isotropic shielding isosurfaces for S_0, vertical T_1 and T_2, and optimised T_1 and T_2 states are shown in Figure 11. The isovalues and geometry orientations emphasize relevant details.

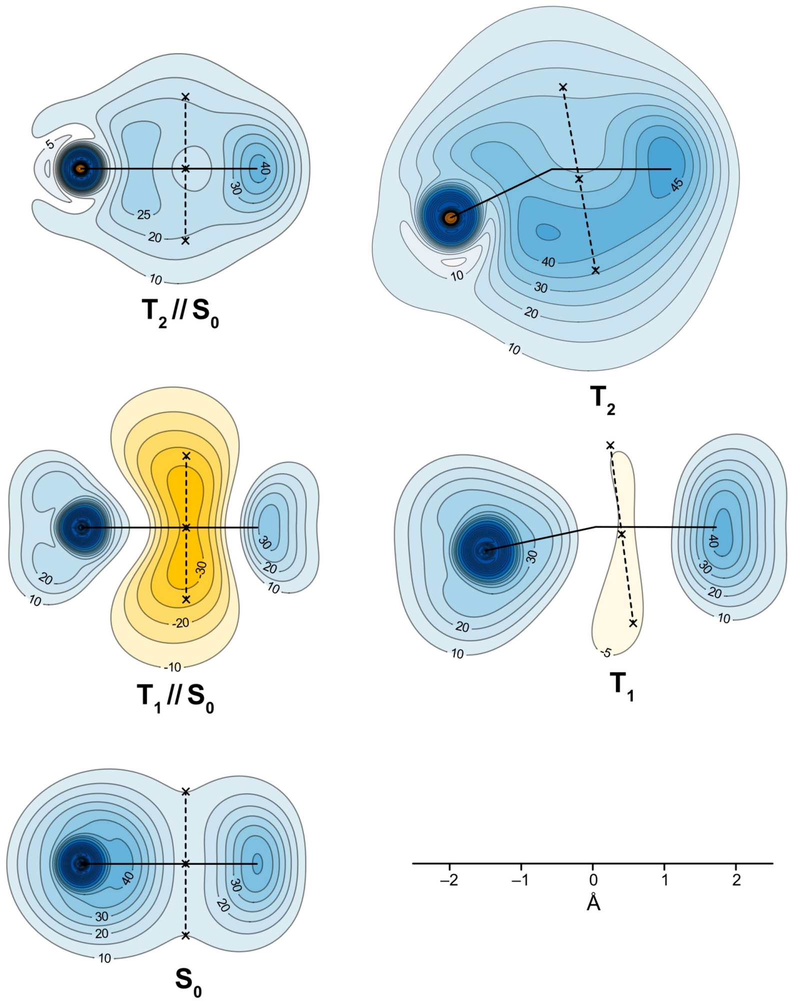

Figure 10: Isotropic shielding contour plots in the vertical symmetry planes passing through the sulfur atoms and the midpoints of the opposite carbon-carbon bonds for the S_0, T_1 and T_2 electronic states of thiophene. Contour levels requested at $-30(5)-5$, $10(5)50$, $60(20)240$ ppm, orange (deshielded) to blue (shielded). Solid black lines show the projections of the carbon-sulfur and carbon-carbon bonds. The positions of NICS(0) and NICS(± 1) are marked by crosses and connected by dashed lines.

The analysis of shielding variations in the S_0 and T_1 states confirms previous findings, showing strong shielding in S_0 and a central deshielded region in vertical T_1.[49,67] The vertical T_2 state exhibits a well-shielded ring interior, making it the first reported example of a 'strongly aromatic' triplet state. Geometry relaxation reduces the deshielded region in T_1 and enhances shielding within the ring interior in T_2, indicating a decrease in antiaromaticity and an increase in aromaticity, respectively.

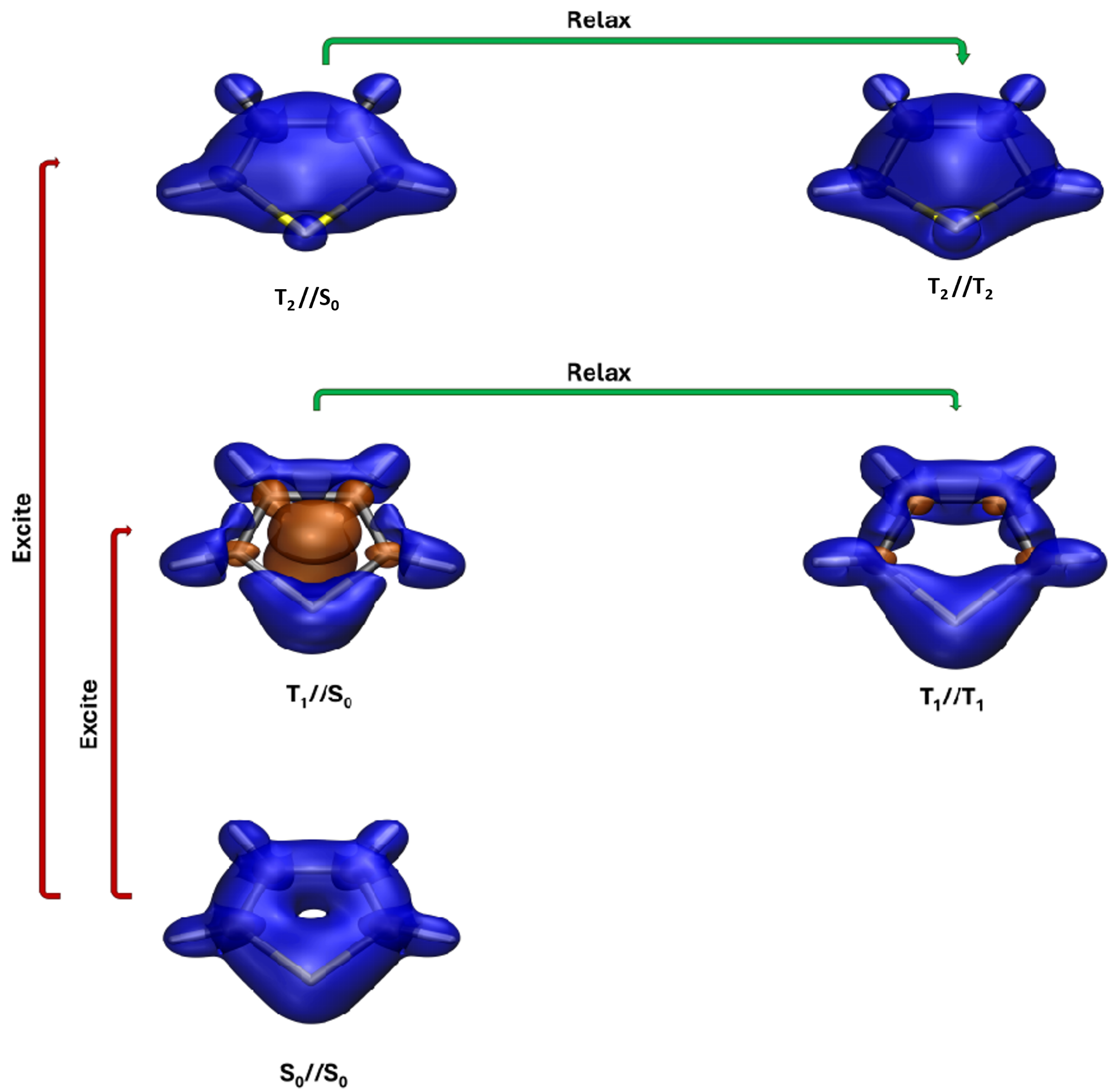

Figure 11: Isotropic shielding isosurfaces for the S_0, T_1 and T_2 electronic states of thiophene. The T_1//S_0 and T_2//S_0 isosurfaces correspond to the $S_0 \rightarrow T_1$ and $S_0 \rightarrow T_2$ vertical excitations, respectively.

Deshielded 'halos' around carbon atoms are observed in all states, suggesting sp^2 hybridisation. In the T_2 state, $\sigma_{\mathrm{iso}}(\mathbf{r})$ changes sign near the sulfur atom, remaining negative at the atomic position, which is supported by Mulliken populations.

Whilst both the structural (HOMA) and magnetic aromatic criteria both suggest aromaticity of the T_2 state, the former suggests weaker aromaticity in T_2 than the S_0, whilst the latter indicates the reverse is true. In terms of aromaticity being a stabilising property, HOMA is most likely a better judge in this case as S_0 is the ground state. However, the magnetic criteria indicates electron delocalisation is greater in the excited state, so a more prominent magnetic response is observed. The magnetic criteria is a powerful tool, but this serves a caution to be careful when directly comparing the magnitudes of magnetic responses from the ground and excited states.

2.3 Conclusions

Thiophene exhibits aromaticity reversals between its electronic ground state and the two lowest triplet states. The S_0 state is aromatic, the vertical T_1 state is antiaromatic, and the vertical T_2 state reverts to aromatic. Geometry relaxation reduces antiaromaticity in T_1 and enhances aromaticity in T_2.

While NICS values are useful indicators of aromaticity trends along a potential energy surface, they may not be reliable for quantitative comparisons between different electronic states. The T_2 state of thiophene exhibits a shielding picture similar to 'strongly aromatic' vertical singlet excited states observed in other molecules. However, comparisons of optimised geometries and HOMA values suggest that the T_2 state is not more aromatic than the S_0 state. The results expand the understanding of excited state aromaticity, demonstrating that 'strongly aromatic' behaviour is not limited to singlet states. However, it is important to consider multiple factors, such as geometry, bond lengths, and shielding patterns, when assessing the aromaticity of excited states. Direct comparison between the magnitudes of magnetic responses from ground and excited states should be taken with care; what may be considered a strong magnetic response in the ground state may not be considered strong in an excited state, despite being of similar magnitude.

The study highlights the complexity of excited state aromaticity and provides insights into the behaviour of thiophene in its ground and lowest triplet states. Further research is needed to fully explore the factors influencing aromaticity reversals in excited states and to develop more comprehensive criteria for evaluating aromaticity in these states.

3 Condensed Thiophenes

3.1 Introduction

This chapter examines aromaticity and bonding in compounds with fused thiophene rings in the ground and lowest triplet excited states, focusing on the properties of these molecules in their respective optimised geometries. Interest in thiophene-containing heteroaromatic compounds such as polythiophenes is associated with their wide range of potential applications which include organic field effect transistors (OFETs)[68–71] and organic light-emitting diodes (OLEDs).[72]

Branching out to other areas of science, thiophene-containing compounds have attracted the attention of astrochemists, since over the past decade, NASA's Mars Curiosity Rover has found them[73–75] during the quest to find Martian biosignatures.[74]

In general, aromatic molecules are stable, in contrast to antiaromatic molecules, which have much smaller HOMO–LUMO gaps[76–78] and singlet-triplet separations[79] and, as a consequence, are less stable. The π electrons in compounds with condensed thiophene rings can traverse alternative conjugation pathways which makes establishing the levels of aromaticity in the singlet ground (S_0) and lowest triplet (T_1) electronic states of these compounds a non-trivial task.

The aromaticity of thiophene **1** is a challenge to quantify, as it is known to be more aromatic than pyrrole (where sulfur is substituted for nitrogen) and furan (where the heteroatom is oxygen).[49] In each of these five-membered heteroaromatics, the heteroatom donates two electrons to the π system, circumventing the need to have a sixth atom in the conjugated ring in order to have a $4n+2$ Hückel aromatic π system similar to that in benzene. Four isomers can be formed by condensing two thiophene rings, namely, thieno[2,3-*b*]thiophene **2**, thieno[3,2-*b*]thiophene **3**, thieno[3,4-*b*]thiophene **4** and thieno[3,4-*c*]thiophene **5**; all of these are examined in this chapter. Thieno[2,3-*b*]thiophene **2** has a central cross-conjugated 'double' bond which prevents the establishment of a conjugation pathway involving three carbon–carbon π bonds. Consequently, its HOMO-LUMO gap is higher than those of thieno[3,2-*b*]thiophene **3** and thieno[3,4-*b*]thiophene

4, where the longer conjugation pathways lead to lower HOMO-LUMO gaps.[80] Due to the variation in the lengths of the conjugation pathways, relative stability and electron-rich nature, the first three thienothiophenes provide useful building blocks for constructing organic semiconductors.[81] The fourth thienothiophene, thieno[3,4-*c*]thiophene **5**, which has resonance structures involving a sulfur atom with a formal oxidation state of +4, is far less stable and has not been isolated in unsubstituted form.

There are twelve dithienothiophene isomers; each of these involves three condensed thiophene rings. This chapter examines two of these isomers, dithieno[3,2-*b*;2′,3′-*d*]thiophene **6** and dithieno[2,3-*b*:3′,2′-*d*]thiophene **7**. Dithienothiophenes appear as intermediates in a number of reactions[82] and can be used as materials for p-type semiconductors in OFETs, due to their planar, sulfur-rich, rigid, conjugated, and highly thermally stable and photostable structures.[80] Some dithienothiophenes are available commercially.[83]

Recent studies of systems involving interconnected heterocycles have shown that these can feature alternative cyclic conjugation pathways with $4n + 2$ or $4n$ π electrons, exhibiting competing aromatic and antiaromatic properties.[2,84] Condensed thiophene rings can form a class of heterocirculenes known as 'sulflowers',[85] with a molecular formula $(C_2S)_n$. A sulflower can be viewed as constructed from an 'outer' $(CS)_n$ ring formed by carbon-sulfur rim bonds and an 'inner' C_n ring formed by carbon-carbon hub bonds; these rings are connected by carbon-carbon 'double' spoke bonds which create opportunities for the establishment of a number of cyclic conjugation pathways. This chapter investigates sulflowers with 6, 7, 8, 9 and 10 condensed thiophene rings: hexathiocirculene **8**, heptathiocirculene **9**, octathiocirculene **10**, nonathiocirculene **11** and decathiocirculene **12**. The most stable of these sulflowers is thought to be $(C_2S)_8$ **10** which has been shown to have the lowest energy per repeat unit.[85,86] Computational studies of more strained sulflowers with 4, 5, 11 and 12 condensed thiophene rings have been carried out by other authors.[86,87] Dianions and dications of $(C_2S)_8$ and other heterocirculenes are thought to have increased stability due to the establishment of a $4n + 2$ Hückel-aromatic π system involving the 'inner' C_8 ring.[88] Further research on sulflowers and similar circulenes[89] has investigated replacing sulfur with other substituents such as oxygen,[90] selenium, and tellurium,[86] as well as broader aspects of the structure and reactivity of heterocirculenes[88,91] and their synthesis.[92–94]

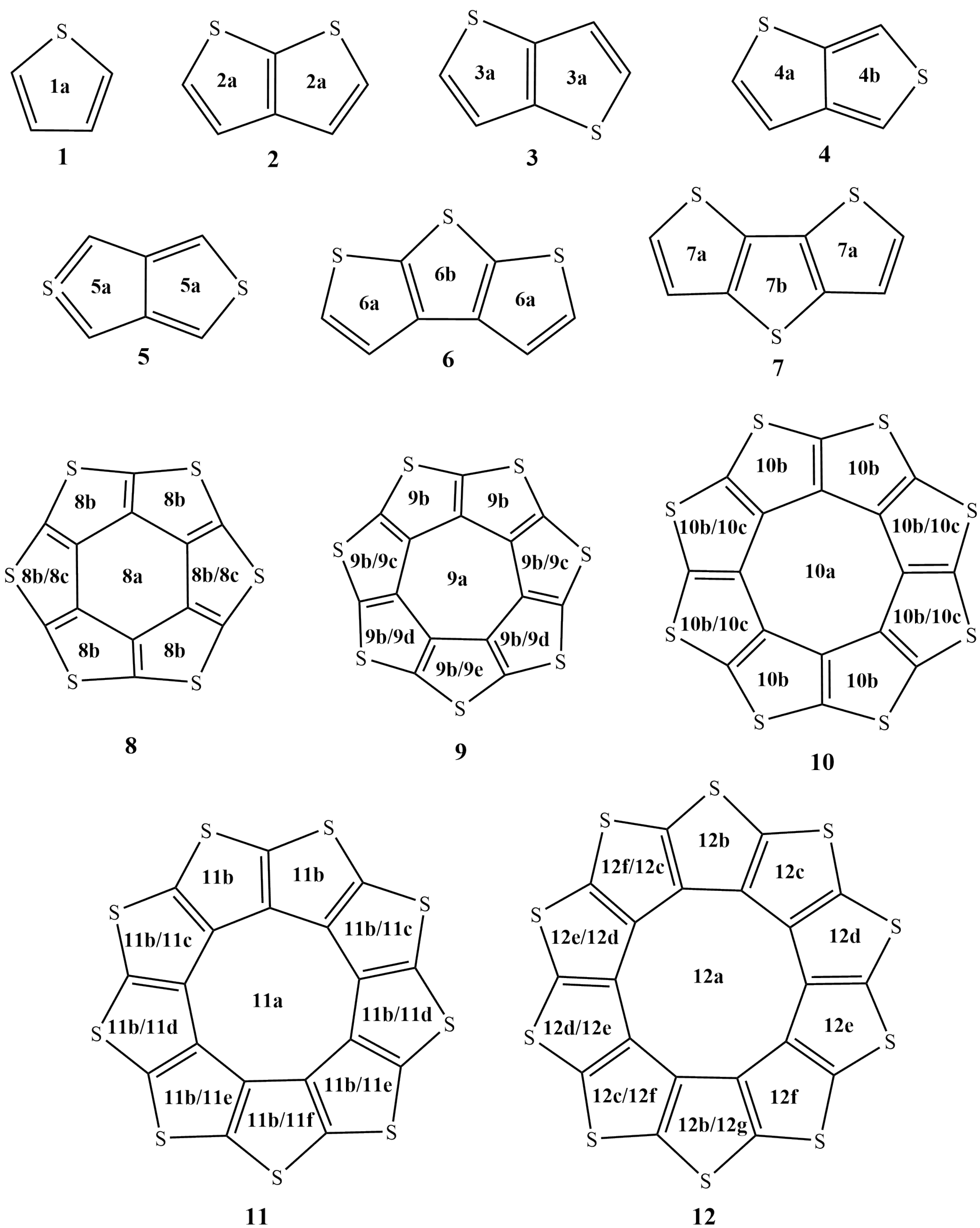

Figure 12: Thiophene **1**, thieno[2,3-*b*]thiophene **2**, thieno[3,2-*b*]thiophene **3**, thieno[3,4-*b*]thiophene **4**, thieno[3,4-*c*]thiophene **5**, dithieno[2,3-*b*;3′,2′-*d*]thiophene **6** and dithieno[3,2-*b*;2′,3′-*d*]thiophene **7**; sulflowers with six **8**, seven **9**, eight **10**, nine **11** and ten **12** C_2S units. Rings are labelled by structure numbers and letters; rings related through symmetry operations share the same label. Ring labels that differ between the S_0 and T_1 optimised geometries are separated by a slash '/', with the S_0 label first.

Structurally, the sulflowers $(C_2S)_6$–$(C_2S)_{10}$ (**8**–**12** in Figure 12) resemble two well-known polycyclic aromatic hydrocarbons (PAHs), coronene ($C_{24}H_{12}$) and corannulene ($C_{20}H_{10}$), which have 24 and 20 π electrons, respectively, and so, while aromatic, do not formally conform to Hückel's $4n + 2$ rule. Similarly, each C_2S unit in a sulflower with a molecular formula $(C_2S)_n$ contributes four π electrons, hence the total number of π electrons is $4n$. This suggests that it would be more appropriate to look at the aromaticities of the individual thiophene rings, and of the $(CS)_n$ rim and C_n hub rings, rather than at the total π electron counts. All individual thiophene rings in **8**–**12** should be aromatic; the rim and hub rings could be thought of as the components of an 'annulene-within-a-heteroannulene' model analogous to the 'annulene-within-an-annulene' (AWA) model[95] suggested in order to explain the aromaticity of corannulene but strongly questioned by subsequent research.[96] According to Baird's rule, some of the individual thiophene rings, as well as the rim and hub rings and could be expected to experience aromaticity reversals in the T_1 state. Clearly, establishing the levels of aromaticity in the electronic ground and excited states of polycyclic conjugated compounds could require more detailed analysis going way beyond straightforward applications of Hückel's and Baird's rules to various cyclic conjugation pathways with $4n + 2$ or $4n$ π electrons. There are well-known examples of molecules with condensed rings exhibiting local aromaticity and local antiaromaticity, respectively, in their electronic ground states such as benzocyclobutadiene[38,97–100] and biphenylene.[38,99,101,102] Recent studies have suggested the existence of Hückel aromatic character in the T_1 states of Cibalackrot-type compounds[103] and mixed Hückel–Baird hybrid aromatic character in the T_1 states of pro-aromatic quinoidal compounds.[104]

3.2 Geometry

The S_0 geometries of molecules **1**–**12** were optimised at the RB3LYP-D3(BJ)/def2-TZVP level; the respective T_1 geometries were optimised at the unrestricted UB3LYP-D3(BJ)/def2-TZVP level.

The C_{2v} symmetry of the optimised electronic ground state geometry of thiophene **1** is reduced to C_s in the respective geometry of its lowest triplet state; this is accompanied by an out-of-plane bending of the hydrogen atoms in the same direction. The thienothiophene in which the sulfur atoms are arranged as in the sulflowers, thieno[2,3-*b*]thiophene **2**, has an S_0 optimised geometry of C_{2v} symmetry, and a T_1 optimised geometry of C_2 symmetry; the symmetry reduction involves an out-of-plane bending of the hydrogen atoms which, in contrast to that observed in thiophene, are in opposite directions for the pairs of hydrogen atoms from the two thiophene rings. The optimised geometries of both the S_0 and T_1 states of thieno[3,2-*b*]thiophene **3** and thieno[3,4-*b*]thiophene **4** were found to be of C_s symmetry. There is no change in the

D_{2h} symmetry of the optimised geometries of thieno[3,4-*c*]thiophene **5** between S_0 and T_1. The optimised geometry of the next sulflower precursor, dithieno[2,3-*b*:3′,2′-*d*]thiophene **6**, switches from C_{2v} symmetry in S_0 to C_2 symmetry in T_1, with a loss of planarity. The symmetry reductions on passing from S_0 to T_1 in **2** and **6** suggest that the T_1 states of sulflowers can be expected to show similar distortions of the respective T_1 optimised geometries. The S_0 and T_1 optimised geometries of dithieno[3,2-*b*;2′,3′-*d*]thiophene **7** were found to be of the same C_{2v} symmetry.

Looking at the sulflowers, the S_0 optimised geometries of $(C_2S)_6$ **8** and $(C_2S)_7$ **9** were found to be bowl-shaped, of C_{6v} and C_{7v} symmetries, respectively; those of $(C_2S)_8$ **10** and $(C_2S)_9$ **11** were found to be planar, of D_{8h} and D_{9h} symmetries, respectively; that of $(C_2S)_{10}$ **12** was found to be of corrugated shape and of C_2 symmetry. The symmetries of the T_1 optimised geometries of the sulflowers studied turned out to be significantly lower than those of their S_0 counterparts, namely C_{2v} for $(C_2S)_6$ and $(C_2S)_8$, as well as C_s for $(C_2S)_7$, $(C_2S)_9$ and $(C_2S)_{10}$, which is an indication of attempts to decrease energy by lowering symmetry. As a consequence, the T_1 optimised geometries of $(C_2S)_6$, $(C_2S)_7$, $(C_2S)_8$, $(C_2S)_9$ and $(C_2S)_{10}$ include 3, 4, 2, 5 and 6 symmetry-unique thiophene rings, respectively, in contrast to the S_0 optimised geometries, amongst which only that of $(C_2S)_{10}$ features more than one symmetry-unique thiophene ring (the number of such rings in the electronic ground state of this sulflower is five).

The S_0 optimised lengths of the carbon-sulfur rim, carbon-carbon hub and carbon-carbon 'double' spoke S_0 bonds in $(C_2S)_8$ **10**, 1.752, 1.417 and 1.381 Å, respectively, provide an almost perfect match for the experimentally measured bond lengths of 1.751, 1.419 and 1.380 Å.[85,86,105]

3.3 Thiophene

The S_0 NICS(0) and NICS(1) values for thiophene, −13.0 and −10.4 ppm, respectively (Table 7), are close to the RB3LYP-GIAO/6-311+G(d,p)//RB3LYP/6-311+G(d,p) values of −12.9 and −10.2 ppm reported by Schleyer and co-workers,[106] as well as to the RHF-GIAO/6-311++G(d,p) and RMP2-GIAO/6-311++G(d,p) NICS(0) and NICS(1) values calculated at the experimental gas-phase geometry of thiophene.[49] As expected, thiophene shows a level of aromaticity in its electronic ground state similar to that of benzene. The T_1 NICS(0), NICS(+1) and NICS(−1) values at the T_1 optimised geometry of 4.3, 3.7 and 5.1 ppm, respectively, indicate that thiophene experiences a Baird-style aromaticity reversal between S_0 and T_1. However, the magnitude of this S_0–T_1 aromaticity reversal appears to be much lower than that reported for benzene: The S_0 NICS(0) and NICS(1) values for benzene, −8.2 and −9.5 ppm, respectively, change to 39.6 and 30.1 ppm, respectively, in T_1; these S_0 and T_1 values were calculated with CASSCF(6,6)-GIAO/6-311++G(2d,2p) wavefunctions (π space complete-active-space self-consistent field with 6 electrons in 6 orbitals' and GIAOs), for a vertical excitation at the experimental electronic ground state geometry.[53] For comparison purposes, the NICS(0) and NICS(1) values for the T_1 state of thiophene at the S_0 optimised geometry were also calculated, that is, for a vertical excitation. This produced much higher NICS(0) and NICS(1) T_1 values of 28.4 and 24.7 ppm, respectively, which are closer to but still noticeably lower than those for the T_1 state of benzene. It has been observed, using naphthalene and anthracene as examples,[57] that, when used to calculate magnetic properties, UB3LYP-GIAO overestimates the antiaromaticity of the T_1 state in comparison to CASSCF-GIAO and a switch to a CASSCF-GIAO description of this state in thiophene (and in the other thiophene-based compounds studied in this chapter) are likely to detect a lower level of antiaromaticity. This is an indication that, whereas the levels of aromaticity of the S_0 states of benzene and thiophene are comparable, the T_1 state of benzene is more antiaromatic than the T_1 state of thiophene. The very significant difference between the NICS(0) and NICS(1) values for the T_1 state of thiophene at the S_0 optimised geometry, and the NICS(0) and NICS($\pm$1) values at the T_1 optimised geometry shows the extent to which the T_1 geometry optimisation allows the molecule to adapt to the antiaromatic character of this state and decrease its level of antiaromaticity. For molecules containing two or more condensed thiophene rings, the magnetic properties of the respective T_1 states are examined at T_1 optimised geometries only—the reason for doing so is that, for some of these molecules, the 'triplet' UB3LYP Kohn-Sham determinant at the S_0 geometry turns out to be of 'broken-symmetry', that is, of spatial symmetry lower than that of the nuclear framework, which leads to unphysical results for the nuclear and off-nucleus shielding tensors, as will be discussed and demonstrated in the annulene section.

The $\sigma_{\text{iso}}(\mathbf{r})$ isosurface plots for the S_0 and T_1 states of thiophene at the respective optimised geometries are shown in Figure 13. As can be seen in this figure, the electronic ground state the five-membered ring is very well-shielded, even slightly more so than the six-membered ring in benzene,[1,48] which is due mostly to placing the same number of π electrons in a ring of a smaller size. This observation is in line with the $\sigma_{\text{iso}}(\mathbf{r})$ contour plots for the electronic ground state of thiophene constructed from shielding data calculated at the RMP2-GIAO/6-311++G(d,p) level[49] and confirms the presence of strong bonding interactions and aromatic stability. By comparison, in the T_1 state of thiophene, the five-membered ring is considerably less shielded, which is a clear indication of a marked decrease in aromaticity. However, the absence of a strongly deshielded central region similar to that present in the electronic ground state of cyclobutadiene (see, for example, ref. 2) makes it difficult to argue in favour of sizeable antiaromatic character.

$\mathbf{1}$ S_0 $\mathbf{1}$ T_1

Figure 13: Shielding around the S_0 and T_1 states of thiophene **1**. Isosurfaces at $\sigma_{\text{iso}}(\mathbf{r}) = +16$ ppm (shielded regions, blue) and $\sigma_{\text{iso}}(\mathbf{r}) = -16$ ppm (deshielded regions, orange).

The differences between the S_0 and T_1 optimised geometries of thiophene are considerable: In addition to the reduction in symmetry (see above), the S–C_1, C_1–C_2 and C_2–C_2 bond lengths (C_1 and C_2 stand for the two symmetry-unique carbon atoms, C_1 is adjacent to S) change from 1.718, 1.365 and 1.422 Å in S_0 to 1.771, 1.463 and 1.343 Å in T_1, respectively, that is, the C_1–C_2 'double' bonds in S_0 become 'single' bonds in T_1 and the C_2–C_2 'single' bond in S_0 becomes a 'double' bond in T_1. These differences are reflected in the decreased shielding over the S–C_1 and C_1–C_2 bonds in T_1 in comparison to S_0 (Figure thiophene-isosurface); the C_2–C_2 bond is more shielded than the C_1–C_2 bonds in T_1 but it is less shielded than in S_0. The last observation suggests that the levels of shielding over corresponding bonds in electronic states that exhibit different levels of antiaromaticity may not reflect correctly the respective differences in bond strength and length—the reason for this is that the presence of a central deshielded region in an antiaromatic ring can cause exaggerated deshielding of the bonds in that ring.

The carbon atoms in the S_0 and T_1 electronic states of thiophene and all other thiophene-based compounds studied in this chapter are surrounded by small ovoid deshielded regions inside which $\sigma_{\text{iso}}(\mathbf{r})$ becomes negative. These regions are more noticeable in the $\sigma_{\text{iso}}(\mathbf{r})$ isosurface plots for the T_1 states in which the carbon-carbon and carbon-sulfur bonds are less shielded. Similar deshielded halos' around sp^2 and sp hybridized carbon atoms and other sp^2 hybridized first main row atoms have been observed previously in conjugated rings,[1,48,49] as well as in open-chain conjugated molecules such as ethene, ethyne and *s-trans*-1,3-butadiene.[50,51] The presence of deshielded 'halos' around the carbon atoms in all $\sigma_{\text{iso}}(\mathbf{r})$ isosurface plots reported in this thesis suggests that the hybridisation states of these atoms are close to sp^2; there are no such 'halos' around the sulfur atoms. The close to sp^2 hybridisation states of the carbon atoms suggests that referring to the Kohn-Sham orbitals in the non-planar thiophene-based compounds examined in this chapter as (almost) σ and π orbitals can be viewed as a reasonable approximation; this approximation is also supported by comparisons between the shapes of these orbitals throughout the series **1**–**12**.

3.4 Thienothiophenes

The four thienothiophenes (**2**–**5** in Figure 12) have NICS(0) values between -13.5 and -7.2 ppm, and NICS(1) values between -11.3 and -6.2 ppm (Table 7). These results show that the positions of the sulfur atoms within the two condensed thiophene rings can significantly influence the respective NICS values and levels of aromaticity—for example, the NICS(0) values for the two thiophene rings in the asymmetric thieno[3,4-*b*]thiophene **4** show a considerable difference, -7.2 and -13.5 ppm for rings **4a** and **4b**, respectively. The different levels of aromaticity of these rings are well-illustrated by the $\sigma_{\text{iso}}(\mathbf{r})$ isosurface plot in Figure 14: While the carbon-carbon and carbon-sulfur bonds in both rings are well-shielded, the shielding hole in the centre of ring **4a** (on the left) is much larger than that in the centre of ring **4b** (on the right). The most shielded thiophene rings within the thienothiophenes **2**–**5** are rings **4b** and **5a**, in which the sulfur atoms are positioned similarly; the higher levels of shielding are in correspondence with the respective NICS values. This shielding behaviour can be attributed to the shorter carbon-sulfur bond lengths in rings **4b** and **5a** in comparison to the respective bond lengths in rings **2a**, **3a** and **4a** (for both of **4b** and **5a**, it is possible to draw resonance structures in which the sulfur atom is engaged in two double' bonds; one of these structures for **5a** is shown in Figure 12). The shorter carbon-sulfur bond lengths allow the two electrons contributed by each sulfur atom to engage more fully in the π systems of rings **4b** and **5a**. As a consequence, the local aromaticities of rings **4b** and **5a** estimated using magnetic shielding criteria are out of line with the ordering of the energies of the S_0 optimised geometries of the four thienothiophenes. The lowest-energy thienothiophene is **3**, closely followed by **2**; the energy gaps between **2** and **4**, and between **4** and **5** are larger. The energy ordering of **2**, **3** and **4** is supported by the NICS values in Table 7, if the NICS values for rings **2a** and **3a** are compared to the average NICS values for rings **4a** and **4b** (the lower shielding over ring **4a** compensates for the higher shielding over ring **4b**). However, the thiophene rings **5a** in the least stable thienothiophene, thieno[3,4-*c*]thiophene **5**, turn out to be more shielded and to have more negative NICS values than rings **2a** and **3a**.

Overall, the S_0 shielding isosurfaces for the other two thienothiophenes (**2** and **3**, Figure 14) are very similar to the outcomes that would be expected from fusing together the S_0 isosurfaces for two thiophene rings over the shared carbon-carbon bond. In general, the geometries of the individual thiophene rings in the S_0 optimised geometries of **2**–**5** retain some features of the S_0 geometry of thiophene such as the positions of the carbon-carbon 'single' and 'double' bonds. Similar observations can be made for the S_0 optimised geometries of the remaining compounds with fused thiophene rings studied in this chapter, **6**–**12**.

The differences between the aromatic properties of the T_1 states of the four thienothiophenes are more pronounced, as illustrated by the respective shielding isosurfaces (Figure 14). The only well-defined Baird-style aromaticity reversal from a distinctly aromatic S_0 state to a distinctly antiaromatic T_1 state is observed for thieno[2,3-*b*]thiophene **2**. The antiaromaticity of the T_1 state of this molecule is associated with the presence of a large strongly deshielded central region outlined by the $\sigma_{\text{iso}}(\mathbf{r})=-16$ ppm isosurface, the shape of which resembles a combination of two dumbbells, one inside each ring, interconnected over the fused carbon-carbon bond. This strongly deshielded region leads to a noticeable reduction of shielding over the peripheral carbon-carbon and carbon-sulfur bonds, in comparison to the shielding picture in S_0, and to a displacement of this shielding toward the exteriors of the rings; there is very little, if any, shielding over the fusion bond. The high antiaromaticity of this T_1 state is emphasized by the NICS(0), NICS(+1) and NICS(−1) values of 35.2, 30.2 and 30.3 ppm, respectively, for the symmetry-equivalent thiophene rings **2a**. Despite the molecular symmetry reduction on switching from S_0 to T_1 (C_{2h} to C_2), the associated changes in the central region of the geometry of the carbon-sulfur skeleton of thieno[2,3-*b*]thiophene **2** are relatively minor; as a result, the off-nucleus shielding picture in T_1 is very similar to those observed for S_0 to T_1 vertical excitations in naphthalene and anthracene,[57] and shows a high level of antiaromaticity. It should be noted that despite the complete deshielding of the fusion bond in the T_1 state, its length in the optimised geometry of this state is not much longer than that in the S_0 optimised geometry, 1.405 against 1.392 Å. Just as in the case of thiophene, this observation can be associated with the strongly deshielded central region which causes exaggerated deshielding of all bonds and, especially, of the fusion bond. In general, the bonds in the T_1 states of **3**–**5** are less deshielded than those in the T_1 state of **2**, and the respective shielding pictures have more in common with that for the T_1 state of thiophene.

The changes in the off-nucleus shielding distributions and hence aromaticity levels of the remaining three thienothiophenes on passing from S_0 to T_1 are less pronounced (compare the isosurfaces for **3**–**5** in Figure 14) and similar to the corresponding change observed in thiophene (Figure 13). The thiophene rings in the T_1 states of **3**–**5** can be separated into two groups according to the behaviour of $\sigma_{\text{iso}}(\mathbf{r})$) in and around these rings. These groups of less and more shielded rings include rings **3a** and **4b**, and rings **4a** and **5a**, respectively. The T_1 NICS(0) and NICS(1) values for ring **3a** are 5.4 and 5.5 ppm, respectively, and the corresponding values for ring **4b** are 7.8 and 7.3 ppm, respectively (see Table 7). While these NICS values are positive, they are not sufficiently high to imply anything other than borderline levels of antiaromaticity. The T_1 NICS(0) and NICS(1) values for rings **4a** and **5a** are negative, −3.6 and −2.8 ppm, respectively, for ring **4a**, and −0.6 and −0.3 ppm, respectively, for ring **5a**. Both sets of values indicate that these two rings are mostly nonaromatic. The partial deshielding of the fusion bonds in the T_1 states of thieno[3,2-*b*]thiophene

3, thieno[3,4-*b*]thiophene **4** and thieno[3,4-*c*]thiophene **5** (Figure 3) suggests a close to evenly balanced competition between aromatic and antiaromatic behaviours. Overall, according to the NICS values and the variations in the off-nucleus shielding, the T_1 states of these three thienothiophenes should be considered as nonaromatic.

The $\sigma_{iso}(\mathbf{r})$ isosurfaces and NICS values obtained for compounds **2**–**5** show clearly that the way in which two thiophene rings are fused together has a significant impact on aromaticity and bonding in the S_0 and T_1 states of the resulting thienothiophene.

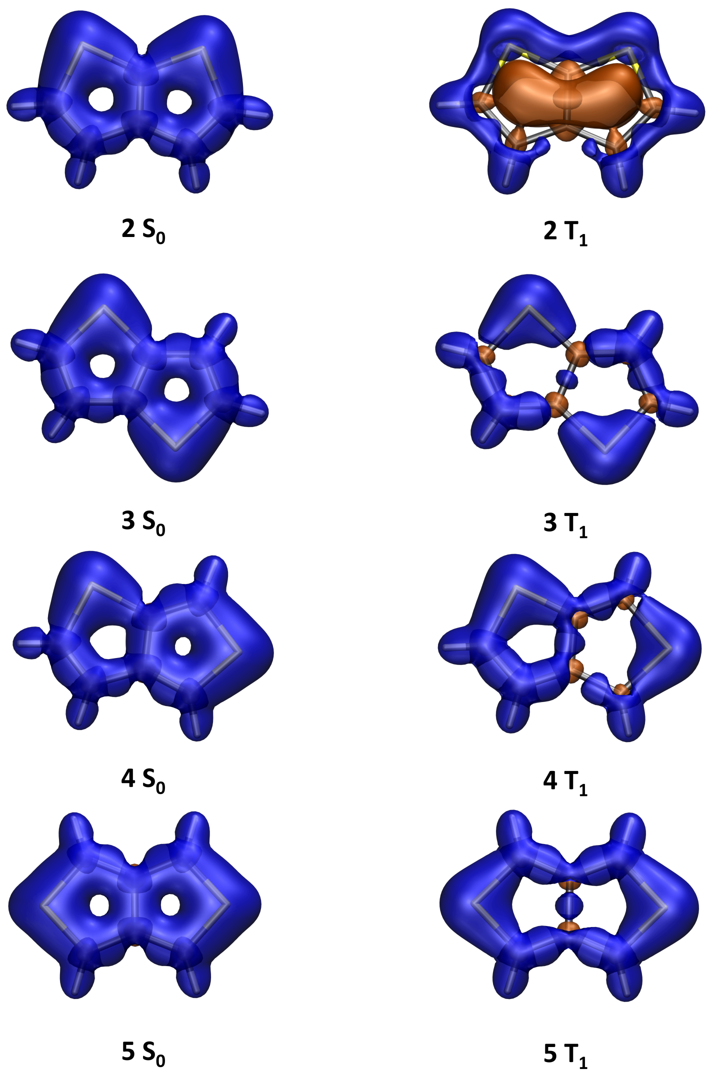

Figure 14: Shielding around the S_0 and T_1 states of thieno[2,3-*b*]thiophene **2**, thieno[3,2-*b*]thiophene **3**, thieno[3,4-*b*]thiophene **4** and thieno[3,4-*c*]thiophene **5**.

Looking at the positions of the carbon–carbon ‘single’ and ‘double’ bonds, the geometries of the individual thiophene rings in the T_1 optimised geometry of **2** are intermediate between the S_0 and T_1 geometries of thiophene, with relatively minor changes in the central region indicating a tendency towards bond equalisation, while those of the individual thiophene rings in the T_1 optimised geometry of **3** are closer to the T_1 geometry of thiophene. This is in line with the observation that the changes in the magnetic shielding picture between the S_0 and T_1 states of **2** resemble those expected for a vertical excitation (see above), while the corresponding changes for **4** resemble those for a thiophene molecule shown in Figure 13. The main changes between the S_0 and T_1 geometries of **4** and **5** are in the rings containing a sulfur atom engaged in two ‘double’ bonds in the S_0 state; the carbon-sulfur bond lengths involving this atom become much longer in the T_1 state which contributes to the deshielding of the interiors of the corresponding rings.

3.5 Dithienothiophenes

The S_0 shielding isosurfaces for dithieno[2,3-*b*:3′,2′-*d*]thiophene **6** and dithieno[3,2-*b*;2′,3′-*d*]thiophene **7** (Figure 15) continue the trend observed in the corresponding shielding isosurfaces for their precursors, thieno[2,3-*b*]thiophene **2** and thieno[3,2-*b*]thiophene **3** (Figure 14) and look very similar to the outcomes that would be expected from fusing together the S_0 isosurfaces for three thiophene rings over the shared carbon-carbon bonds. All three thiophene rings in both molecules are well-shielded which indicates that each of these rings is aromatic.

On switching states from S_0 to T_1, the central ring **6b** in **6** becomes strongly antiaromatic, as shown by the extensive interior deshielding of the ring and the carbon–carbon bonds fusing it to the adjacent **6a** rings. With its NICS(0) value of 41.9 ppm and NICS(1) value of 34.5 ppm, ring **6b** turns out to be the most antiaromatic thiophene ring amongst the T_1 states of all thiophene-based compounds studied in this thesis. The peripheral **6a** rings are less deshielded but, with NICS(0), NICS(+1) and NICS(−1) values of 12.2, 12.4 and 12.8 ppm, respectively, these rings are also antiaromatic. Dithieno[2,3-*b*:3′,2′-*d*]thiophene **6** and its precursor, thieno[2,3-*b*]thiophene **2**, share the orientations of the fused thiophene rings observed in the sulflowers **8**–**12**. The results show that both **2** and **6** are definitely Hückel-aromatic in their S_0 states and Baird-antiaromatic in their T_1 states. It is reasonable to expect that the S_0 and T_1 states of the next two members of this series, with four and five thiophene rings, respectively, thieno[3′,2′:4,5]thieno[2,3-*b*]thieno[3,2-*d*]thiophene and thieno[3′,2′:4,5]thieno[2,3-*b*]thieno[3′,2′:4,5]thieno[3,2-*d*]thiophene, will behave similarly; however, it would be premature to make analogous assumptions about sulflowers (see below).

While the different orientations of the thiophene rings in **6** and **7** do not lead to noticeable differences between the aromaticities of the respective electronic ground states, the T_1 state of **7** is significantly less antiaromatic than the T_1 state of **6**. This is demonstrated by the much lower levels of deshielding of the interiors of rings **7a** and **7b** as opposed to those of rings **6a** and **6b** (compare the corresponding isosurfaces in Figure 15) and the much lower T_1 NICS(0) and NICS(1) values of 0.5 and 1.5 ppm for ring **7a**, and 4.6 and 4.7 ppm for ring **7b**, respectively. In fact, according to these NICS values the T_1 state of dithieno[3,2-*b*;2′,3′-*d*]thiophene **7** should be classified as mostly nonaromatic.

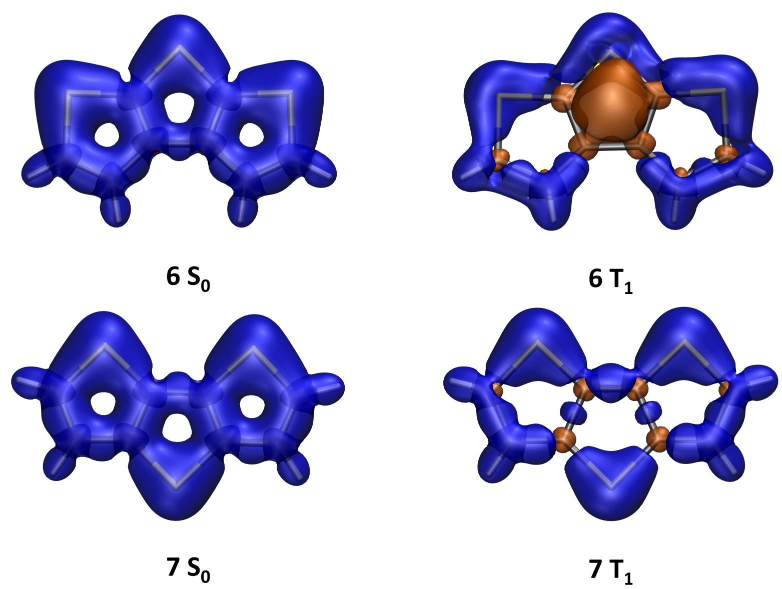

Figure 15: Shielding around the S_0 and T_1 states of dithieno[2,3-*b*:3’,2’-d]thiophene **6** and dithieno[3,2-*b*;2’,3’*d*]thiophene **7**.

The comparison of the geometries of the individual thiophene rings in the T_1 optimised geometries of **6** and **7** to the S_0 and T_1 optimised geometries of thiophene shows that the positions of the ‘single’ and ‘double’ carbon-carbon bonds in the terminal rings **6a** in the T_1 geometry of **6** match the positions of the corresponding bonds in the T_1 geometry of thiophene, but the bond length alternation pattern in the central ring **6b**, while similar to that in the S_0 geometry of thiophene, is more bond-equalised, with shorter carbon-sulfur bonds and longer carbon-carbon bonds. The positions of the ‘single’ and ‘double’ carbon-carbon bonds in all three rings in the T_1 geometry of **7** match the positions of the corresponding bonds in the T_1 geometry of thiophene. The nonplanar geometry of the T_1 state of **6** decreases the conjugation between bonds from different thiophene rings and helps enhance the local traits in the electronic structure;

together with the bond alternation pattern in the central ring in **6** this feature makes the deshielding of this central ring more pronounced, as in the case of a vertical excitation.

3.6 Sulflowers

The S_0 shielding isosurfaces for $(C_2S)_6$–$(C_2S)_{10}$ (**8**–**12**) shown in Figure 16 suggest that the electronic ground states of these sulflowers are aromatic: Each individual thiophene ring is well-shielded, similarly to those in thieno[2,3-*b*]thiophene **2** (Figure 14) and dithieno[2,3-*b*:3′, 2′-*d*]thiophene **6** (Figure 15), which implies that the fusion of thiophene rings to form a sulflower preserves the aromaticities of these rings and produces an aromatic molecule.

The shielding over the carbon–carbon and carbon–sulfur bonds in the S_0 state of $(C_2S)_6$ is predominantly inside the bowl; there is noticeably less shielding over these bonds outside the bowl. This is an indication that the thiophene rings in $(C_2S)_6$ are less aromatic than their counterparts in $(C_2S)_7$–$(C_2S)_{10}$ which is most likely due to stronger ring strain resulting in a deeper bowl and less electron presence and shielding activity outside the bowl. Ring strain in the S_0 optimised geometries of the series $(C_2S)_6$–$(C_2S)_{10}$ initially decreases, through the bowl-shaped $(C_2S)_6$ **8** and $(C_2S)_7$ **9**, to the planar $(C_2S)_8$ **10** and $(C_2S)_9$ **11**, and then increases again, to produce the corrugated-shape $(C_2S)_{10}$ **12** (see below). Despite these variations in ring strain, the differences between the shielding over corresponding carbon-carbon and carbon-sulfur bonds in **9**–**12** in their electronic ground states are relatively minor and difficult to distinguish visually. Each of the S_0 shielding distributions for **8**–**12** includes a relatively small deshielded region around the centre of the respective inner ring (rings **8a**, **9a**, **10a**, **11a** and **12a**); these regions can be examined in detail using lower chemical shift thresholds when examining the GAUSSIAN cube files included in the supplementary material for our paper. The sizes of the deshielded regions and the levels of deshielding suggest that none of the inner rings in the S_0 states of **8**–**12** show more than borderline levels of antiaromaticity and that it might be more appropriate to consider all of these ‘inner’ rings as nonaromatic; however, the presence of these regions is a feature which cannot be explained using simple electron-counting rules.

The comparison between the S_0 NICS(0), NICS(+1) and NICS(−1) values for rings **8b**, **9b**, **10b**, **11b** and **12b**–**12f** (see Table 7), and their counterparts for thiophene shows that each of the fused rings in the respective sulflower is less aromatic than thiophene itself. According to the NICS data, the aromaticity of the individual thiophene rings initially increases between **8** and **10**, and then decreases between **10** and **12**.

Table 7: NICS(0) and NICS(±1) values for the symmetry-unique rings in the S_0 and T_1 electronic states of **1**–**12** (in ppm). For planar geometries, NICS(−1) = NICS(+1).

Ring	S_0 NICS(0)	S_0 NICS(−1)	S_0 NICS(+1)	T_1 NICS(0)	T_1 NICS(−1)	T_1 NICS(+1)
1a	−13.0	−10.4	−10.4	4.3	3.7	5.1
2a	−11.0	−8.8	−8.8	35.2	30.2	30.3
3a	−11.2	−8.9	−8.9	5.4	5.5	5.5
4a	−7.2	−6.2	−6.2	−3.6	−2.8	−2.8
4b	−13.5	−10.8	−10.8	7.8	7.3	7.3
5a	−12.7	−11.3	−11.3	−0.6	−0.3	−0.3
6a	−11.3	−8.7	−8.7	12.2	12.4	12.8
6b	−8.9	−7.0	−7.0	41.9	34.5	34.5
7a	−11.3	−8.5	−8.5	0.5	1.5	1.5
7b	−9.4	− 7.4	− 7.4	4.6	4.7	4.7
8a	0.8	−6.9	3.0	−12.9	−20.7	−5.6
8b	−7.0	− 7.2	−2.6	−9.1	−12.1	−3.2
8c	—	—	—	−6.2	−9.7	−1.3
9a	6.7	−0.3	4.3	3.5	−2.4	2.0
9b	−8.6	− 7.8	−4.7	−0.6	1.4	3.3
9c	—	—	—	−5.6	−4.5	−2.5
9d	—	—	—	−10.1	−8.6	−5.5
9e	—	—	—	−12.5	−10.6	−7.0
10a	5.4	2.6	2.6	4.1	2.6	2.7
10b	−9.7	−6.9	−6.9	14.1	14.3	15.8
10c	—	—	—	8.3	9.7	10.7
11a	4.8	3.0	3.0	1.5	0.3	0.4
11b	−9.3	−6.5	−6.5	8.9	9.0	9.7
11c	—	—	—	−4.0	−2.2	−1.8
11d	—	—	—	−9.3	−6.6	−6.6
11e	—	—	—	−9.5	−6.8	−6.7
11f	—	—	—	−10.1	− 7.5	− 7.3
12a	4.7	3.1	3.1	3.7	2.1	2.3
12b	−9.0	−6.4	−5.8	−1.4	1.3	2.1
12c	−9.0	−6.4	−5.8	−0.6	1.5	−0.1
12d	−8.8	−6.5	−5.5	−8.1	−6.2	−4.8
12e	−9.1	−6.2	−6.2	−9.1	−6.8	−6.1
12f	−8.8	−6.5	−5.5	−9.3	−7.0	−6.0
12g	—	—	—	−8.5	−6.8	−4.9

It is instructive to juxtapose the S_0 NICS values for the inner rings in **8**–**12** with the corresponding values for benzene (D_{2h} symmetry), NICS(0) = −7.6 ppm and NICS(1) = −9.9 ppm, and rectangular cyclobutadiene (D_{2h} symmetry), NICS(0) = 27.2 ppm and NICS(1) = 17.8 ppm, calculated at the level of theory outlined in the annulenes chapter. It should be noted that rectangular cyclobutadiene is considerably less antiaromatic than square cyclobutadiene (D_{4h} symmetry).[53] While this is not meant to suggest that NICS values provide a strictly linear aromaticity scale, it is observed that all NICS(0), NICS(−1) and NICS(+1) values for the inner rings in **8**–**12** (Table 7) are either below or very close to the averages of the NICS(0) and NICS(1) values for benzene and rectangular cyclobutadiene, ca. 9.2 and 3.6 ppm, respectively, which confirms the predominantly nonaromatic character of these rings.

The S_0 states of **8**–**12** are aromatic because the fusion of 6–10 locally aromatic thiophene rings and the establishment of a mostly nonaromatic inner ring should produce a globally aromatic molecule. On the basis of examining the net magnetically induced current strengths (the sums of the magnetically induced current strengths along the 'inner' and 'outer' rings), Karaush-Karmazin and co-authors,[86] who studied the electronic ground states of a wider range of sulflowers, $(C_2S)_5$–$(C_2S)_{12}$, assert that $(C_2S)_5$–$(C_2S)_7$ are antiaromatic, $(C_2S)_8$–$(C_2S)_{10}$ are mostly nonaromatic, and the more strained nonplanar $(C_2S)_{11}$ and $(C_2S)_{12}$ are aromatic, despite reporting NICS(0) values for the thiophene rings in $(C_2S)_6$–$(C_2S)_{10}$ and a NICS(1) value for ring **10b** which are reasonably close to those obtained in the current work and acknowledging that these thiophene rings are locally aromatic. A local minimum of D_{9h} symmetry was obtained for the electronic ground state of $(C_2S)_9$, but the data reported in ref. 86 suggests that the planar $(C_2S)_9$ geometry used in that thesis is of a lower C_{2v} symmetry—this difference is most likely due to the inclusion of empirical dispersion corrections and the use of a larger basis set in the current work. The ring currents from two adjacent rings in a sulflower $(C_2S)_n$ of D_{nv} or C_{nv} symmetry cancel or nearly cancel along the spoke bond fusing these rings. Magnetically induced currents can be integrated to produce shielding tensors by means of the Biot-Savart law (see, for example, ref. 107), and the expectation is that no or next to no current density along the spoke bonds would result in low levels of magnetic shielding over these bonds. However, the S_0 shielding isosurfaces for $(C_2S)_6$–$(C_2S)_{10}$ (**8**–**12**) shown in Figure 16 demonstrate that all spoke bonds in these sulflowers are well-shielded; a very similar discrepancy between ring currents and shielding over spoke bonds is observed in coronene and corannulene.[108] These observations suggest that magnetically induced currents do not account properly for the local aromaticities of the individual thiophene rings in sulflowers, and of the individual benzene rings in coronene and corannulene. As a consequence, the predictions about the aromaticities of fused compounds of this type made on the basis of magnetically induced ring currents can be questionable and contradictory to chemical intuition.

Upon initial inspection, the changes in the shapes of the shielding isosurfaces for **8**–**12** on passing from S_0 to T_1 are anything but uniform. As shown in Figure 16 , the carbon-carbon and carbon-sulfur bonds and the interior of the inner ring in the smallest sulflower investigated, $(C_2S)_6$ **8**, are noticeably more shielded in T_1 than in S_0, which is a clear indication of a higher level of aromaticity. This observation is supported by the T_1 NICS(0) and NICS(−1) values for rings **8b** and **8c**, −9.1 and −6.2 ppm, and −12.1 and −9.7 ppm, respectively (Table 7). The T_1 NICS(+1) values for both types of ring calculated outside the bowl are smaller in magnitude and fall within the nonaromatic region. In addition, in the T_1 state $(C_2S)_6$ no longer features a deshielded region around the centre of its inner ring; in fact, this ring (**8a**) is characterized by T_1 NICS(0), NICS(−1) and NICS(+1) values of −12.9, −20.7 and −5.6 ppm, the first two of which suggest strong aromaticity. In contrast, the shielding distributions in the S_0 and T_1 states of $(C_2S)_7$ **9** show relatively minor differences: in S_0, all symmetry-equivalent thiophene rings are equally shielded, whereas in T_1 three thiophene rings (**9d** and **9e**) are more shielded than in S_0, two others (**9c**) are slightly less shielded, and the remaining two (**9b**) are significantly less shielded. Shielding around the 'inner' ring **9a** remains largely unchanged between the two states, and the deshielded central region observed in S_0, where shielding drops to -4 ppm, persists in T_1. These results suggest that $(C_2S)_7$ **9** undergoes minimal change in aromaticity upon excitation to T_1, which is consistent with the S_0 and T_1 NICS(0), NICS(−1), and NICS(+1) values for rings **9a**–**9e** shown in Table 7.

Adding an additional thiophene ring to form $(C_2S)_8$ **10** leads to a substantial change in the shielding distribution in the T_1 state: all eight thiophene rings become antiaromatic, with deshielded regions located above and below the centre of each ring, predominantly inside the bowl. In four of these rings (**10b**, see Figure 16), $\sigma_{\text{iso}}(\mathbf{r})$ reaches approximately −20 ppm; in the remaining four rings (**10c**) it drops to around −13 ppm. Although the positions used to evaluate the T_1 NICS(0) and NICS(+1) values for **10b** and **10c** are not at the most deshielded locations (Table 7), the positive NICS(−1) values reaching up to 15.8 ppm for **10b** support the conclusion that **10** is antiaromatic in T_1. The shielding around the 'inner' ring **10a** is reduced relative to S_0; as in S_0, a deshielded region remains near the centre, where NICS(0) = 4.1 ppm.

Signs of antiaromaticity in the T_1 state of $(C_2S)_9$ **11** are more limited: only the two symmetry-equivalent thiophene rings **11b** show deshielded regions near their centres, with $\sigma_{\text{iso}}(\mathbf{r})$ approaching −11 ppm. Two further rings, **11c**, are less shielded compared to S_0, while the remaining five thiophene rings, **11d**–**11f**, exhibit similar shielding to **11b** in S_0. According to the T_1 NICS(0) and NICS(+1) values in Table 7, rings **11d** and **11e** maintain similar aromaticity to that of **11e** in S_0, and **11f** appears to be even more aromatic. Overall, the T_1 state of $(C_2S)_9$ **11** contains two antiaromatic, two nonaromatic, and five aromatic thiophene rings. The 'inner' ring has a small central deshielded region, but the magnitude of deshielding and associated NICS values suggest it remains nonaromatic.

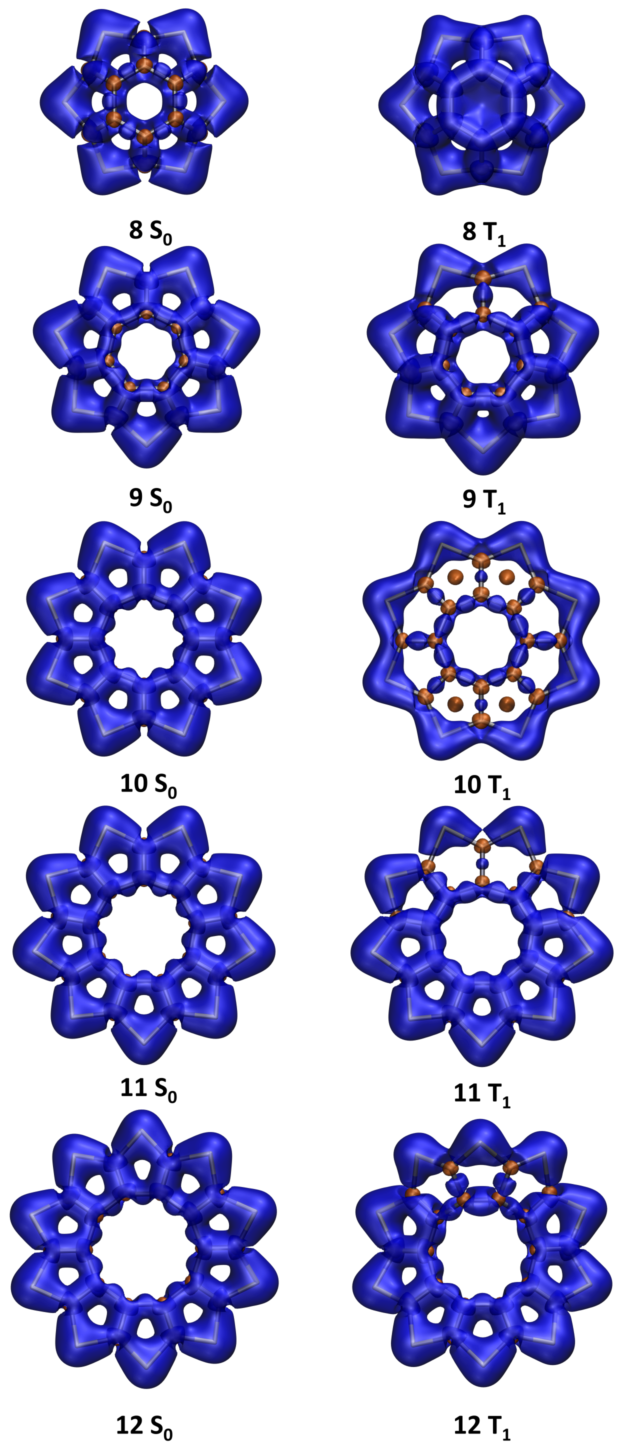

Figure 16: Shielding around the S_0 and T_1 states of sulflowers with six **8**, seven **9**, eight **10**, nine **11** and ten **12** thiophene rings. Views from top for bowl-shaped geometries.

For **12**, the shielding isosurfaces and NICS values indicate that none of the ten thiophene rings are antiaromatic in the T_1 state. Three rings (**12b** and **12c**) exhibit some deshielding and lower NICS values than in S_0, while the remaining seven rings retain shielding characteristics and NICS values similar to those seen in S_0. These results imply that the T_1 state of **12** comprises three nonaromatic and seven aromatic thiophene rings. Shielding around the 'inner' ring **12a** is comparable to S_0; the central deshielded region persists, with NICS(0) = 3.7 ppm (1 ppm lower than in S_0) confirming its nonaromatic character in T_1.

These findings indicate that the smaller sulflowers $(C_2S)_6$ **8** and $(C_2S)_7$ **9** are resistant to developing T_1 antiaromaticity, whereas in the larger sulflowers $(C_2S)_9$ **11** and $(C_2S)_{10}$ **12**, any antiaromaticity is restricted to a few thiophene rings. The clearest aromaticity reversal in the series **8**–**12** occurs in $(C_2S)_8$ **10**, where the most aromatic sulflower in S_0 becomes the most antiaromatic in T_1.

The unexpected increase in aromaticity of $(C_2S)_6$ **8** upon excitation to the T_1 state is supported by a comparison of their optimised geometries. The C_{6v} symmetry of the S_0 geometry gives rise to three symmetry-unique bond lengths: carbon–sulfur rim bonds (1.780 Å), carbon–carbon spoke bonds (1.367 Å), and carbon–carbon hub bonds (1.424 Å). The reduced C_{2v} symmetry in the T_1 state introduces three distinct carbon–sulfur rim bond lengths of 1.785, 1.784 and 1.751 Å (each repeated four times), two spoke bond lengths of 1.400 Å (four bonds) and 1.381 Å (two bonds), and two hub bond lengths of 1.426 Å (four bonds) and 1.406 Å (two bonds). Overall, the combined lengths of the bonds forming both the outer and inner rings are reduced in T_1, and the thiophene rings show a greater degree of bond equalisation. These features are consistent with the increased shielding seen across all bonds in the T_1 state (Figure 16).

The optimised T_1 geometry of $(C_2S)_7$ **9** displays both nonaromatic and aromatic traits in line with the shielding isosurfaces. The spoke bond linking the two **9b** rings is long (1.475 Å) and weakly shielded, resembling a typical carbon–carbon single bond. In contrast, the better-shielded bonds connecting **9b** to **9c** are notably shorter (1.399 Å), and all other spoke bonds have lengths consistent with carbon–carbon double bonds. The thiophene rings **9b** exhibit geometries between those of S_0 and T_1 thiophene, while rings **9c**–**9e** are more similar to S_0 thiophene.

In $(C_2S)_8$ **10**, the T_1 geometry (C_{2v} symmetry) contains two distinct types of thiophene rings: **10b** and **10c**. The former exhibit structures intermediate between S_0 and T_1 thiophene and show a clear trend toward carbon–carbon bond equalisation; the latter more closely resembles the S_0 geometry. The longest and least shielded spoke bonds are those connecting pairs of **10b** rings, consistent with the deep deshielding observed in their interiors (Figure 16). The T_1 geometries of $(C_2S)_9$ **11** and $(C_2S)_{10}$ **12** include thiophene rings that match the T_1 geometry of thiophene (**11b**, **12b**), rings intermediate between S_0 and T_1 geometries (**12c**), and rings more closely resembling the S_0 geometry (**11c**–**11f**, **12d**–**12g**). This classification is reflected in the shielding isosurfaces shown in Figure 16.

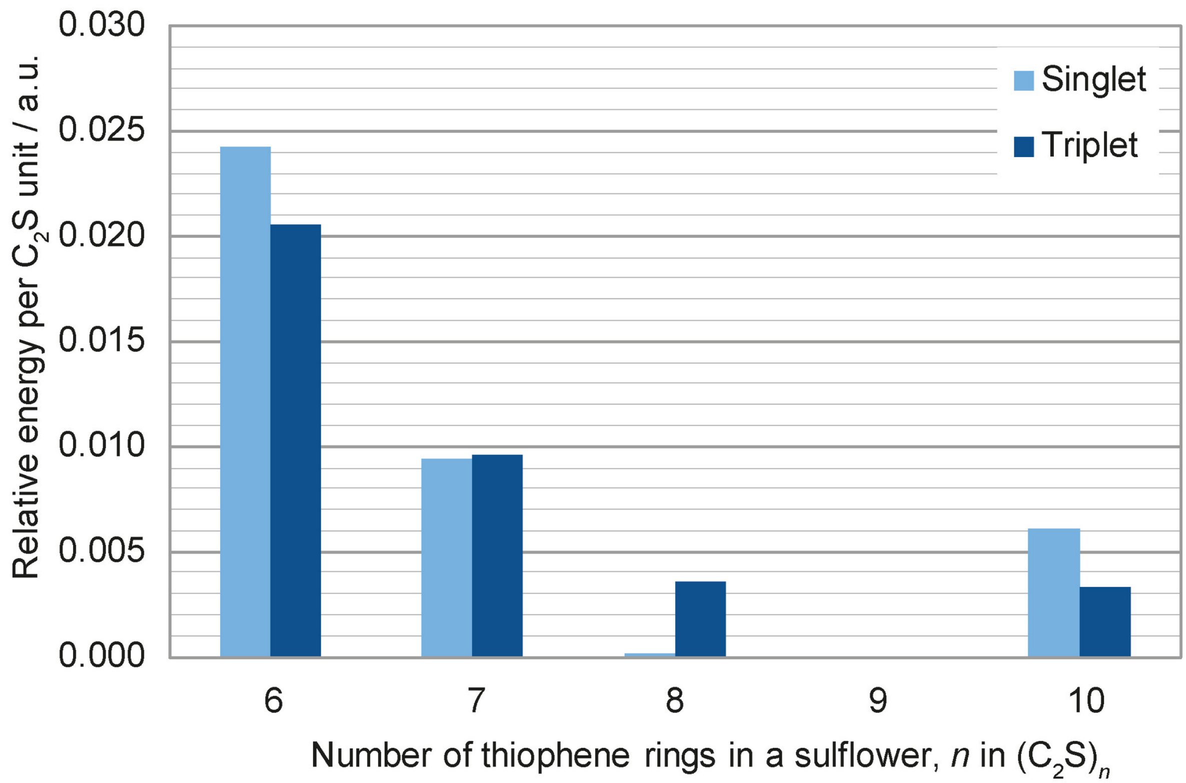

Figure 17: Relative energies per C_2S unit of the S_0 and T_1 electronic states of the sulflowers $(C_2S)_6$–$(C_2S)_{10}$ (**8**–**12**).

To analyse ring strain in the S_0 and T_1 electronic states of $(C_2S)_6$–$(C_2S)_{10}$ (**8**–**12**), a procedure analogous to that adopted for the S_0 electronic states of sulflowers in refs. 85 and 86 was followed, and the respective energies per C_2S unit,

$$E_{C_2S \text{ in } (C_2S)_n} = \frac{E_{(C_2S)_n}}{n} \tag{30}$$

were calculated.

The $E_{C_2S \text{ in } (C_2S)_n}$ values obtained at the RB3LYP-D3(BJ)/def2-TZVP and UB3LYP-D3(BJ)/def2-TZVP levels, for the S_0 and T_1 electronic states, respectively, are shown in Figure 17 relative to the S_0 and T_1 $E_{C_2S \text{ in } (C_2S)_9}$ values which turned out to be the lowest ones for both states. The changes in ring strain in the S_0 electronic states of $(C_2S)_6$–$(C_2S)_{10}$ are very similar to those reported in refs. 85 and 86, with one difference: At the RB3LYP/6-311++G(d,p) level, the S_0 $E_{C_2S \text{ in } (C_2S)_8}$ value was found to be slightly lower, by 0.2 kcal mol^{-1}

than that for $(C_2S)_9$,[86] while the results indicate that the S_0 $E_{C_2S \text{ in } (C_2S)_8}$ value is slightly higher, by just 0.1 kcal mol^{-1} (2.0×10^{-4} a.u.), than that for $(C_2S)_9$. Ring strain in the T_1 electronic states of $(C_2S)_6$ –$(C_2S)_{10}$ follows a trend close to that observed in the respective S_0 electronic states: Bowl depth and ring strain decrease from $(C_2S)_6$ to $(C_2S)_8$, $(C_2S)_9$ becomes almost planar and then $(C_2S)_{10}$ assumes a geometry which is significantly more corrugated than the geometry of this sulflower in its ground electronic state. In T_1, the difference between $E_{C_2S \text{ in } (C_2S)_8}$ and $E_{C_2S \text{ in } (C_2S)_9}$ increases to 2.2 kcal mol^{-1} (3.6×10^{-3} a.u.).

3.7 HOMO-LUMO and Singlet-Triplet Gaps

The HOMO-LUMO and singlet-triplet gaps for compounds **1**–**12** are shown in Figure 18. The two types of gap follow rather similar trends (with the exception of thiophene **1**) despite the fact that the singlet-triplet gaps in Figure 7 correspond to the differences between the energies of separately optimised T_1 and S_0 geometries rather than to vertical excitation energies. Two of the factors influencing the HOMO-LUMO gaps in **1**–**12** are relatively straightforward to account for: These are aromatic stabilisation which increases the HOMO-LUMO gap, and conjugation pathway length which acts in the opposite direction.

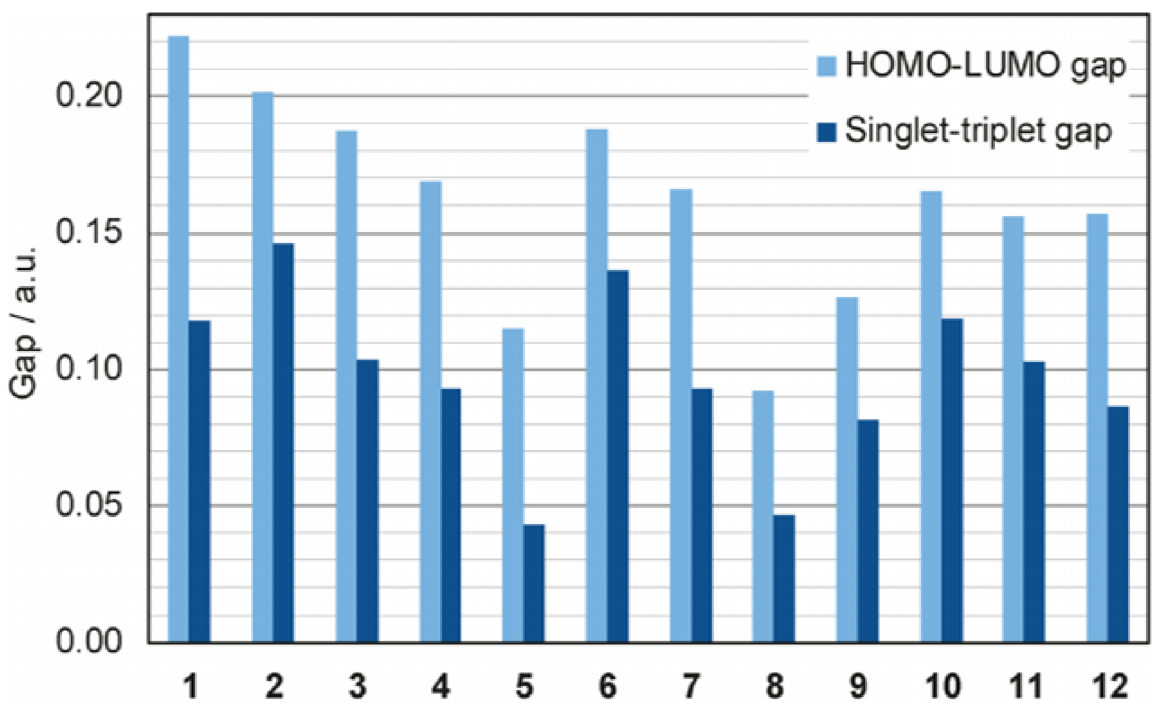

Figure 18: HOMO–LUMO gaps for thiophene and the condensed thiophene rings and the total energy difference of the singlet and triplet state, calculated at the B3LYP-D3(BJ)/def2-TZVP level in GAUSSIAN.

The cross-conjugated **2** and **6** feature the largest HOMO-LUMO gaps amongst compounds **2**–**12**. According to our magnetic shielding results, the differences between the S_0 aromaticities of the individual thiophene rings in **2** and **3**, and **6** and **7** are very minor, so that the difference between the HOMO-LUMO gaps in **2** and **3**, and in **6** and **7** can be attributed to the differences between the respective conjugation pathways lengths only. However, **5** which according to our magnetic shielding results involves the most S_0 aromatic thiophene rings amongst **2**–**5** and has conjugation pathways shorter than those in **3** shows the smallest HOMO-LUMO gap amongst the four dithienothiophenes. This is an indication that there are additional important factors influencing the sizes of the HOMO-LUMO gaps which are not that easy to account for qualitatively, for example, the positions of the sulfur atoms.

The HOMO-LUMO gaps of the sulflowers **8**–**12** show better correlation with our magnetic shielding estimates of the S_0 aromaticities of the individual thiophene rings: The HOMO-LUMO gap increases between **8** and **10** and then decreases slightly in **11** and **12**. The corresponding singlet-triplet gaps are in even better agreement with the NICS data in Table 7: The singlet-triplet gaps increase in the sequence **8**–**10** and then noticeably decrease in the sequence **10**–**12**.

3.8 Conclusions

The analysis of the variations of the off-nucleus isotropic magnetic shielding, $\sigma_{\text{iso}}(\mathbf{r})$, around thiophene, thienothiophenes, dithienothiophenes and sulflowers in their electronic ground and lowest triplet states, and of the connection between these variations and the geometries of the respective states, reveals that some of the features of aromaticity and bonding in these molecules do not fit in with predictions based on the popular Hückel's and Baird's rules. Thiophene and the thienothiophenes and dithienothiophenes studied in this chapter are systems with $4n + 2$ π electron counts of 6, 10 and 14, equal to those of benzene, naphthalene, and anthracene, respectively. As expected, magnetic shielding calculations have confirmed that the electronic ground states of these molecules are aromatic. On the other hand, any sulflower with a molecular formula $(C_2S)_n$ has $4n$ π electrons. However, logic suggests that, irrespective of this π electron count, the fusion of aromatic thiophene rings to form a sulflower will produce a molecule aromatic in its electronic ground state, and this is supported by the shielding pictures and NICS values.

Each of the series of compounds with one, two and three fused thiophene rings including thiophene **1**, thieno[2,3-*b*]thiophene **2** and dithieno[2,3-*b*:3′,2′-*d*]thiophene **6**, or thiophene, thieno[3,2-*b*]thiophene **3** and dithieno[3,2-*b*;2′,3′-*d*]thiophene **7**, can be viewed as a thiophene-based heterocyclic analogue of the series comprised of benzene, naphthalene, and anthracene. However, our electronic ground state NICS results for these two thiophene-based series of compounds do not exhibit trends consistent with the set of disputed predictions made on the basis of the NICS values for benzene, naphthalene, and anthracene [109,110] known as the 'anthracene problem', [57,111,112] according to which both rings in naphthalene, as well as the central ring in anthracene should be more aromatic than the benzene ring, and the central ring in anthracene should be more aromatic than the outer rings. Instead, our NICS results suggest that the thiophene ring **1a** is more aromatic than the thienothiophene rings **2a** and **3a** which show levels of local aromaticity close to those of the dithienothiophene outer rings **6a** and **7a**; the central dithienothiophene rings **6b** and **7b** are less aromatic than the respective outer rings.

The switch in aromaticity between the S_0 and T_1 states of condensed thiophene molecules in this chapter are much less pronounced than those observed in benzene, naphthalene, and anthracene [48,53,57]; surprisingly, the results indicate that hexathio[6]circulene **8** which is relatively weakly aromatic in its electronic ground state becomes more aromatic in its lowest triplet state. The magnitude of the changes in aromaticity between the S_0 and T_1 states of the molecules examined in this chapter are reduced by the use of geometries optimised separately for the two states: It is well-known that antiaromatic molecules try to break free from antiaromaticity through a symmetry reduction, for example, square cyclobutadiene distorts to a rectangular geometry with 'single' and 'double' carbon-carbon bond. [113] Well-defined Baird-style aromaticity reversals between the S_0 and T_1 states of only three of the twelve thiophene-based compounds we investigated, thieno[2,3-*b*]thiophene **2**, dithieno[3,2-*b*;2′,3′-*d*]thiophene **7** and hexathio[8]circulene **10**.

The results suggest that the geometry of thiophene changes considerably between the S_0 and T_1 states: Not only is its symmetry reduced from C_{2v} to C_s with a loss of planarity but, more importantly, the carbon-carbon 'double' and 'single' bonds in the S_0 state turn into 'single' and 'double' bonds, respectively, in the T_1 state. Identifying thiophene rings with geometries resembling those of a thiophene molecule in its S_0 or T_1 state can help rationalise the levels of antiaromaticity in the T_1 states of some of the compounds with fused thiophene rings studied in this chapter.

Similarly to the situation observed in the T_1 state of anthracene, [57] the most antiaromatic rings in the T_1 states of dithieno[2,3-*b*:3′,2′-*d*]thiophene **6** and dithieno[3,2-*b*;2′,3′-*d*]thiophene **7** turn out to be the central rings **6b** and **7b**; the outer rings **6a** and **7b** are significantly less aromatic and very much nonaromatic, respectively. This is an indication that in longer polyacene chains and in their heterocyclic analogues T_1 antiaromaticity is likely to affect mostly the central ring (or pair of central rings); rings sufficiently far away from the central ring(s) could even remain aromatic.

4

Sulfinfinitines

4.1 Introduction

Aromaticity manifests in cyclic molecules and, from a geometrical perspective, often motivates the design of new structures. The most notable example of this is buckminsterfullerene, C_{60}.[114–116] Extending the idea of fusing thiophene rings, this section suggests possible interesting molecules for aromaticity studies and possible synthetic targets. In particular, inspiration was drawn from the synthesis of infinitene,[117] a [12]circulene twisted in a figure-of-eight loop resembling the infinity symbol, and voted by C&EN readers as molecule of the year for 2021,[118] which prompted the search for other fused benzene-based molecules exhibiting similar structural patterns. Rzepa reported calculations on infinitene analogues with 11 and 10 benzene rings in his blog,[119] but the optimised geometries of these species suggest higher levels of strain. Infinitene can be assembled by applying an imaginary "cut–twist–restitch" sequence to two coronene ([6]circulene) molecules (Figure 19); to assemble the [11]infinitene and [10]infinitene mentioned above one would need one coronene and one corannulene ([5]circulene), or two corannulenes, respectively. The use of corannulene component(s) can be expected to produce a more strained infinitene (corannulene is bowl-shaped and more strained than coronene).

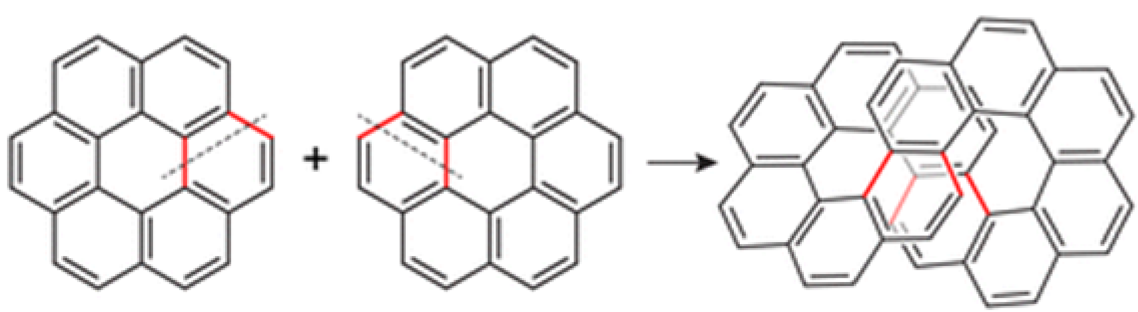

Figure 19: Imaginary "cut–twist–restitch" assembly of infinitene from two coronene molecules.

While it is possible to consider other [m + n]infinitene analogues assembled from an [m]circulene and an [n]circulene, computational research on [n]circulenes[120] indicates that strain increases very quickly for n < 6, and a bit slower for n > 6, with higher circulenes adopting first saddle and then helical geometries.

Indeed, experimental data shows that bowl depth in a derivative of [4]circulene (quadrannulene)[121] is higher than that in corannulene, and that [7]circulene[122–124] and a derivative of [8]circulene[125] have saddle-shaped geometries. So, while [m + n]infinitenes with m and n outside the 5–7 range can be studied computationally, such infinitenes would be highly strained and of low synthetic feasibility. One way to reduce strain in circulene analogues is to include acene units, as in kekulene,[126,127] a close-to-planar cycloarene with 12 benzene rings. Infinitene analogues constructed from cycloarenes have been suggested and studied computationally[128] but have yet to be synthesised. The junctions in such infinitene analogues[128,129] differ from the naphthalene junctions in [12]infinitene and calculations suggest[129] that a [12]infinitene analogue with anthracene junctions has a lower energy than the original [12]infinitene.

4.2 Geometry

An imaginary "cut–twist–restitch" sequence (as illustrated in Figure 19) can be applied to two sulflowers to construct heteroinfinitenes. To mitigate the risk of computational artefacts, the gas-phase ground-state geometries of [n]sulflowers with 5–10 thiophene rings, $(C_2S)_n$ (n = 5–10), and those of the heteroinfinitenes ('sulfinfinitenes') resulting from combining two [n]sulflowers, $(C_2S)_{2n}$, were optimised at two DFT levels of theory, B3LYP-D3(BJ)/def2-TZVP and M06-2X/def2-TZVP. The B3LYP-D3(BJ)/def2-TZVP optimised geometries of the [n]sulflowers with n = 6–10 are identical to those reported previously in Chapter 3;[67] note that the lengths of the carbon–sulfur rim, carbon–carbon hub and carbon–carbon spoke bonds in the [8]sulflower of 1.752, 1.417 and 1.381 Å, respectively, provide an almost perfect match for the experimentally measured bond lengths of 1.751, 1.419 and 1.380 Å.[85,86,105] The respective M06-2X/def2-TZVP optimised bond lengths of 1.744, 1.417 and 1.371 Å show that this approach slightly underestimates the lengths of the carbon–sulfur rim and carbon–carbon spoke bonds. Beyond this, no major qualitative differences in geometry or energy were observed between the two levels of theory. The B3LYP-D3(BJ)/def2-TZVP optimised geometries of the [n]sulflowers and [2n]sulfinfinitenes with n = 5–10 are shown in Figures 20 and 21, respectively; the respective M06-2X/def2-TZVP optimised geometries are very similar in appearance. The junctions in all sulfinfinitenes are thieno[3,2-*b*]thiophene units. The individual rings have been highlighted using the PaperChain visualisation algorithm[130] implemented in VMD[46] which colours each ring according to the ring pucker amplitude. Regions coloured dark red to brown represent highly puckered and non-planar segments, which can be associated with torsional strain and significant out-of-plane displacement. Orange to red zones indicate moderate puckering, while pale pink corresponds to nearly planar regions, suggestive of low strain and greater structural regularity. The presence of blue in the central cavity of the largest macrocycle (**6**) denotes an unoccupied void space or a region excluded from the ring puckering calculation.

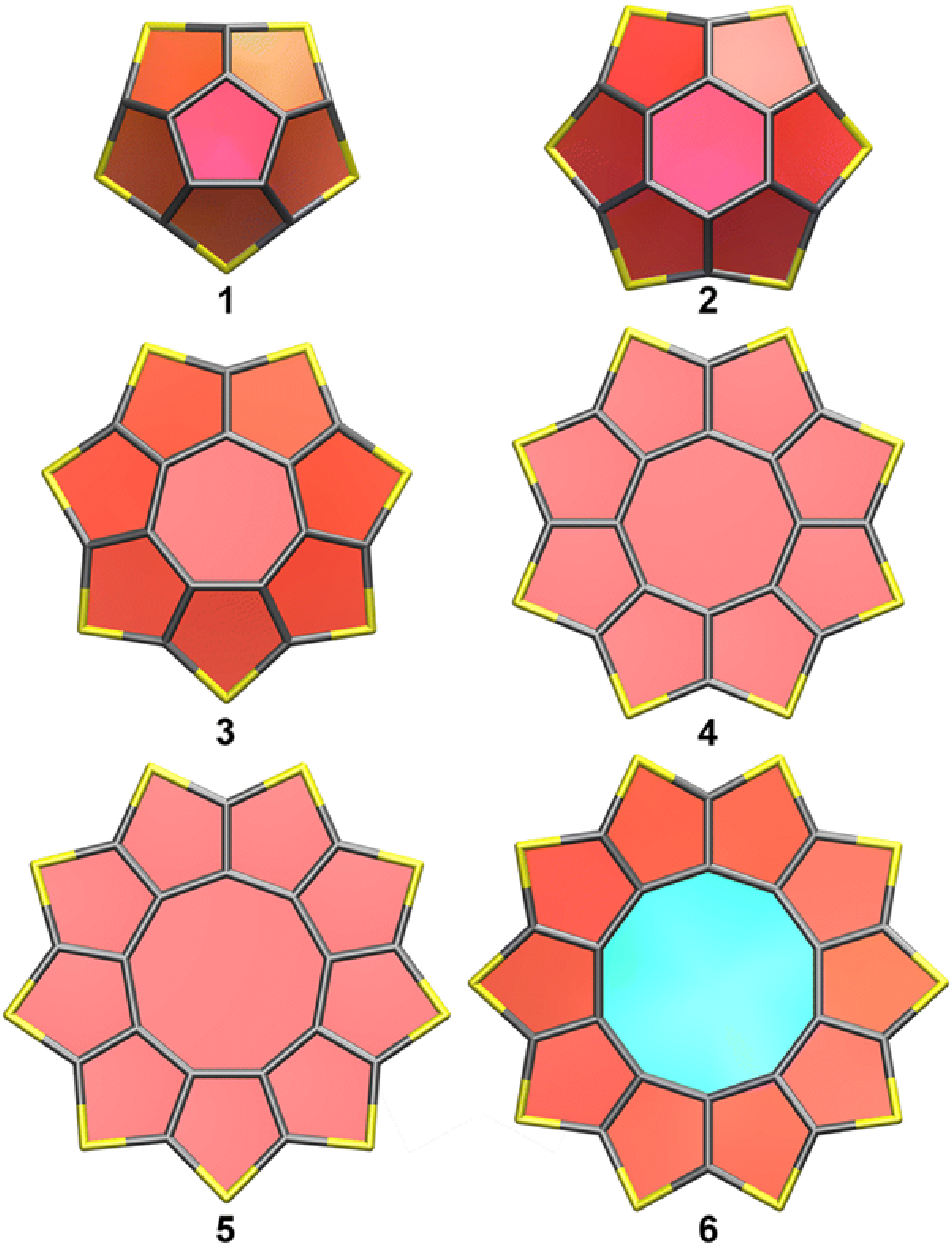

Figure 20: B3LYP-D3(BJ)/def2-TZVP optimised geometries of the [n]sulflowers with n = 5–10.

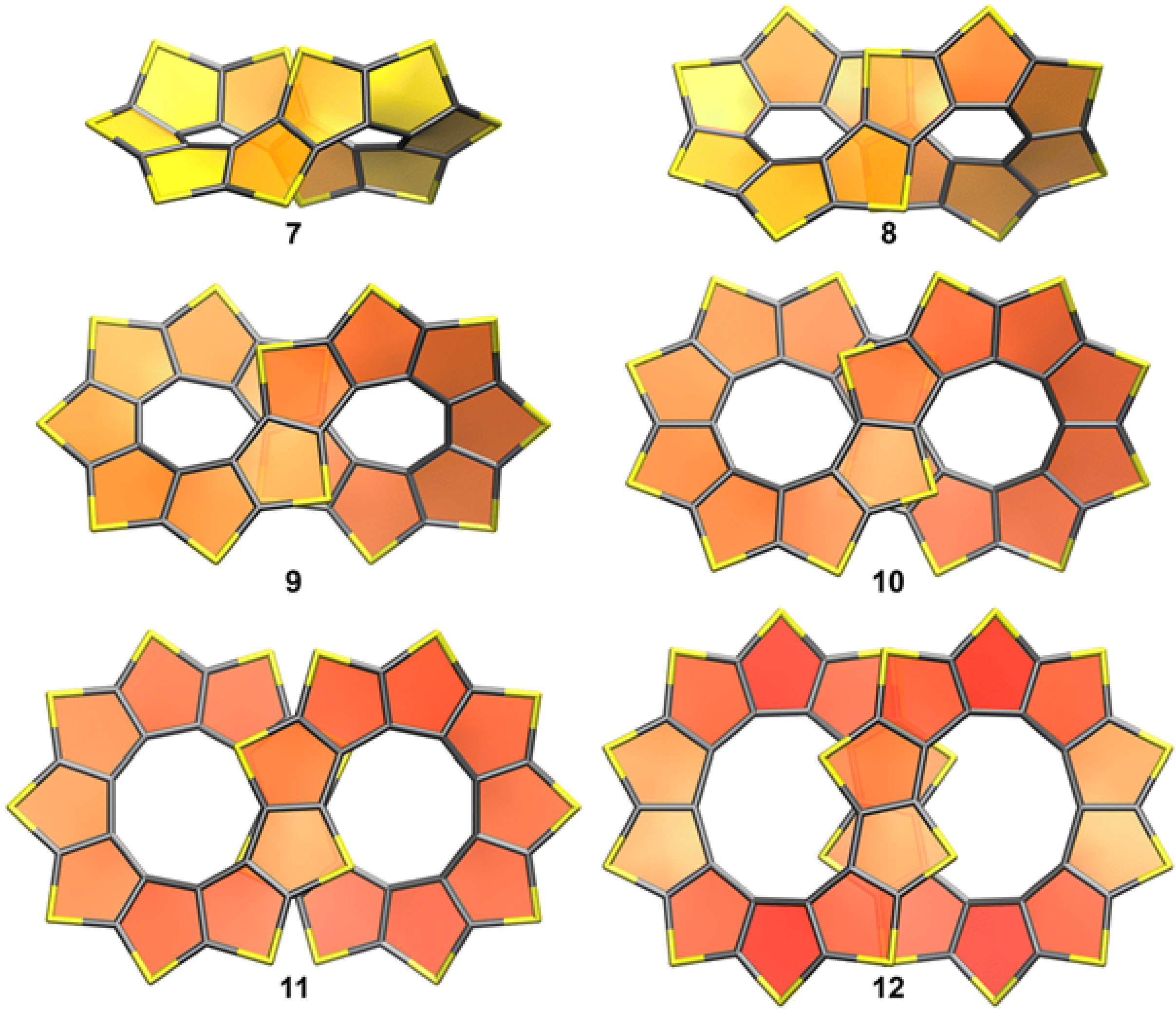

Figure 21: B3LYP-D3(BJ)/def2-TZVP optimised geometries of the [2n]sulfinfinitenes with n = 5–10.

Looking at the sulflower series, the rings' colours show that the pucker amplitudes of the individual thiophene rings decrease through **1**–**3** (geometries of C_{5v}, C_{6v} and C_{7v} symmetries, respectively), become zero in the planar **4** and **5** (geometries of D_{8h} and D_{9h} symmetries, respectively), and then increase in the non-planar **6**, which has a saddle-shaped geometry of C_2 or D_2 symmetry at the B3LYP-D3(BJ)/def2-TZVP or M06-2X/def2-TZVP level, respectively. Similarly, in the sulfinfinitene series, the ring pucker amplitudes decrease through **7**–**9**, become much the same for rings in matching positions in **10** and **11**, and then increase in **12**. The geometries of **7** and **8** are of C_2 symmetry, and those of **9**–**12** are of D_2 symmetry, similar to that of [12]infinitene.

4.3 Energy

The changes in strain energy in the sulflower series can be quantified by calculating the energy per C_2S unit, $E(n)/n$, where n is the number of C_2S units in **1**–**6** (5–10, respectively).[67,85,86] An analogous quantity, $E(2n)/(2n)$, can be calculated for each member of the sulfinfinitene series **7**–**12**. The energies per C_2S unit of **1**–**12** are shown in Figure 22, relative to the lowest value of this type at each level of theory. At both levels of theory, **5** exhibits the lowest energy per C_2S unit, with **4** coming a close second.

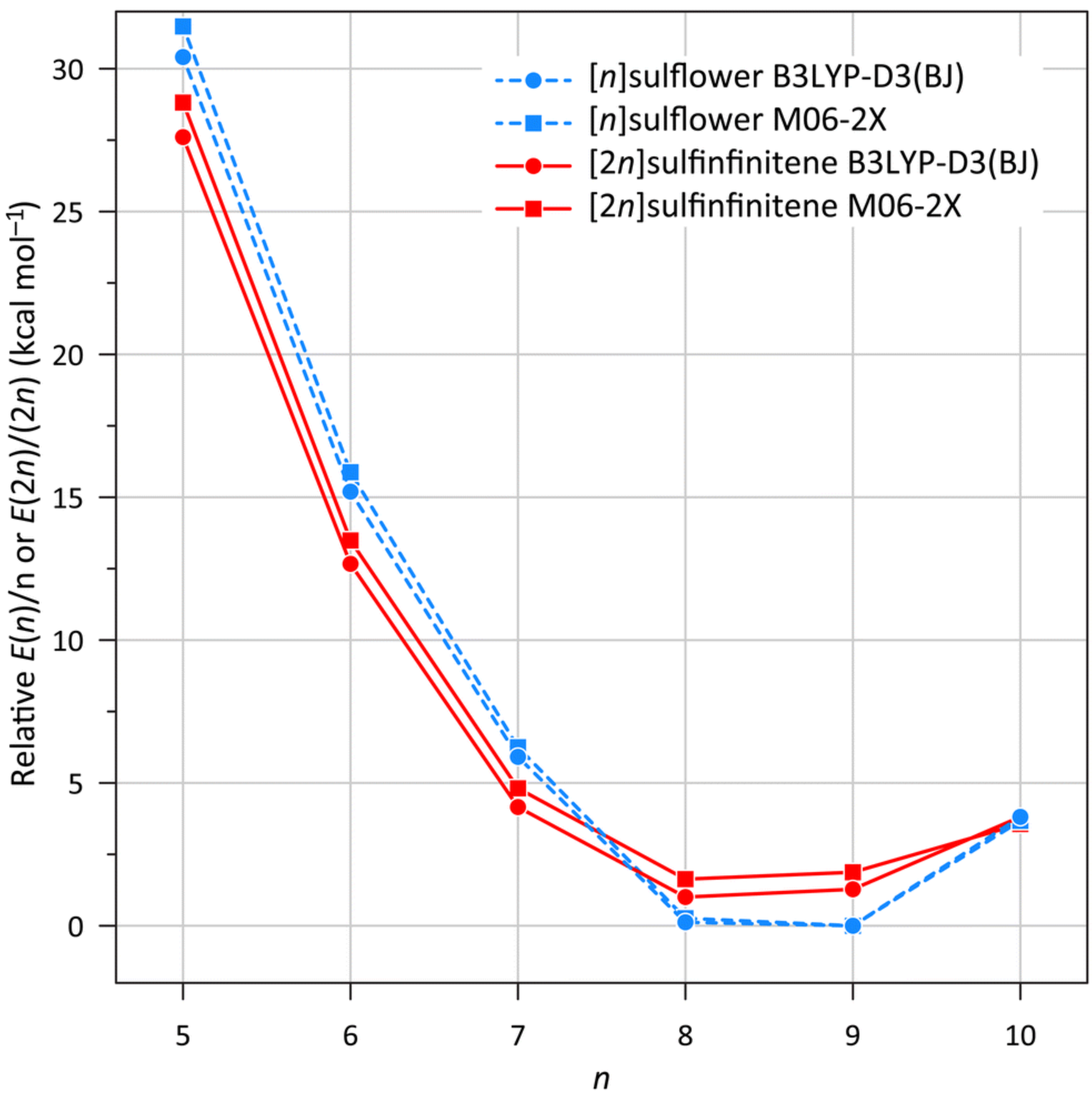

Figure 22: B3LYP-D3(BJ)/def2-TZVP and M06-2X/def2-TZVP energies per C_2S unit of the [n]sulflowers and [2n]sulfinfinitenes with n = 5–10 (1–12), relative to that of the [9]sulflower (5).

The variations in the energy per C_2S unit show that if an [n]sulflower is nonplanar (n = 5–7, 10), the corresponding [2n]sulfinfinitene is slightly less strained; however, for planar [n]sulflowers (n = 8, 9), the corresponding [2n]sulfinfinitenes are slightly more strained. The reaction energies (ΔE) for the assembly of [16]sulfinfinitene from two [8]sulflowers through a homodesmotic scheme analogous to that shown in Figure 19, calculated at the B3LYP-D3(BJ)/def2-TZVP and M06-2X/def2-TZVP levels, are 14.1 and 21.9 kcal mol^{-1}, respectively. These ΔE values are significantly lower than that of combining two coronene molecules into infinitene, which, according to our calculations, the geometries optimised at the B3LYP-D3(BJ)/def2-TZVP and M06-2X/def2-TZVP levels, are 78.5 and 84.3 kcal mol^{-1}, respectively. The [8]sulflower is less "stiff" than coronene, which helps reduce ΔE for the assembly of [16]sulfinfinitene. This is well-illustrated by the difference between the frequencies of the lowest a_{2u} normal modes of the [8]sulflower and coronene, in which the atomic displacements are similar to the initial geometry changes required for an assembly such as that shown in Figure 19: the lowest a_{2u} normal mode of the [8]sulflower is ν_1, 59.6 and 59.8 cm^{-1}, at the B3LYP-D3(BJ)/def2-TZVP and M06-2X/def2-TZVP levels, respectively; the corresponding numbers for the lowest a_{2u} normal mode of coronene, ν_2, are higher, 124.1 and 123.9 cm^{-1}, respectively. The HOMO–LUMO energy gaps of **1**–**12**, which are often used as qualitative measures of reactivity, are shown in Figure 23. The HOMO–LUMO energy gaps increase rapidly between the [5] and [8]sulflowers (**1**–**4**) and then decrease slightly and then plateau for the [9] and [10]sulflowers (**5** and **6**). A similar tendency is observed in the sulfinfinitene series, but the gap changes are less pronounced. These observations suggest that the [8]sulflower and the [16]sulfinfinitene are the least reactive and most stable members of the respective series. It should be noted that although the M06-2X HOMO–LUMO gaps are systematically higher than their B3LYP counterparts, the tendencies displayed by the gaps calculated with both DFT methods are very much the same. For reference, the HOMO–LUMO energy gaps in infinitene and coronene calculated at the same levels of theory as those shown in Figure 23 are 3.18 and 4.02 eV, respectively (B3LYP), and 5.02 and 5.87 eV, respectively (M06-2X).

The separations between the carbon atoms from the central carbon–carbon bonds in the stacked thieno[3,2-*b*]thiophene junction units in [16]sulfinfinitene and [18]sulfinfinitene, 3.086 and 3.160 Å at the B3LYP-D3(BJ)/def2-TZVP level, and 3.085 and 3.147 Å at the M06-2X/def2-TZVP level, are close to the corresponding separation between the carbon atoms from the central carbon–carbon bonds in the stacked naphthalene junction units in infinitene, 2.961 and 2.966 Å at the B3LYP-D3(BJ)/def2-TZVP and M06-2X/def2-TZVP levels, respectively (the experimentally measured separation has been reported as 2.920 Å)[117].

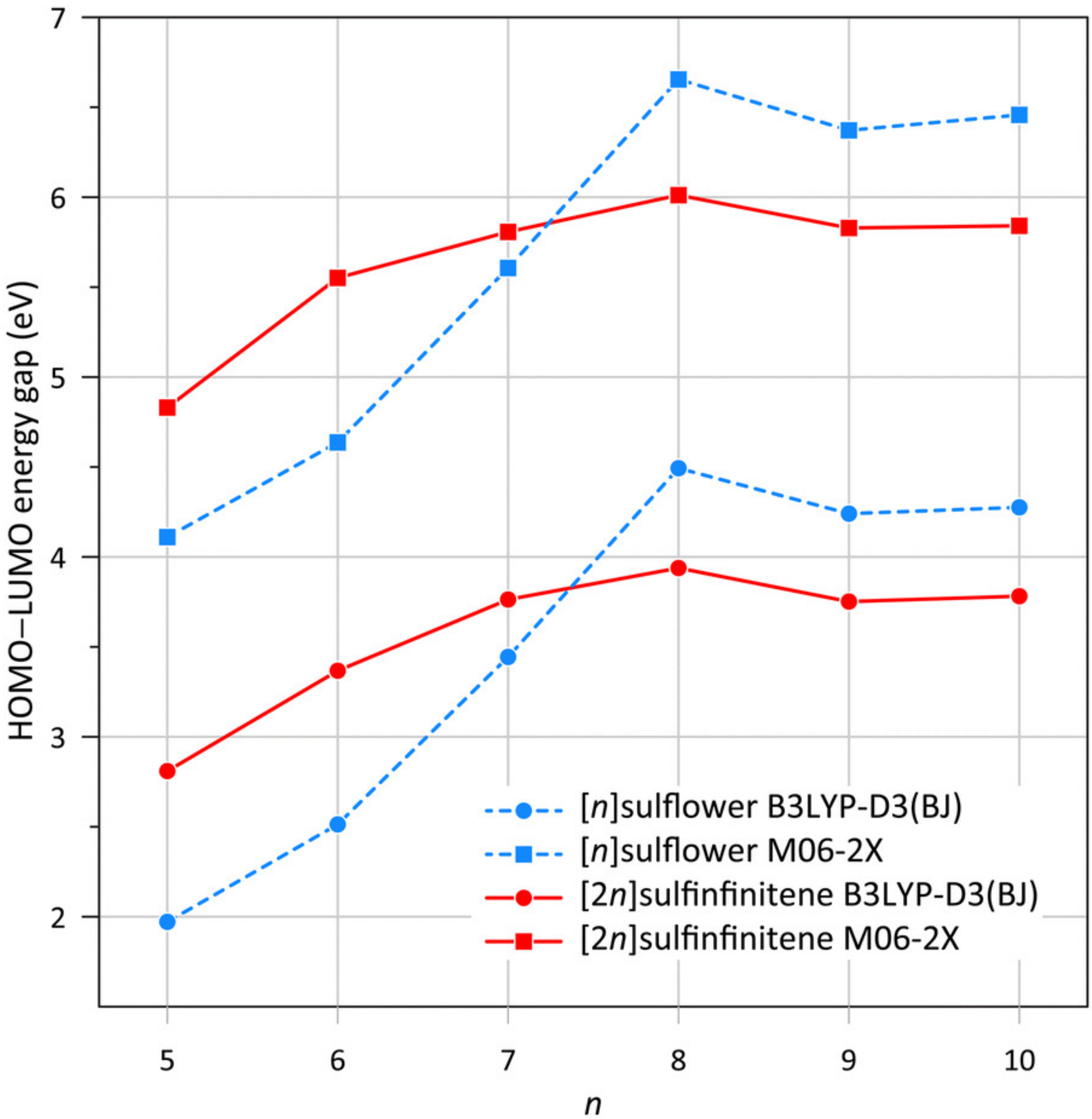

Figure 23: B3LYP/def2-TZVP//B3LYP-D3(BJ)/def2-TZVP and M06-2X/def2-TZVP//M06-2X/def2-TZVP HOMO–LUMO energy gaps of the [n]sulflowers and [2n]sulfinfinitenes with n = 5–10 (1–12).

4.4 Aromaticity

The numbering scheme for each thiophene ring is that the first C_2S unit (i = 1) is the one involving the central carbon-carbon double bond in the top thieno[3,2-*b*]thiophene junction; the numbers of the atoms in this unit are S_1, C_2 and C_3. Subsequently, counting is continued around C_2S units clockwise, with the second one (i = 2) comprised of S_4, C_5S and C_6S. The NICS values associated with a C_2S unit are those for the thiophene ring including the atoms from this unit and the carbon atoms from the next C_2S unit;

for the first C_2S unit these are S_1, C_2, C_3, C_6 and C_5. Due to its D_2 symmetry, [16]sulfinfinitene has four symmetry-unique thiophene rings.

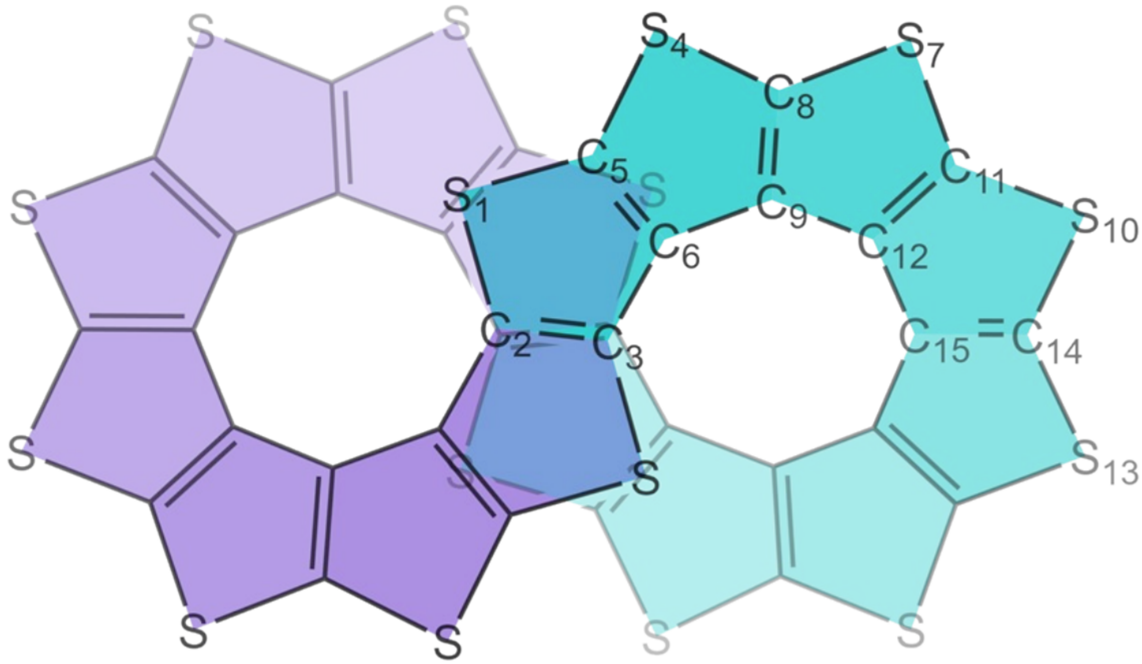

Figure 24: The numbering scheme for the atoms in sulfinfinitenes

Whilst not as thorough as the magnetic shielding isosurfaces generated in the majority of this thesis, the aromaticities of the individual thiophene rings are briefly investigated with nucleus-independent chemical shifts (NICS) values, presented in Table 8. According to the NICS(0) and NICS($\pm$1) values of the thiophene rings in the sulfinfinitenes (Table 8), each of the rings in **7**–**12** is less aromatic than thiophene itself, which has NICS(0) and NICS(1) values of -13.0 and -10.4 ppm, respectively. The NICS data indicate that, in general, the aromaticities of the individual thiophene rings in the [n]sulflowers and [2n] sulfinfinitenes initially increase for $5 \leq n \leq 8$, and then decrease for $8 \leq n \leq 10$, in line with the behaviour of the respective energies per CS_2 unit (Figure 22).

Apart from the more highly strained **7** and **8**, the variation between the NICS values for the individual thiophene rings in the sulfinfinitenes is relatively small, for example, the NICS(0) range observed in **9**–**12** is between -10.1 and -8.2 ppm. **7** has nonaromatic NICS values for rings 2 and 5, but has particularly weak shielding for ring 4, which has a NICS(0) value of just -0.6 ppm. This can be attributed to not only the non-planarity of this ring, but also how twisted it is. It should be noted that the computed ^{33}S isotropic shieldings increase with sulfinfinitene size, which can be attributed to the possibility that longer conjugation pathways involving the sulfur atoms can form. The same is true for increasing the size of the sulflowers.[131]

Table 8: NICS values and nuclear shieldings in sulfinfinitenes, **7**–**12**. For ring labelling, see text and Figure 24.

i	NICS(0)	NICS(+1)	NICS(−1)	$^{33}S_{(i-1)+1}$	$^{13}C_{(i-1)+2}$	$^{13}C_{(i-1)+3}$
[10]sulfinfinitene (**7**, C_2)						
1	-8.2	-7.3	-6.5	222.2	39.4	24.9
2	-5.9	-5.6	-4.5	221.3	26.5	57.2
3	-9.2	-7.2	-6.5	190.9	32.0	34.8
4	-0.6	-3.0	0.5	165.7	39.7	7.0
5	-5.6	-4.7	-4.2	89.5	-0.3	43.9
[12]sulfinfinitene (**8**, C_2)						
1	-8.6	-7.5	-7.0	203.5	33.0	42.5
2	-7.3	-4.4	-6.4	220.9	18.8	47.2
3	-6.8	-4.1	-6.1	200.2	18.2	39.5
4	-9.1	-5.7	-7.3	211.9	31.9	39.0
5	-8.6	-5.7	-7.3	232.5	35.5	44.7
6	-8.3	-5.8	-7.3	236.3	26.3	52.5
[14]sulfinfinitene (**9**, D_2)						
1	-9.3	-7.6	-6.8	266.4	39.8	39.8
2	-9.5	-6.8	-6.9	270.6	27.7	48.8
3	-9.0	-6.4	-6.5	260.7	29.9	49.4
4	-9.1	-6.4	-6.4	257.3	32.8	49.4
[16]sulfinfinitene (**10**, D_2)						
1	-9.8	-7.6	-7.5	283.2	42.4	42.4
2	-10.0	-6.8	-7.4	301.1	31.8	47.3
3	-9.1	-6.5	-6.2	299.9	30.8	48.1
4	-9.0	-6.5	-6.3	299.3	31.4	48.6
5	-9.0	-6.3	-6.5	299.3	31.4	49.6
[18]sulfinfinitene (**11**, D_2)						
1	-10.1	-7.4	-8.1	297.3	44.5	44.5
2	-9.7	-6.5	-7.0	305.5	33.5	48.1

i	NICS(0)	NICS(+1)	NICS(−1)	$^{33}S_{(i-1)+1}$	$^{13}C_{(i-1)+2}$	$^{13}C_{(i-1)+3}$
3	-9.3	-6.6	-6.0	319.8	33.4	46.2
4	-8.9	-6.4	-5.9	320.7	32.2	45.8
5	-8.7	-6.0	-6.0	317.7	30.1	47.1
[20]sulfinfinitene (**12**, D_2)						
1	-10.0	-7.1	-8.3	306.6	45.8	45.8
2	-9.8	-6.3	-7.9	307.5	31.5	48.5
3	-9.4	-6.3	-6.0	324.3	31.3	46.3
4	-8.7	-6.2	-5.2	330.7	34.0	41.4
5	-8.2	-5.9	5.3	324.2	30.6	41.7
6	-8.2	-5.3	5.9	324.2	29.1	43.9

4.5 Conclusions

The results of the current calculations strongly suggest that [16]sulfinfinitene, which can be formally obtained by combining two molecules of the least strained member of the sulflower series, the [8]sulflower (octathio[8]circulene),[85] should be considered as a promising synthetic target. [18]sulfinfinitene and its precursor, the [9]sulflower (nonathio[9]circulene) shows slightly higher strains and slightly lower HOMO–LUMO gaps and could also be of synthetic interest. No [m + n] sulfinfinitenes with different m and n values were considered in this chapter, but it can be expected that a reasonable combination, for example, [8 + 9], would have a strain energy similar to [16]sulfinfinitene and [18]sulfinfinitene. The magnetic shielding in sulfinfinitene rings suggest the rings are all similarly aromatic, provided ring strain is not too great.

5 Condensed Furans

5.1 Introduction

Furan containing compounds are abundantly used in medicine,[132] photoinitiators,[133] optoelectronics[134] and biomass fuel,[135] so understanding the bonding in fused furan rings is of great interest to many areas of chemistry. In five-membered heteroaromatics, the heteroatom donates two electrons to the π system, circumventing the need to have a sixth atom in the conjugated ring in order to have a $4n + 2$ Hückel aromatic π system similar to that in benzene. Furan is no exemption. Four isomers can be formed by condensing two furan rings, namely, furo[2,3-*b*]furan **2**, furo[3,2-*b*]furan **3**, furo[3,4-*b*]furan **4** and furo[3,4-*c*]furan **5**; all of these are examined in this chapter. There are 12 difurofuran isomers, and in this work two are examined, difuro[3,2-*b*;2',3'-*d*]furan **6** and difuro[2,3-*b*:3',2'-*d*]furan **7**, as shown in Figure 25.

Condensed furan rings may be arranged to form a class of heterocirculenes known as 'oxiflowers' first proposed by Nguyen[90] with a molecular formula $(C_2O)_n$. Another way to view oxiflowers is an 'outer' $(CO)_n$ ring formed by carbon-oxygen rim bonds encompassing an 'inner' C_n ring formed by carbon-carbon hub bonds; with both rings are connected by carbon-carbon 'double' spoke bonds allowing the possibility of several cyclic conjugation pathways. Interconnected heterocycles can display competing aromatic and antiaromatic properties due to alternative cyclic conjugation pathways with 4n + 2 or 4n π electrons.[2,84] Based on the energetic findings of Nguyen,[90] this chapter investigates oxiflowers with 12, 13, 14, 15 and 16 condensed furan rings: dodecafuro[12]circulene **8**, tridecafuro[13]circulene **9**, tetradecafuro[14]circulene **10**, pentadecafuro[15]circulene **11** and hexadecafuro[16]circulene **12**. The most stable of these oxiflowers is thought to be $(C_2O)_{14}$ **10** which has been shown to have the lowest energy per repeat unit.[90] The bonding in S_0 and T_1 states of conjugated cyclic systems are traditionally governed by two π electron counting rules: Hückel's well-known classification of systems with 4n + 2 and 4n π electron systems as aromatic and antiaromatic, respectively,[136–138] and Baird's rule, which reverses Hückel's designation in the lowest vertical $\pi\pi^*$ triplet state.[139]

Oxiflowers $(C_2O)_{12}$–$(C_2O)_{16}$ (**8**–**12** in Figure 25) are structurally similar to the polycyclic aromatic hydrocarbons (PAHs) coronene ($C_{24}H_{12}$) and corannulene ($C_{20}H_{10}$), which have 24 and 20 π electrons, respectively. These hydrocarbons fail to formally conform to Hückel's 4n + 2 rule but are aromatic. Each C_2O unit in an oxiflower with a molecular formula $(C_2O)_n$ provides four π electrons to the total system and hence the total number of π electrons is 4n. Hence, the individual furan rings, and of the $(CO)_n$ rim and C_n hub rings are more likely to govern aromaticity than at the total π electron counts. Every furan ring in **8**–**12** should be aromatic; the rim and hub rings could be thought of as the components of an 'annulene-within-a-heteroannulene' model analogous to the 'annulene-within-an-annulene' (AWA) model[95,140] suggested in order to explain the aromaticity of corannulene but challenged by subsequent research.[96]

Baird's rule suggests some individual furan rings, rim and hub rings may experience aromaticity reversals in the T_1 state. The degree of aromatic reversal will be dictated by the geometry of the triplet state, since the molecular aromaticity is evaluated at the optimised electronic T_1 geometry in this chapter. Even for single rings, aromatic reversals are far more pronounced for vertical excitations than adiabatic ones.[141] The degree of aromaticity in the electronic ground and excited states of polycyclic conjugated compounds could require more detailed analysis, going significantly further than straightforward applications of Hückel's and Baird's rules to various cyclic conjugation pathways with $4n+2$ or $4n$ π electrons. Condensing any rings, such as a single benzene and cyclobutadiene ring in benzocyclobutadiene[38,74,97,99,100] or two benzene and one cyclobutadiene ring in biphenylene[38,99,101,102] has highlighted small systems can exhibit both local aromaticity and local antiaromaticity in their electronic ground states. Hückel aromatic character in the T_1 states of Cibalackrot-type compounds[103] and mixed Hückel-Baird hybrid aromatic character in the T_1 states of pro-aromatic quinoidal compounds[104] are further investigations which have shown the different bonding in systems. In light of all this research, the way the oxiflowers and other condensed furans will change aromaticity upon excitation is difficult to predict, and hence warrants investigation.

This chapter closely follows the previous chapter based on condensed thiophene rings.[67] In that study, the aromaticity of thiophene, thienothiophenes, dithienothiophenes and sulflowers were assessed through magnetic shielding. Comparisons can also be made to the series of benzene, naphthalene, anthracene[57] and then coronene or corannulene which are circulenes with 6 and 5 benzene rings. Trials of selenium and tellurium as the heteroatom[142] in addition to broader aspects of the structure and reactivity of heterocirculenes[88,91] and their synthesis[92–94] highlights the interest in such molecules. Given the reduced aromaticity of furan **1** (Figure 25) compared to both thiophene and benzene along with other heterocyclic rings such as pyrrole[49] and furans abundance in molecules, this chapter explores how varying the heteroatom changes the aromaticity in the molecule.

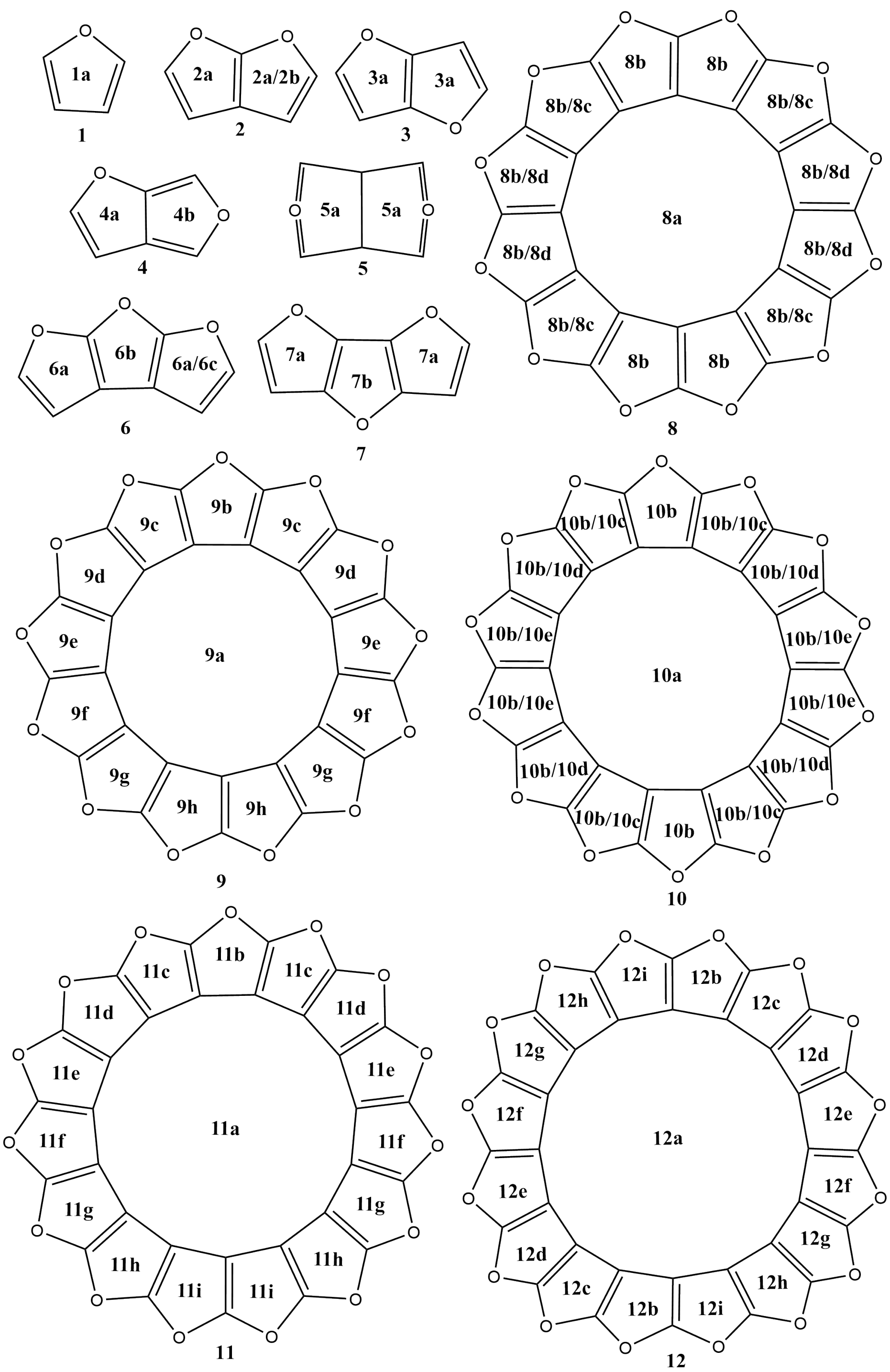

Figure 25: Furan **1**, furo[2,3-*b*]furan **2**, furo[3,2-*b*]furan **3**, furo[3,4-*b*]furan **4**, furo[3,4-*c*]furan **5**, difuro[2,3-*b*:3′,2′-*d*]furan **6** and difuro[3,2-*b*;2′,3′-*d*]furan **7**; oxiflowers with twelve **8**, thirteen **9**, fourteen **10**, fifteen **11** and sixteen **12** C_2O units, $(C_2O)_{12}$–$(C_2O)_{16}$. All rings are labelled by structure numbers followed by letters; rings related through symmetry operations share the same label. Ring labels that differ between the S_0 and T_1 optimised geometries are separated by a slash '/', with the S_0 label first.

5.2 Geometry

The S_0 geometries of molecules **1**–**12** were optimised at the RB3LYP-D3(BJ)/def2-TZVP level (restricted B3LYP[16,17,143,144] with Grimme's D3 empirical dispersion corrections and Becke–Johnson damping,[145] within the def2-TZVP[146] basis set); the respective T_1 geometries were optimised at the unrestricted UB3LYP-D3(BJ)/def2-TZVP level. All optimised geometries were confirmed as local minima through analytical harmonic frequency calculations.

In this chapter, carbon and their accompanying hydrogen atoms in furan are labelled clockwise from oxygen atom. The C_{2v} symmetry of the optimised electronic ground state geometry of furan **1** is reduced to C_1 in the respective geometry of its lowest triplet state; notably an unequal out-of-plane bending of the H_1 and H_4 atoms in the same direction, with a difference in z-coordinates of H atoms with their bonded C atoms of 0.353 (C_1– H_1) and 0.690 Å (C_4– H_4). However crucially, just as with thiophene, the C_2–C_3 single and C_1–C_2/C_3–C_4 double bonds switch to double and single bonds, respectively. These bond length changes help identify which rings in condensed systems are most affected by excitation.

Furo[2,3-*b*]furan **2** undergoes the same symmetry switch as furan, C_{2v} to C_1 upon switching from the optimised ground to lowest triplet state. Ring **2a** remains largely planar and unchanged by the excitation, whilst 2b has a geometry closer to **1a** in the T_1 state. The symmetry of the optimised electronic ground states of furo[3,2-*b*]furan **3**, furo[3,4-*b*]furan **4** and furo[3,4-*c*]furan **5** are planar, with C_{2h}, C_s and D_{2h}, respectively. Switching to the optimised T_1 causes **3** and **4** to become C_i and C_1, respectively, largely due to out-of-plane bending of hydrogen atoms. **5** retains its planar D_{2h} symmetry upon excitation, with the most noticeable change being the lengthening of C–O bonds from 1.351 to 1.392 Å.

Both difuro[2,3-*b*:3′,2′-*d*]furan **6** and difuro[3,2-*b*;2′,3′-*d*]furan **7** have planar C_{2v} symmetry. **7** retains this symmetry when optimised to the T_1 state, whilst **6** reduces to C_1 symmetry as ring **6c** bends significantly out of plane. The C–C bond connecting rings **6b** and **6c** significantly lengthens from 1.365 to 1.535 Å.

$(C_2O)_{12}$ has a 'bowl-shaped' geometry in both electronic states, but looses some symmetry in the excitation from C_{6v} symmetrical S_0 electronic state to the C_{2v} symmetrical T_1 state. The next three oxiflowers are crinkled and non-planar: $(C_2O)_{13}$ has C_2 symmetry in both the ground and lowest triplet optimised state; $(C_2O)_{14}$ switches from D_{7d} to C_{2h} after optimisation and $(C_2O)_{15}$ goes from C_2 to C_s. $(C_2O)_{16}$ has C_2 symmetry in both states, resembling a 'pringle' shape (or in mathematical terms is saddle shaped), but curvature increases substantially for the excited state. Oxiflowers have far less symmetry than the sulflowers, with more significant deviations from planarity leading to far more symmetry unique rings.

5.3 Furan

Schleyer and co-workers calculated NICS(0) for furan as -12.3 ppm using RHF-GIAO/6-31+G(d).[38] Increasing the basis set size to 6-311++G(d,p) reveals similar results with NICS(0) and NICS(1) of -12.2 and -9.2 ppm, respectively.[49] MP2-GIAO/6-311++G(d,p) is also similar at -12.6 and -9.7 ppm.[49] Our results (at the RB3LYP-GIAO/6-311++G(d,p) level) are -11.9 and -9.1 ppm, respectively, almost identical to the RB3LYP-GIAO/6-311+G(d,p) results of -11.9 and -9.4 ppm, respectively.[106] Our T_1 NICS(0), NICS($+1$) and NICS(-1) values at the T_1 optimised geometry of 3.1, 2.2 and 2.9 ppm, respectively, indicate that furan experiences an aromaticity neutralisation between S_0 and T_1. Thiophene's aromaticity change is greater, with an identical model chemistry, with NICS(0) switching from -13.0 to 4.3 ppm, and NICS(1) of -10.4 ppm diverging to NICS($+1$) and NICS(-1) of 3.7 and 5.1 ppm, respectively. However, the magnitude of this S_0–T_1 aromaticity reversal appears to be much lower than that reported for benzene: The S_0 NICS(0) and NICS(1) values for benzene, -8.2 and -9.5 ppm, respectively, change to 39.6 and 30.1 ppm, respectively in T_1; these S_0 and T_1 values were calculated with CASSCF(6,6)-GIAO/6-311++G(2d,2p) wavefunctions (π space complete-active-space self-consistent field with '6 electrons in 6 orbitals' and GIAOs), for a vertical excitation at the experimental electronic ground state geometry.[53]

For comparison purposes, we also calculated the NICS(0) and NICS(1) values for the T_1 state of furan at the S_0 optimised geometry, that is, for a vertical excitation. This produced much higher NICS(0) and NICS(1) T_1 values of 18.6 and 14.4 ppm, respectively, which are closer to but still noticeably lower than those for the T_1 state of benzene. The vertical excitation for thiophene also had a far greater aromatic reversal to 28.4 and 24.7 ppm, respectively. This trend suggests that the greater the aromatic reversal, the greater the aromatic the initial S_0 state.

It has been observed on the examples of naphthalene and anthracene[57] that, when used to calculate magnetic properties, UB3LYP-GIAO overestimates the antiaromaticity of the T_1 state in comparison to CASSCF-GIAO and a switch to a CASSCF-GIAO description of this state in furan (and in the other furan-based compounds studied in this chapter) is likely to detect a lower level of antiaromaticity. This is an indication that, whereas the levels of aromaticity of the S_0 states of benzene, thiophene and furan are comparable, the T_1 state of benzene is more antiaromatic than the T_1 state of thiophene, which is in turn more antiaromatic than furan. The very significant difference between the NICS(0) and NICS(1) values for the T_1 state of thiophene at the S_0 optimised geometry, and the NICS(0) and NICS($\pm$1) values at the T_1 optimised geometry shows the extent to which the T_1 geometry optimisation allows the molecule to adapt to the antiaromatic character of this state and decrease its level of antiaromaticity. For molecules containing two or more condensed furan rings we examine the magnetic properties of the respective T_1 states at T_1 optimised geometries only—the reason for doing so is that, for some of these molecules, the 'triplet' UB3LYP Kohn-Sham determinant at the S_0 geometry turns out to be of 'broken-symmetry', that is, of spatial symmetry lower than that of the nuclear framework, which leads to unphysical results for the nuclear and off-nucleus shielding tensors.

Table 9: NICS(0) and NICS(1) values for the symmetry-unique rings in the S_0 and T_1 electronic states of **1**–**12** (in ppm). For planar geometries, NICS(−1) = NICS(+1). For further details, see text.

	S_0 NICS(0)	S_0 NICS(−1)	S_0 NICS(+1)	T_1 NICS(0)	T_1 NICS(−1)	T_1 NICS(+1)
1a	-11.9	-9.1	-	3.1	2.9	2.2
2a	-10.4	-8.0	-	2.0	1.8	-
2b	-	-	-	-5.1	-4.1	-
3a	-11.2	-8.4	-	1.3	1.5	-
4a	-14.4	-10.0	-	4.8	4.6	-
4b	-7.3	-5.8	-	-5.2	-4.5	-
5a	-14.1	-10.8	-	-1.4	-2.8	-
6a	-11.4	-8.0	-	-6.8	-5.4	-
6b	-9.5	-6.8	-	1.4	2.0	-
6c	-	-	-	2.0	2.2	-
7a	-11.8	-8.2	-	-1.4	0.3	-
7b	-10.9	-7.5	-	-0.7	1.1	-
8a	2.6	0.9	2.6	2.4	2.1	2.1
8b	-10.5	-8.1	-6.2	-5.1	-2.6	-3.5
8c	-	-	-	1.7	4.9	1.1
8d	-	-	-	12.6	10.4	9.7
9a	2.7	2.0	2.0	1.9	1.4	1.4
9b	-10.6	-7.2	-7.2	-10.9	-7.4	-7.4
9c	-10.6	-7.2	-7.1	-10.5	-7.2	-7.4
9d	-10.6	-7.2	-7.2	-10.7	-7.1	-7.4
9e	-10.6	-7.2	-7.2	-10.5	-6.9	-7.2
9f	-10.6	-7.2	-7.2	-9.4	-5.4	-6.6

	S_0 NICS(0)	S_0 NICS(−1)	S_0 NICS(+1)	T_1 NICS(0)	T_1 NICS(−1)	T_1 NICS(+1)
9g	-10.7	-6.9	-7.2	-1.4	0.8	-0.6
9h	-10.5	-7.2	-6.3	1.1	1.4	2.1
10a	2.3	1.8	1.8	0.0	1.8	1.8
10b	-10.7	-7.1	-7.1	-11.0	-7.5	-7.5
10c	-	-	-	-9.7	-6.1	-6.5
10d	-	-	-	-4.8	-3.1	-2.5
10e	-	-	-	2.3	3.3	1.9
10f	-	-	-	2.3	3.3	1.9
10g	-	-	-	-4.8	-3.1	-2.4
10h	-	-	-	-9.7	-6.1	-6.5
11a	2.0	1.6	1.6	1.8	1.4	1.4
11b	-10.5	-7.1	-6.1	0.4	0.9	1.8
11c	-10.7	-7.0	-6.9	-1.5	-0.5	0.0
11d	-10.7	-7.1	-7.1	-8.8	-6.9	-5.1
11e	-10.7	-7.1	-7.1	-10.6	-7.8	-6.5
11f	-10.7	-7.1	-7.1	-10.7	-7.7	-6.6
11g	-10.7	-7.1	-7.1	-10.5	-7.3	-7.2
11h	-10.7	-7.1	-7.1	-10.8	-6.7	-7.6
11i	-10.7	-8.2	-7.5	-10.5	-6.4	-7.9
12a	1.9	1.6	1.6	1.3	1.1	1.0
12b	-10.6	-7.9	-6.1	-10.1	-5.8	-7.6
12c	-10.2	-7.5	-6.6	-9.3	-5.3	-6.9
12d	-10.8	-6.7	-7.4	-4.3	-2.5	-2.3
12e	-10.3	-6.0	-7.9	2.0	2.9	2.3
12f	-10.3	-6.0	-7.9	1.0	2.8	1.8
12g	-10.8	-6.7	-7.4	-7.1	-4.4	-4.1
12h	-10.2	-7.4	-6.7	-9.9	-5.8	-7.3
12i	-10.6	-7.9	-6.1	-9.5	-5.4	-7.3

The $\sigma_{\text{iso}}(\mathbf{r})$ isosurface plots for the S_0 and T_1 states of furan at the respective optimised geometries are shown in Figure 26. The electronic ground state the five-membered ring is very well-shielded, even slightly more so than the six-membered ring in benzene,[1,48] which is due mostly to placing the same number of π electrons in a ring of a smaller size. This observation is in line with the $\sigma_{\text{iso}}(\mathbf{r})$ contour plots for the electronic ground state of furan constructed from shielding data calculated at the RMP2-GIAO/6-311++G(d,p) level[49] and confirms the presence of strong bonding interactions and aromatic stability. By comparison, in the T_1 state of furan (Figure 26) the five-membered ring is considerably less shielded, which is a clear indication of a marked decrease in aromaticity. However, the absence of a strongly deshielded central region similar to that present in the electronic ground state of cyclobutadiene (see, for example, ref. [2]) makes it difficult to argue in favour of sizeable antiaromatic character.

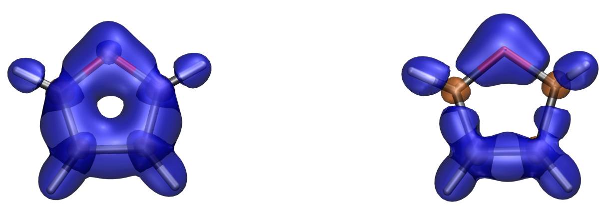

1 S_0 **1** T_1

Figure 26: Shielding around the S_0 and T_1 states of furan **1**. Isosurfaces at $\sigma_{\text{iso}}(\mathbf{r}) = +16$ ppm (shielded regions, blue) and $\sigma_{\text{iso}}(\mathbf{r}) = -16$ ppm (deshielded regions, orange).

The differences between the S_0 and T_1 optimised geometries of furan are considerable: In addition to the reduction in symmetry (see above), the O–C_1, C_1–C_2 and C_2–C_2 bond lengths (C_1 and C_2 stand for the two symmetry-unique carbon atoms in the S_0 state, C_1 is adjacent to O) change from 1.362, 1.355 and 1.433 Å in S_0 to 1.409/1.394 , 1.489/1.432 and 1.348 Å in T_1, respectively. This mimics the observed behaviour in thiophene; the C_1–C_2 'double' bonds in S_0 become 'single' bonds in T_1 and the C_2–C_2 'single' bond in S_0 becomes a 'double' bond in T_1. These differences are reflected in the decreased shielding over the O–C_1 and C_1–C_2 bonds in T_1 in comparison to S_0 (Figure 26); the C_2–C_2 bond is more shielded than the C_1–C_2 bonds in T_1 but it is less shielded than in S_0. The last observation suggests that the levels of shielding over corresponding bonds in electronic states that exhibit different levels of antiaromaticity may not reflect correctly the respective differences in bond strength and length—the reason for this is that the presence of a central deshielded region in an antiaromatic ring can cause exaggerated deshielding of the bonds in that ring.

The carbon atoms in the S_0 and T_1 electronic states of furan and all other furan-based compounds studied in this chapter are surrounded by small ovoid deshielded regions inside which $\sigma_{iso}(\mathbf{r})$ becomes negative. As explained in Chapter 3, this suggests that the hybridisation states of these atoms are close to sp^2 so referring to the Kohn-Sham orbitals in the non-planar oxygen-based compounds examined in this chapter as (almost) σ and π orbitals can be viewed as a reasonable approximation.

5.4 Furofurans

According to the NICS values that we obtained, all furan rings in the electronic ground states of the four furofurans studied in this chapter (**2**–**5** in Figure 25) are aromatic, with NICS(0) values between −14.4 and −7.3 ppm, and NICS(1) values between −10.8 and −5.8 ppm (Table 9). These results show that the positions of the oxygen atoms within the two condensed furan rings can influence significantly the respective NICS values and levels of aromaticity—for example, the NICS(0) values for the two furan rings in the asymmetric furo[3,4-*b*]furan **4** show a considerable difference, −7.3 and −14.4 ppm for rings **4a** and **4b**, respectively. The different levels of aromaticity of these rings are well-illustrated by the $\sigma_{iso}(\mathbf{r})$ isosurface plot in Figure 27: While the carbon-carbon and carbon-oxygen bonds in both rings are well-shielded, the shielding 'hole' in the centre of ring **4a** (on the left) is much larger than that in the centre of ring **4b** (on the right). This behaviour is identical to the thienothiophenes. The most shielded furan rings within the furofurans **2**–**5** are rings **4b** and **5a**, in which the oxygen atoms are positioned similarly; the higher levels of shielding are in correspondence with the respective NICS values. This shielding behaviour can be attributed to the shorter carbon–oxygen bond lengths in rings **4b** and **5a** in comparison to the respective bond lengths in rings **2a**, **3a** and **4a** (for both of **4b** and **5a**, it is possible to draw resonance structures in which the oxygen atom is engaged in two 'double' bonds; one of these structures for **5a** is shown in Figure 25). The shorter carbon–oxygen bond lengths allow the two electrons contributed by each oxygen atom to engage more fully in the π systems of rings **4b** and **5a**. As a consequence, the local aromaticities of rings **4b** and **5a** estimated using magnetic shielding criteria are out of line with the ordering of the energies of the S_0 optimised geometries of the four furofurans. According to our results, the lowest-energy thienothiophene is **3**, closely followed by **2**; the energy gaps between **2** and **4**, and between **4** and **5** are larger. The energy ordering of **2**, **3** and **4** is supported by the NICS values in Table 9, if we compare the NICS values for rings **2a** and **3a** to the average NICS values for rings **4a** and **4b** (the lower shielding over ring **4a** compensates for the higher shielding over ring **4b**). However, the furan rings **5a** in the least stable furofuran, furo[3,4-*c*]furan **5**, turn out to be more shielded and to have more negative NICS values than rings **2a** and **3a**.

Overall, the S_0 shielding isosurfaces for the other two furofurans (**2** and **3**, Figure 27) are very similar to the outcomes that would be expected from fusing together the S_0 isosurfaces for two furan rings over the shared carbon–carbon bond. In general, the geometries of the individual furan rings in the S_0 optimised geometries of **2**–**5** retain some features of the S_0 geometry of furan such as the positions of the carbon–carbon 'single' and 'double' bonds. Similar observations can be made for the S_0 optimised geometries of the remaining compounds with fused furan rings studied in this chapter, **6**–**12**.

The differences between the aromatic properties of the T_1 states of the four furofurans are more pronounced than the S_0 states, as illustrated by the respective shielding isosurfaces (Figure 27), but significantly less variation than observed in T_1 thienothiophenes. This predominantly due to thieno[2,3-*b*]thiophene and furo[2,3-*b*]furan. Thieno[2,3-*b*]thiophene undergoes the only well-defined Baird-style aromaticity reversal from a distinctly aromatic S_0 state to a distinctly antiaromatic T_1 state. The T_1 state has C_2 symmetry, causing both rings to be identical, with antiaromaticity associated with the presence of a large strongly deshielded central region outlined by the $\sigma_{\text{iso}}(\mathbf{r}) = -16$ ppm isosurface, the shape of which resembles a combination of two dumbbells, one inside each ring, interconnected over the fused carbon-carbon bond.

However, in furo[2,3-*b*]furan, both the geometry and $\sigma_{\text{iso}}(\mathbf{r})$ resembles a fusion of S_0 (ring **2a**) and T_1 (**2b**) furan. The single-point NICS values do not reveal the same detail as the shielding plot, with a NICS(0) for **2a** and **2b** of −5.1 and 2.0 ppm not mimicking −11.9 and 3.1 ppm from S_0 and T_1 furan, respectively. Ring **2b** is similar, but **2a** is considerably less aromatic. The electron sharing is disrupted around the carbon atom in the O–C–O bond. Nevertheless, the asymmetry of the T_1 removes the serve antiaromaticity in thieno[2,3-*b*]thiophene, which as highlighted in ref. 67, is because the excitation is similar to a vertical excitation, similar to naphthalene and anthracene.[57]

In general, the behaviour of shielding in both the S_0 and T_1 states of **3**–**5** are strongly resembles their thienothiophene counterparts, meaning all furofurans in both optimised states have geometries and respective shielding pictures have much common with the respective states of furan. The furan rings in the T_1 states of **2**–**5** (Figure 27) can be separated into two groups according to the behaviour of $\sigma_{\text{iso}}(\mathbf{r})$ in and around these rings. These groups of less and more shielded rings include rings **2b**, **3a**, **4b**, and rings **2a**, **4a** and **5a**, respectively.

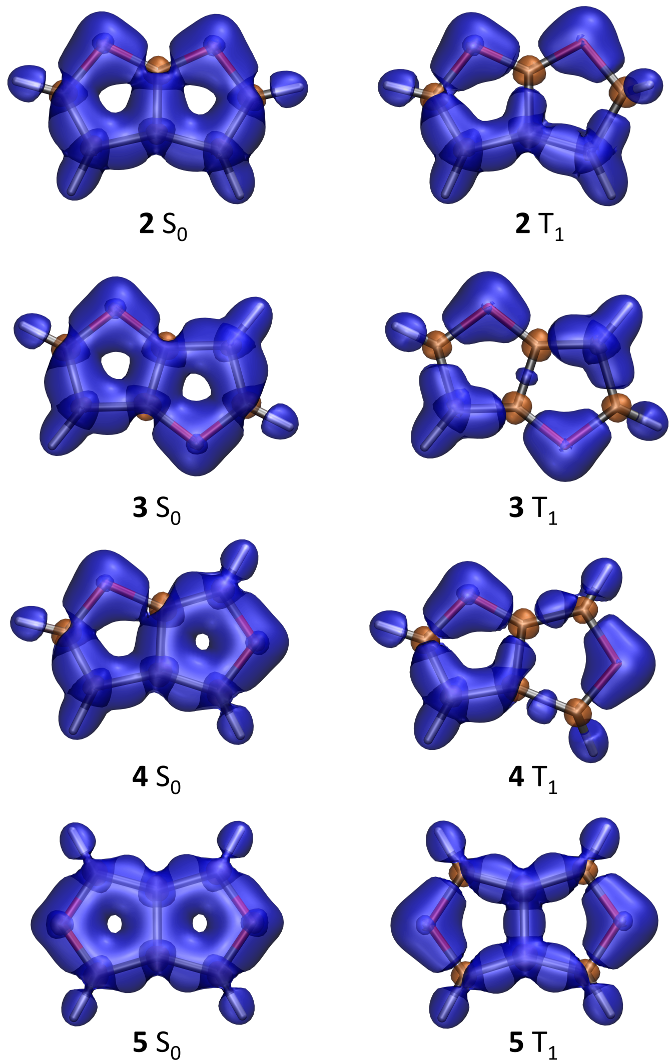

Figure 27: Shielding around the S_0 and T_1 states of furo[2,3-*b*]furan **2**, furo[3,2-*b*]furan **3**, furo[3,4-*b*]furan **4** and furo[3,4-*c*]furan **5**. Isosurface details as for Figure 5.

The T_1 NICS(0) and NICS(1) values for ring **3a** are 1.3 and 1.5 ppm, respectively, and the corresponding values for ring **4b** are 4.8 and 4.6 ppm, respectively (see Table 9). While these NICS values are positive, they are not sufficiently high to imply other than borderline levels of antiaromaticity. The T_1 NICS(0) and NICS(1) values for rings **4a** and **5a** are negative, -5.2 and -4.5 ppm, respectively, for ring **4a**, and -2.8 and -1.4 ppm, respectively, for ring **5a**. Both sets of values indicate that these two rings are mostly nonaromatic. The partial reduction in shielding of the fusion bonds in the T_1 states of furo[3,2-*b*]furan

3, furo[3,4-*b*]furan **4** and furo[3,4-*c*]furan **5** (Figure 27) suggests a close to evenly balanced competition between aromatic and antiaromatic behaviours. Overall, according to the NICS values and the variations in the off-nucleus shielding, the T_1 states of all four furofurans should be considered as nonaromatic.

The $\sigma_{iso}(\mathbf{r})$ isosurfaces and NICS values obtained for compounds **2**–**5** demonstrates that the way in which two furan rings are fused together has an impact on aromaticity and bonding in the S_0 and T_1 states of the resulting furofurans, but there is less variety than thienothiophenes.

The position of 'single' and 'double' bonds in S_0 **2** and **3** are identical to two fused S_0 furan **1** rings. Upon excitation, **2a** retains the S_0 geometry and **2b** switches to a T_1 geometry.**3a** both have bond lengths similar to T_1 furan. **4** has bond lengths as close as can be expected two fused furans in this orientation, but with the C–C fusion bond closer to an optimal length for ring **4b** than **4a**. Upon excitation, **4b** resembles T_1 furan, whilst **4a** resembles S_0 furan, but C–C bond lengths also approach equalisation. **5a** bonds change little under excitation, with only the C–O bonds undergoing a significant lengthening. Neither ring displays T_1 geometry, making the excitation similar to vertical one.

5.5 Difurofurans

The S_0 shielding isosurfaces for difuro[2,3-*b*:3′,2′-*d*]furan **6** and difuro[3,2-*b*;2′,3′-*d*]furan **7** (Figure 28) outer rings appear similar to follow the trend observed in the corresponding shielding isosurfaces for their precursors, furo[2,3-*b*]furan **2** and furo[3,2-*b*]furan **3** (Figure 27) and look very similar to the outcomes that would be expected from fusing together the S_0 isosurfaces for three furan rings over the shared carbon-carbon bonds. Although all three furan rings in both molecules are shielded, the central ring shielding is less, particularly in **6**. NICS(0) and NICS(1) are -9.5 and -6.8 ppm for the central ring, whilst -11.4 and -8.0 ppm for the outer rings, respectively. In **7**, the differences are smaller, with NICS(0) and NICS(1) of -7.5 and -10.9 ppm for **7b**, and -11.8 and -8.0 ppm for **7a**, respectively.

Shielding after an excitation to the T_1 state for both difurofurans is also similar to the shielding of the furofuran precursors. **6** maintains a well-shielded ring, whilst the other two switch to nonaromatic. This is supported by NICS(0) values for rings **6a**, **6b** and **6c** of -6.8, 1.4 and 2.0 ppm, respectively. NICS(+1) and NICS(−1) are similar (see Table 9), with the largest difference for NICS(−1) for **6a**, which assumes the value -5.0 ppm.

Shielding in **7a** and **7b** have similar NICS(0) and NICS(1) values of -1.4 and -0.7, and, 0.3 and 1.1 ppm, respectively. The shielding plots, whilst strongly supporting a nonaromatic classification, offer greater detail, in particular that strong shielding around external carbons in **7a** opposite the oxygen atom, in contrast to the weak shielding in the central ring.

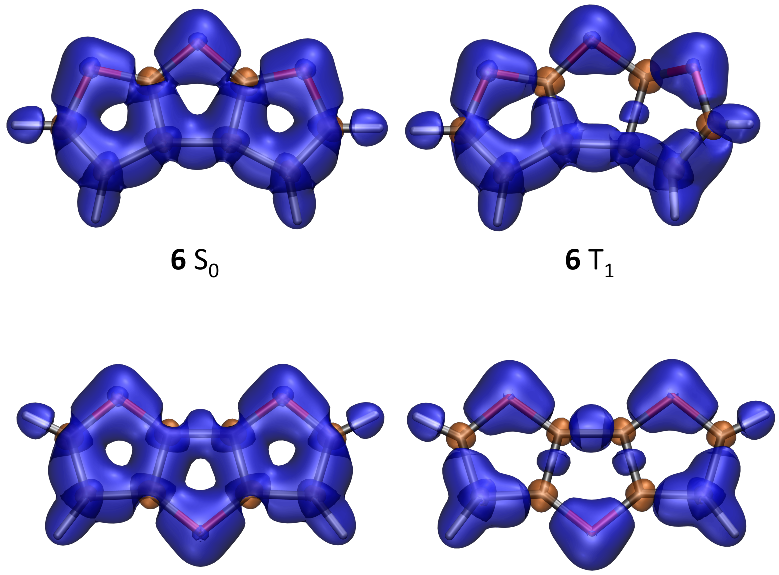

6 S_0 **6** T_1

7 S_0 **7** T_1

Figure 28: Shielding around the S_0 and T_1 states of difuro[2,3-*b*:3′,2′-*d*]furan **6** and difuro[3,2-*b*;2′,3′-*d*]furan **7**. Isosurface details as for Figure 5.

5.6 Oxiflowers

At the ground state, all the Oxiflowers investigated have the similar levels or aromaticity. Lower magnitude NICS values and $\sigma_{\text{iso}}(\mathbf{r})$ around all furan rings (shown in Figure 29) is considerably less aromatic than furan itself. NICS(0) and NICS($\pm$1) for each individual furan ring is around 7 and 10.5 ppm, respectively.

One of the largest variations is for bowl-shaped $(C_2O)_{12}$, which NICS($-$1) values (outside of the bowl) are -6.2 ppm and NICS($+$1) values (inside the bowl) are -8.1 ppm, which is inline with previous work on bowl-shaped molecules. C-C hub bonds in $(C_2O)_{12}$ become shorter than in furan, at 1.424 Å compared to 1.433 Å. This is a consequence of the rings being pulled closer to fit with this molecular geometry. The C–C spoke bonds and C–O rim (outer ring) bonds elongate, with the former becoming 1.369 and 1.378 from 1.355 Å in furan, and the latter 1.364 and 1.381 to furan's 1.362 Å. Given that the bonds are now more equalised, one might assume that a geometrical indices would suggest a more aromatic system. However, the HOMA index of furan is 0.200, which in itself is not very aromatic and the furan rings in $(C_2O)_{12}$ only change slightly to 0.179. This indicates the lack of sensitivity in the HOMA metric and its inability to detect the shifts in aromaticity that magnetic shielding can, hence HOMA shall not be used for investigating these condensed furans further.

$(C_2O)_{13}$ hub bonds do not vary greatly, being either 1.432 or 1.433 Å, and despite an almost identical match to furan, aromaticity is still far weaker. This may be because the spoke bonds are 1.376 Å except those connecting rings **9g**/**9h** and **9h**/**9h** which are 1.372 and 1.368 Å, respectively) are considerably longer than those in furan. The C–O rim bonds are also elongated, varying between 1.365 and 1.367 Å. $(C_2O)_{14}$ has hub, spoke and rim bonds of 1.452, 1.380 and 1.355 Å, respectively, continuing the trend of shorter hub and rim bonds, but longer spoke bonds. NICS(0) and NICS(±) values are 10.6 and 7.1 ppm, respectively.

$(C_2O)_{15}$ hub, spoke and rim bonds are 1.472, 1.383/1.384, 1.346/1.347 Å, respectively except the **11i** rings whose values are 1.476, 1.380 (**11h**/**11i**)/1.374(**11i**/**11i**) and 1.348(**11h**/**11i**)/1.343(**11i**/**11i**) Å. The NICS(0) values all sit in the range 10.5–10.7 ppm and the shielding plots are not able to detect the difference in bonding for rings **11h** or **11i**. NICS(±1) does offer some insight, yielding values of 7.1 ppm for rings **11c**-**11g**, but 7.0/6.9 ppm for **11h**, 7.1/6.1 ppm for **11i** and 8.2/7.5 ppm **11b**. $(C_2O)_{16}$ rim bonds are between 1.377 to 1.359 Å with the longest and shortest bonds in this range being in the same rings, namely those in **12b**, **12e**, **12f** and **12i**. The hub bonds vary between 1.472 and 1.476 Å, whilst spoke bonds vary from 1.378 to 1.391 Å, with the shortest connecting rings **12b** and **12i**, and the longest **12e** and **12f**.

Upon excitation, the switch to nonaromatic rings is localised to specific rings, whilst others remain aromatic. This is once again, unsurprising given the results of thiophene molecules, but there is a difference in the most antiaromatic of the Oxiflowers. The only molecule to have gain truly antiaromatic rings (with a negative deshielded region in the centre of the **8d** rings) is $(C_2O)_{12}$, yet when examining the sulflowers we found the 'bowl-shaped' molecule $(C_2S)_6$ actually became more aromatic upon excitation. Rings **8b**, **8c** and **8d** having NICS(0) values of −5.1, +1.7 and +12.6 ppm, respectively, support the variety of different shielding in Figure 29.

Rings **9b**–**9f** are relatively unaffected by the excitation to T_1 with well shielded bonds. NICS(0) and NICS(±1) values for **9b**–**9e** are greater than −10.5 and −6.9 ppm, respectively, and **9f** only experiences a slight aromatic reduction with a less than 1.5 ppm decrease in the magnitude of NICS indicators. **9g** becomes nonaromatic, NICS(0) of −1.4 ppm, which is adjacent to the weakly antiaromatic **9h** rings, with NICS(0), NICS(+1) and NICS(−1) are 6.2, 4.6 and 4.0 ppm, respectively. The shielding in Figure 29 shows weakened shielding around carbon atoms on the rim, revealing the deshielded ovoids around **9h** carbons.

The bonds lengths of aromatic rings **9b**–**9f** do not vary greatly from the aromatic rings in other molecules. With the except of **9h**, whose hub bonds are 1.401 Å, the shortest hub bond is 1.425 Å for ring **9b**, and these bond lengths get progressively longer moving clockwise and anticlockwise around the oxiflower until ring **9g** (1.436 Å). Despite the shorter hub bonds, **9h** has longer C–O rim bonds,1.472 Å compared to only 1.369 Å in **9b**. For **9h**, these bond length elongations and contractions explain the severely decreased shielding. Additionally, decreased shielding in both **9g** and **9h** is due to the spoke bond connecting them, at 1.455 Å it is a single bond that prevents any conjugation.

Rings **10b** and **10c** are aromatic whilst **10d** and **10e** are nonaromatic. The $\sigma_{\text{iso}}(\mathbf{r})$ surface displays this clearly, with **10d** and **10e** being analogous to **9g** and **9h**, respectively. The long spoke bonds of 1.472 Å between connected **10e** rings is largest disruptor of conjugation in the rings, evidenced by the minimal shieldings along these bonds. **10b** has a NICS(0) of -11.0 ppm whilst **10c** is slightly less at -9.7 ppm, but both are aromatic. **10d** and **10e** are nonaromatic with NICS(0) values of -4.8 and 2.3 ppm, respectively.

Rings **11e**–**11i** have NICS(0) shieldings with magnitudes greater than -10 ppm and **11d** possesses a value of -8.8 ppm, all of which can be considered aromatic, supported with the $\sigma_{\text{iso}}(\mathbf{r})$ plot. The C–C hub bonds experience only slight reductions in length to around 1.46 Å, apart from **11c** with a significantly contracted 1.362 Å hub bond length. **11b** and **11c** have NICS(0) values of 1.5 and 0.4 ppm, respectively and the most noticeable geometrical change from the ground state is 1.502 Å C–C spoke bonds between the two rings. These elongations of spoke bonds are easily identifiable in the shielding isosurface.

The $\sigma_{\text{iso}}(\mathbf{r})$ plot reveals **12b**, **12c**, **12h** and **12i** remain aromatic, with the magnitude of NICS(0) greater than 9 ppm in each ring. There is, however, a significant increase in non-planarity of the molecule overall; the difference between the largest and smallest z coordinate grows from 2.64 to 3.81 Å upon excitation from S_0 to T_1. This is reflected in the difference in NICS($+1$) and NICS(-1) values for these rings, which differ but up to 2 ppm, depending on the side selected for investigation. The smallest of these is **12c**, with a NICS(-1) of just -5.3 ppm. The NICS indicators of **12g** give contrasting ideas of the aromaticity, with NICS(0) suggesting aromaticity at -7.0 ppm, whilst NICS(±1) are -4.1 and -4.4 ppm. The shielding isosurface at ±16 ppm show no continuous shielding around the ring, with a gap around the rim carbons, clearly indicating the ring is nonaromatic. The shielding isosurface around **12d** is almost identical to the shielding around **12g**, yet the NICS(0) and NICS(±1) values are much smaller, -4.3, -2.5 and -2.7 ppm, respectively. This illustrates the importance of shielding plots when dealing with non-planar molecules. The final two rings **12e** and **12f** have weaker bonding with NICS(0) values of 2.0 and 1.0 ppm, respectively and sharing the same elongated spoke bond (1.480 Å) which is less well-shielded than other bonds.

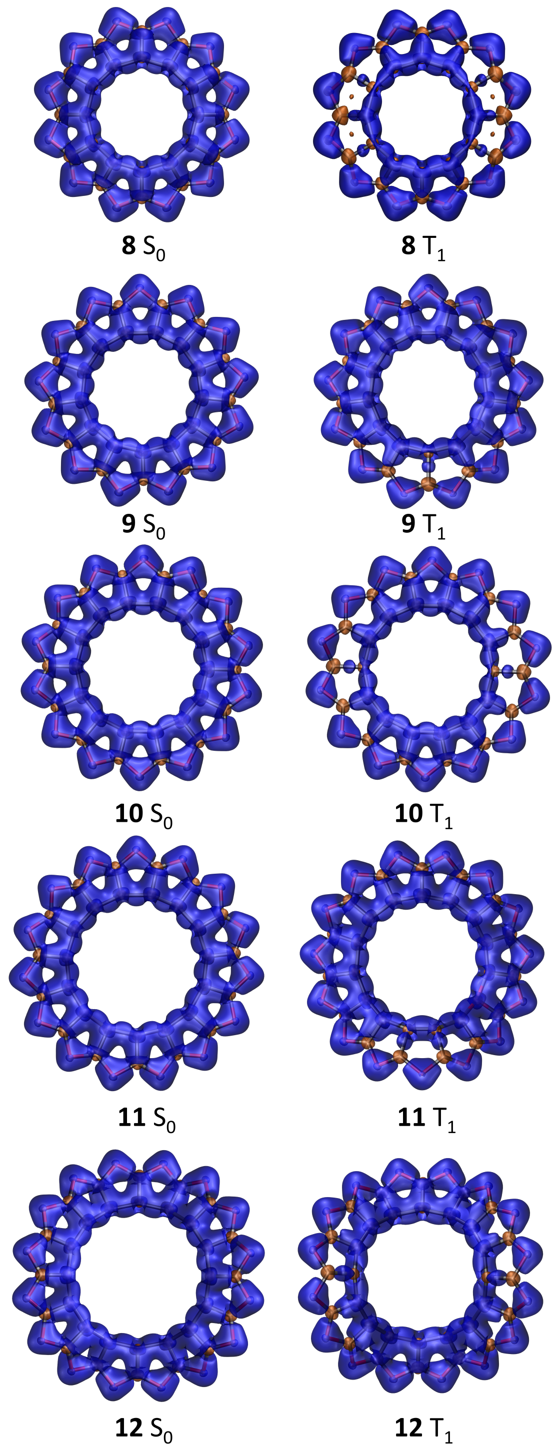

Figure 29: Shielding around the S_0 and T_1 states of oxiflowers with twelve **8**, thirteen **9**, fourteen **10**, fifteen **11** and sixteen **12** furan rings. Isosurface details as for Figure 5.

To analyse ring strain in the S_0 and T_1 electronic states of $(C_2O)_{12}$–$(C_2O)_{16}$ (**8**–**12**) we followed a procedure analogous to that adopted for the S_0 electronic states of sulflowers in refs. [85], [86] and [67], and calculated the respective energies per C_2O unit,

$$E_{C_2O \text{ in } (C_2O)_n} = \frac{E_{(C_2O)_n}}{n} \tag{31}$$

The $E_{C_2O \text{ in } (C_2O)_n}$ values obtained at the RB3LYP-D3(BJ)/def2-TZVP and UB3LYP-D3(BJ)/def2-TZVP levels, for the S_0 and T_1 electronic states, respectively, are shown in Figure 30 relative to the S_0 $E_{C_2O \text{ in } (C_2O)_{14}}$ and T_1 $E_{C_2O \text{ in } (C_2O)_{15}}$ values which were of the lowest energy for each states.

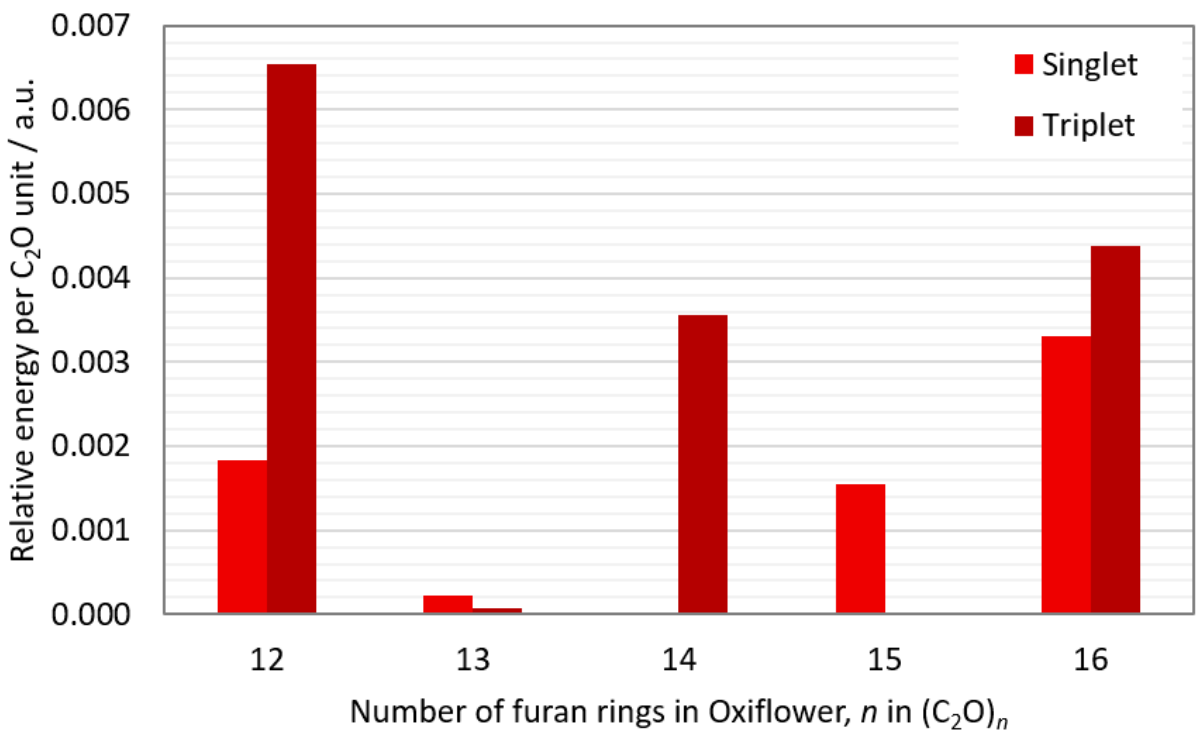

Figure 30: Relative energies per C_2O unit of the S_0 and T_1 electronic states of the oxiflowers $(C_2O)_{12}$–$(C_2S)_{16}$ (**8**–**12**). For further details, see text.

The changes in ring strain in the S_0 electronic states of $(C_2O)_{12}$–$(C_2O)_{16}$ are very similar to sulflowers,[67,85,86] with the $E_{C_2O \text{ in } (C_2O)_n}$ following a 'parabola-like' shape around the most stable structure. The 13 oxiflower is similar has a very similar monomer energy to the 14 oxiflower, differing by just 0.14 kcal mol^{-1}, which is even closer than sulflowers with 8 and 9 condensed thiophene rings which differed by only 0.2 kcal mol $^{-1}$.[67] The ordering of these oxiflower monomer energies may vary depending upon the model chemistry, as studies have shown similar, but different ordering of sulflower monomer energies.[67,85,86] One of the most notable changes between the sulflowers and oxiflowers is the range on monomer energies, being far less in oxiflowers (2.1 kcal mol^{-1}) than sulflowers (15.2 kcal mol^{-1}). This can be attributed to three factors: firstly, sulfur is a heavier element, secondly there are more monomer chains in oxiflowers, and finally the specific oligomers selected for study. The first two of these suggest that when a new monomer is added or removed, the total energy will be increased more and there will be a greater change in ring strain in sulflowers than oxiflowers. The final factor can be realised as if the smallest sulflower is excluded from energy range, the S_0 only span 5.9 kcal mol^{-1}. If we had continued our study into smaller oxiflowers, such as the 'bowl'-shaped $(C_2O)_{11}$, the range would likely be significantly higher.

Ring strain in the T_1 electronic states of $(C_2O)_{12}$–$(C_2O)_{16}$ follows a very different trend to the respective S_0 electronic states. $(C_2O)_{15}$ has the smallest T_1 monomer energy, followed closely by $(C_2O)_{13}$ (separated by only 0.045 kcal mol^{-1}). In contrast, the $(C_2O)_{14}$ T_1 monomer energy is considerably higher (2.2 kcal mol^{-1}). Hence, the relatively large monomer singlet–triplet energy difference in $(C_2O)_{14}$ (6.8 kcal mol^{-1}) may account for the stability of the structure.

Compared to their thiophene counterparts, **2** and **6** have singlet–triplet energy gaps much more comparable to the other two and three condensed ring systems, respectively. This is consistent with the shielding in the triplet states, where **2** and **6** significant geometry differences between the S_0 and T_1 states, which were not so apparent in their thiophene analogues. The conjugation pathways are significantly reduced by these geometry changes, reduces the antiaromatic character and hence reduces the singlet–triplet energy via a reduction in the triplet energy.

5.7 HOMO–LUMO and Singlet–Triplet Gaps

Figure 31 compares the HOMO–LUMO and singlet–triplet gaps for compounds **1**–**12**. HOMO-LUMO gaps in these molecules are governed by aromatic stabilisation which increases the HOMO–LUMO gap, and conjugation pathway length which acts in the opposite direction. The two types of energy gap follow identical trends for **1**–**7** even though singlet–triplet gaps in Figure 31 correspond to the differences between the energies of separately optimised T_1 and S_0 geometries rather than to vertical excitation energies, (which HOMO–LUMO gaps can be approximated to, by ignoring the electron-hole interaction energy).

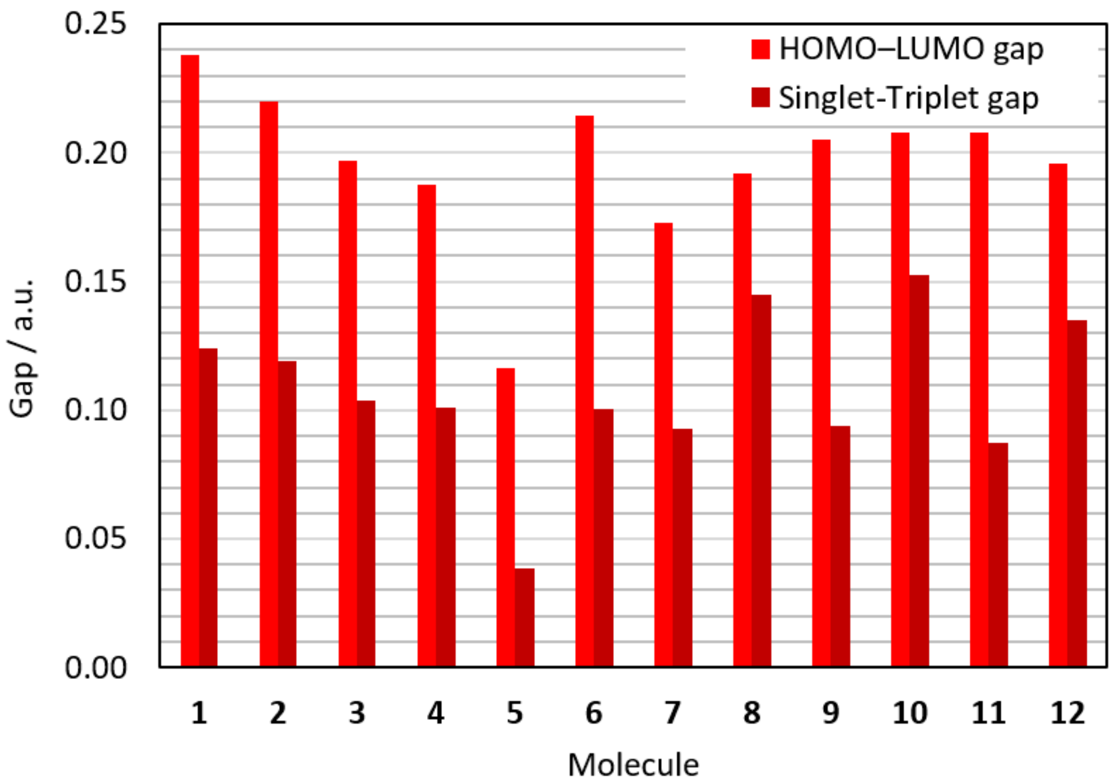

Figure 31: HOMO–LUMO and singlet–triplet gaps for molecules **1**–**12**.

However, **5** which according to our magnetic shielding results involves the most S_0 aromatic furan rings amongst **2**–**5** and has conjugation pathways shorter than those in **3** shows the smallest HOMO-LUMO gap amongst the four furofurans. This is an indication that there are additional important factors influencing the sizes of the HOMO-LUMO gaps which are not that easy to account for qualitatively, for example, the positions of oxygen atoms. Moving sequentially across furofurans **2**–**5**, both the HOMO–LUMO and singlet–triplet gap decrease. Particularly, the energy gaps in **5** are considerably small. This is identical to thieno-3,4-*c*-thiophene in the thienothiophene series. Despite this apparent instability, shielding isosurfaces demonstrate this is the most aromatic furofuran in the ground state. NICS(0) and NICS(1) of **5** are the second and first most negative, respectively, of all the respective indicators in **2**–**12**.

Variation is small in the HOMO–LUMO gaps of oxiflowers **8**–**12**, but the largest occurs in **11**, closely followed by **10**. However, the singlet–triplet gaps of both **9** and **11** are small compared to the other oxiflowers. This mimics the relative energy per C_2O unit in triplet oxiflowers, and is further supported by the magnetic shielding data, with fewer nonaromatic rings in the T_1 states **9** and **11** than **8**, **10** and **12**. The greater proportion of aromatic rings in these T_1 oxiflowers is reducing the triplet energy.

5.8 Conclusions

The analysis of the variations of the off-nucleus isotropic magnetic shielding, $\sigma_{\text{iso}}(\mathbf{r})$, around furan, furofurans, difurofurans and oxiflowers in their electronic ground and lowest triplet states, suggests that not all features of aromaticity and bonding in these molecules are consistent with predictions based on the popular Hückel's and Baird's rules. The oxygen containing heterocycle series, furan, the furofurans and difurofurans, studied in this chapter are systems with $4n + 2$ π electron counts of 6, 10 and 14, equal to both the hydrocarbon series of benzene, naphthalene, and anthracene, respectively and the sulfur containing series of thiophene, thienothiophenes and dithienothiophenes. As expected, the results of the current off-nucleus isotropic magnetic shielding calculations confirm that the electronic ground states of these molecules are aromatic.

Comparisons of condensing furans into oxiflowers can be made to hydrogens coronene and corannulene, circulenes with 6 and 5 benzene rings, respectively and to sulflowers, made of condensed thiophene rings. Similar to these other systems, fusing n furan rings in oxiflowers yields an aromatic molecule in its electronic ground state, despite having a $4n$ total π electron count. In contrast to the hydrocarbon and sulfur containing molecules, the oxygen containing molecules often have far weaker shielding in $\sigma_{\text{iso}}(\mathbf{r})$ plots than the single ring building block (in this case furan), although this is far less detectable in the NICS indices.

Contrasting results between series of one, two and three condensed furan rings such furan **1**, furo[2,3-*b*]furan **2** and difuro[2,3-*b*:3',2'-*d*]furan **6**, or furan, furo[3,2-*b*]furan **3** and difuro[3,2-*b*;2',3'-*d*]furan **7**, with the hydrocarbons series of benzene, naphthalene, and anthracene have been revealed. The latter group shows a trend which is commonly referred to as the 'anthracene problem',[57,109,111,112] according to which both rings in naphthalene, as well as the central ring in anthracene are more aromatic than benzene, and the central ring in anthracene is more aromatic than the outer rings. Both furan series show only show a slight decrease in NICS values as furan rings are added, although these changes are often small enough to be considered insignificant. However, the $\sigma_{\text{iso}}(\mathbf{r})$ surfaces display a reduction in aromatic character in fused ring furan systems. The outer rings of **6** and **7** are more aromatic than the central rings. This trend with furan is identical to those seen in their thiophene analogues. Aromaticity shifts between the S_0 and T_1 states of condensed furans studied in this chapter are less noticeable than those for similar condensed thiophenes and far less pronounced than those observed in comparable hydrocarbon series.[48,53,57]

Only a single molecule out the twelve investigated, dodecafuro[12]circulene **8**, experiences a well-defined Baird-style aromaticity reversal upon excitation between the S_0 and T_1 state as evidenced by a deshielded region at the rings centre **8d**. Molecule **8** switching to antiaromatic is one of the largest departures from condensed thiophene studies, where rings of the most 'bowl-shaped' heterocirculene, hexathio[6]circulene, actually increased its aromaticity when excited from the ground to lowest triplet state.

Furans geometry shifts drastically between the S_0 and T_1 states, even more so than thiophene, with its symmetry reduced from C_{2v} to C_1 and an accompanying loss of planarity. As with thiophene, the carbon-carbon 'double' and 'single' bonds in the S_0 state (see structure 1 in Figure 25) turn into 'single' and 'double' bonds, respectively, in the T_1 state. Hence, via inspection of bond lengths it is possible to predict which rings are antiaromatic in the T_1 state of fused furan rings.

Contrary to T_1 state of anthracene,[57] dithieno[2,3-*b*:3',2'-*d*]thiophene and dithieno[3,2-*b*;2',3'-*d*]thiophene;[67] the central ring of furo[2,3-*b*:3',2'-*d*]furan **6b** is not the least shielded in the molecule. The significant deviation from planarity leads to an aromatic ring **6a** and nonaromatic ring **6c**. Likewise, both types of ring in difuro[3,2-*b*;2',3'-*d*]furan **7** have similar levels of nonaromaticity according to NICS values, although the outer rings appear slightly more shielded in the $\sigma_{\mathrm{iso}}(\mathbf{r})$ plot. These difurofuran results go against the previous predictions[147,147] and results[148] of longer chains of fused aromatic rings in which T_1 antiaromatic reversals are likely to be concentrated in central ring (or the pair of central rings) and rings sufficiently far away from the central ring(s) could even remain aromatic.

6 Norcorrole

6.1 Introduction

Computational chemistry stimulates the imagination of new compounds, with interesting shapes and properties. One such compound is norcorrole (H_2Nc), first envisaged theoretically using DFT calculations,[149] then subsequently the smallest cyclic tetrapyrrole porphyrin analogue synthesised, and the only to date.[150,151] Ni^{II} norcorrole (NiNc) is another popular variant, with Ni in the centre and two fewer hydrogen atoms (Figure 32). An antiaromatic conjugated pathway in Figure 32(b) was often depicted in the literature,[150–153] but it provided no explanation for the stability of this type of molecule. Prior research by Karadakov, (see ref. 2) demonstrated that magnetic shielding in both S_0 norcorrole variants reveals a strongly deshielded antiaromatic 'internal cross', the boundary of which follows the conjugation pathway suggested in Figure 32(a). However, the stability of NiNc and H_2Nc is generated an aromatic 'halo' formed by increased shielding along a peripheral conjugation pathway, which can be considered to involve either 18 atoms and 18 π electrons (Figure 32(c)), or 14 atoms and 14 π electrons, bypassing the C_α– C_α bonds through homoconjugation (Figure 32(d)).[2] This chapter expands on Karadakov's earlier work,[2] by extending the study to include excitation to the lowest triplet state. For context and to facilitate comparisons, conclusions of the ground state properties of ref. 2 will be reiterated throughout this chapter in the context of the excited state.

Baird's rule typically reverses aromatic character upon excitation to a T_1 or S_1 state, but for molecules like NiNc and H_2Nc whose bonding is comprised of competing aromatic and antiaromatic macrocyclic cycles in the S_0 state it is not straightforward to suggest how bonding changes in its lowest excited states. The theoretical estimates of the vertical excitation energy for the transition from S_0 to S_1 of NiNc of 0.8 eV[84] suggests that the S_1 state might be benefitting from aromatic stabilisation. In this chapter, the ground state bonding of both norcorrole variants is summarised from previous work[2] and then compared to the lowest triplet and singlet excited states. The majority of calculations follow the same methods as the rest of this thesis. However, there are a couple of points of note. Firstly, TDA-B3LYP has been used rather than time-dependent B3LYP (TD-B3LYP) following recommendations in literature.[154,155] Secondly, HOMA calculations were performed with Multiwfn[156] using the default parameterisation, rather than HOMER, a reparameterisation of HOMA for triplet excited states,[27] to enable better comparison of the aromaticity at the optimised S_0, T_1 and S_1 geometries of NiNc and H_2Nc.

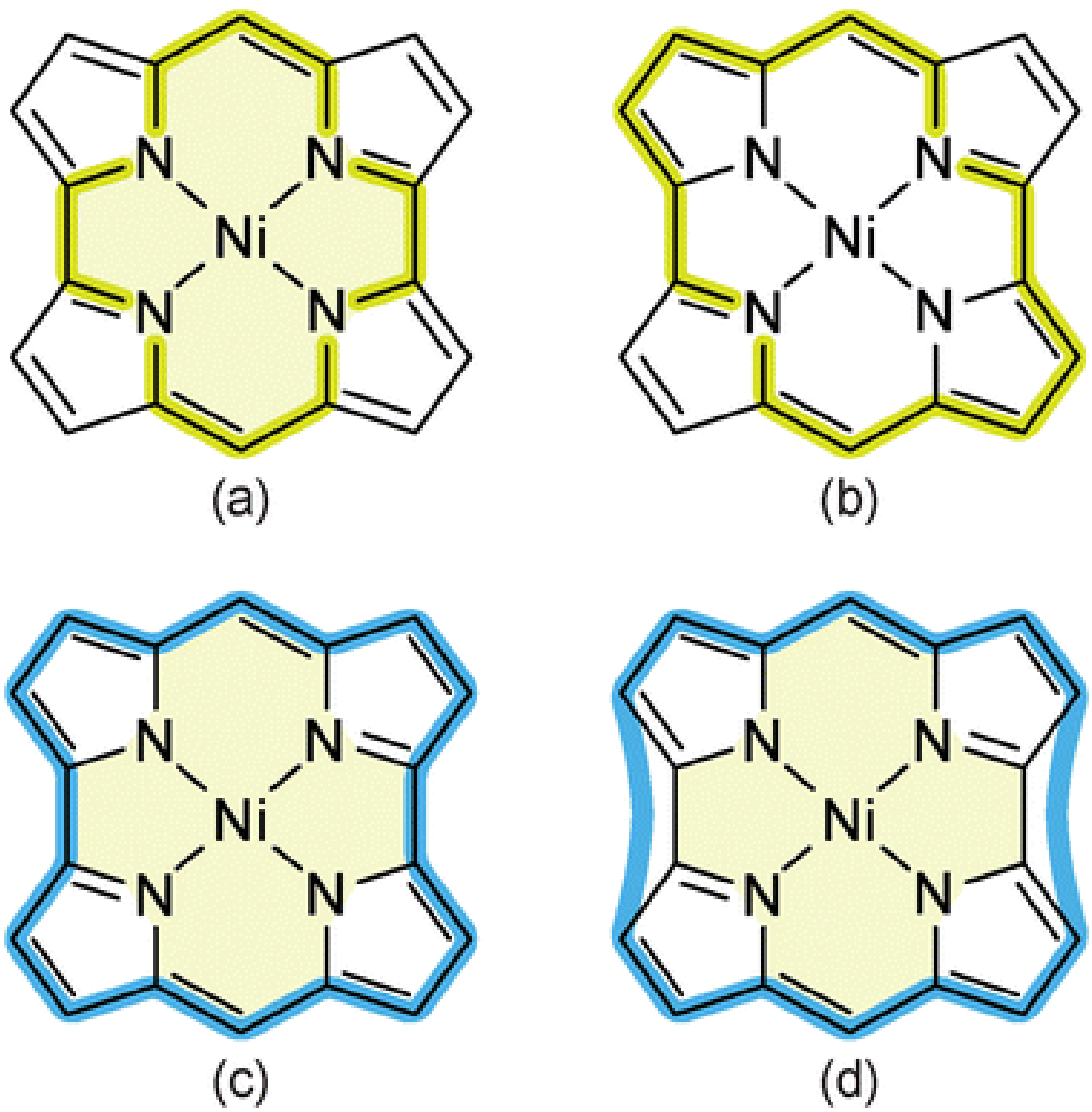

Figure 32: Conjugation pathways in NiNc. (a) Antiaromatic 'internal cross' (ic), with 14 atoms and 16 π electrons; (b) antiaromatic, with 16 atoms and 16 π electrons; (c) and (d) aromatic peripheral (p), with 18 atoms and 18 π electrons, or with 14 atoms and 14 π electrons. The deshielded area within the 'internal cross' is shaded in (a), (c) and (d). Adapted with permission from P. B. Karadakov, Org. Lett., 2020, 22, 8676–8680. Copyright 2020 American Chemical Society.

6.2 Structure

The gas-phase ground state potential energy surface of NiNc at the B3LYP-D3(BJ)/def2-TZVP level[150] showed that requiring the molecule to be planar yielded a transition state of D_{2h} symmetry, with an imaginary vibrational frequency of 36.7i cm^{-1} perpendicular to the molecular plane. NiNc has two equivalent bowl-shaped local minima of C_{2v} symmetry, resulting from this vibration. Similarly, the potential energy surface of H_2Nc contains a planar 2nd-order saddle point of C_{2h} symmetry, which serves as a transition state connecting two pairs of local minima, two with C_i symmetry and two with a bowl-shaped C_2 symmetry. This second-order saddle-point has two imaginary frequencies, ν_1 = 127.6i cm^{-1} and ν_2 = 59.5i cm^{-1}. The first of which corresponds to the normal modes associated with the transition between the C_i local minima, and the second the bowl-to-bowl inversion of the C_2 local minima.[2] T_1 and S_1 potential energy surfaces of NiNc are similar to the surface in the S_0 state, with each having two equivalent bowl-shaped local minima of C_{2v} symmetry, are joined by a planar transition state of D_{2h} symmetry. The energy to overcome the inversion barrier in ground state NiNc was very small (0.7 kcal mol−1), but this doubles to 1.4 kcal mol^{-1} in T_1 (at both the UB3LYP-D3(BJ) and TDA-B3LYP-D3(BJ) levels) and increases further to 1.7 kcal mol^{-1} in S_1, at the TDA-B3LYP-D3(BJ) level. The gas-phase T_1 and S_1 potential energy surfaces of H_2Nc no longer contain a planar C_{2h} SOS, and are instead replaced with a C_i symmetrical transition state between just two equivalent bowl-shaped local minima of C_2 symmetry. The H_2Nc bowl-to-bowl S_0 inversion barrier of 2.0 kcal mol^{-1} increases to 3.2 and 3.1 kcal mol^{-1} in T_1, at the UB3LYP-D3(BJ) and TDA-B3LYP-D3(BJ) levels, respectively, and to 4.6 kcal mol^{-1} in S_1, at the TDA-B3LYP-D3(BJ) level. The increase in the bowl-to-bowl inversion barriers can be contextualised by considering the bowl depths. Bowl depths are calculated by measuring the difference between the largest and the smallest atomic z coordinates (the z axes coincide with the C_2 symmetry axes at the C_{2v} NiNc and C_2 H_2Nc local minimum geometries). Table 10 displays the bowl depths for NiNc and H_2Nc in each of the electronic states. It is clear that the bowl-to-bowl inversion barrier is directly linked to the bowl depth.

Table 10: Bowl depths at the S_0 B3LYP-D3(BJ), T_1 U = UB3LYP-D3(BJ), T_1 TDA = TDA-B3LYP-D3(BJ) and S_1 TDA = TDA-B3LYP-D3(BJ) local minimum geometries of NiNc and H_2Nc (in Å).

Molecule	S_0	T_1 U	T_1 TDA	S_1 TDA
NiNc	0.912	1.082	1.082	1.149
H_2Nc	1.496	1.576	1.580	1.710

This raises a question as to why the bowl depths increase, which can in turn be addressed by examining the molecular geometries. Key bond lengths from the S_0 B3LYP-D3(BJ), T_1 UB3LYP-D3(BJ) and TDA-B3LYP-D3(BJ), and S_1 TDA-B3LYP-D3(BJ) local minimum geometries of NiNc (C_{2v}) and H_2Nc (C_2) are shown in Figure 33.

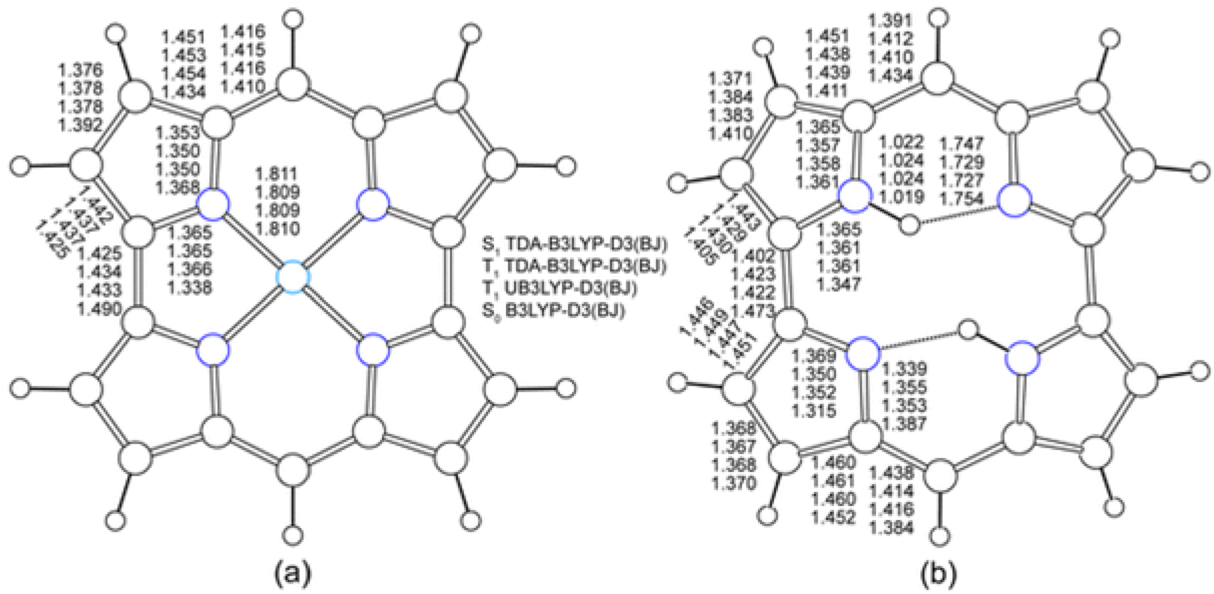

Figure 33: Selected symmetry unique bond lengths (in Å) from the S_0, T_1 and S_1 local minimum geometries of (a) NiNc and (b) H_2Nc, arranged in columns of four values each including, from bottom to top, S_0 B3LYP-D3(BJ), T_1 UB3LYP-D3(BJ), T_1 TDA-B3LYP-D3(BJ) and S_1 TDA-B3LYP-D3(BJ) results. (a) and (b) show the S_0 B3LYP-D3(BJ) NiNc (C_{2v}) and H_2Nc (C_2) local minimum geometries, looking at the top of each bowl.

C–C and C–N bonds are affected by excitation to varying extents, the most drastic in both molecules is the shortening of the C_α–C_α bonds that directly connect the pyrrole rings in both $S_0 \rightarrow T_1$ and $S_0 \rightarrow S_1$ excitations. The C_α–C_α bonds contract when transitioning to either state, but experience a larger contraction in the S_1 state than in T_1, of about 0.07 Å. In contrast, the Ni–C distances and the C–H bond lengths within the 'internal cross' of H_2Nc remain much the same in all three states. Hence, the increases in bowl depth (Table 10) can therefore be viewed as attempts of the respective structures to alleviate the additional strain caused by the shortening of the C_α–C_α bonds. The larger bowl depths at the S_0, T_1 and S_1 local minimum geometries of H_2Nc can be explained by the steric repulsion between the hydrogens within the 'internal cross'.

Whilst comparing individual bond lengths can be informative, with the variety of bonds in systems such NiNc and H_2Nc, it is often useful to summarize the information into a single index to compare the overall effect of the geometry change and the bonding. Hence Table 11 displays the HOMA values for the conjugation pathways following the 'internal cross', Figure 32(a), and the periphery, Figure 32(c). HOMA does not detect the ground-state antiaromatic characters of the "inner crosses" but there are sizeable increases in the HOMA values for the two 'internal crosses' when exciting from S_0 to T_1 or S_1. This is a consequence of significant decreases in bond length alternation which usually suggest increases in aromaticity. The HOMA values for the peripheries of NiNc and H_2Nc also increase, although less dramatically, when transitioning from S_0 to T_1 or S_1.

HOMA values for the planar D_{2h} transition state geometries of NiNc; the planar C_{2h} second-order saddle-point in S_0 H_2Nc, and the C_i transition state geometries of H_2Nc in its S_1 and T_1 states are smaller than those at the local minima. Hence, energy decreases on passing from these transition state and second-order saddle-point geometries to the respective local minima can be attributed to an additional aromatic stabilisation despite the parallel loss of planarity in the S_0, T_1 and S_1 states of NiNc, and S_0 state of H_2Nc.

Table 11: HOMA values for the 'internal cross' (ic) and peripheral (p) conjugation pathways at the S_0 B3LYP-D3(BJ), T_1 U = UB3LYP-D3(BJ), T_1 TDA = TDA-B3LYP-D3(BJ) and S_1 TDA = TDA-B3LYP-D3(BJ) optimised geometries of NiNc and H_2Nc

Pathway	Geometry	S_0	T_1 U	T_1 TDA	S_1 TDA
NiNc (ic)	C_{2v}	0.550	0.834	0.833	0.858
	D_{2h} (TS)	0.467	0.774	0.773	0.799
NiNc (p)	C_{2v}	0.475	0.504	0.505	0.513
	D_{2h} (TS)	0.382	0.409	0.408	0.408
H_2Nc (ic)	C_2	0.602	0.883	0.883	0.860
	C_i (T_1/S_1 TS)	0.580	0.840	0.838	0.821
	C_{2h} (S_0 SOS)	0.524			
H_2Nc (p)	C_2	0.455	0.544	0.539	0.459
	C_i (T_1/S_1 TS)	0.451	0.473	0.470	0.419
	C_{2h} (S_0 SOS)	0.372			

The very close HOMA values obtained for the T_1 states of NiNc and H_2Nc at the UB3LYP-D3(BJ) and TDA-B3LYP-D3(BJ) optimised geometries highlight the similarity between these geometries; the HOMA values for the T_1 and S_1 states of the two molecules at the respective TDA-B3LYP-D3(BJ) optimised geometries also suggest reasonable levels of similarity between the geometries of these states. HOMA is formulated to only explicitly depend on bond lengths so does not account for the increase in bowl depth upon excitation of NiNc and H_2Nc from S_0 to T_1 or S_1. The decrease in the degree of bond length alternation upon excitation favours aromaticity but the increase in bowl depth makes the structures less planar, which reduces conjugation along the bonds.

The symmetries of the TDA-B3LYP descriptions of the $T_1//S_0$, $S_1//S_0$, $T_1//T_1$ and $S_1//S_1$ states of NiNc and H_2Nc (the S_0 B3LYP or T_1 or S_1 TDA-B3LYP local minimum geometry, of C_{2v} and C_2 symmetry for NiNc and H_2Nc, respectively, is shown after the double slash) are identical, A_2 for NiNc and A for H_2Nc. The symmetries of the triplet UB3LYP Kohn–Sham determinants for the $T_1//S_0$ and $T_1//T_1$ states of the two molecules (with $T_1//T_1$ utilizing the respective triplet UB3LYP local minimum geometries) coincide with those of the corresponding TDA-B3LYP descriptions. All of the TDA-B3LYP excited state descriptions are dominated by the HOMO to LUMO orbital excitations. The very low S_0 to T_1 and S_0 to S_1 TDA-B3LYP and UB3LYP vertical (VEE) and adiabatic (AEE) excitation energies of NiNc and H_2Nc (Table 12) suggest that the S_0 states of the two molecules experience antiaromatic destabilisation, whereas the corresponding T_1 and S_1 states experience aromatic stabilisation. For reference, the B3LYP HOMO–LUMO gaps at the C_{2v} NiNc and C_2 H_2Nc S_0 local minimum geometries are 1.480 and 1.654 eV, respectively. The S_0 to T_1 and S_0 to S_1 VEEs and AEEs obtained using other TDA-DFT and UDFT methods may show some differences, but the qualitative features of the TDA-B3LYP and UB3LYP descriptions of the T_1 and S_1 states of NiNc and H_2Nc are unlikely to change. For example, the VEEs calculated using TDA-PBE0[157] are in close agreement with their TDA-B3LYP counterparts, and the respective VEEs calculated using TDA-ωB97X[158] are higher by between 0.156–0.449 eV but would still be considered fairly low; the TDA-PBE0 and TDA-ωB97X excited state descriptions continue to be dominated by the HOMO to LUMO orbital excitations.

Table 12: Vertical and adiabatic S_0 to T_1 and S_0 to S_1 excitation energies of NiNc and H_2Nc (in eV, U = UB3LYP, TDA = TDA-B3LYP)

State	VEE U	VEE TDA	AEE U	AEE TDA
NiNc T_1 ($1\,^3A_2$)	0.501	0.458	0.295	0.259
NiNc S_1 ($1\,^1A_2$)		0.841		0.608
H_2Nc T_1 ($1\,^3A$)	0.671	0.607	0.380	0.338
H_2Nc S_1 ($2\,^1A$)		0.999		0.635

6.3 Magnetic Shielding

The NICS values and carbon, nitrogen and proton isotropic shieldings for the S_0 and T_1 electronic states of NiNc and H_2Nc, computed using B3LYP-GIAO and UB3LYP-GIAO, respectively, are shown in Figure 34. The software used to calculate S_0 and T_1 magnetic shieldings (GAUSSIAN) is unable to do so for higher excited states, so other software such as Dalton,[159] is required to calculate the S_1 state, as has been done previously.[160] However, sensible NiNc and H_2Nc shieldings for the S_1 state could not be readily obtained. CASSCF(2,2)-GIAO ('2 electrons in 2 orbitals' complete active space self-consistent field with GIAOs) calculations were trialled with a variety of basis sets on the S_1 state of NiNc, utilizing the Hartree–Fock HOMO and LUMO as the initial guesses for the active space orbitals. Very low or even negative values for all proton isotropic shieldings suggested these results were unphysical, and not computationally robust. CASSCF(2,2)-GIAO calculations on the S_1 states of other molecules[160] did not have the same unphysical nature, so most likely due to the size of the molecule it would be expected that in order to obtain reasonable estimates of the quantities included in Figure 34 for the S_1 states of the two molecules might require full π space CASSCF(24,24)-GIAO calculations. Consulting previous literature on CASSCF-GIAO calculations[48] suggests such calculations are beyond the capabilities of the existing codes and our computational facilities.

T_1//T_1 data was obtained at the respective T_1 UB3LYP-D3(BJ) local minimum geometries.[161] The NICS(+1) positions are above the bowl (closer to the viewer), and the NICS(−1) positions are inside the bowl. Other details as for Figure 33. The NICS(0) and NICS(±1) values at positions in, above and below the 'internal crosses' in NiNc and H_2Nc clearly show that the 'internal crosses' in both molecules switch from antiaromatic to aromatic upon vertical excitation from S_0 to T_1. The NICS(0) of NiNc 'internal cross' switches approximately 50 ppm to −16 ppm and H_2Nc undergoes a similar switch from *circa*. 35 ppm to *circa*. −14 ppm. The geometry relaxation only slightly improves aromaticity in NiNc, with all NICS indices only increasing in magnitude by a maximum of 2 ppm. The geometry relaxation of H_2Nc does not influence the aromaticity greatly, with values changing no more than 2 ppm, but in some cases the magnitude decreases. This is of limited significance for the assessment of aromaticity and is more attributable to the increased bowl depth as was found for the heterocirculenes. In parallel, the NICS(0) and NICS(±1) values for the pyrrole rings indicate that these rings switch from moderately antiaromatic to moderately aromatic or aromatic (the pyrrole rings with hydrogen atoms in H_2Nc). Interestingly, geometry relaxation leads to relatively minor changes in the NICS values (compare the T_1//S_0 and T_1//T_1 results); while the general trend is towards more negative NICS values and higher levels of aromaticity, a small number of the $T_1//T_1$ NICS values are slightly less negative than their $T_1//S_0$ counterparts which can be attributed to the choices of the positions at which the NICS(0) and NICS(±1) values are evaluated. The S_0 NICS(0) and NICS(1) values for the planar Ni^{II} porphyrin complex (NiP), calculated at a level of theory identical to that used in this chapter, B3LYP-GIAO/6-311++G(d,p)/B3LYP-D3(BJ)/def2-TZVP, and at positions in and above the 'internal cross' defined analogously to those for NiNc and H_2Nc, are −21.7 and −18.0 ppm, respectively,[84] which suggests that the 'internal crosses' in the T_1 states of NiNc and H_2Nc are not that far off in their levels of aromaticity.

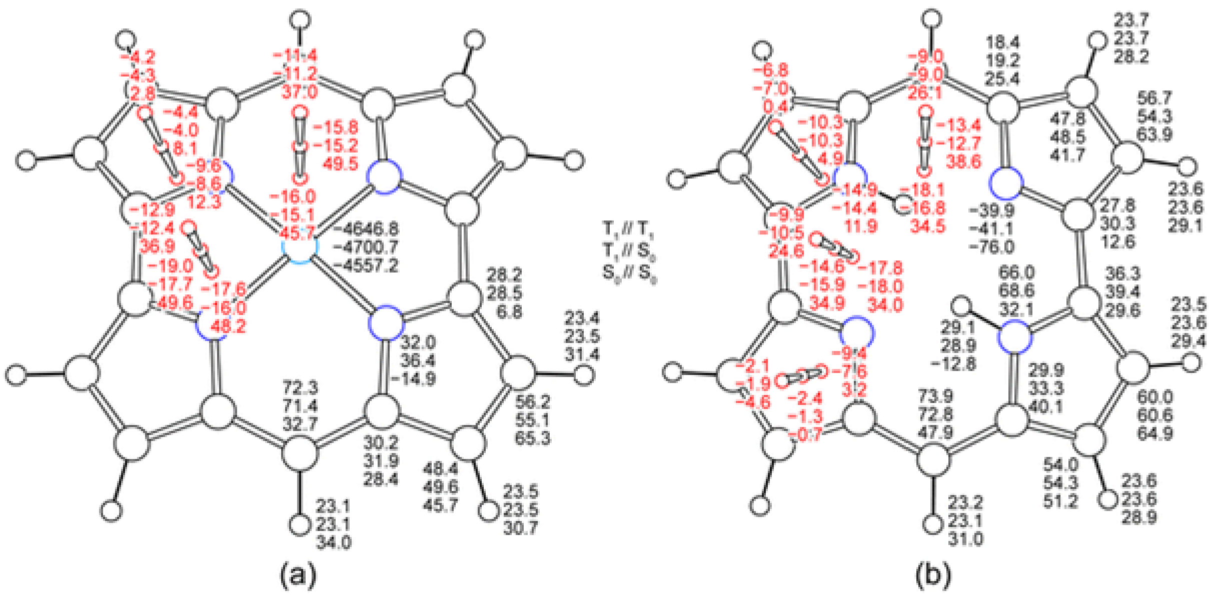

Figure 34: Symmetry unique NICS values (in red) and carbon, nitrogen and hydrogen isotropic shieldings (in black) for the S_0 and T_1 electronic states of NiNc (a) and H_2Nc (b), arranged in columns of three numbers each including, from bottom to top, $S_0//S_0$, $T_1//S_0$ and $T_1//T_1$ results (in ppm).

Apart from the changes in the NICS values, the aromaticity reversals between the S_0 and T_1 states of NiNc and H_2Nc are also well-illustrated by the parallel changes in the hydrogen isotropic shieldings. The 'external' hydrogens, connected to α and meso carbon atoms, are much more shielded in the S_0 states of the two molecules than they are in the respective T_1 states. On the other hand, the 'internal' hydrogens in H_2Nc which are strongly deshielded in S_0, become strongly shielded in T_1.

In the ground state, Ni amplifies the antiaromaticity of the central region in NiNc by introducing additional conjugation pathways. To check if Ni contributes electrons to the π system, natural population analyses (NPA) were carried out at the level of theory used in the geometry optimisations. The NPA charge on Ni was obtained as 0.470e, and the NPA charge distributions in NiNc and H_2Nc turned out to be reasonably similar (Figure 35). Thus, the Ni contribution to the NiNc π system is minor and does not need to be taken into account in π electron counts. Comparing the NICS values to the NPA charges for the S_0, T_1 and S_1 states of NiNc and H_2Nc (Figure 35), highlights that the change of the electronic state has far more readily detected through magnetic shieldings (Figure 34) than electronic density distributions. This is most clearly illustrated by the shieldings on H atoms inside the 'internal cross' of H_2Nc changing drastically, from ca. -13 to 29 ppm upon the exciting S_0 to T_1 (Figure 34) whilst the corresponding NPA charges increase by just 0.002e (Figure 35).

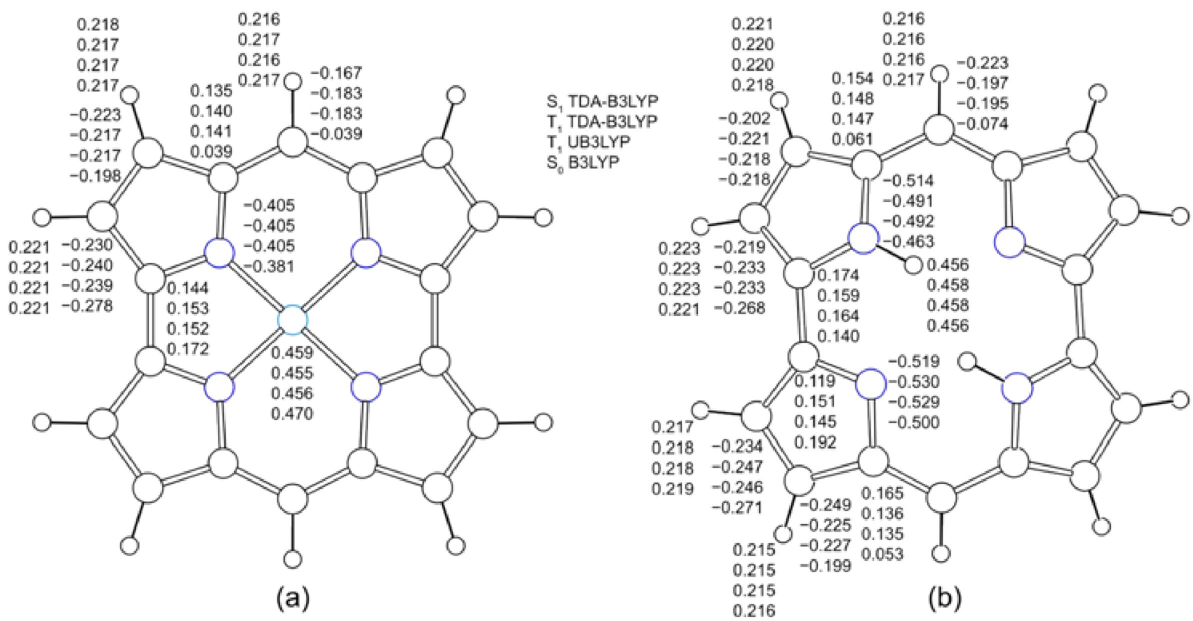

Figure 35: Symmetry unique natural population analysis (NPA) charges (in units of e) at S_0, T_1 and S_1 local minimum geometries of (a) NiNc and (b) H_2Nc, arranged in columns of four numbers each including, from bottom to top, S_0 B3LYP, T_1 UB3LYP, T_1 TDA-B3LYP and S_1 TDA-B3LYP results. (a) and (b) show the S_0 B3LYP-D3(BJ) NiNc (C_{2v}) and H_2Nc (C_2) local minimum geometries, looking at the top of each bowl.

It is also worth noting that the NPA charges (Figure 35) highlight the close similarity between the UB3LYP and TDA-B3LYP descriptions of the T_1 states of NiNc and H_2Nc, as well as the less close but still well-defined similarity between the UB3LYP and TDA-B3LYP descriptions of the T_1 states and the TDA-B3LYP descriptions of the S_1 states of the two molecules. This is in agreement with the bond lengths (Figure 33) and shielding data (Figure 34).

The $\sigma_{iso}(\mathbf{r})$ isosurfaces for S_0 and T_1 electronic states of NiNc and H_2Nc are shown in Figure 36. The $\sigma_{iso}(\mathbf{r})$ isosurfaces for the S_0 electronic states of the two molecules were drawn using GAUSSIAN cube files taken from previous work.[2] In order to be consistent with the majority of this thesis, the plots have been adapted to $\sigma_{iso}(\mathbf{r})$ = ± 16 ppm, instead of their originally reported $\sigma_{iso}(\mathbf{r})$ = ± 12 ppm.

The S_0 $\sigma_{iso}(\mathbf{r})$ isosurfaces illustrate the antiaromatic deshielded 'internal crosses' and the aromatic shielded 'halos' in NiNc and H_2Nc, calculated previously.[2] At the time of these calculations took place, it was generally accepted the antiaromaticity of NiNc follows from the pathway in Figure 32(b) . However, in light of magnetic shielding results, previous investigations could be contextualized. Large magnetically induced current densities over the pathway in Figure 32(a) were observed in previous studies of NiNc[162] and Ni^{II} cyanonorcorrole.[163] Whilst researchers used ACID plots to suggest that for substituted NiNc the main ring current 'flows along the inner periphery involving four nitrogen atoms and 14 bonds'[164,165] their ACID plots depict significant paratropic currents all over the NiNc unit. Other current-based aromatic criterion such as GIMIC[166] have been used to study octaethylporphyrin Zn^{II} dication,[167] which shares the same 16 π electron count as NiNc but two fewer carbon atoms. Once again the antiaromatic pathway is comparable to NiNc (Figure 32(a)). A 2D NICS contour plot for a NiNc derivative[168] equivalent to a plane in Figure 32(b) showed deshielding beneath the area of this pathway.

Inspecting the region between Ni and N atoms (Figure 36(a)) suggests Ni–N bonding, as although they only expand a small volume at the 16 ppm threshold, shielded ovoids are still observable at 72 ppm. The central deshielded regions in both norcorrole variants is similar (although larger) than the archetypal antiaromatic molecules C_4H_4. Two 'weaker' links across C_α–C_α bonds along the NiNc perimeter are analogous to the 'single' bonds in C_4H_4, although in norcorrole variants these are more shielded. The entire antiaromatic 'core' in NiNc is surrounded by a shielded 18-membered ring with 18 π electrons suggesting prominent bonding interactions. This 18 π electron conjugated ring could be considered as Hückel aromatic, but the absence of magnetic shielding along C_α- C_α bonds suggests the four C_α carbons are bypassed via a through-space conjugation similar to homoconjugation[169–171] between the β carbons. This homoconjugation, reduces the conjugated ring around the perimeter of NiNc to 14 atoms and 14 π electrons (so follows a pathway in Figure 32(d) instead of 32(c)) but retains Hückel aromaticity. The minimal shielding along C_α–C_α bonds suggests these bonds as the weakest and hence the most reactive along the NiNc outer perimeter, which is direct agreement with Shinokubo *et al.* who experimentally confirmed that when heated NiNc is oxidised to Ni^{II} 10-oxacorrole.[172] The deshielded central region in H_2Nc involves a 14-membered circuit with 16 π electrons, but it smaller and resembles a cross shape, which suggests weaker antiaromatic character. However, the aromatic character is also weakened, with less peripheral ring shielding suggesting two interacting dipyrrin fragments with much less if any homoconjugation across the links between these fragments. C_2 symmetry H_2Nc has a larger central antiaromatic region, closer in both size and shape to that in NiNc than the C_i variant. Large deshielding of the two hydrogens in the interior of H_2Nc is a consequence of the positioning of these hydrogens inside the central deshielded region of this molecule (Figure 36). These findings are supported through experimental investigations of H_2Nc.[153] To confirm this point further, these hydrogens have high positive NPA charges 0.456e, consistent with the idea that deshielding reflects instability and a highly perturbed electronic wavefunction in this region.

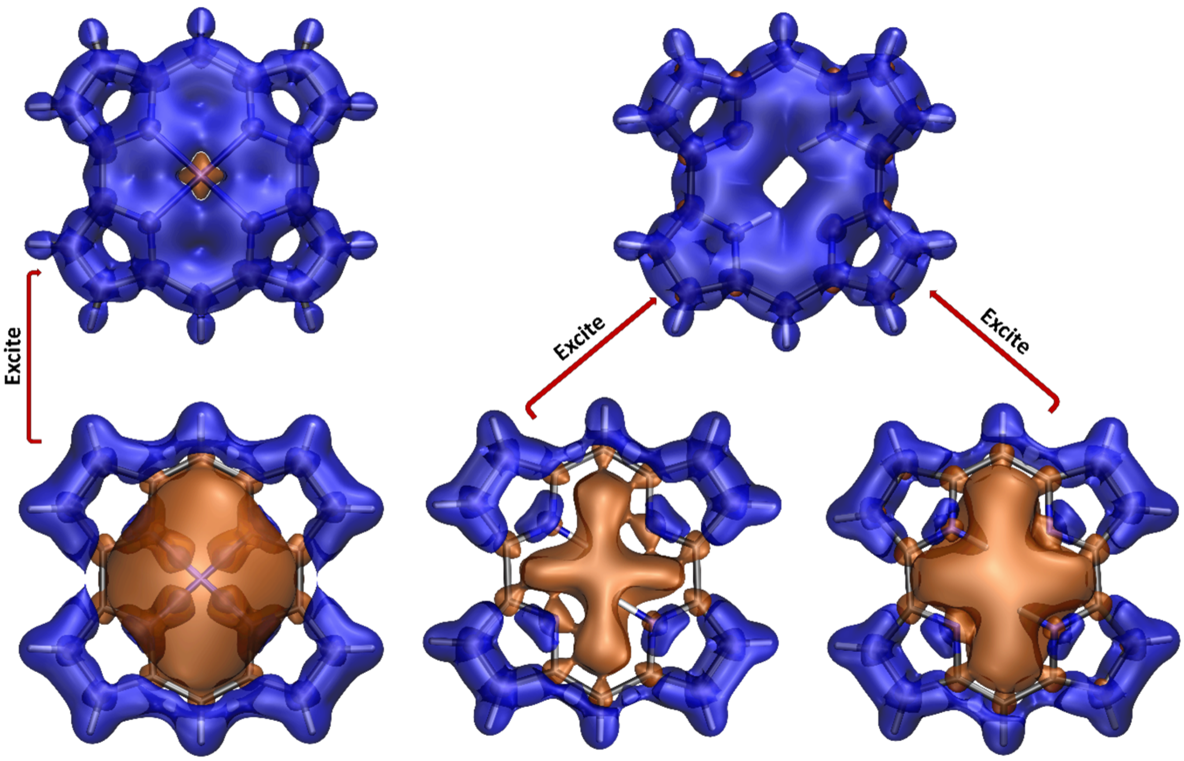

Figure 36: Isotropic magnetic shielding around the S_0 [2] and T_1 electronic states of NiNc and H_2Nc (looking at the top of each bowl). Isosurfaces at $\sigma_{iso}(\mathbf{r})$ = +16 ppm (shielded regions, blue) and $\sigma_{iso}(\mathbf{r})$ = −16 ppm (deshielded regions, orange). S_0//S_0 and T_1//T_1 results as in Figure 34.

The $\sigma_{iso}(\mathbf{r})$ plots concur with the NICS values of both S_0 and T_1 states (Figure 34), as the large deshielded regions in S_0 disappears in T_1, except for a small deshielded region surrounding the Ni atom. Hence, T_1 states of NiNc and H_2Nc become fully aromatic and do not retain any traces of antiaromatic behaviour, nor gain any antiaromaticity around the periphery. There are slight depressions above the bowls across their 'internal crosses', where the shielding is reduced. This takes the form of thin lines in H_2Nc at $\sigma_{iso}(\mathbf{r})$ = 16 ppm, but at 12 ppm, this shielding encompasses the entire 'internal cross'. The depressions in the shielding for NiNc are most pronounced in the centre of four rings connecting connected to Ni. There is an absence of shielding in the centre of the molecule as expected due to the large size of the ring. This absence of shielding is not as symmetrical as in benzene, but this is due to the H atoms within the ring, and due to the ring size, this ring should be classed as definitively aromatic.

Such abundant shielding is absent in the nonaromatic and saturated isosurface of planar H_8NiNc.[84] The NICS(+1) values (above the bowls) positioned in the 'internal cross' fall within these areas of reduced shielding (Figure 34) which explains their lower values. Beneath the bowls, there is better shielding overall and there are no such depressions in the respective parts of the T_1 $\sigma_{iso}(\mathbf{r})$ = 16 ppm isosurfaces for NiNc and H_2Nc, which accounts for the observed NICS(−1) values. The S_0 aromatic shielded 'halos' shift towards the interiors of the molecules in T_1 and more closely follow the individual C–C, C_α–H and C_{meso}–H bonds; the T_1 shielding pictures over these bonds in both molecules closely resemble those in the S_0 state of H_8NiNc.[84] The T_1 states the aromatic shielded 'halos' merge with the shielded 'internal crosses' to produce Baird-aromatic triplet systems with 24 π electrons each.

The presence of such deshielded regions around the carbon and nitrogen atoms in the S_0 and T_1 states of NiNc and H_2Nc suggests that the respective hybridisation states of these atoms are close to sp^2, as in the S_0 state of NiP, despite the non-planar bowl-shaped geometries of the two states, and we can still approximately describe electrons as (mostly) σ or π. The deshielded surroundings of the Ni atom which in the S_0 state of NiNc are submerged within the 'internal cross' deshielded region are in line with the negative isotropic shieldings of this atom in the S_0 and T_1 states (Figure 34) and with the positive NPA charges on these atoms (Figure 35).

6.4 Conclusions

Examining the magnetic shielding of the S_0 and T_1 electronic states of Ni^{II} norcorrole and norcorrole strongly suggest an aromatic reversal upon the excitation. The strongly deshielded antiaromatic 'internal crosses' spanning 16 atoms and 16 π electrons, becomes well-shielded enough to combine with the peripheral aromatic 'halos' (which do not undergo aromaticity reversals) to produce Baird-aromatic triplet systems with 24 π electrons each. The magnetic shielding studies are validated by the changes in the HOMA values between the optimised geometries of the S_0 and T_1 states of both molecules. Given their close alignment, the optimised geometries of the T_1 and S_1 states of NiNc and H_2Nc and between the corresponding HOMA values, it is sensible to suggest that the two molecules undergo similar aromaticity reversals in their S_1 states. Geometries of fully aromatic T_1 and S_1 states of both NiNc and H_2Nc have greater bowl depths than the corresponding S_0 geometries at which both molecules display prominent antiaromatic features, despite being more non-planar. The increases in bowl depths are a consequence of the decreases of the C_α–C_α bond lengths, changes that at the same time make the T_1 and S_1 geometries more aromatic and less planar. The very low vertical and adiabatic excitation energies of NiNc and H_2Nc from the ground to lowest triplet and singlet state suggest antiaromatic destabilisation of the S_0 states and aromatic stabilisation of the T_1 and S_1 states of the two molecules and indicate that either of the lower-lying excited states in each molecule can be readily accessed from S_0. The changes in the bowl depths of NiNc and H_2Nc upon excitation could be exploited in the design of new low-amplitude "flapping" fluorophores, similar to those based on π-expanded cyclooctatetraenes and oxepins.[173–175]

The norcorrole variants are interesting molecules whose magnetic shielding provides a picture of bonding which is supported by other computational methods and experimental data. The isosurface plots demonstrate their value in providing a more complete picture. In the ground state, NICS correctly identifies the antiaromatic features of NiNc and H_2Nc, but fails to identify the global networks of conjugation resulting in the aromatic 'halos' surrounding these molecules. This is significantly different from heterocirculenes, such as sulflowers and oxiflowers, where only the local ring aromatic conjugation pathways are at play.

7

Boron Clusters, B_n^q

7.1 Introduction

With the applications of graphene rapidly increasing,[176–180] two-dimensional materials have excited many chemists, prompting numerous explorations into graphene-like 2D systems. Only a few candidates contain a single element, including phosphorene, silicene, germanene and stanene.[181] Carbon's bonding is particularly interesting because of its ability to form hybridised sp^3, sp^2, and sp bonding; none of these alternative 2-dimensional (2D) materials have this flexibility and their graphene analogues buckle from planarity. The usefulness of graphene has energised chemists to search for other 2D materials with the same chemical properties as graphene.

Enter boron, an extremely fascinating element. As the fifth element, boron is often overshadowed by its neighbour carbon, which forms the basis of organic chemistry. However, boron has a wide range of unexplained chemical behaviours.[182,183] Unlike most atoms, boron can form bonds with nearly all elements, and for around 150 years,[184,185] boron was only found and studied in various compounds. Boron allotropes were only discovered in the latter half of the last century,[186] where the extremely complex structured bulk γ-B_{106} was observed. After over half a century of research, there are multiple bulk boron polymorphs, but of those, only a fraction have known crystal structures,[187] and happen to all be interlinked polyhedra.[188] The boron equivalent of graphene, borophene, has properties including metallicity, transparency, mechanical flexibility, and superconductivity.[189]

Boron is used to create superhard materials and in nuclear reactors as control rods to absorb excess neutrons emitted by fission.[190] Additionally, boron is crucial in biochemistry by keeping cell wall structure, maintaining membrane function, and supporting metabolic activities.[191] Recently, through liquid phase exfoliation (LPE) methods, chemists have synthesised boron quantum dots (BQDs). Experimental results prove that BQDs possess broadband saturable absorption (SA) and good third-order nonlinear optical susceptibility, which are comparable to graphene. The significant ultrafast nonlinear optical properties can be used in optical devices.[192] Boron and carbon have similar electronic properties. Recently, quasi-planar structures have been investigated for their applicability to optoelectronic devices.[193] Whilst the photon-capturing ability of these clusters makes them poor candidates for a photon absorption layer, their use for charge transportation appears more promising. Specifically, B_{12} could be used for electron transporting, whilst larger clusters of B_{36} and B_{50} are candidates for hole transporting layers.[193] Boron clusters are also promising candidates for antiviral drug design.[194,195]

But what makes boron so versatile and capable of forming a variety of bonds in a vast array of structures? Well, boron has only three valence electrons, of which, the single 2p electron would favour metallicity, but its orbital radius is too similar to that of the 2s orbital,[196] which causes some electronic configurations to sufficiently localise causing non-metallic behaviour. This facilitates boron to form both strongly covalent two-centre bonds and metallic-like multi-centre bonds, creating highly diverse bonding in bulk phases. These multi-centre bonds are responsible for the dominant manifestation of bulk boron, B_{12} icosahedron (not to be confused with the quasi-planar B_{12} covered in this chapter), along with other boron allotropes that can accommodate the electronic deficiency of boron.[188] The multi-centre bonds commonly consist of three atomic centres sharing two electrons, so are referred to as 3c–2e bonds. In some geometries, four centres share two electrons, forming 4c–2e bonds form instead, although these are less common.

Electrons in multi-centre 3c–2e and 4c–2e bonds are delocalised, but unlike traditional local delocalisations which involve the overlapping of π orbitals above and below the molecular plane, these multi-centre bonds form within the plane due to the direct overlap of σ orbitals. Hence, molecules with this bonding are referred to as having σ-aromaticity and for the rest of this chapter, what is usually described as 'aromatic' will be called 'π-aromatic'. As one can imagine, bonding in boron clusters is often more complex than carbon's, with both σ- and π-delocalisation highly responsible for the molecular properties. The term 'double aromaticity' is used to refer to a molecule with both types. However, σ-aromaticity as a concept is not unique to inorganic chemistry, for over half a century it has been used to describe organic bonding in the cyclopropenyl ion.[197–202] Previous attempts to model σ-aromaticity have been successful. Using the electron localisation function (ELF) it was shown σ and π electrons delocalise according to different criteria.[203] The $2p_\sigma$ radial overlapping of peripheral boron atoms decreases with ring size, meaning ring size is responsible for σ-electron delocalisation. This means that very small rings can possess considerable delocalisation and hence aromaticity, despite the unavailability of π-electrons. This is evidenced by the boron triangles comprising most boron clusters (not only those which are planar) with two electrons delocalised over three centres. Hückel's 4n + 2 rule can be used as a predictor for π-delocalisation, and similarly to carbon, the cluster size is not quite as important,[203] although the geometry may determine the electrons available to the π-system.

There are many stable isomers of boron clusters, just between B_6 and its singly charged ions, there are 19 stable structures.[204] This becomes more complicated with increasing cluster size; $B_{20}{}^-$ has had over 200 local minima identified.[205] This is partly due to boron's diverse bonding nature facilitating many interesting geometries. These include boron toroids, B_{2n} for which those with even n experience double aromaticity, whilst those of odd n experience mixed aromaticity.[206] One of boron's most stable forms is constituted of three-dimensional B_{12} icosahedral cages.[207–209] However, small boron clusters can be planar,[210–212] with the formation of gas phase planar boron clusters up to B_{15} observed experimentally.[213–215]

Kiran *et al.* determined the critical transition from quasi-planar to 3-dimensional (3D) materials occurs around B_{20}, using both experimental (photoelectron spectroscopy) and theoretical (density functional techniques and Monte Carlo sampling) methods.[205] Crucially, the charge of the species is also important, with neutral B_{20} significantly preferring a toroidal structure, whilst many 2D structures of $B_{20}{}^-$ have a similar energy to a toroidal geometry.[205] B_{20} is the smallest stable 3D boron cluster (5.2 Å diameter) and may be considered the thinnest boron nanotube. Some quasi-planar allotropes with sizes greater than the $n = 20$ guideline exist[216] and some smaller 3D cages such as the B_{12} icosahedron are highly favourable, but all planar B_n^+ ions with $n \leq 20$ have been experimentally observed through collision-induced dissociation methods such as a typical mass distribution by laser ablation.[217,218]

This approximate critical number of atoms appears to be a trend for second-period atoms, with carbon favouring 3D cages instead of 2D rings at C_{20} (the smallest fullerene).[219] It has been proposed that because internal boron atoms create more delocalised σ-bonds than peripheral boron atoms, the closing of planar structures into tubes or spheres occurs to increase the ratio of internal to peripheral boron atoms in larger clusters.[220] In nanotubes, peripheral boron atoms are only present at the ends and fullerenes remove peripheral atoms altogether. The number of bonds between atomic pairs in the cluster, and hence binding energy per atom, increases with the greater average coordination number of the constituting atoms. This means that in the diatomic model, in general, planar clusters should be less stable than their nanotubular or fullerene-like counterparts with the same number of atoms.[220] The contrasting behaviour is expected in the case of small clusters because of significant polarity correction to the binding energy per atom. Within the framework of the diatomic model, further refinement of the binding energy can be achieved by rejecting the equality between all the bond lengths. Different boron–boron atomic separations cause an otherwise perfectly planar cluster to become quasi-planar.[220]

Not all boron clusters are aromatic, in either the σ- or the π- sense, even if they are comprised of boron triangles. Additionally, the charges of boron clusters are essential for ensuring that all boron atoms satisfy the octet rule. King[216] published a paper using 'electron bookkeeping' to indicate the number of electrons available to the π-system, once the peripheral single B–B bonds, 3c–2e B–B–B bonds, 4c–2e B–B–B–B bonds and any internal B–B single bonds were accounted for. In this chapter, we use his aromatic planar boron clusters (B_n) with sizes $n = 6$-15 as a rough guide to optimising boron clusters. King restricted the systems to be completely planar, whilst we have allowed quasi-planar configurations to ensure (at least a local) minima in the potential energy surface. Naturally, the symmetry of the molecule will vary,[212,221] since our structures allow deviations from planarity; both point groups are reported for comparison. Also, making use of his results, the charges required to satisfy Hückel's rule determined 'electron book-keeping' are the only charges investigated. It is expected that B_6 and $B_7{}^+$ will have just two π-electrons (making them comparable to the cyclopropenyl ion) whilst $n = 8$-14 will have six π-electrons (like benzene) and $n = 15$ clusters will have eight π-electrons (similar to cyclooctatetraene).

These isosurfaces are determined by dictating a chemical shift threshold, and any point at or above this chemical shift is displayed on the isosurface plot. The most common chemical shift thresholds are typically $\sigma_{\text{iso}}(\mathbf{r}) = \pm 12$ or ± 16 ppm. To enable a fair comparison between the different isosurface plots in this chapter to both each other and those generated in organic chemistry, a plot at $\sigma_{\text{iso}}(\mathbf{r}) = \pm 16$ ppm is provided for all clusters. However, σ-delocalisation is still visible at much greater chemical shift thresholds; therefore, additional plots have been included to illustrate the regions of highest electron delocalisation. The exact chemical shift threshold used is not scientifically rigorous but is typically 2–3 ppm below the critical chemical shift threshold — the lowest chemical shift at which no positive isosurface is visible. The precise difference for the critical chemical shift threshold varies according to how 'interesting' the isosurface plots become.

7.2 $B_3{}^-$, B_3 and $B_3{}^+$

B_3^- is a single boron triangle anion, with each boron atom contributing three valence electrons to the system to create a ten-electron system. There are three traditional single bonds around the perimeter, and a 3c–2e bond shared between all boron atoms (i.e. σ-aromaticity), leaving two electrons for a π-aromatic system. This produces an incredibly high NICS(0) value of −73.73 ppm, which must be heavily influenced by the σ- aromaticity. The magnitude of the shift is significantly reduced to −28.12 ppm for NICS(1), however, this cannot be used to indicate π-aromaticity as illustrated by B_3^+. B_3^+ has two fewer electrons so has zero electrons available for a π-aromatic system. Despite this, the NICS(1) value is still large, at −17.16 ppm. This is greater than benzene, which with CASSCF(6,6)-GIAO/6-311++G(2d,2p) yields NICS(0) and NICS(1) of just −8.17 and −9.53 ppm, respectively. The σ-aromaticity of B_3^+ also produces a high NICS(0) of −65.51 ppm. The unpaired electron in B_3 does not significantly change either the isosurface plots of the NICS values; B_3 is intermediate between its charged counterparts with NICS(0) of −67.68 ppm and NICS(1) of −22.04 ppm. Each boron triangle has D_{3h} symmetry.[222]

The magnetic shielding plots in Figure 37 demonstrate the incredibly high shielding from σ-bonds, and without directly comparing the systems, the nature of π-aromaticity can not be extracted from the plots. The removal of π-electrons is noticeable at the high $\sigma_{\text{iso}}(\mathbf{r}) = \pm 60$ ppm shielding, with the radius of the central shielded region decreasing. The fact that these molecules have any visible isosurfaces off of nuclei at these high chemical shifts would be extremely rare in ground state organic chemistry. All these shielding plots are very different to carbon chemistry,[48,49,57,223] with shielding localised in the centre of these triangles, instead of along the single bonds. π-aromatic systems have doughnut-shaped holes in the centre of their rings,[48,49,57,223] but this is all dwarfed by the σ-aromaticity in the systems.

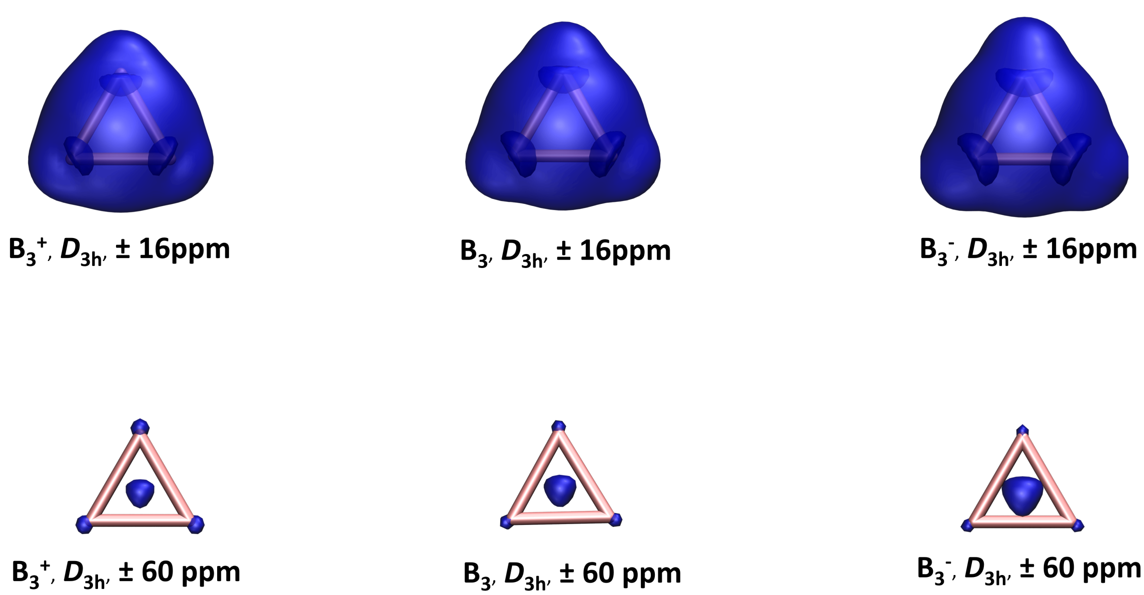

Figure 37: Isotropic magnetic shielding isosurfaces for ${B_3}^+$, B_3 and ${B_3}^-$ each at D_{3h} symmetry.

The shielding for five- and six-membered organic rings is well known,[48,49,57,223] but the smaller size of a triangular unit may impact the results. For a fairer comparison, Figure 38 displays the isosurface of ${C_3H_3}^+$. By comparison to Figure 37, the isosurface is similar around the central triangle at $\sigma_{\text{iso}}(\mathbf{r}) = \pm 16$ ppm. However, the critical chemical shift threshold is far lower, occurring around $\sigma_{\text{iso}}(\mathbf{r}) = \pm 30$ ppm. Approaching this threshold yields a very different shielding picture to the $n = 3$ boron clusters; there is electron localisation above and below the single bonds connecting the carbon atoms, but no in-plane contribution at this shift threshold. Additionally, as expected in second-row atoms, there is significant deshielding (indicated by the orange isosurface) around carbon centres. Hence, the three-membered carbon ring produces quite a different shielding to the previously examined five- and six-membered organic rings, which may be due to the added feature of σ-aromaticity,[197–202] which is not present in the larger rings. However, if this is the case, the σ aromaticity has a far less prominent effect in $C_3H_3^+$ than in isolated boron triangles. The NICS(0) and NICS(1) values of -23.04 and -14.75 ppm, respectively, also indicate strong aromaticity.

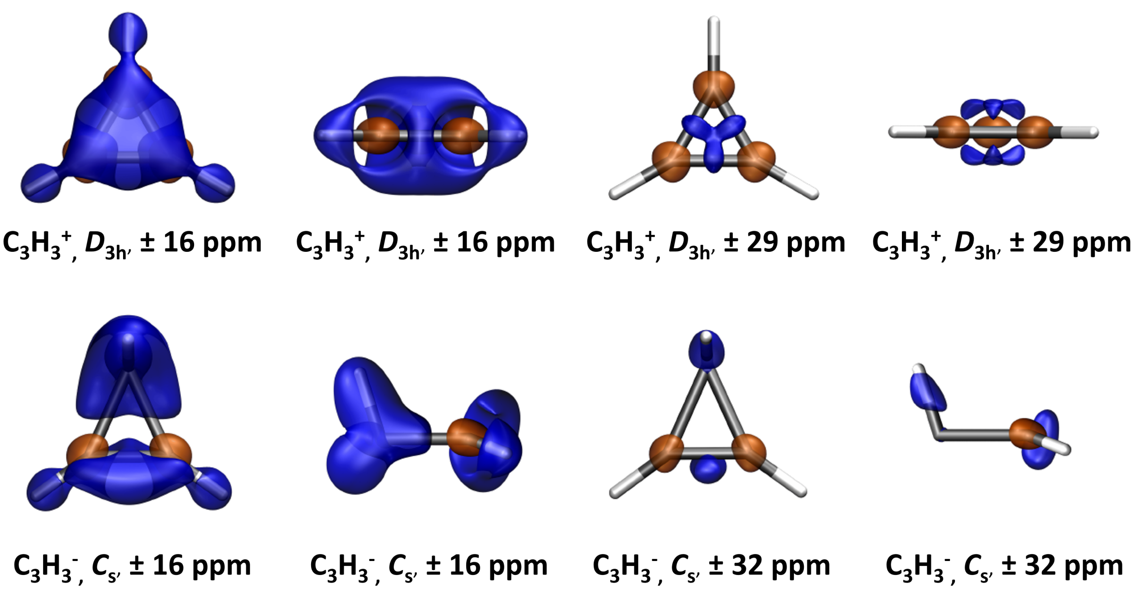

Figure 38: Isotropic magnetic shielding isosurfaces for $C_3H_3^+$ and $C_3H_3^-$ at D_{3h} and C_s symmetries, respectively.

$C_3H_3^-$ contains an additional two electrons, which distort the geometry to a C_s point group, with hydrogens buckling significantly out of the plane. The equal bond lengths of 1.36 Å in $C_3H_3^+$ become 1.29 and 1.58 Å in the anion, and this bond length alternation is an indicator of antiaromaticity. However, NICS(0) at -11.71 ppm suggests aromaticity, conflicting with weak antiaromaticity implied by NICS(+1) at 7.79 ppm, and nonaromaticity of NICS(−1) at 3.24 ppm. This is a prime example of why magnetic shielding plots are important for determining the true nature of aromaticity. Figure 38 demonstrates the lack of bonding along the single bonds at $\sigma_{\text{iso}}(\mathbf{r}) = \pm 16$ ppm. Whilst there is still an isosurface present at higher chemical shifts, $\sigma_{\text{iso}}(\mathbf{r}) = \pm 32$ ppm, these regions are heavily localised on a hydrogen substituent and along the double bonds. A deshielded region is absent in the centre of the ring, which is typical of antiaromatic molecules, but there is enough evidence from Figure 38 that the molecule is moderately antiaromatic.

$C_3H_3{}^+$ is generally a better example to compare the boron allotropes to, as most clusters are π-aromatic, however comparing $C_3H_3{}^-$ to $B_3{}^+$ highlights some key features. Firstly, the geometry is far more distorted in the organic system. But crucially, there is a lack of shielding at the organic ring's centre at just $\sigma_{iso}(\mathbf{r}) = \pm 16$ ppm, yet $B_3{}^+$ has the strongest shielding here, still visible at ±60 ppm. Whilst the former's π-antiaromaticity is due to an absence of electrons, and the latter's is caused by four π-electrons, the difference in the bonding of these molecules is noteworthy.

7.3 B_4 and $B_5{}^-$

Condensing two boron triangles produces B_4 with a D_{2h} point group.[222] Eight of the twelve valence electrons are distributed in single bonds around the perimeter. There appears to be an internal single B–B bond causing a deviation from a square structure. The remaining electrons enter a π-aromatic system.[222] Consequently, the isosurface is only visible at lower chemical shifts, unlike B_3 and its ions as there is no σ-aromaticity. NICS(0) is still quite large, −23.62 ppm, but NICS(1) is only −7.55 ppm. The NICS values indicate the molecule has no σ aromaticity, however, the magnetic shielding plot, shown in Figure 39, indicates electron localisation at the molecular centre and not along single B–B around the edges indicating some σ-aromatic character. Conversely, when the occupied orbitals are visualised, it is clear that there is one π-orbital delocalised over all atoms. The isosurface also rapidly vanishes at increasing chemical shifts unlike the $n = 3$ allotropes, a $\sigma_{iso}(\mathbf{r}) = \pm 16$ ppm is already near the critical chemical shift threshold. This conflicting information suggests that the bonding is possibly more complex than separating σ- and π-aromaticity. Additionally, although unrelated to bonding, the deshielded regions (indicated by the orange isosurface in Figure 39 are common and expected for second-row elements. It is present here, but not in the $n = 3$ systems, indicating that σ-aromaticity disrupts this core electron deshielding phenomenon, or at least our ability to detect it.

$B_5{}^-$ has C_{2v}[224] symmetry, with 16 valence electrons: ten are used in five peripheral B–B bonds, four in two internal single bonds, leaving just two. These enter a π-aromatic system, spreading across each triangle as confirmed in Figure 39. Once again, the shielding is only present within the molecule, with no isosurface engulfing the peripheral bonds. The NICS(0) and NICS(1) values are −13.81 and −15.81 ppm, respectively for the central triangle but reduced to −4.71 and −12.84 ppm, respectively for the outer triangles. These values are comparable to organic aromatic systems, and the small NICS(0) values indicate no σ-aromaticity. Whilst others have come to this conclusion before, it is interesting since instead of forming two internal single bonds, two 3c–2e bonds could form in the outer triangles. However, our shielding highlights this is not the case, with outer rings having significantly less delocalisation than the inner ring. The rest of the geometries in this chapter are based on those indicated by King. B_6, $B_7{}^+$, $B_8{}^{2-}$ and $B_9{}^-$ each have a wheel shape structure, with a single central boron atom, surrounded by a planar outer ring of boron atoms. Islas *et al.* [225] have visualised induced magnetic fields of similar clusters; boron wheels but with the central atom belonging to group 14, namely carbon, silicon and germanium. Separating out the σ- and π- components to aromaticity, they demonstrated that each of these wheels were indeed doubly aromatic.

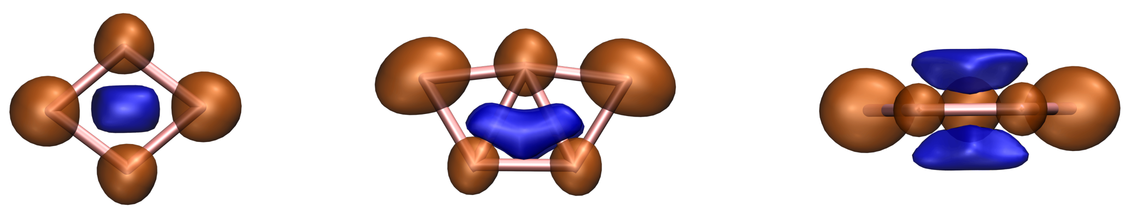

Figure 39: Isotropic magnetic shielding isosurfaces for B_4 and $B_5{}^-$ at D_{2h} and C_{2v} symmetries, respectively.

7.4 B_6 and $B_7{}^+$

In the case of B_6, the central atom varies by over 40° from the plane containing the remaining atoms, meaning NICS(+1) of any boron triangle is taken at a point almost directly above the central atom, which could heavily influence the results. The NICS(+1) and NICS(−1) values are dramatically different, −43.99 and −1.45 ppm, respectively, which indicate extreme aromaticity and nonaromaticity, respectively. The NICS(0) value is still high at −27.56 ppm. Out of the 18 valence electrons, ten are used in the five peripheral bonds, two form an internal bond connecting the central boron to the outer ring and there are two 3c–2e bonds. This leaves two electrons for a π-aromatic system. Since the molecule has C_{5v} symmetry (and D_{5h} symmetry in King's work), we see no indication of the single bond on the isosurface plot, as the structure resonates between the different forms, similar to naphthalene. The two remaining electrons can form a π-aromatic system. $B_7{}^+$ is similar, with 20 valence electrons, but with six peripheral bonds and no internal bond since it is not necessary to separate the 3c–2e regions, of which there are three. Consequently, there are also two electrons available for a π-system. King's structure was planar with D_{6h} symmetry, whilst ours is C_{6v}. However, the disagreement from planarity is reduced to under 28°. Monajjemi *et al.* [221] received the same point groups as us when searching for the global minimum. ${B_7}^+$ NICS indices indicate a reduction in aromaticity, with NICS(0), NICS(+1) and NICS(−1) of −15.65, −29.62 and −2.60 ppm, respectively. Hence, despite theoretically greater σ-aromaticity (three 3c–2e bonds instead of two) ${B_7}^+$ is less aromatic than B_6, although (ignoring NICS(−1)) both are significantly more aromatic than benzene. The magnetic shielding isosurfaces of both are shown in Figure 40. At $\sigma_{\text{iso}}(\mathbf{r}) = \pm 16$ ppm, both isosurfaces are similar, but as we approach the critical chemical shift threshold, it is clear that B_6 has greater shielding, as comparable surfaces are visible at 10 ppm higher in B_6 compared to B_7. Greater shielding is at least partly due to B_6's geometry, where the triangles are closer and hence contributing to electron delocalisation measured at a central point more than in ${B_7}^+$. The $\sigma_{\text{iso}}(\mathbf{r}) = \pm 50$ and ± 40 ppm isosurfaces indicate that although shielding is reduced compared to a single boron triangle, σ-aromaticity is still incredibly high.

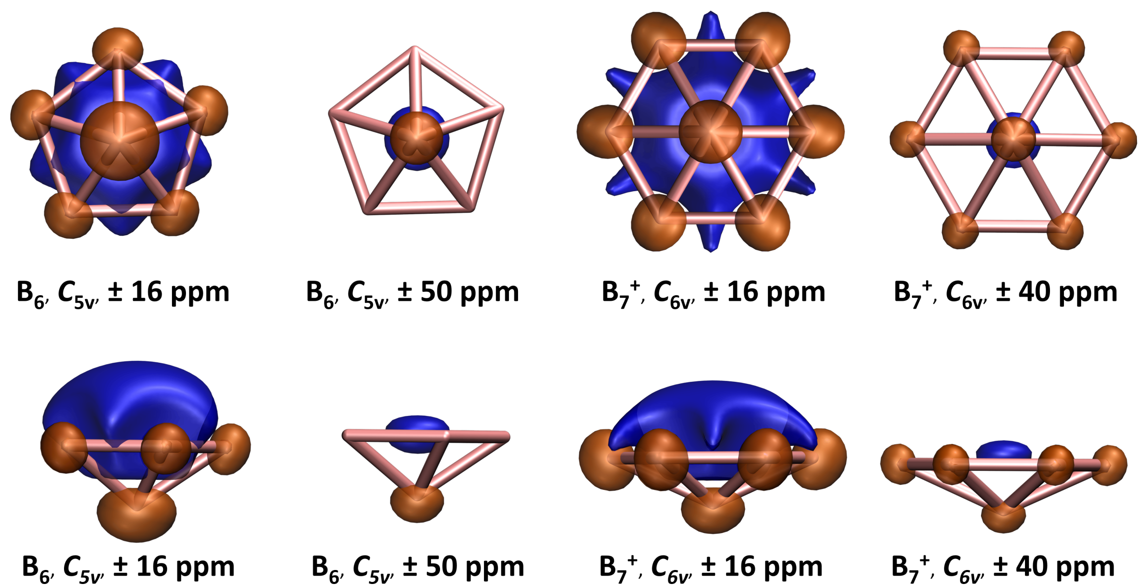

Figure 40: Isotropic magnetic shielding isosurfaces for B_6 and B_7^+ at C_{5v} and C_{6v} symmetries, respectively.

7.5 ${B_8}^{2-}$ and ${B_9}^-$

${B_8}^{2-}$ and ${B_9}^-$ are completely planar. ${B_8}^{2-}$ has 26 valence electrons, 14 of which form the peripheral bonds, four form two 3c–2e bonds and two create a 4c–2e bond. Thus, ${B_8}^{2-}$ would be π-aromatic according to Hückel's rule, with six π-electrons. Our point group is identical to King's (D_{7h}). NICS(0) is −40.91 ppm and NICS(1) is −19.15 ppm for each triangle, indicating strong aromaticity again. ${B_9}^-$ has two 4c–2e bonds, and only one 3c–2e bond, which along with the eight peripheral bonds, 22 of the 28 valence electrons are used, leaving six for a π-system. Whilst still planar, ${B_9}^-$ has four different triangular environments yielding a

C_{2v} point group instead of King's D_{8h}, with similar NICS(0) values ranging from −33.93 to −36.31 ppm, and NICS(1) indicators spanning −18.95 to −19.20 ppm. The aromaticity is therefore very comparable between these allotropes. The isosurfaces of these planar wheels are also very similar, and approach the critical chemical shift threshold at similar values, ($\sigma_{\text{iso}}(\mathrm{r}) = \pm 32$ and ± 36 ppm for $B_8{}^{2-}$ and $B_9{}^{-}$, respectively). The positive isosurface actively avoids the boron atoms on the perimeter, contrary to organic studies. At higher chemical shifts, the σ-aromaticity is further exemplified, with isosurfaces in both wheels concentrated by a ring around the central atom, but not encompassing any of the peripheral single bonds.

Whilst not strictly related to aromaticity, the deshielded regions (shown by the orange isosurface) in Figure 52) around the nuclei are interesting. Deshielding around nuclei is both less prominent and more localised in $B_8{}^{2-}$ than B_9. With a bond radius of 0.1 Å, the central boron atom appears to have no deshielding isosurface at −16 ppm in $B_8{}^{2-}$ (Figure 41) and the shift must be reduced to below −10 ppm for any visible surface. Even at −1 ppm, a complete deshielding sphere is not shown. B_9 has a small 2-dimensional circumference isosurface at −16 ppm around the central boron atom, with a flattened (but not flat) sphere only visible at −8 ppm. Even at −1 ppm, this does not become an actual sphere. This is also in contrast to the non-planar wheels where deshielding is greater in the centre of the wheel than on the periphery.

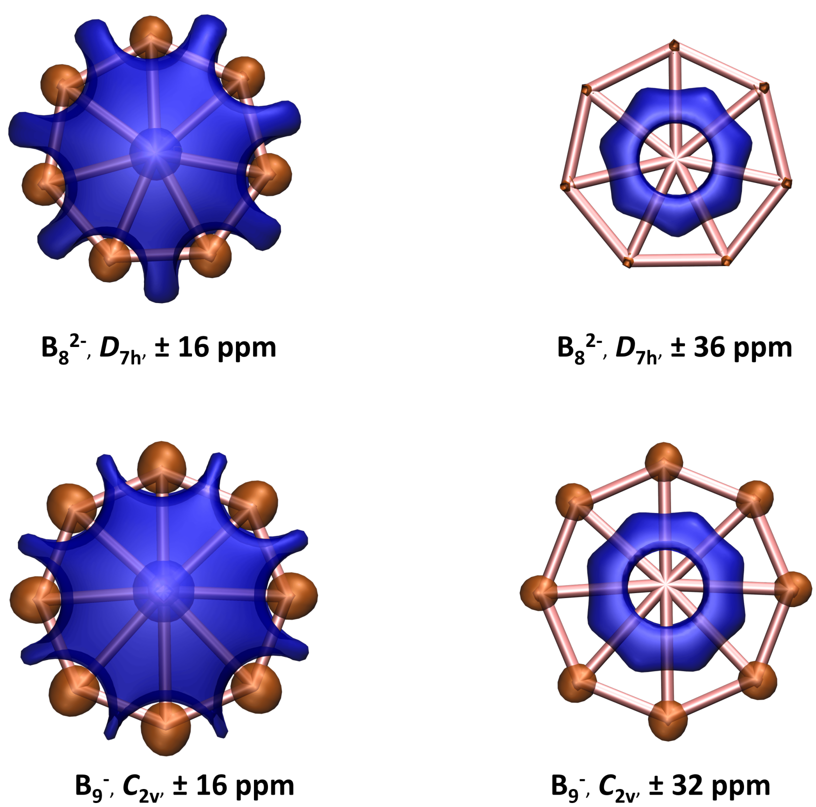

Figure 41: Isotropic magnetic shielding isosurfaces for $B_8{}^{2-}$ and B_9^- at D_{7h} and C_{2v} symmetries, respectively.

7.6 B_{10} and B_{11}

B_{10} is the smallest cluster to deviate from a wheel, with two internal boron atoms. Our geometry was C_{2h}, with internal boron atoms coming out of the plane in opposite directions, unlike King's strictly planar D_{2h} structure. This time, in terms of bonding, the surrounding eight boron atoms do not completely enclose the central atoms, with only six peripheral B–B bonds.[216] The remaining external boron forms a peripheral 3c–2e bond, so 14 electrons are used for the peripheral bonds in total. As expected, there are five internal 3c–2e bonds, so only 24 of the 30 valence electrons form these bonds, allowing six electrons to enter a π-aromatic system. The global aromaticity appears to be reduced compared to the boron wheels, with NICS(0) of -26.28 ppm for the central triangles, -22.29 ppm in triangles adjacent to the centre and -22.56 ppm for the outer triangles. NICS($\pm$1) values are smaller and approach benzene's values, ranging from -10.02 to -14.27 ppm. This is consistent with Duong *et al.*[226] which suggest B_{10} is only π-aromatic and not σ-aromatic. On the other hand, the shielding plot at 16 ppm, shown in Figure 42, demonstrates electron delocalisation within the boron triangles, and some outer bonds not engulfed in an isosurface. Increasing the threshold to display the isosurface to $\sigma_{\text{iso}}(\mathbf{r}) = \pm 25$ ppm shows the highest shielded regions. Whilst each region of the isosurface intersects sides of boron triangles, the isosurface is closer to being perpendicular to these sides, than parallel (as would expected for single bonds). There is also a region of isosurface within each triangle. Hence, Figure 42 highlights the σ-aromaticity of the system but indicates it is weaker than in many of the other systems in this chapter.

B_{11}^- has C_{2v} symmetry, with two internal boron atoms like B_{10}, but is simpler with the nine peripheral boron atoms using 18 of the 33 valence electrons to form B–B bonds and a further five 3c–2e bonds form internally using a further ten electrons. This once again leaves six electrons for the π-aromatic system. The only point of note with B_{11}^- 's structure is the square created in which there are no 3c–2e bonds. This is highlighted by the small NICS(0) values of -6.03 and -7.76 ppm in the two triangles that could have been formed. This is in contrast to the other triangles, where σ-aromaticity exists and NICS(0) ranges from -15.30 to -26.64 ppm. The smallest of these is directly above the square, which should have a prominent 3c–2e bond according to King, possibly suggesting a more localised bond, although still σ-aromatic. The other two (each degenerate) boron environments where a 3c–2e bond is expected indicate higher aromaticity, both with a magnitude just greater than -26.60 ppm. Whilst still slightly reduced, the NICS(1) values for the square (-13.91 and -12.51 ppm) are much closer to the other values, ranging from -15.65 ppm (directly above the square) to -19.38 ppm. This emphasises that the π-aromatic system extends over the entire molecule, whilst σ-aromaticity is localised within the given triangles. At $\sigma_{\text{iso}}(\mathbf{r}) =$

±16 ppm, Figure 42 demonstrates the shielding isosurface avoiding the peripheral boron atoms, similar to B_{10}. As expected from the NICS measurements, there is an absence of shielding in the square, but the single peripheral bond is still shielded. The σ-aromaticity of the triangles appears to influence the shielding of this single bond, as it is shorter and still does not extend across the length of the bond, as would be observed in organic chemistry. Raising the threshold to display the isosurface to $\sigma_{\text{iso}}(\mathbf{r}) = \pm 25$ ppm reveals two regions of high electron delocalisation. Fascinatingly, unlike its little brother B_{10}, these regions avoid all sides of boron triangles, creating loops extending above and below the plane.

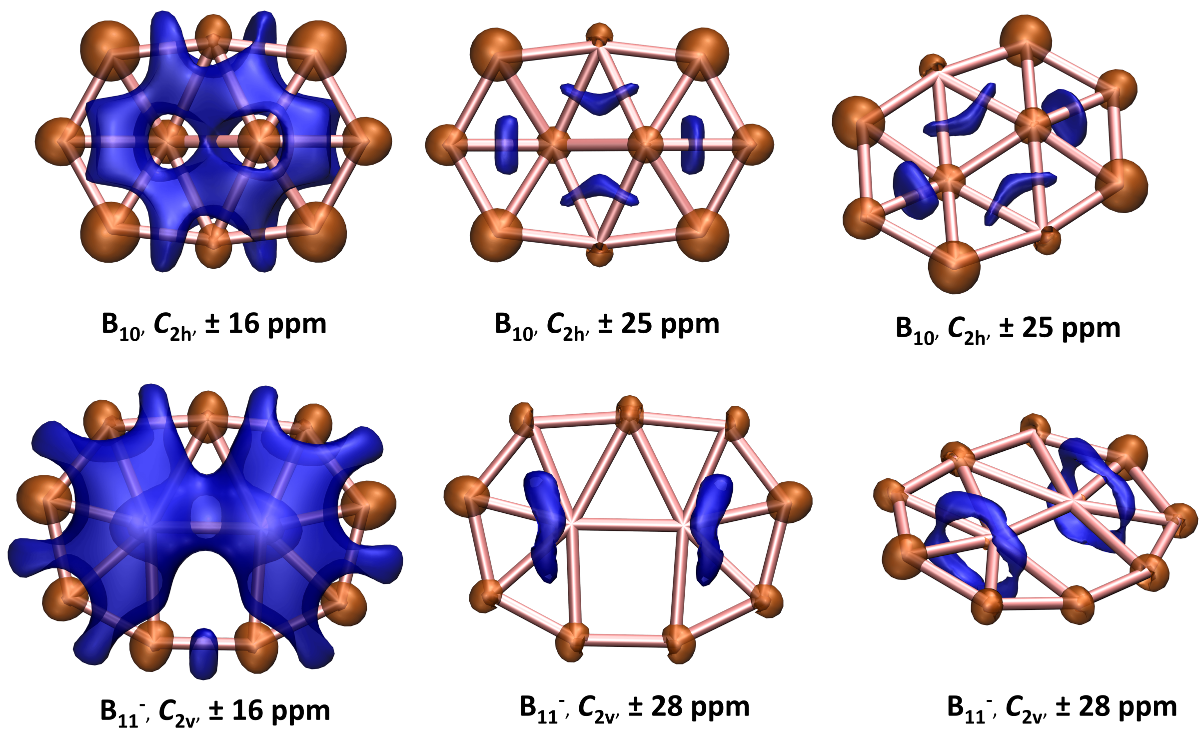

Figure 42: Isotropic magnetic shielding isosurfaces for B_{10} and B_{11} at C_{2h} and C_{2v} symmetries, respectively.

7.7 B_{12}

B_{12} has three interior atoms. King investigated a D_{3h} topology, and ours has C_{3v} symmetry. The nine peripheral boron atoms use 18 of the 36 electrons, whilst the six 3c–2e bonds use twelve more, leaving six electrons for a π aromatic system. The absence of internal bonds allows B_{12} to have the greatest ratio of 3c–2e bonds to boron atoms (exactly 0.5, see section 7.11), which along with the neutral charge and six π-electrons, makes it the most comparable boron allotrope to benzene. The NICS values are not that different from the other six π-electron boron clusters investigated with NICS(0) spanning −25.28 to

−29.10 ppm for triangles with 3c–2e bonds and −17.13 to −18.79 ppm for those which do not. NICS(±1) experience a significant variation for both types, ranging from −9.14 to −23.65 ppm for non 3c–2e rings, but −11.83 to −25.83 ppm for 3c–2e rings. The quasi-planar system has an interesting isosurface shown at ±16 ppm in Figures 43. Viewing from the concave surface the isosurface appears to engulf the entire molecule, but examining a view from the convex surface (Figure 43) reveals that only in the vicinity of the three interior atoms is their an isosurface both above and below the molecule. The isosurface is also not present underneath two-thirds of the peripheral single bonds, indicating a lack of shielding. This was also observed in the non-planar B_6 and $B_7{}^-$ clusters, and to a lesser extent, is similar to organic 'bowl-shaped' structures where NICS(1) is far greater off the concave plane than convex. Increasing the chemical shift threshold to $\sigma_{\text{iso}}(\mathbf{r}) = \pm 32$ ppm highlights the localisation above the interior atoms in addition to a ring above the central boron triangle, looking similar to rings in organic chemistry, albeit not actually localised on any bonds. Approaching the critical isosurface threshold at $\sigma_{\text{iso}}(\mathbf{r}) = \pm 37$ ppm, displays only a small isosurface above each of interior atoms, however, these are all slightly shifted towards the outer triangles.

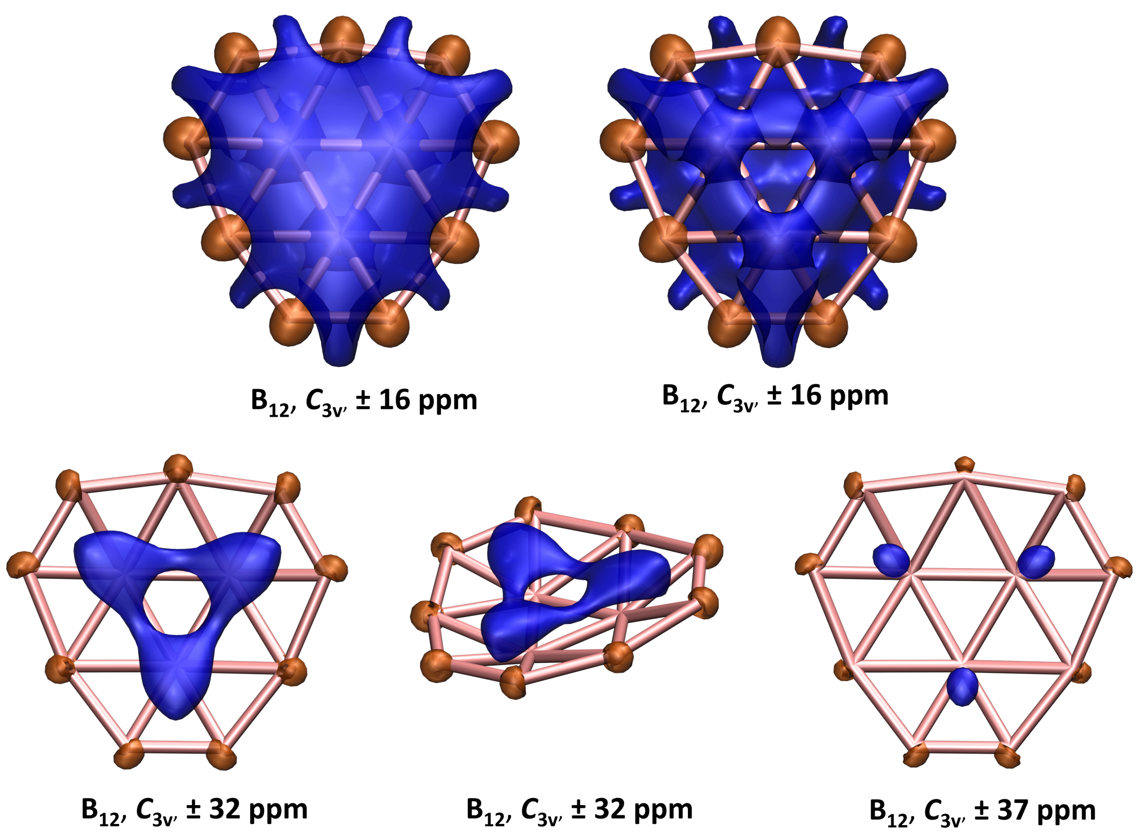

Figure 43: Isotropic magnetic shielding isosurfaces for B_{12} at C_{3v} symmetry.

7.8 B_{13}^+ and B_{13}^-

King[216] determined that both B_{13}^+ and B_{13}^- have C_{2v} symmetry and six π-electrons available for a π-system. Both have three internal atoms and ten peripheral B–B single bonds. B_{13}^+ has five 3c–2e bonds and two internal single bonds and King states B_{13}^- has only three 3c–2e bonds and one internal B–B single bond, with two 4c–2e bonds. Contrary to the allocation of electrons by King; Arvanitidis *et al.*[227] conclude that B_{13}^- primarily consists of 4c–2e bonds, instead of 3c–2e bonds, through adaptive natural density partitioning (AdNDP) analysis. The residual between the total electron densities and those expected were smaller assuming 4c–2e bonds than 3c–2e bonds. The 4c–2e bonds resonate, similar to benzene so create two Clar's sextets, partitioned by the central boron atoms.[227] Furthermore Arvanitidis *et al.* suggest there are eight π-electrons in B_{13}^- and fewer σ bonds. To complicate the matter further, on inspection of the molecular orbitals generated by our optimised structure, we observed five occupied orbitals with π character. B_{13}^- could therefore by π-aromatic (as suggested by King with six π-electrons, or us with ten π-electrons) or antiaromatic (as proposed by Arvanitidis *et al.* with eight π-electrons).

Results indicate that both ions have similar levels of σ-aromaticity, with NICS(0) ranging from -11.45 to -22.91 ppm in B_{13}^+, and -12.42 to -24.01 ppm (excluding values taken within the bottom square of B_{13}^+ (see Figure 44) where 3c–2e bonds are not expected to form). However, NICS(1) metrics differ significantly, with the non-planar B_{13}^- NICS(± 1) spanning -3.70 ppm to -14.97 ppm, with an average of just -7.21 ppm. Planar B_{13}^+ appears to be far more aromatic with an average over twice the size, -16.85 ppm. This may be an indication that although both ions have similar σ-aromaticity, the π-aromaticity of B_{13}^+ is greater than B_{13}^- and hence support Arvanitidis *et al.*'s conclusion of eight π-electrons[227] over King's six.[216] However, given the variability in NICS indicators from other boron clusters in this work, we do not believe any assessment of the number of π- or σ- bonds can be ascertained for B_{13}^- from magnetic shielding.

B_{13}^+ has a similar topology to B_{12} but is planar with an additional atom on the periphery, similar to the change from B_{10} to B_{11}^-. There is greater shielding within the square this time (Figure 44), however, shielding is still less than most boron triangles in the structure. Some peripheral bonds of triangles also experience a surprising lack of shielding. Increasing the chemical shift threshold to ± 23 ppm, a doughnut-shaped ring forms around the centre of the molecule. Unlike B_{12}, this extends both above and below the plane. A small increase in the threshold to $\sigma_{iso}(\mathbf{r}) = \pm 25$ ppm reveals a localisation over the three internal atoms, with the last remaining in plane isosurface not passing through the central triangle. These 'c-shaped' isosurfaces become little dots above and below the plane if the chemical shift threshold is increased further.

Hence B_{13}^+ behaves similarly to B_{12}, but the chemical shift threshold must be reduced by around 10 ppm to get comparable plots, indicating weaker aromaticity.

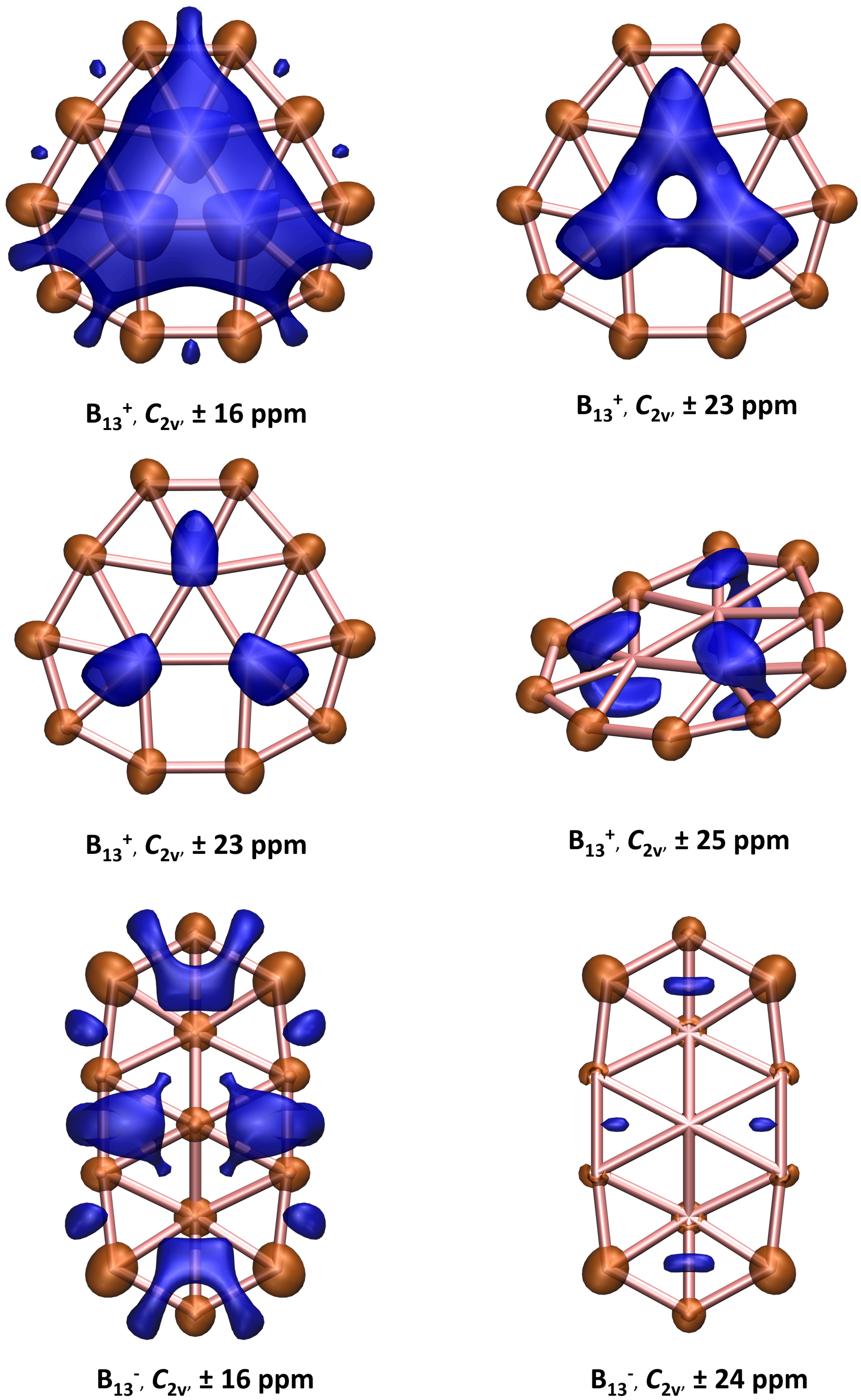

Figure 44: Isotropic magnetic shielding isosurfaces for B_{13}^+ and B_{13}^- at C_{2v} symmetry.

Figure 44 displays the vastly different topology of B_{13}^-, appearing as two fused B_7^+ wheels sharing a single atom (with three additional electrons) but the isosurface appears nothing like any of the wheels. Additionally, the proposed resonant structures of 4c–2e bonds of Arvanitidis *et al.*[227] appears to disagree with our shielding plot. In each example they provide, the central triangles above and below the central atom, have neither 3c–2e or 4c–2e bonds. Figure 44 demonstrates this is actually one of the regions with the highest electron delocalisation. A slightly lower maximum shielding occurs in B_{13}^- as opposed to B_{13}^+, with regions centred both within triangles and across bonds at $\sigma_{\text{iso}}(\mathbf{r}) = \pm 24$ ppm.

7.9 B_{14}

The B_{14} isomers have very similar energies. One is shaped closer to a diamond, with four interior boron atoms (Figure 45), whilst the other is shaped closer to a club with only three interior boron atoms. We calculate the former had a C_{2v} point group and the latter a C_s, however, King considered very similar structures, but the point groups were the opposite way round. The 'diamond-shaped' cluster with four internal boron atoms has ten external B–B bonds, six 3c–2e bonds and two internal B–B bonds. This uses 36 of the 42 valence electrons, permitting six to form an aromatic π-system. The 'club-shaped' cluster with three internal atoms has eleven peripheral B–B bonds but only one internal B–B bond in addition to six 3c–2e bonds. Hence both systems have a similar capacity for aromaticity, with six 3c–2e sites and six π-electrons. Diamond B_{14} contains the largest NICS(0) value within the top and bottom point, -32.68 ppm, and is likely because the triangle is σ-aromatic in both resonant structures. The smallest NICS(0) values are located on either side of this point, forming no 3c–2e bonds in either resonance structure (-7.65 ppm). From this alone, it may be inferred that the weaker NICS indices are a result of π aromaticity, however, NICS(+1) inside the bowl is only -4.68 ppm, and NICS(-1) is -0.91 ppm. These indicate nonaromaticity and the delocalised π-electrons are not overly present at these sites. The centre beneath has only has NICS(-1) of -0.91 ppm as well, but the greater NICS(+1) value of -8.64 ppm indicates greater aromaticity, and this difference is expected for 'bowl-shaped' structures,[67] so these rings are aromatic. The club B_{14} is similar with a couple of rings appearing to be nonaromatic, but the majority aromatic. This is an example of unequal bond lengths for systems still appearing aromatic, contrary to the common observations in organic chemistry where bond lengths of aromatic molecules are almost equal. The most aromatic triangle according to a NICS(0) of -21.43 ppm has bond lengths varying from 1.55 Å to 1.81 Å.

Both isomers show significant shielding near the centre of the molecule at $\sigma_{\text{iso}}(\mathbf{r}) = \pm 16$ ppm (Figure 45), but the C_s variant has less shielding overall with a higher proportion of triangles with very little or no shielding at this threshold. Increasing the threshold to $\sigma_{\text{iso}}(\mathbf{r}) = \pm 21$ ppm causes approaches the limit for C_s B_{14} as shown in Figure 45, whilst the C_{2v} isomer's limit is nearer $\sigma_{\text{iso}}(\mathbf{r}) = \pm 27$ ppm. Interestingly, both have four regions of high electron delocalisation near the limit. The C_s isomer has two regions along the length of the molecule, one positioned on a bond, and the other within a triangle. This electron localisation is evidence of the single internal B–B bond, and there are two such regions in the C_{2v} isomer, indicating the two internal bonds. The most shielded regions of these isomers are the two triangles in C_{2v} isomer, where 3c–2e bonds provide σ-aromaticity. Interestingly, neither particularly indicate the number of 3c–2e bonds overall, nor allude to the location of the π-aromatic electrons.

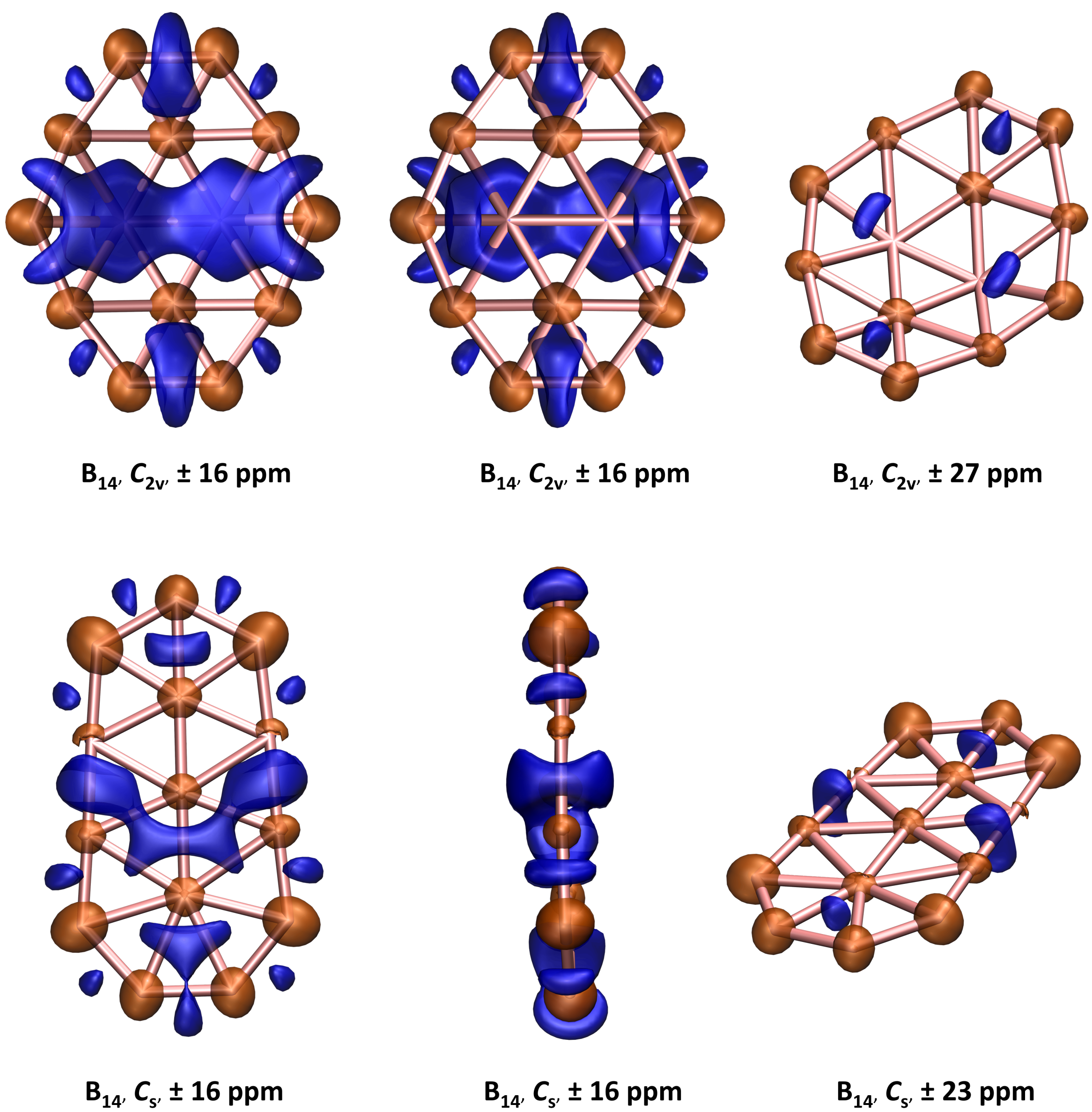

Figure 45: Isotropic magnetic shielding isosurfaces for B_{14} with C_{2v} and C_s symmetry.

7.10 B_{15}^-

There are B_{15}^- isomers with similar energy, one with C_1 and C_s symmetry. Both contain twelve single B–B bonds and seven 3c–2e bonds, but the C_1 state contains four internal atoms instead of the three in the C_s state. Hence both isomers have eight π-electrons so would be π-antiaromatic. These would be the closest analogues to cyclooctatetraene studied here. The C_s state has greater aromaticity, with the average boron triangle having a NICS(0) of −32.80 ppm, compared to the still significantly aromatic −23.04 ppm in the C_1 state. This extends to NICS(1) metrics, with an average of −17.65 ppm for C_1 state, compared to −13.18 ppm. Similarly, the greatest NICS(0) value is −37.51 ppm and −33.89 ppm, respectively. This implies that the σ-aromaticity vastly exceeds π-antiaromaticity, and the nature of π systems can not be determined when σ-aromaticity is present.

The magnetic shielding isosurface of C_1 B_{15}^- at $\sigma_{iso}(\mathbf{r}) = \pm 16$ ppm in Figure 46 reveals a mixture of internal boron environments, from nearly entirely deshielded (even at larger elevations from the molecular plane) to just non-shielded in the immediate vicinity. At ±25 ppm, it is clear there is more delocalisation slightly out of the plane, and that aromaticity is weaker in the centre. Approaching the maximum chemical shift threshold at $\sigma_{iso}(\mathbf{r}) = \pm 30$ ppm, it is apparent that there are two regions of high electron delocalisation. Another appears to be caused by an internal single bond, but the isosurface is most likely only visible due to σ-delocalisation of the neighbouring triangles.

The far neater isomer with C_s symmetry is geometrically similar to two condensed B_8^{2-} wheels, sharing a single boron atom. The magnetic shielding plots are also very similar at both $\sigma_{iso}(\mathbf{r}) = \pm 16$ and ±32 ppm, shown in figure 46. The only deviation from B_8^{2-} occurs at the central atom, which forms additional bonds and hence does not participate in σ-delocalisation. The C_s isomer has greater delocalisation than the C_1, having a greater volume of isosurface at higher chemical shifts. For these larger molecules to have such high chemical shifts is not common in organic chemistry. The C_s isomer informs us that π-antiaromaticity has a much smaller effect than the σ-aromaticity, as B_8^{2-} has a similar maximum chemical shift. The other comparable π-antiaromatic and σ-aromatic systems investigated were the B_3 ions, which also demonstrated the usual magnetic shielding observed in π-delocalised systems has a minimal effect compared to σ-delocalisation in the same systems. Nevertheless, the information obtained about the σ-delocalisation and bonding extracted by magnetic shielding studies is rich and plentiful.

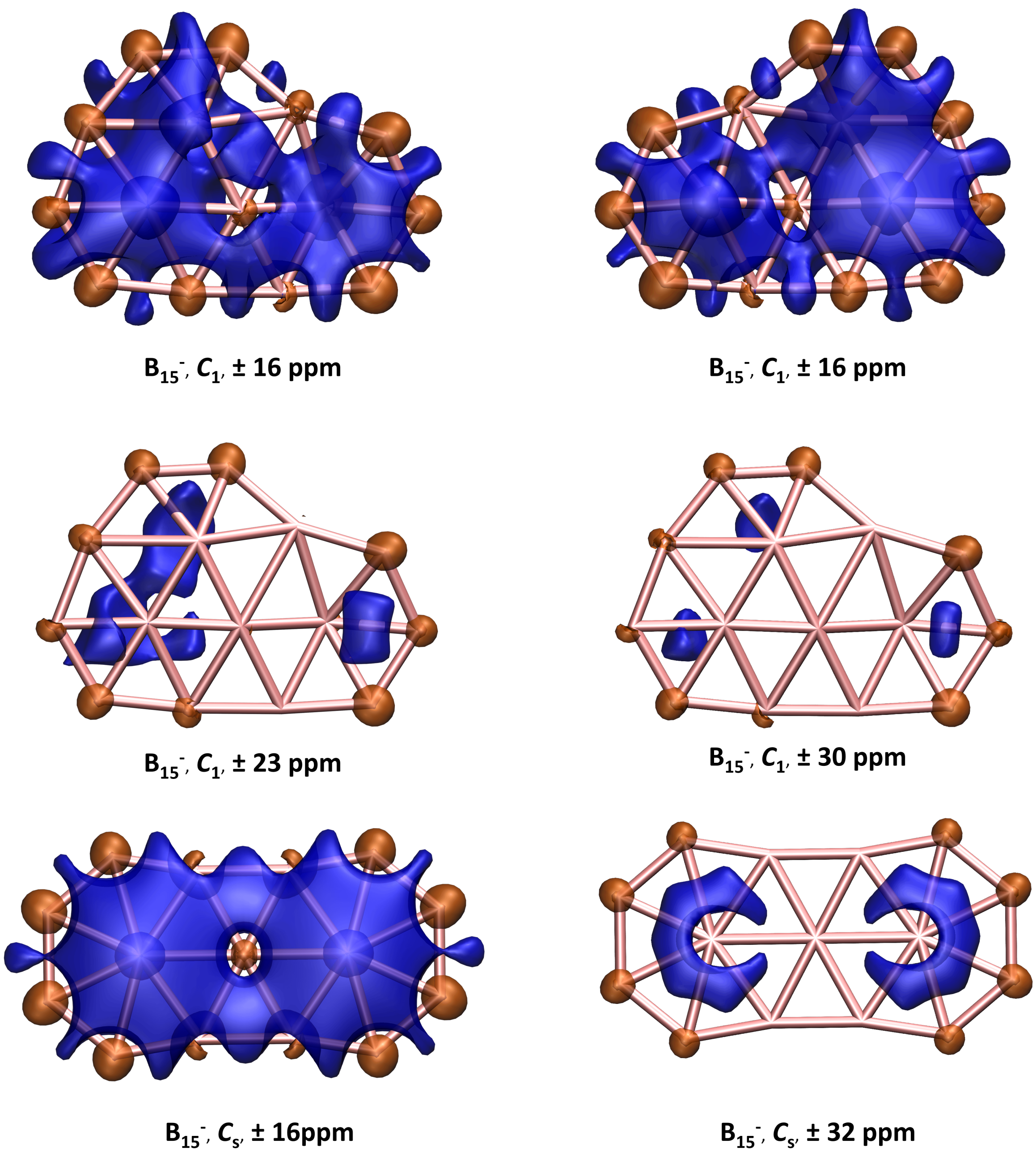

Figure 46: Isotropic magnetic shielding isosurfaces for B_{15}^- with C_1 and C_s symmetry.

7.11 Linking to stability

King proposed that B_{12} is the boron analogue of benzene. By comparing the average number and type bond per boron atom, as shown in Figure 47, it is apparent that B_{12} has the highest proportion of delocalised valence electrons (50%) of each allotrope. Hence we can confirm that B_{12} is the most aromatic boron cluster with six π-electrons (of those investigated).

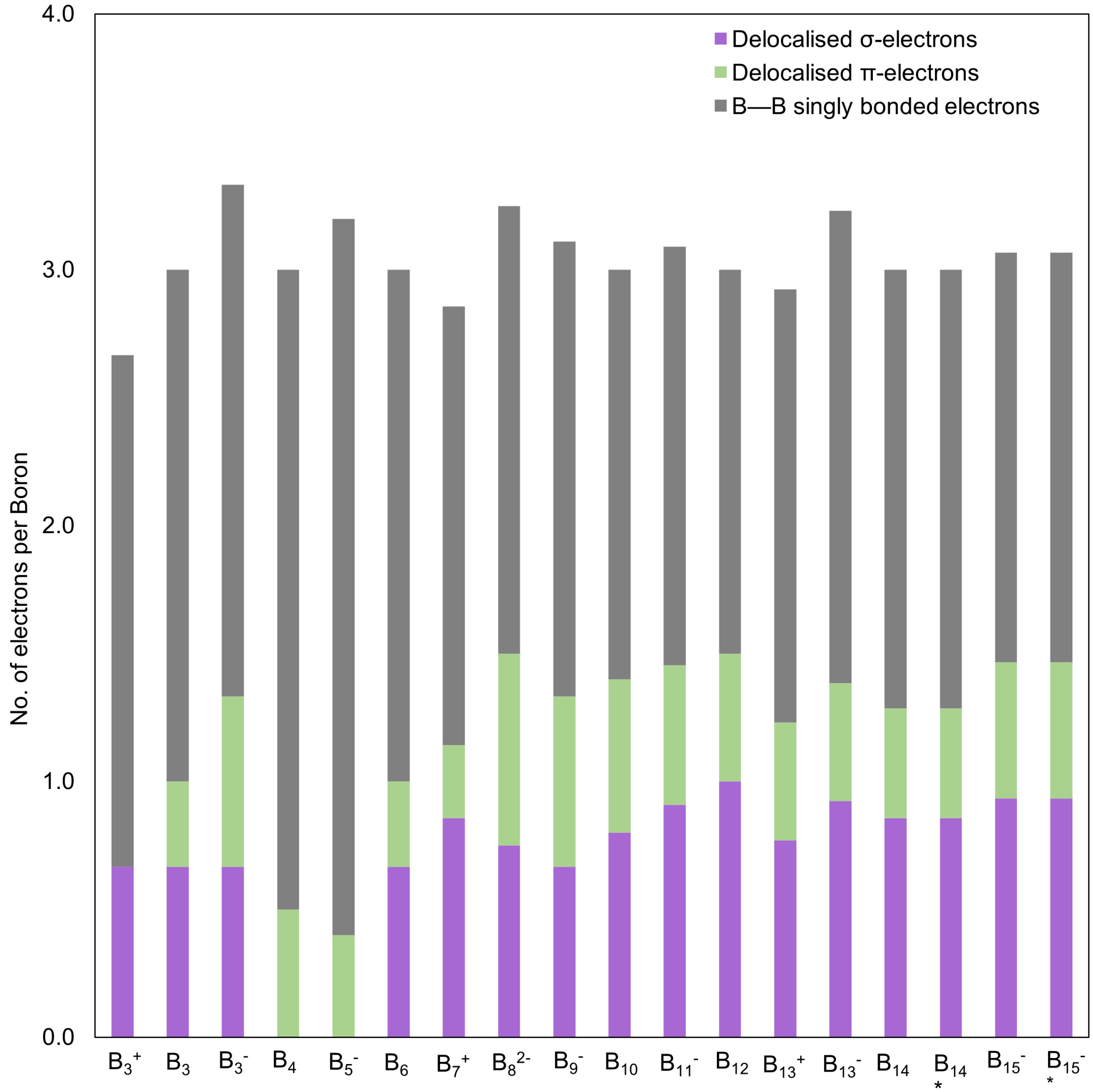

Figure 47: The number of electrons per boron atom in different bond types in boron clusters. Those indicated with a '*' are those with less symmetry. See text for details.

Aromaticity is often associated with stability, with the delocalisation of electrons causing an energy reduction. This could be tested by comparing average NICS values to either the HOMO–LUMO separation or an average energy per boron atom. Unfortunately, these two properties do not correlate with each other, with a correlation coefficient of $R^2 = 0.004$, so it would be problematic to only use one of these as an indicator of stability. These indicators appear to align better with larger clusters.[228] Since aromaticity usually causes stability, by increasing the average number of σ-bonds per atom it may be expected that the boron atomisation energy per atom would increase as more energy would be required to break bonds. However, comparing these properties also produced no correlation, $R^2 = 0.014$. Whilst it should be made clear that NICS is a local aromaticity measure, averaging over each ring in organic chemistry can provide an, albeit loose, indication of global aromaticity. Comparing the average number of σ-bonds per atom to the average NICS value per triangle, yields no correlation either, $R^2 = 0.006$. Comparing the average number of σ-bonds per atom to the HOMO–LUMO also produced no correlation, $R^2 = 0.003$. It has previously been shown that atomisation energies per boron atom are smaller for allotropes with n $\leq$ 6, typically in the two or three hundreds of kJ mol^{-1} as opposed to being in the four hundreds for n $>$ 6.[203] We can confirm this, but beyond relating this to the lack of double aromaticity for those smaller clusters, the larger clusters show no such trend. Hence, the stability of each cluster relative to each other is difficult to determine since any link of stability to aromaticity is non-existent. σ-aromaticity is therefore very different to π-aromaticity, offering little additional stability to the system. Hence, our results indicate the similarities to π-aromaticity stop at the delocalisation of electrons and their ability to be detected via magnetic shielding — not a stabilisation.

7.12 Conclusions

Magnetic shielding has been utilized to study the bonding within aromatic quasi-planar boron clusters, B_n of size $n = 3$–15. σ-aromaticity appears to dominate off-nucleus chemical shifts, rendering π-aromaticity almost undetectable through magnetic shielding in systems with σ-aromaticity. This is even the case for suspected π-antiaromatic clusters (such as $B_3{}^+$ or $B_{15}{}^-$) where σ-aromaticity dominates to produce high NICS values and well shielded magnetic shielding plots. Additionally, the number of π- or σ-aromatic electrons cannot be determined by the plots, and unlike organic systems, it is difficult to determine the number of delocalised subsystems.

Nevertheless, magnetic shielding plots are valuable resources and indicate regions of high electron delocalisation which varies drastically between clusters. In some clusters, the shielding is greatest on either side of the plane, and far weaker within it, even for fully planar structures like $B_{13}{}^+$. The aromaticity can cause the greatest shielding to create loops perpendicular to the molecular plane, such as $B_{11}{}^-$. Non-planar wheels B_6 and $B_7{}^+$, have the greatest shielding above their central atom, whilst the planar wheels $B_8{}^{2-}$ and $B_9{}^-$, have the greatest shielding (and hence electron delocalisation) in a ring within the molecular plane. The cluster's symmetry also has a significant impact on the shielding, with both B_{14} and $B_{15}{}^-$ isomers having vastly different shielding plots. The more disordered the cluster, the more disordered the shielding isosurface becomes, breaking into multiple isolated regions at high chemical shifts. The reason for these vastly different manifestations requires further investigation.

There are greater regions of non-shielding around atomic centres than those experienced in organic chemistry. There appears to be no completely consistent rule as to which nuclei are less deshielded, however, in most cases, it is internal atoms which experience less deshielding whilst peripheral atoms are deshielded well. Given that internal atoms have a greater proportion of their electrons in σ-delocalised orbitals, this observation can be rationalized as internal boron atoms overcome the traditional effects, whilst peripheral atoms typically form two single bonds, so cannot.

The stability of boron clusters is theoretically problematic to determine, with no correlation between any HOMO–LUMO gaps, atomisation energies per boron atom, average NICS values, and the number of σ-bonds. It appears that σ-aromaticity must only be compared to traditional π-aromaticity when considering that electrons are delocalised over more than two atoms. Traditional properties of aromaticity such as stabilisation are not extended to σ-aromaticity, and the properties of so-called σ-aromaticity are far closer to being a single bond shared across multiple atoms.

The highlight of this study is the power of magnetic shielding to indicate the regions of delocalisation in these boron clusters. The high NICS values reaching -73.73 ppm in $B_3{}^-$ is unusual for organic chemistry and solely π-aromatic systems. Visualising these magnetic shielding isosurfaces which are not localised on atoms or along two-centre bonds, consistently at $\sigma_{\text{iso}}(\mathbf{r}) \geq 30$ ppm, emphasises the high influence of σ-aromaticity on magnetic shielding and hence bonding.

8

Ethane, Ethene and Ethyne

As a precursor to the large following chapter on annulenes, this brief chapter inspects the linear molecules, ethane, ethene and ethyne in order to understand the shielding around molecules which are not cyclic, and hence can not be aromatic or antiaromatic. Magnetic calculations were performed at the B3LYP-GIAO/6-311++G(2d,2p)//B3LYP/def2TZVP level (restricted DFT for singlet states and unrestricted for triplet states) and isosurfaces were constructed with a grid spacing of 0.05 Å. All other computational details are in line with those stated in other chapters. The key difference is that four geometrical/electronic environments were evaluated as the system is inspected along a journey starting at the ground state (S_0), after a vertical excitation (T_1//S_0), adiabatic relaxation (T_1), and finally a vertical de-excitation (S_0//T_1).

All bonds and atoms in ethane experience large shielding in the ground state, as shown by the blue isosurface in Figure 48. Unlike the cyclic systems covered later, the C–H bonds are surrounded by similar shielding to the C–C bond. This is a consequence of each bond only containing two electrons, unlike aromatic systems where delocalisation is present, or antiaromatic systems which contain some double C=C bonds. The shielding around ethane appears to be the result of the overlap between shielded regions over close C–C and C–H bonds. A vertical excitation creates an unstable system large ‘dumbbell-shaped’ shielded region, which is aligned with the molecular axis. Having a shielded region so far away from the molecular bonds indicates that electrons are not localised within the system, which offers a destabilising effect as nuclei experience more electrostatic repulsion. Furthermore, there is a large ‘doughnut-shaped’ deshielded region encircling the C–C bond, as indicated by the orange isosurface in Figure 48. An optimal triplet state geometry could not be calculated, as the preference is to create two CH_3 radicals and the triplet shielding in the ground state geometry supports this conclusion.

Ethene has well-shielded bonds, however there is slightly greater shielding along the C=C bond than the C–H bonds. The shielding is closer to the molecule, and the bonding is more localised than in ethane. Upon vertical excitation, the C=C bond loses the majority of the shielding, with only a small amount remaining at the centre of the bond. The C–H bonds remain well shielded. This is because there is a clear candidate for excitation, one of the electrons in the double C=C bond, hence the non-shielded molecular centre is most likely a result of the superposition of shielding from the single bond and a deshielding region from the double bond. Relaxing the molecule changes the symmetry from D_{2h} to D_{2d} as the CH_2 units rotate, 90^o to each other. This facilitates shielding along the C–C bond, albeit weaker than the ground state optimised geometry. The bond length increases to 1.443 Å. The rotation of the CH_2 unit prevents the overlap of (what are typically thought of as) p_z orbitals to form the double bond, allowing the electrons to occupy different orbitals without placing too much strain on the molecule. The vertical de-excitation emphasises why the triplet optimised geometry is poor for the ground state, as these carbon 'p_z' orbitals are perpendicular to each other, so can not form a second C–C bond. This creates deshielded regions approximately simulating non-bonding p_z orbitals in their respective orientations. A further indication of instability is the shielded region extending significantly beyond the molecule, similar (albeit far less extreme) to T_1 ethane at the S_0 geometry.

Ethyne's shielding depicts all bonds are well shielded, but the triple carbon bond experiences even greater shielding than C–H bonds, as would be expected, due to the higher concentration of electrons. The bond length is reduced to just 1.197 Å, shorter than any other bond considered in this work. A vertical excitation yields an extremely unstable molecule, as indicated by the deshielding engulfing the entire molecule, including the C–H bonds. The C–H bonds themselves are not broken, but the immense destabilisation of the carbon bonds deshields the entire region, including the hydrogen centres. Relaxing ethyne indicates the triple C–C bond is broken, and the carbon separation elongates to 1.324 Å, which is (approximately) the same length as a C=C bond in ethene. The hydrogen atoms also shift away from the molecular axis in the same direction. Shielding is restored along each of the bonds, with the most prominent shielding between the carbons, as expected as there is still a double bond. A small deshielded region is now present between the hydrogen atoms. This is analogous to antiaromatic annulenes, in which a deshielded region lies in the centre of the carbon ring, except the ring is not closed and hydrogen atoms are part of the structure. Further similarities to antiaromatic molecules exist as a double C=C bond has a C–H bond on either side, so an alternating pattern of double and single bonds is generated. A vertical de-excitation removes the deshielded region between the H atoms, but C–H bonds are left non-shielded. The shielding around the C–C bonds intensifies and shifts in the same direction as the H atoms. Both the lack of shielding long C–H bonds and the shielding away from the molecule indicate that this is a non-optimal structure and is a trend observed annulenes in the following sections.

Shielding around $T_1//S_0$ ethane demonstrated that an excitation can not produce a stable structure. Firstly, the C–C bond is deshielded significantly and secondly, the dumbbell-shaped shielding regions highlight that electrons are shifting away from the nuclei and hence no bond is formed. Whilst this is more extreme than observed in most annulenes, the former links to indicator (2) outlined in the conclusions chapter, and the latter to indicator (3), that the magnetic response is unphysical. This contextualises the $S_0//T_1$ states where the carbon ring is well shielded, but the structure is not optimal.

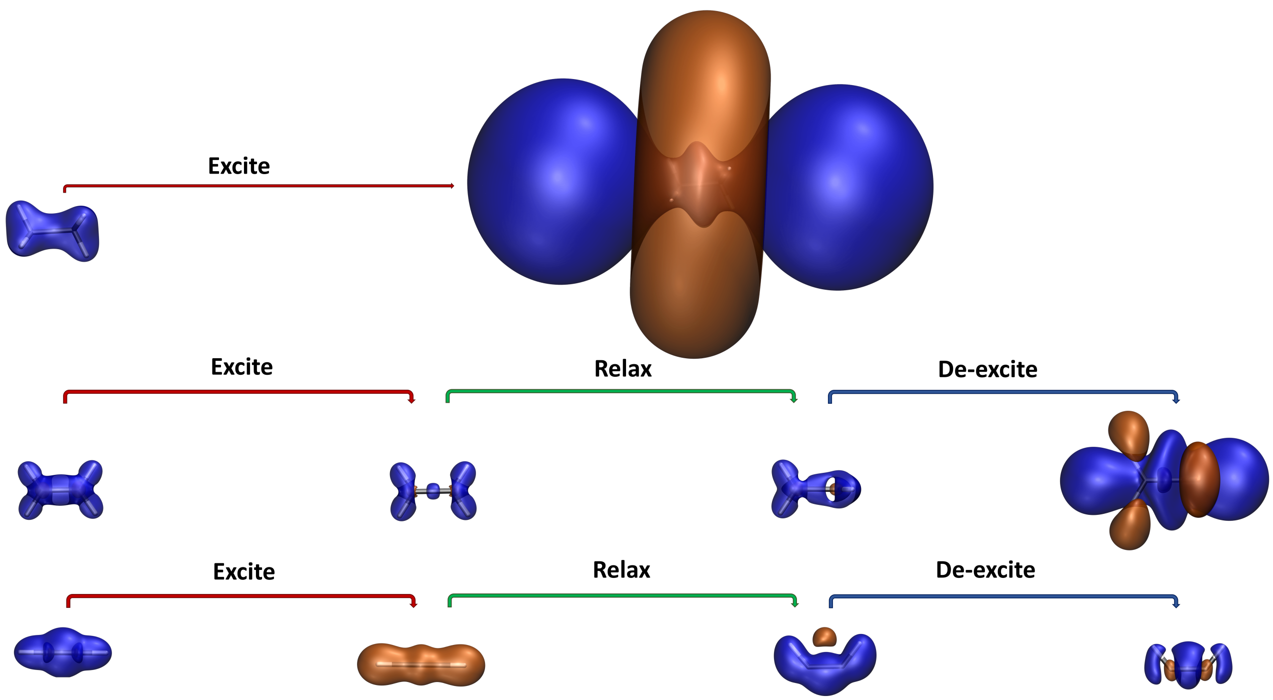

Figure 48: Shielding around C_2H_6 (top), C_2H_4 (middle) and C_2H_2 (bottom) at $\sigma_{\text{iso}}(\mathbf{r}) = +16$ ppm (shielded regions, blue) and $\sigma_{\text{iso}}(\mathbf{r}) = -16$ ppm (deshielded regions, orange). The latter two start from the $S_0//S_0$ state, vertically exciting to $T_1//S_0$, adiabatically relaxing to $T_1//T_1$ and vertically de-exciting to $S_0//T_1$. The former has calculated shielding shown in the $S_0//S_0$ state and after a vertical excitation to $T_1//S_0$ state. See details in text.

The $\sigma_{\text{iso}}(\mathrm{r})$ around ethene through the four electron environments highlight the influence of a π-system, and why the staggered form is sub-optimal for the ground state (deshielding in non-overlapping p_z orbitals). Furthermore, vertical excitation decreases shielding along the C=C. Whilst aromatic annulenes do not contain‘double-bonds’ (only delocalised electrons and single bonds), this explains why some bonds are non-shielded or experience less shielding. This is particularly noticeable in ‘single’ C–C bonds in the antiaromatic 4 π-electron systems C_4H_4 and $C_6H_6{}^{2+}$ in the optimised ground state. The ‘single’ bond maintains a molecular structure, whilst the electrons are concentrated elsewhere, in these cases towards the ‘double’ bonds. Comparing ethyne’s $\sigma_{\text{iso}}(\mathrm{r})$ in the T_1 state for the vertical excitation and relaxed geometry highlighted the significance that reducing symmetry can have on the shielding and overcoming severe antiaromaticity. The $T_1//T_1$ state reveals that the deshielded region observed at the centre of antiaromatic annulenes are not an exclusive consequence of delocalisation, and is more of a reflection of unstable bonds in close proximity to each other.

The ground state shielding of ethane, ethene and ethyne demonstrates that three-dimensional magnetic shielding isosurfaces do not easily identify increased shielding of double and triple bonds compared to single bonds. A proper comparison would require consideration of not just the extent but also the intensity of the shielded regions. Using two-dimensional contour plots, as shown by Karadakov and Horner[50] better shows differences in shielding intensities. However, the differences in shielding intensity is best examined by Horner by calculating the shielding at the centre of the C–C bonds.[41] It was found that the shielding for ethane and ethene were comparable at approximately 50 ppm, whilst ethyne shielding was around 70 ppm (depending on model chemistry). At 1 Åabove the C–C bond, ethane displayed less shielding (*ca.* 6 ppm) whilst ethene and ethyne are similar at *ca.* 15 ppm.[41] Given both of these measurements, it can be rationalised that the C–C bond in ethyne is more well shielded than ethene, which is in turn more well shielded than ethane. However, the three-dimensional shielding plots do not show this, and almost suggest the opposite due to the selection of the low chemical shift threshold. This should not be an issue for the rest of this thesis as all other molecules contain delocalised electrons or alternating double and single bonds, so they can readily be compared to each other. Afterall, the chemical shift threshold of ± 16 ppm was chosen to best represent aromatic and antiaromatic hydrocarbons.

More crucially to the main topic of this thesis, the characteristic deshielded region in the centre of antiaromatic molecules has been shown not to be an electron delocalisation phenomenon intrinsic to antiaromaticity, as the π-systems in in T_1 ethyne form a comparable deshielded region, despite the molecule and molecular orbitals not forming a closed loop.

9

Annulenes, $C_nH_n^q$

9.1 Introduction

As computational capability continues to expand, the analysis of off-nucleus shielding volume data has become an increasingly more accessible tool to study aromaticity. Whilst previous studies have applied this tool to the examination of ground and excited state aromaticity in one or two annulenes, a systematic study of this type for a wide range of annulene systems has not been attempted so far. In this chapter isotropic magnetic shielding isosurfaces are analysed for annulene systems with an odd and even numbers of carbon atoms, $C_nH_n^{+,-}$ for $n = 3, 5, 7, 9$, and $C_nH_n^{2+,0,2-}$ for $n = 4, 6, 8, 10$. DFT calculations for these annulene systems are carried out in four subsequent electron environments: (i) the optimised ground state (S_0) geometry, $S_0//S_0$, (ii) following vertical excitation to the lowest triplet (T_1) state, $T_1//S_0$, (iii) at the optimised T_1 geometry, $T_1//T_1$, and (iv) following vertical de-excitation from T_1 back to S_0, $S_0//T_1$. The use of these four electron environments allows us to investigate the effect of geometry relaxation on the aromaticity induced by both vertical excitations and de-excitations, going further than existing studies of the aromaticity gain or antiaromatic relief provided by the optimisation of the T_1 geometry.[229,230]. Understanding the aromaticity changes that a molecule experiences during its journey starting at S_0, followed by a vertical excitation to T_1, then relaxation of the T_1 geometry and, finally, vertical de-excitation back to S_0 can aid the design of molecular photoswitches[231,232] and molecular motors,[233–235] and rationalising experimental observations on photochemical reactions such as excited-state intramolecular proton transfers.[236,237]

Benzene in the B3LYP model chemistry used in this thesis yields NICS(0) and NICS(1) of −7.6 and −9.9 ppm, respectively. This very close to widely considered superior method of RMP2-GIAO/6-311++G(2d,2p) results of −7.6 and −10.0 ppm, respectively.[53] Using the same basis set (6-311++G(2d,2p)), but implementing CASSCF(6,6)-GIAO, these values are changed to −8.2 and −9.5 ppm, respectively.[53] Whilst B3LYP is slightly off, it is close enough to give a general appreciation of the nature of the bonding.

Our benchmark antiaromatic molecule, C_4H_4, has NICS(0) and NICS(1) of 27.2 and 17.8 ppm, respectively. This deviates more than benzene using RMP2-GIAO/6-311++G(2d,2p), which calculates these values to be

30.0 and 19.8 ppm, respectively.[53] CASSCF(4,4)-GIAO/6-311++G(2d,2p), suggests that both of these model chemistries overestimate the antiaromaticity in the molecule, as NICS(0) and NICS(1) are 18.4 and 12.3 ppm, respectively.[53] The differences here indicate that antiaromaticity is exaggerated in B3LYP shielding calculations. However, within the same model chemistry, the trends are repeated, so remaining within the same model chemistry, different annulenes can be compared. Additionally, the shielding surfaces presented remove any ambiguity that single-point NICS calculations may produce, by indicating the degree of localisation or delocalisation around the whole of each molecule.

As will be discussed in detail later in this chapter, magnetic shielding results in different model chemistries yield significantly different values, some far too extreme to be physical and some which suggest opposite aromatic characterisation to each other. This chapter goes further than the others by performing a critical analysis of the significance of the model chemistry and assesses them against Hückel's, Baird's and Möbius aromatic criteria. In addition to B3LYP, magnetic shielding is also evaluated in the DFT functionals M06,[238] M06-2X,[238] CAM-B3LYP[239] and PBE0[157] and using the Hartree–Fock (HF)[240,241] and MP2[18] methods. The isosurface shielding plots are only evaluated at the B3LYP level, as were the optimised geometries used in the other calculations, but NICS values have been evaluated in each of these model chemistries. Whilst compared in the text, the values are also listed in tables as part of the Appendix.

First, the relative energies and bond lengths in the optimised B3LYP/def-2TZVP will be compared in the following two subsections. Subsequently, shielding calculations were performed with various electronic structure methods in the 6-311++G(2d,2p) basis set. The B3LYP shielding isosurfaces were each constructed using a grid spacing of 0.05 Å.

9.2 Relative Energies

With the exception of the charge, q, each annulene can be considered an oligomer with repeat unit $(CH)_n$. Hence, the energy per CH unit in $C_nH_n^q$ was computed using the formula

$$E_{\mathrm{CH\ in\ C}_n\mathrm{H}_n^q} = \frac{E_{\mathrm{C}_n\mathrm{H}_n^q}}{n} \tag{32}$$

The $E_{\mathrm{CH\ in\ C}_n\mathrm{H}_n^q}$ for every annulene in each of the four states are shown in Figure 49. The energies of the annulenes per CH unit do not change according to Hückel's rules, but vary by charge. For each of these closed-shell molecules, the cations by far have the highest energy per CH unit, followed by the anions, and where applicable, the neutral molecules are the most stable. Thus, the stabilization induced by aromatic electronic states is small compared to the destabilization resultant of charging molecules. All four environments of each annulene have similar energies, and there are far more pronounced energy differences between the same sized annulenes with different charges than the four environments of those annulenes.

As expected, annulenes in the $S_0//S_0$ environment (green bars in Figure 49) are all lower than the respective energies in the $S_0//T_1$ (yellow in Figure 49) environment. The average CH unit energy at the triplet geometry is an average of 3.2 kcal mol^{-1} above that of the optimised structure. Likewise, $T_1//T_1$ energies (blue bars in Figure 49) are all lower than the respective $T_1//S_0$ energies (red bars in Figure 49). The average $T_1//S_0$ energy per CH unit is an average of 2.2 kcal mol^{-1} higher than its $T_1//T_1$ energy. Both of these observations are expected, since this is the purpose of the geometry optimisation, to find the lowest energy structure.

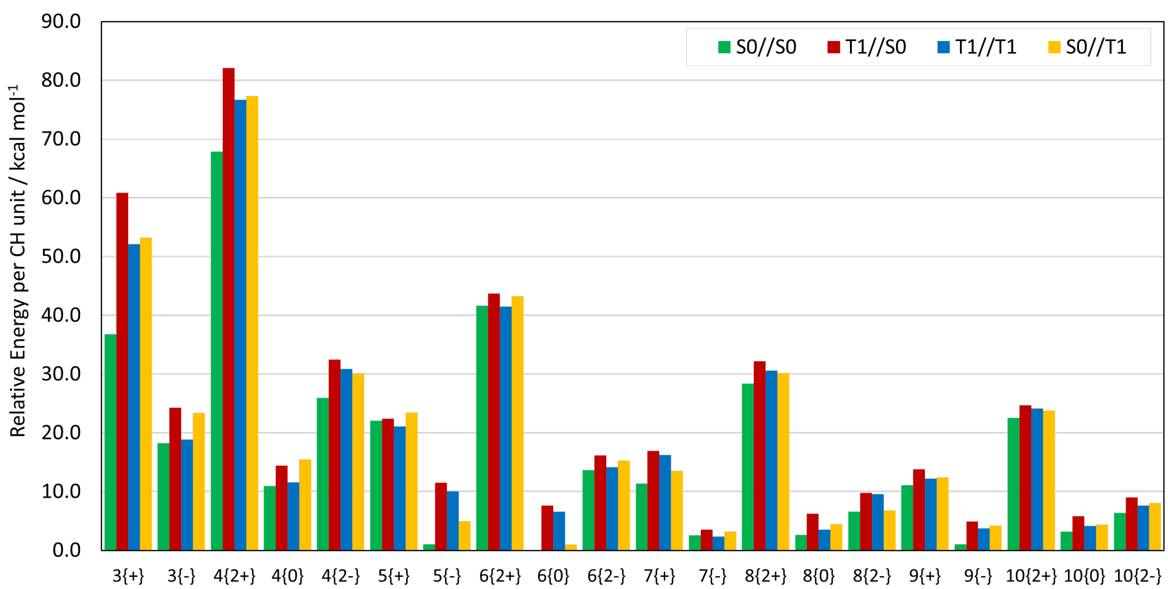

Figure 49: Energy per CH unit in charged annulenes, relative to $S_0//S_0$ C_6H_6. The number of carbons (n) is given in each annulene is given next to the charge of the molecule.

In all but three cases, the relaxed singlet state structures have lower energies than the relaxed triplet state structures. This would be expected in most molecules as electrons have a tendency to create closed shells when bonding into molecules. The three annulenes for which this is not the case are $C_5H_5{}^+$, $C_6H_6{}^{2+}$and $C_7H_7{}^-$. The first two of these are four π electron systems and the latter is an eight π electron system. Hence, these are all antiaromatic in the ground state, and experience an aromatic reversal upon excitation to an aromatic state. The energies per CH unit are 0.9, 0.1 and 0.2 kcal mol^{-1} more stable in the relaxed triplet states than the relaxed ground states in these molecules, respectively.

9.3 Bond Length Criteria

Table 13: The symmetry point groups (PG) and C–C bond lengths (with the number of each bond in brackets) from the S_0 and T_1 optimised geometries of neutral and charged annulenes.

	S_0		T_1	
	PG	C–C bond lengths	PG	C–C bond lengths
C_2H_6	D_{3d}	1.526[1]	(*See text*)	
C_2H_4	D_{2h}	1.325[1]	D_{2d}	1.443[1]
C_2H_2	$D_{\infty h}$	1.197[1]	C_{2v}	1.324[1]
$C_3H_3^+$	D_{3h}	1.358[3]	C_1	1.318[1] 1.358[1] 1.962[1]
$C_3H_3^-$	C_s	1.292[1] 1.585[2]	C_s	1.451[2] 1.455[1]
$C_4H_4^{2+}$	D_{2d}	1.423[4]	C_{2v}	1.347[2] 1.453[1] 2.036[1]
C_4H_4	D_{2h}	1.330[2] 1.576[2]	D_{4h}	1.438[4]
$C_4H_4^{2-}$	C_{2h}	1.471[2] 1.491[2]	C_s	1.509[2] 1.534[2]
$C_5H_5^+$	C_{2v}	1.342[2] 1.445[2] 1.571[1]	D_{5h}	1.420[5]
$C_5H_5^-$	D_{5h}	1.411[5]	C_s	1.400[2] 1.432[1] 1.509[2]
$C_6H_6^{2+}$	C_{2h}	1.388[4] 1.456[2]	D_{3d}	1.423[6]
C_6H_6	D_{6h}	1.390[6]	D_{2h}	1.382[4] 1.515[2]
$C_6H_6^{2-}$	C_{2v}	1.363[2] 1.490[4]	C_{2v}	1.431[4] 1.442[2]
$C_7H_7^+$	D_{7h}	1.391[7]	C_2	1.391[2] 1.392[2] 1.419[2] 1.470[1]
$C_7H_7^-$	C_2	1.347[2] 1.394[2] 1.453[2] 1.491[1]	D_{7h}	1.409[7]
$C_8H_8^{2+}$	D_{2d}	1.403[8]	D_2	1.383[4] 1.411[2] 1.463[2]
C_8H_8	D_{2d}	1.334[2] 1.467[2]	D_{8h}	1.398[8]
$C_8H_8^{2-}$	D_{4d}	1.412[8]	D_{4h}	1.372[4] 1.434[4]
$C_9H_9^+$	C_2	1.377[2] 1.388[2] 1.404[2] 1.412[2] 1.419[1]	C_2	1.395[2] 1.397[2] 1.399[2] 1.401[2] 1.402[1]
$C_9H_9^-$	D_{9h}	1.397[9]	C_2	1.400[2] 1.402[2] 1.409[1] 1.413[2] 1.417[2]
$C_{10}H_{10}^{2+}$	C_2	1.381[2] 1.389[2] 1.400[2] 1.411[1] 1.427[1] 1.424[2]	C_2	1.402[4] 1.403[4] 1.403[2]
$C_{10}H_{10}$	C_2	1.330[2] 1.337[2] 1.348[1] 1.460[2] 1.467[2] 1.476[1]	D_{2d}	1.364[4] 1.414[4] 1.474[2]
$C_{10}H_{10}^{2-}$	C_2	1.396[2] 1.405[1] 1.411[2] 1.413[2] 1.413[2] 1.434[1]	D_{5d}	1.418[5]

The differences between the S_0 and T_1 optimised geometries of different molecules are often considerable and result in a change of symmetry. Discussions including the geometry are often useful, as those based solely around shielding may be misleading. Most notably, the degree of shielding over corresponding bonds in electronic states that exhibit different levels of antiaromaticity may not correctly reflect the respective differences in bond strength and length. This is due to the presence of a central deshielded region in an antiaromatic ring which can cause exaggerated deshielding of the bonds in that ring.

Before we systematically examine the bond lengths in various annulenes, it makes sense to establish a starting point for aromaticity and antiaromaticity. Table 13 lists the C–C bond lengths and symmetry of hydrocarbons investigated in this thesis, in both the ground and excited states. For molecules with unequal bonds, the shortest bonds have been listed first. Antiaromaticity is characterised by closed circuits with alternating single and double bonds and arguably the most well-known example is cyclobutadiene. From Table 13, the bond lengths in the rectangular ground state geometry are 1.576 Å and 1.330 Å, aligning well with isolated bond lengths of single and double C–C bonds in ethane (1.526 Å) and ethene (1.325 Å), respectively. Benzene has identical C–C bond lengths, in its well-known ground state D_{6h} geometry — 1.390 Å. Note that the benzene C–C bond length lies between that of single and double bonds, but is closer to the latter, rather than being the arithmetic average. This reflects the stabilisation inherent in aromaticity. It should be noted that bond lengths themselves cannot conclusively determine aromaticity (neither can magnetic shielding or any other magnetic criteria). Bond lengths will be influenced by many factors including ring strain, as sp^2-hybridized orbitals are forced into different orientations.

9.4 $\mathbf{n = 3}$

The $C_3H_3{}^+$ cation has two electrons in the π-electron system, making it the smallest aromatic hydrocarbon via Hückel's rule. The cation is considered to be a pivotal intermediate in ion–molecule reactions in space and has been detected in the gas-phase.[242] The D_{3h} structure has identical bond lengths of 1.358 Å to support an aromatic characterisation, with bond lengths actually shorter than benzene. The shielding in Figure 50 further supports this idea, as do the NICS indicators shown in Table 14, e.g. NICS(0) is −22.9 ppm. Other methods produce similar results: CAM-B3LYP (−23.4 ppm), M06 (−23.2 ppm), M06-2X (−22.9 ppm), PBE0 (−23.2 ppm), HF (−24.3 ppm), and MP2 (−24.7 ppm). Despite having a greater magnitude than benzene, a greater NICS magnitude does not indicate greater aromaticity in this case. Comparing the ring strain, illustrated in Figure 49, C_3 $H_3{}^+$ has the third highest ring strain (an additional 37 kcal mol^{-1} compared to benzene) of the twenty ground state annulenes investigated. This is an example where examining the nuclear magnetic shielding for annulenes NICS can be quite misleading. The centre of a three-membered carbon ring will be very close to the single C–C bonds, and hence would experience a stronger influence from each of them than the centre of a ten-membered carbon ring would have contributions from each of the single bonds. Consequently, a negative NICS(0) for a small ring would indicate a lower degree of aromaticity than a much larger ring with the same NICS value.

A vertical excitation produces an antiaromatic molecule, with deshielding bulging out from the centre, encompassing not only C–C single bonds, but extending into the C–H bonds as well. Whilst the $\sigma_{\text{iso}}(\mathbf{r})$ plot initially appears credible, the NICS(0) value of 1125.7 ppm is clearly too extreme and an amplification of the destabilisation. For $T_1//S_0$, the methods diverge sharply. M06 (2949.1 ppm), and M06-2X (212.7 ppm) also yield extreme positive values, whilst CAM-B3LYP (3.1 ppm) suggests nonaromaticity. PBE0 (−31.5 ppm), HF (−159.6 ppm) and MP2 (−329.9 ppm) return increasingly negative NICS(0) values, all of which violate Baird's rule by suggesting aromaticity. In a trend which shall be exemplified in later examples, MP2 stands out as the most extreme.

After relaxation in the lowest triplet state, a closed loop could not be achieved in the geometry optimisation. A minimum energy structure (i.e. one with no imaginary vibrational modes) could be located; however, there is no bond connecting the cycle, with a C–C separation of 2.386 Å far exceeding what would be considered a single bond. The other bonds are only slightly shorter than the single bonds in the ground state at 1.355 Å. The point group is C_{2v}. In this case, the NICS values also offer very little insight, as the probe positions are so close to the central carbon. A B3LYP NICS(0) of −85.5 ppm is an order of magnitude greater than benzene, but electrons are clearly not delocalised. The shielding broadly traces around the molecule with two points of interest. There is additional shielding around the hydrogen atoms, particularly the end hydrogens where shielding is concentrated on the outer sides of the molecule. Additionally, there are deshielded regions around either side of the carbon centre as shown in Figure 50. On inspection of the orbitals, the β LUMO exhibits a change in phase across the external carbon centres in the molecular plane as does the α HOMO−1 orbital. Perhaps the single electron in this orbital could be responsible for this deshielding. At the relaxed T_1 geometry ($T_1//T_1$), all other methods investigated predict shielding, though much reduced from the vertical excitation case: MP2 (−29.7 ppm), M06 (−32.1 ppm), M06-2X (−25.6 ppm), CAM-B3LYP (−32.1 ppm), HF (−37.6 ppm), and PBE0 (−33.4 ppm).

A vertical de-excitation leads to an approximate reversal of shielded and deshielded regions. The internal hydrogen is non-shielded with larger deshielded regions on either side. The shielding plot demonstrates a highly unstable structure, whilst the NICS(0) and NICS(1) values of −38.1 and −14.7 ppm incorrectly indicate a strongly aromatic structure, further highlighting the importance of shielding plots over NICS values. NICS(0) of other model chemistries agree with B3LYP: M06, CAM-B3LYP, HF, and PBE0 give modestly negative values (−38.1 to −4.9 ppm), whereas MP2 again stands out with an unphysically large shielding (−1372.1 ppm). Conversely, the M06-2X functional predicts the opposite aromatic character (150.9 ppm).

Over the four states, the $C_3H_3{}^-$ anion behaves interestingly. The system has four electrons in its π-electron system, so is antiaromatic (via Hückel's rule) in the electronic ground state. The bond length alternates between a short 'double' bond of 1.292 Å and the longer 'single' bonds of 1.585 Å. The shielding in Figure 50 gives a better description than NICS values can at this small ring size, with a lack of shielding along two of the C–C bonds but no deshielded region in the centre, indicating a weakly antiaromatic molecule. The lack of C–C shielding suggests that the σ bonds are weak in this state. At this small size, the NICS values are not very descriptive, with an aromatic B3LYP NICS(0) of −12.1 ppm, but an antiaromatic NICS(−1) of 7.7 ppm. The NICS(0) values are similar across all methods: MP2 (−14.9 ppm), M06 (−10.4 ppm), M06-2X (−11.1 ppm), CAM-B3LYP (−13.3 ppm), HF (−16.4 ppm), and PBE0 (−12.9 ppm), and for each the NICS(±1) have the opposite sign.

After excitation, shielding materialises around all C–C bonds and in the centre of the molecule. But for the carbon with no symmetrical equivalent, shielding is lacking. When relaxed, the shielding becomes aromatic according to the shielding plot, but the NICS values once again do not provide a clear picture. All methods yield more negative NICS values: B3LYP (−19.9 ppm), MP2 (−23.7 ppm), M06 (−18.1 ppm), M06-2X (−52.3 ppm), CAM-B3LYP (−24.6 ppm), HF (−27.1 ppm), and PBE0 (−22.1 ppm).

Both states of $C_3H_3{}^-$ have a C_s point group symmetry, but the C–C bond lengths equalise to 1.358 Å in the triplet state, strongly suggesting aromaticity. At the T_1 optimised structure aromaticity strengthens as predicted by Baird's rule, as shown by unanimously more negative NICS(0) values: B3LYP (−31.9 ppm), MP2 (−33.0 ppm), M06 (−32.3 ppm), M06-2X (−31.1 ppm), CAM-B3LYP (−32.7 ppm), HF (−37.0 ppm), and PBE0 (−33.3 ppm). The B3LYP shielding is also strongly supportive of an aromatic characterisation.

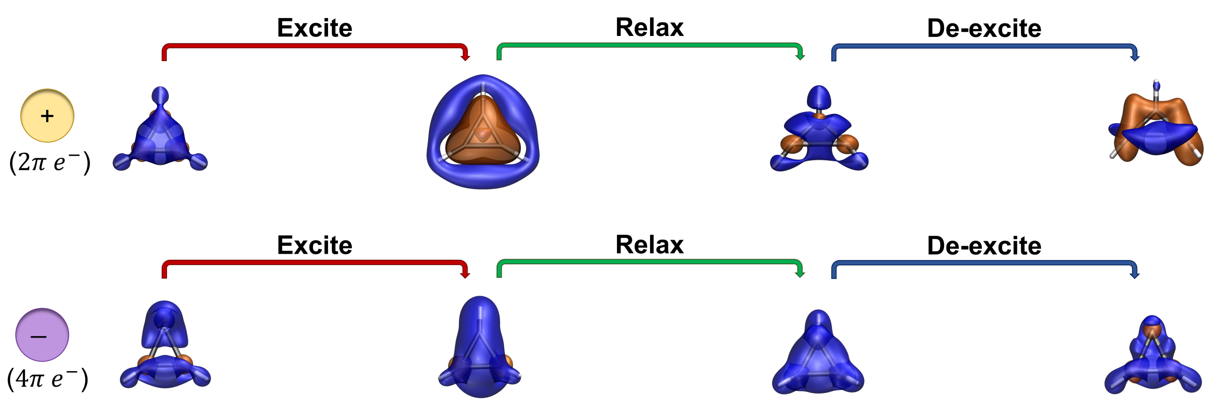

Figure 50: The shielding of $C_3H_3{}^+$ (top) and $C_3H_3{}^-$ (bottom) starting from the $S_0//S_0$ state, vertically exciting to $T_1//S_0$, adiabatically relaxing to $T_1//T_1$ and vertically de-exciting to $S_0//T_1$.

After a vertical de-excitation, the molecule is less well shielded than the T_1 state at the T_1 optimised geometry, however, shielding is greater than with the S_0 optimised geometry (whose energy per CH unit is 5.2 kcal mol^{-1} lower). NICS(0), NICS(+1) and NICS(−1) are −64.0, −43.2 and −25.4 ppm, respectively. This goes against the notion that the shielding can indicate stability, as this sub-optimal structure is more well-shielded than the optimal one. Upon further inspection, it appears that this shielding is from a higher singlet state, not the S_0, as the first excitation energy is negative with a TDA-B3LYP/6-311++G(2d,2p). NICS(0) values are more negative than the optimised ground state across all hybrid methods, from −64.0 ppm (B3LYP) to −105.9 ppm (M06), with HF reaching −344.4 ppm. MP2 is again an outlier, deviating from the trend with a large positive value of 682.1 ppm. With the exception of S_0//T_1, $C_3H_3{}^-$ has far closer agreement between the different model chemistries.

According to B3LYP, both species behave as expected under Baird's rule: $C_3H_3{}^+$ is aromatic in the S_0 and antiaromatic in the T_1 state, while $C_3H_3{}^-$ is antiaromatic in the S_0 and aromatic in the T_1 state. The overall agreement among hybrid functionals is good, with MP2 producing inconsistent extremes, especially in S_0//T_1 state. An 'aromatic presenting' S_0//T_1 $C_3H_3{}^-$ is due to computational limitations locating a higher singlet state due to the geometry changes.

9.5 $\mathrm{n} = 4$

The two π-electron S_0 state of $C_4H_4{}^{2+}$ has four identical bond lengths of 1.423 Å and is expected to be aromatic in its singlet ground state. All model chemistries support this, with negative NICS(0) values: B3LYP (−7.0 ppm), MP2 (−6.5 ppm), M06 (−7.8 ppm), M06-2X (−5.1 ppm), CAM-B3LYP (−6.7 ppm), HF (−8.9 ppm), and PBE0 (−7.2 ppm). The greater in magnitude NICS(1) values (−14.8 ppm for B3LYP) than the NICS(0) values are a result of the 'puckered' C_{2h} geometry, placing the NICS(1) sites closer to some nuclei than the NICS(0) location. The shielding plot in Figure 51 can be considered aromatic as well, although the close proximity of each atomic centre to bonds raises the possibility of the shielding regions of the single bonds overlapping to create an enclosed surface. The non-planarity of the molecule also weakens the case for aromaticity, but on balance, the molecule does appear to be weakly aromatic.

Vertical excitation produces an antiaromatic molecule, with a magnetically deshielded region expanding outwards from the centre and encompassing all C–C bonds, with high NICS(0) and NICS(1) values of 265.2 and 308.1 ppm, respectively. Most methods yield large positive values indicative of strong deshielding with NICS(0) values: HF (160.5 ppm), MP2 (363.5 ppm), CAM-B3LYP (327.3 ppm), PBE0 (251.3 ppm), and especially M06 (919.2 ppm). In contrast, M06-2X gives a negative value (−99.4 ppm), inconsistent with the others and most likely incorrect.

The optimised T_1 structure resembles cis-buta-2,3-diene more than cyclobutadiene, with C–C bond lengths of 1.347, 1.453 and 2.036 Å. This geometry prevents an antiaromatic state with NICS(0) and NICS(1) values of −2.1 and −1.9 ppm, respectively, showing the molecule is nonaromatic. The shielding plot offers further details, the σ-bonds are quite weak, with only slight shielding at +16 ppm. The shielding does not extend over the carbon centres themselves, suggesting the weakness of the bonds. The deshielded ovoids around the nuclei are clearly visible here, whilst they are often obscured in other plots. There are no significant discrepancies with other methods, with NICS(0) values: MP2 (0.3 ppm), M06 (−1.0 ppm), M06-2X (0.4 ppm), CAM-B3LYP (−2.0 ppm), HF (−2.7 ppm), and PBE0 (−2.1 ppm).

The vertical de-excitation results in a large deshielded region encompassing the molecule, whilst the shielding ring perpendicular to the molecule encompasses the 2.036 Å separated carbons, and an in-plane shielded region beneath the double-bonded carbons. NICS(0) and NICS(1) vary significantly, being 129.0 and 18.0 ppm, respectively, but both lie within the deshielded region. The $\sigma_{\text{iso}}(\mathbf{r})$ highlights the highly unstable nature of this state, with high electron density outside the molecule. However, there is dramatic disagreement among the methods. The B3LYP NICS(0) value is supported by M06 (102.9 ppm), and M06-2X (14.0 ppm) indicates some deshielding, while CAM-B3LYP (−129.1 ppm), PBE0 (−670.9 ppm), and MP2 (−115.1 ppm) yield large negative values. The method-dependent sign change implies the magnetic response is particularly sensitive to the model chemistry at distorted geometries.

In the S_0 state, the Hückel antiaromatic C_4H_4 has D_{2h} symmetry with clear alternating double and single bonds, as discussed above. This is supported by large positive NICS(0) values from all methods: B3LYP (27.2 ppm), MP2 (26.9 ppm), M06 (26.8 ppm), M06-2X (31.9 ppm), CAM-B3LYP (27.7 ppm), HF (27.0 ppm), and PBE0 (27.4 ppm). The B3LYP shielding isosurface displays a vertical column of deshielding through the ring, characteristic of antiaromaticity. Shielding along the ‘double-bonds’ highlights they are stronger than the single bonds.

Upon vertical excitation, the structure changes to a nonaromatic, with each C–C bond shielded, but the shielding region does not approach the centre to create a ‘doughnut’-shaped ring. The NICS(0) and NICS(1) values consolidate the assertion that the molecule is nonaromatic, at 2.1 and −5.0 ppm, respectively. Other methods do not disagree, with NICS(0) values similar at: MP2 (3.1 ppm), M06 (2.1 ppm), M06-2X (4.5 ppm), CAM-B3LYP (2.4 ppm), HF (−1.9 ppm), and PBE0 (1.6 ppm).

Relaxing the geometry in the T_1 state causes bond lengths to equalise to 1.438 Å, as expected by Baird's rule, and shift to weak aromaticity in the NICS(0) and NICS(1) values of −1.5 and −6.5 ppm, respectively. The former still indicates nonaromaticity and the latter is at most weakly aromatic. The shielding plot itself indicates a loss of coherent magnetic structure but the planar D_{4h} geometry suggests aromaticity. This does not appear to be model chemistry dependant since other methods have NICS(0) values of MP2 (−0.6 ppm), M06 (−1.6 ppm), M06-2X (0.4 ppm), CAM-B3LYP (−1.3 ppm), HF (−5.4 ppm), and PBE0 (−2.0 ppm), whilst other aromatic indicators such as HOMA suggest the same.[243]

Similar to $C_3H_3^-$, a vertical de-excitation of C_4H_4 produces far greater shielding than at the ground state optimal geometry. The C–H bonds are non-shielded, which may indicate why this structure is less stable than the D_{2h} structure. Just like $C_3H_3^-$, this is a computational artifact where the computation links this geometry to a higher singlet state. Care must be taken when interpreting these shielding plots and NICS values. Unstable molecules can have extremely well-shielded rings, yet are unstable. C_4H_4, with an S_0 electron configuration but the T_1 optimal geometry, has a well-shielded centre, however C–H bonds are unshielded. But by reducing the shielding threshold to ±15 ppm, a slightly deshielded region is visible around the outside of the molecule. Reducing the threshold to ±10 ppm, shows the formation of a complete loop of deshielding around the molecule, which would not be present in aromatic molecules. The NICS(0) values all suggest the calculations have produced a higher singlet excited state, with: B3LYP (−344.4 ppm), MP2 (−1398.7 ppm), M06 (−467.7 ppm), M06-2X (−172.6 ppm), CAM-B3LYP (−295.1 ppm), HF (−418.7 ppm), and PBE0 (−346.7 ppm).

Adding a further two electrons to the ground state structure yields a system close to aromaticity, although there are two bond lengths, 1.471 and 1.491 Å, these bond lengths are similar, but much closer to a single bond in length than a bond with and additional π-system. The NICS(0) and NICS(1) of −58.8 and −27.5 ppm, respectively, indicate high electron delocalisation as well as the shielding surface encompassing the centre of the molecule. However, the deshielded regions alongside each hydrogen are not characteristic of an aromatic system. Although electron delocalisation is high, the lack of H atom shielding suggests the molecule is unstable. NICS(0) of: M06 (−12.7 ppm), M06-2X (−12.7 ppm), CAM-B3LYP (−53.0 ppm), HF (−31.8 ppm), and PBE0 (−20.5 ppm) indicate shielding consistent B3LYP, but MP2 gives a strongly positive value (31.2 ppm), contrary to the rest.

Vertical excitation creates a shielding similar to S_0 C_4H_4, with deshielding in the centre of the plot in Figure 51 and NICS(0) values across all methods: B3LYP (28.0 ppm), MP2 (35.8 ppm), M06 (31.8 ppm), M06-2X (55.0 ppm), CAM-B3LYP (28.9 ppm), HF (20.9 ppm), and PBE0 (27.2 ppm) suggesting antiaromatic character.

Relaxing in the T_1 state reduces the symmetry from C_{2h} to C_s, as three hydrogens bend out-of-plane in the opposite direction to the other. The relaxation elongates both bonds and increases the separation between bond lengths, but the impact is not very pronounced, only increasing bond lengths to 1.509 and 1.534 Å, respectively. The shielding does not form a 'doughnut'-shape with shielding failing to create a loop near one carbon centre. The B3LYP NICS(0), NICS(+1) and NICS(−1) are −4.6, −7.3 and 2.1 ppm, respectively. The other model chemistries yield similar results. Given the close proximity of the centres, NICS(+1) is most likely not indicating aromaticity, and the molecule is nonaromatic overall.

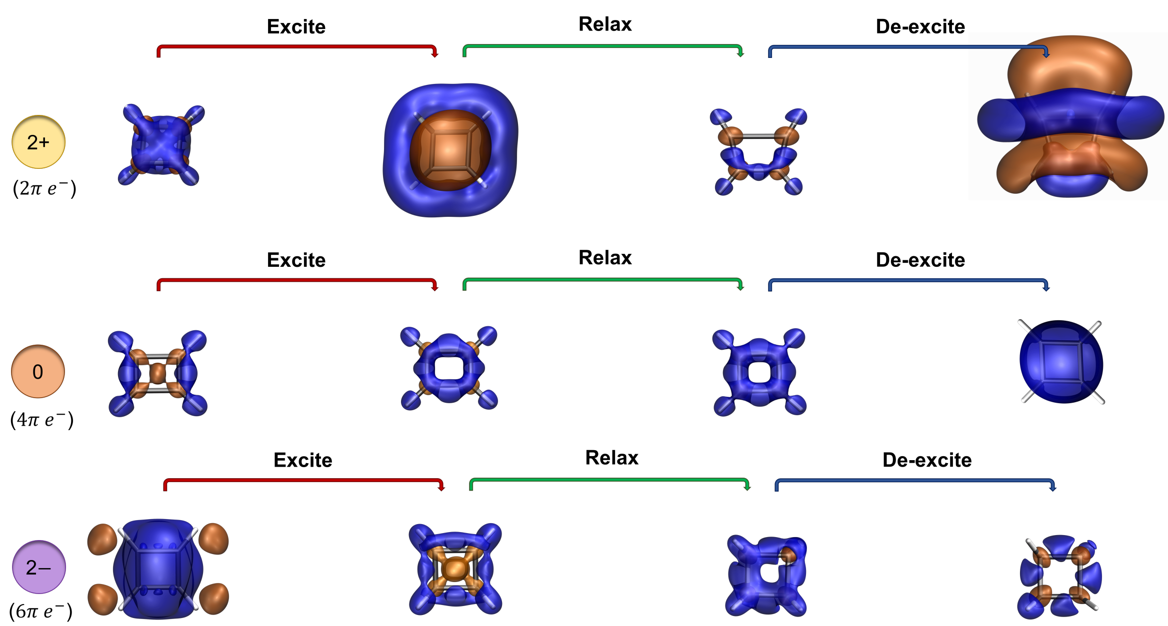

Figure 51: The shielding of $C_4H_4{}^{2+}$ (top), C_4H_4 (middle) and $C_4H_4{}^{2-}$ (bottom) starting from the $S_0//S_0$ state, vertically exciting to $T_1//S_0$, adiabatically relaxing to $T_1//T_1$ and vertically de-exciting to $S_0//T_1$.

The vertical de-excitation shifts the molecule to very weak antiaromaticity, with NICS(0), NICS(+1) and NICS(−1) of 10.6, 3.8 and 11.3 ppm, respectively. Although no deshielding is present on the isosurface plot at +16 ppm, there is a lack of internal shielding along the C–C bonds, which also alludes to antiaromaticity. Poor H atom shielding supports this further. For $S_0//T_1$, most methods report small positive values: M06-2X (3.2 ppm), CAM-B3LYP (9.0 ppm), HF (9.1 ppm) and PBE0 (4.5 ppm), but M06 yields a much larger value of 87.9 ppm, while MP2 gives a strongly shielded result of −44.6 ppm, again suggesting MP2 is the least reliable.

Overall, the C_4H_4 series demonstrates the sensitivity of NICS results to both geometry and method. The dication and dianion exhibit aromaticity in the singlet state and a breakdown in the triplet, while neutral

C_4H_4 follows the opposite trend, in agreement with Baird's rule. However, structural distortions and the extreme behaviour of certain methods (particularly MP2) make conclusions more questionable.

9.6 $\mathrm{n = 5}$

Expanding to five-membered carbon rings, shielding can be more easily compared to benzene due to the similar ring sizes. $C_5H_5^+$ has two bonds of length 1.342 and 1.445 Å, and one of 1.571 Å in the lowest energy singlet state. This generates a system of bonds that could be classified as double, delocalised and single, all within the same ring. The bond length alternation in the four π electron system suggests this is an antiaromatic system. This is perfectly illustrated in Figure 52 with a large deshielded region expanding from the centre and minor shielding at the periphery. This external shielding does not encompass the single bond, similar to cyclobutadiene. The deshielding is even more pronounced, extending far out of the plane. The antiaromaticity is supported by the NICS(0) and NICS(1) values of 87.2 and 66.5 ppm, respectively. MP2 (72.6 ppm), M06 (74.5 ppm), M06-2X (100.3 ppm), CAM-B3LYP (87.4 ppm), HF (47.2 ppm), and PBE0 (86.6 ppm) all correctly identify antiaromaticity.

Due to the lower energy of the lowest triplet state compared to lowest singlet (see the 9.1 Relative Energies), transferring to the lowest triplet state is technically a vertical de-excitation and yields NICS(0) and NICS(1) values of -1.6 and -9.3 ppm, respectively. The $\sigma_{\text{iso}}(\mathbf{r})$ plot demonstrates the structure is more stable, however, .the central void of the toroidal shielding region is too wide and not symmetrical enough to suggest the system is aromatic. MP2 (-9.9 ppm), M06 (-9.4 ppm), M06-2X (-9.5 ppm), CAM-B3LYP (-9.4 ppm), HF (-10.2 ppm), and PBE0 (-9.4 ppm) all concur that the triplet state disrupts the antiaromatic character, in agreement with Baird's rule, which predicts aromatic stabilisation for 4 π electron systems in the lowest triplet state.

Relaxation of the T_1 state equalises all bond lengths to 1.420 Å, shifting from C_{2v} to D_{5h} symmetry. This yields a more aromatic system with a cylindrical non-shielded region in the centre of the molecule. The NICS(0) and NICS(1) values do not change significantly, adjusting to -2.1 and -9.9 ppm, respectively. The hydrogen atoms are shielded, but the C–H bonds are not. The methods M06 (-10.0 ppm), M06-2X (-10.0 ppm), CAM-B3LYP (-9.9 ppm), HF (-10.0 ppm), and PBE0 (-10.0 ppm) better highlight the aromaticity in system. It should be noted that the MP2 calculation did not complete.

Vertical excitation back to a singlet state creates an extremely well-shielded carbon ring, with B3LYP NICS(0) and NICS(1) -63.1 and -63.8 ppm. The similarity of these values indicates the uniformity of the shielding in the molecule. There is still an absence of shielding along the C–H bonds and some H atoms are very poorly shielded, which indicates why the structure is not optimal. This once again corresponds to a higher singlet state. The other DFT methods also produce strongly negative NICS(0) values: M06 (−70.2 ppm), M06-2X (−58.5 ppm), CAM-B3LYP (−61.9 ppm), and PBE0 (−64.4 ppm) consistent with strong shielding. HF gives an even more extreme value of −148.9 ppm. However, MP2 returns a positive NICS(0) of 36.9 ppm, which is in disagreement with all others, but is still less antiaromatic than MP2 predicts at the optimal geometry so MP2 supports the incorrect indication of the other models that this geometry is more stable.

As would be expected, S_0 $C_5H_5^-$ is aromatic, having the same number of delocalised π electrons as benzene, with five equal bond lengths of 1.411 Å and D_{5h} symmetry. Whilst these bond lengths are longer than benzene's, the shielding is very aromatic, the B3LYP isosurface exhibits a continuous, symmetrical torus of shielding above and below the ring, indicative of strong aromaticity with just a small hole in the 'doughnut-shaped' isosurface. The NICS(1) value is similar to benzene's at −9.4 ppm, but NICS(0) is greater at −12.0 ppm. This is in contrast to magnetic susceptibility and current density studies in which $C_5H_5^-$ is less aromatic than benzene.[244] Regardless, despite its charge, this is a very stable molecule, with the relative energy per CH unit only 1.1 kcal mol^{-1} greater than the benzene energy. All model chemistries give consistently negative NICS(0) values: B3LYP (−12.0 ppm), MP2 (−12.2 ppm), M06 (−12.1 ppm), M06-2X (−12.0 ppm), CAM-B3LYP (−11.7 ppm), HF (−13.6 ppm), and PBE0 (−12.4 ppm).

Upon excitation, $C_5H_5^-$ becomes antiaromatic, as signified by the intense column of deshielding perpendicular to the ring plane at the molecular centre. There are strong similarities between this plot and S_0 $C_5H_5^+$ which nicely demonstrates Baird's rule. The NICS values suggest greater antiaromaticity; NICS(0) and NICS(1) are 92.3 and 76.7 ppm, respectively. The external shielding is greater than S_0 $C_5H_5^+$, particularly around the top hydrogen, where shielding is so expansive that it connects to the other shielding sections. This could be due to the geometry as unlike S_0 $C_5H_5^+$, the bond lengths are shorter and equal. In particular, the shorter bond at the bottom of the molecule brings the two sides of the molecule closer together, allowing greater shielding. The DFT methods: M06 (77.2 ppm), M06-2X (156.8 ppm), CAM-B3LYP (72.8 ppm), and PBE0 (57.6 ppm) all predict large deshielding, implying antiaromatic character, consistent with Baird's rule. HF gives a small negative value (−5.0 ppm) and the MP2 calculation once again failed to complete.

An adiabatic relaxation removes the antiaromaticity. There are two single bonds (1.509 Å) located next to each other and two 1.400 Å bonds separated by a 1.432 Å bond. All of these bonds are longer than the delocalised bonds in benzene, which indicates this system is close to nonaromatic. The NICS(0) values: B3LYP

(3.8 ppm), MP2 (−0.3 ppm), M06 (3.8 ppm), M06-2X (3.8 ppm), CAM-B3LYP (3.5 ppm), HF (−1.1 ppm), and PBE0 (2.2 ppm) confirm this. Instead of a cylindrical hole in shielding or a deshielded centre, shielding is very much concentrated along the C–C bonds creating a 'star-shaped' hole in the shielding at the molecular centre. The molecule's stability is further exemplified by the strong shielding along C–H bonds.

A vertical de-excitation returns the molecule to aromaticity, although not quite as strong as in the optimised geometry. The 'hole' in the 'doughnut'-shaped shielded region is slightly larger and C–H bonds, although still shielded well, are less shielded than at the optimised geometry. This expected behaviour is supported across all model chemistries: B3LYP (−5.4 ppm), MP2 (−8.6 ppm), M06 (−8.1 ppm), M06-2X (−8.4 ppm), CAM-B3LYP (−8.1 ppm), HF (−8.3 ppm), and PBE0 (−8.4 ppm).

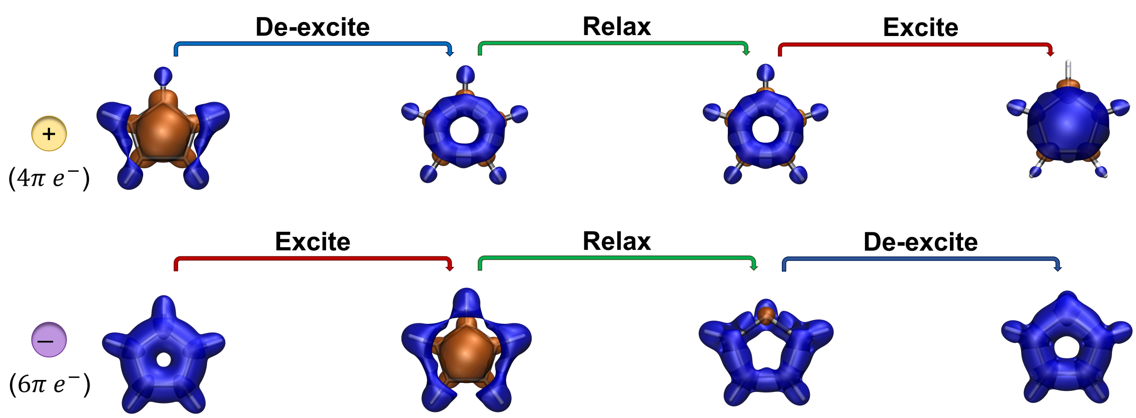

Figure 52: The shielding of $C_5H_5^+$ (top), $C_5H_5^-$ (bottom) starting from the $S_0//S_0$ state, vertically exciting to $T_1//S_0$, adiabatically relaxing to $T_1//T_1$ and vertically de-exciting to $S_0//T_1$.

Overall, the C_5H_5 ions display the most important behaviours of these annulenes. The anion is aromatic and becomes antiaromatic upon vertical excitation, illustrating Baird's rule perfectly. Relaxation removes this antiaromaticity to create a nonaromatic molecule. The cation is antiaromatic and becomes nonaromatic with excitation, but relaxation does not change the aromatic nature of the molecule significantly. The de-excitation then shows large internal shielding in a sub-optimal geometry, compared to a deshielded region in the optimal geometry as the computation utilises a higher singlet state. Results across functionals are in broader agreement than other molecules investigated but MP2 continues to be the most unreliable method.

9.7 $n = 6$

$C_6H_6{}^{2+}$ has alternating C–C bond lengths of 1.388 and 1.456 Å, suggesting an antiaromatic system in the lowest energy singlet state as predicted by Hückel's rule. The molecule is very unstable, with the second highest CH unit energy among the annulenes, being 41.7 kcal mol^{-1} greater than benzene. The shielding plot is quite empty and featureless compared to the other annulenes, with many non-shielded regions, particularly along the two 1.456 Å C–C bonds. Although the hydrogens are themselves shielded, not all C–H bonds are, only the 1.388 Å bonds are visibly shielded. The NICS values point to some antiaromaticity: B3LYP (10.9 ppm), M06 (10.9 ppm), M06-2X (13.1 ppm), CAM-B3LYP (11.5 ppm), HF (11.1 ppm), PBE0 (10.8 ppm), and MP2 (12.3 ppm) all predict weakly antiaromatic character.

Given the lower energy of the singlet state (see Section 9.1), transferring an electron to form a triplet represents a vertical de-excitation, and shifts the molecule towards aromaticity, with NICS(1) of −8.5 ppm. However, the NICS(0) value only shifts to nonaromatic character across all model chemistries: B3LYP (−2.0 ppm), M06 (−1.8 ppm), M06-2X (−0.3 ppm), CAM-B3LYP (−1.5 ppm), HF (−1.8 ppm), PBE0 (−1.9 ppm), and MP2 (−0.7 ppm). The B3LYP shielding plot resembles a that generated from nonaromatic magnetic response, with shielding mainly restricted to the C–C bonds and not the characteristic aromatic 'doughnut'-shaped hole in the shielding.

Relaxation equalises the bond lengths to 1.420 Å, which would normally suggest an aromatic structure. However, the shielding changes very little; B3LYP NICS(0) and NICS(1) become −1.3 and −8.6 ppm, respectively. The shielding around the carbon ring does more closely resemble a 'doughnut-shape', but the hole is still very large. C–H bonds also lack shielding and high CH unit energy demonstrates instability. This is also an annulene which is slightly more stable in the optimised T_1 than the ground state, the CH units are 0.1 kcal mol^{-1} lower in energy. A higher level of theory would be required to confirm this conclusively. The other model chemistries: M06 (−1.3 ppm), M06-2X (0.2 ppm), CAM-B3LYP (−1.0 ppm), HF (−2.1 ppm), PBE0 (−1.2 ppm), and MP2 (−0.2 ppm), yield NICS(0) values similar to B3LYP.

Further comparisons to $C_5H_5^+$ can be drawn when $C_6H_6{}^{2+}$ vertically returns to lowest energy singlet state (in what is vertical excitation). The ring becomes so well-shielded that there isn't even a hole in the centre of the shielding plot. The C–H bonds have weak shielding, but still more than the optimised geometry. NICS(0) values across all model chemistries: B3LYP (−47.7 ppm), M06 (−58.2 ppm), M06-2X (−46.7 ppm), CAM-B3LYP (−44.9 ppm), HF (−153.0 ppm), PBE0 (−48.3 ppm), and MP2 (−166.6 ppm) confirm this extreme shielding. As with previous cases, this shielding corresponds to an electronically excited singlet state.

Benzene, the neutral six-membered ring, is the prototypical aromatic system, with uniform bond lengths of 1.390 Å and planar D_{6h} symmetry. The shielding is highly symmetrical, producing a toroidal region of aromatic ring current above and below the molecular plane. B3LYP gives NICS(0) and NICS(1) values of −7.6 and −10.2 ppm, respectively. This shielding is reflected consistently across all other model chemistries: MP2 (−7.6 ppm), M06 (−7.6 ppm), M06-2X (−7.0 ppm), CAM-B3LYP (−7.5 ppm), HF (−9.3 ppm), and PBE0 (−7.7 ppm). These results confirm the archetypal aromaticity of benzene, which all methods agree upon quantitatively.

Vertical excitation of C_6H_6 to the lowest triplet state while retaining the singlet geometry produces a dramatic reversal in magnetic response. The aromatic ring current is replaced by a strongly deshielded central region. As with many other annulenes, before relaxation, the symmetry of the isosurface is different to that of the molecule as a whole, as the isosurface exhibits the symmetry of the triplet wavefunction, not optimal the ground state structure. This behaviour is predicted across all methods: NICS(0) values are: 107.1 ppm (B3LYP), 111.1 ppm (M06), 127.5 ppm (M06-2X), 90.4 ppm (CAM-B3LYP), 38.4 ppm (HF), 92.6 ppm (PBE0), and 65.6 ppm (MP2). These large positive values are consistent with strong antiaromaticity, in agreement with Baird's rule, which predicts triplet-state antiaromaticity for 6π electron systems.

The relaxation does reduce antiaromaticity, as the deshielded region in the centre contracts in size and there is greater shielding on the periphery. Four C–C bonds of length 1.382 Å are partially shielded whilst two of 1.515 Å in length are not. Whilst the latter is of a single bond length, the former is far closer to the delocalised bonds in the ground state. The system becomes antiaromatic and is similar to cyclobutadiene. NICS(0) values are 31.1 ppm (B3LYP), 31.4 ppm (M06), 36.6 ppm (M06-2X), 27.2 ppm (CAM-B3LYP), 11.7 ppm (HF), 28.1 ppm (PBE0), and 24.7 ppm (MP2).

Vertical de-excitation to the singlet state at the T_1 geometry ($S_0//T_1$) results in restoration of aromaticity, with NICS(0) values returning only slightly lower in magnitude than those of the original geometry: B3LYP (−7.4 ppm), M06 (−7.3 ppm), M06-2X (−6.8 ppm), CAM-B3LYP (−7.4 ppm), HF (−9.1 ppm), PBE0 (−7.5 ppm), and MP2 (−7.4 ppm). The shielding plot is also similar to benzene, with slightly less shielding along C–H bonds and a wider hole in the centre of the ring.

S_0 ${C_6H_6}^{2-}$ should be antiaromatic according to Hückel, with eight π electrons. Alternating bond lengths of 1.363 and 1.490 Å support this however the shielding suggests the structure is far closer to aromaticity. Whilst NICS(0) and NICS(−1) are −4.1 and −4.7 ppm, respectively (suggesting nonaromaticity); NICS(+1) at location inside the bowl-shaped molecule is −10.0 ppm. Whilst the C_{2v} geometry elongates the 'doughnut-shaped' hole, the plot clearly illustrates the molecule is not antiaromatic. Additionally, C–H bonds are remarkably well shielded. The other model chemistries suggest even greater aromaticity: M06 (−9.0 ppm), M06-2X (−10.4 ppm), CAM-B3LYP (−9.6 ppm), HF (−14.1 ppm), PBE0 (−10.5 ppm), and MP2 (−10.6 ppm).

Vertical excitation shifts the molecule to comfortably nonaromatic, compared to the aromatic tendencies S_0 shielding. The B3LYP shielding does not extend far into the carbon ring, instead being localised on the C–C bonds. The C–H bonds remain well shielded. The NICS(0), NICS(+1) and NICS(−1) all become nonaromatic as well, assuming the values −0.9, −5.5 and −0.5 ppm, respectively. Vertical excitation to T_1 produces mixed magnetic responses. Other NICS(0) values at $T_1//S_0$ are: M06 (−1.9 ppm), M06-2X (−5.6 ppm), CAM-B3LYP (−6.3 ppm), HF (0.1 ppm), PBE0 (−6.0 ppm), and MP2 (5.4 ppm), suggesting a range of aromatic characterisations.

Similarly to $C_4H_4{}^{2-}$, upon relaxation these bond lengths do not equalise, however are close at 1.431 and 1.442 Å, which could indicate some aromatic character. However, NICS(0), NICS(+1) and NICS(−1) are 7.4, −1.6 and −0.2 ppm, respectively, suggesting a nonaromatic molecule. The shielding is very localised to C–C bonds and does not extend into the molecular centre, suggesting little delocalisation. This relaxed structure also appears to have weaker C–H bonds than its unrelaxed counterpart. PBE0 (5.2 ppm) agrees with the nonaromatic characterisation of B3LYP, yet the other methods M06 (−16.8 ppm), M06-2X (−7.0 ppm), CAM-B3LYP (−8.9 ppm), HF (−10.9 ppm), and MP2 (−9.0 ppm) suggest aromaticity, which is in better agreement with Baird's rule. The reason for the discrepancy between B3LYP and PBE0 with the other model chemistries is not known, but possibly indicates an issue with magnetic shielding describing charged systems in excited states.

After a vertical de-excitation, the molecule is more aromatic according to the shielding plot than the optimal S_0 geometry. With a smaller, symmetrical 'doughnut-shaped' hole and strong C–H bond shielding, it is difficult to justify why this structure is not optimal for $C_6H_6{}^{2-}$. The shielding according to NICS, is greater than benzene at −10.7, −13.9 and −12.1 ppm, respectively. Other model chemistries provide consistently more negative values than they predicted at a more optimal geometry: M06 (−10.6 ppm), M06-2X (−17.7 ppm), CAM-B3LYP (−18.2 ppm), HF (−19.0 ppm), PBE0 (−10.9 ppm), and MP2 (−28.8 ppm), reinforcing the notion that the shielding once again corresponds to a higher singlet state. $C_6H_6{}^{2-}$is also interesting, as the optimal geometries have very similar CH unit energy, 13.7 and 14.1 kcal mol^{-1} for the relaxed S_0 and T_1 states, respectively, which indicates the structure is quite unstable. The shielding picture of the molecule is misleading overall, as benzene is so similar yet so much more stable. A six-membered carbon ring can achieve the optimal sp^2 hybridized orbitals, with a 120° bond angle, but this T_1 structure buckles with

C_{2v} symmetry. Anions are naturally more unstable as they attempt to lose electrons. Nevertheless, the shielding disagrees significantly with Hückel's rule and warns of how these rules oversimplify many bonding interactions. Unlike other sub-optimal structures, C–H bonds and H atoms are well-shielded; shielding is not concentrated far from the molecule and there is little deshielding around the molecule when the iso-surface threshold is decreased, which makes the shielding harder to identify as belonging to a higher singlet state without also inspecting the excitation energies.

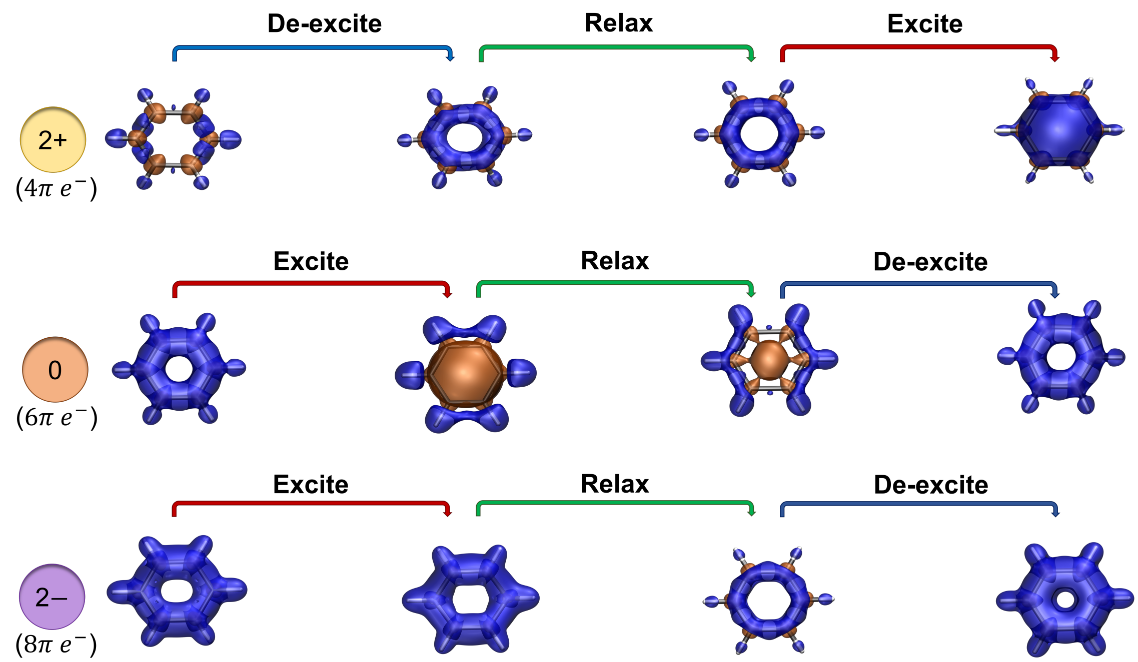

Figure 53: The shielding of $C_6H_6{}^{2+}$ (top), C_6H_6 (middle) and $C_6H_6{}^{2-}$ (bottom) starting from the $S_0//S_0$ state, vertically exciting to $T_1//S_0$, adiabatically relaxing to $T_1//T_1$ and vertically de-exciting to $S_0//T_1$.

In conclusion, C_6H_6 behaves as expected: it is aromatic in S_0 and antiaromatic in T_1, in agreement with Hückel's and Baird's rules. The ions show greater model chemistry dependence and shielding results from the dianion is particularly at odds with known rules.

9.8 n = 7

$C_7H_7^+$ not only shares the same number of π-electrons as benzene but it also has a very similar bond length of 1.391 Å. The $\sigma_{iso}(\mathbf{r})$ plot in Figure 56 displays aromaticity; there is a circular 'doughnut-shaped' hole, and although it is quite large, this is a consequence of the increasing ring size. NICS(0) and NICS(1) values of −6.0 and −9.4 ppm, respectively indicate aromaticity as well, albeit weaker than benzene. The shielding along C–H bonds is also weaker, indicating some instability. To the contrary, Fowler and Steiner,[244] found $C_7H_7^+$ to be more aromatic than benzene, with both the π current density and magnetic susceptibilities. They also acknowledge that NICS measurements agree with our ordering. That being said, use of other computational methods, including MP2 (−9.4 ppm), M06 (−9.4 ppm), M06-2X (−9.2 ppm), CAM-B3LYP (−9.4 ppm), HF (−10.3 ppm), and PBE0 (−9.4 ppm) does suggest $C_7H_7^+$ is more aromatic than benzene.

A vertical excitation yields a very antiaromatic molecule, a thick B3LYP shielded region is pushed far beyond the ring, not even starting until outside the hydrogen atoms, as a 'dumbbell-shaped' deshielded region extends above and below the molecular plane. The molecule should be antiaromatic in this state according to Baird, but most model chemistries yield results that are too extreme to be fully realistic. The NICS(0) values exaggerate the antiaromaticity, with values B3LYP (946.8 ppm), CAM-B3LYP (365.5 ppm), M06 (577.1 ppm), and PBE0 (411.1 ppm). To the contrary, M06-2X (−242.0 ppm) predicts the molecule is extremely aromatic. Neither MP2 nor HF completed the calculation.

A switch from D_{7h} symmetry to C_2 under relaxation removes a considerable amount of antiaromaticity in the molecule, reducing NICS(0) values: B3LYP (17.2 ppm), MP2 (17.1 ppm), M06 (17.2 ppm), M06-2X (20.0 ppm), CAM-B3LYP (16.1 ppm), HF (8.6 ppm), and PBE0 (16.7 ppm), making them all fairly consistent and reasonably antiaromatic. The new bond lengths of 1.391, 1.392, 1.419 and 1.470 Å further indicate antiaromaticity. As these structures get larger, bond alternation can become more irregular, as in this case. The bond lengths suggest a weakly antiaromatic system, since there is significant variation in bond length (hence antiaromatic); however, none are comparable to a double bond (so only weakly antiaromatic). There is a small 'horse-shoe' shaped region of deshielding in the molecule. This connects the C–C bond with the least shielding along it, namely the 1.470 Å bond. The other bonds are stronger so there is no visible deshielding. The C–H bonds are generally well shielded, apart from the C–H bond connected to a carbon with two 1.419 Å C–C bonds. Both of these areas of shielding indicate the correlation between weaker bonds and less shielding.

A vertical de-excitation creates a very weakly aromatic structure. The hole in the shielding resembles a polygon as electrons are restricted to single bonds instead of the delocalised ring. All model chemistries concur that the molecule is nonaromatic: B3LYP (−3.2 ppm), MP2 (−3.6 ppm), M06 (−3.0 ppm), M06-2X (−2.1 ppm), CAM-B3LYP (−3.1 ppm), HF (−4.0 ppm), and PBE0 (−3.1 ppm). Relaxation in this ground state is required to produce an aromatic structure.

$C_7H_7^-$ has bond lengths of 1.348, 1.392, 1.455 and 1.498 Å in its lowest energy singlet optimised geometry, signalling the antiaromatic structure predicted by Hückel for this eight π-electron system. This system is comparable to cyclooctatetraene, with its shortest bond approaching a double bond and largest a single. NICS(0) and NICS(1) values of 156.5 and 126.8 ppm, respectively support this analysis. The shielding has the C_2 symmetry of the molecule, producing an interesting plot in Figure 56. The shielding is exiled to the periphery, encompassing the entire molecule. Whilst not quite as extreme as B3LYP, MP2 (56.6 ppm), M06 (52.4 ppm), M06-2X (67.6 ppm), CAM-B3LYP (52.7 ppm), HF (36.0 ppm), and PBE0 (56.0 ppm) all also correctly suggest antiaromaticity.

The molecule has lower energy triplet energy than singlet (see 9.1 Relative Energies), so it is a vertical de-excitation to a triplet state permits a nonaromatic system, with B3LYP NICS(0) and NICS(1) values of −4.4 and −5.5 ppm, respectively. This is confirmed with the shielding plot, with a hole closer to a polygon than a circle, as electrons are localised along the C–C bonds. This demonstrates the 'desire' of the molecule to be aromatic but the strict bond alternation prevents an even sharing of electrons. Nevertheless, H atoms and C–H bonds are well-shielded. MP2 (−14.8 ppm), M06 (−9.0 ppm), M06-2X (−4.8 ppm), CAM-B3LYP (−6.0 ppm), HF (−3.6 ppm), and PBE0 (−5.7 ppm) all have NICS(0) values suggesting a shift to at least nonaromatic, but some suggest aromaticity even at this suboptimal geometry.

Relaxation equalises the C–C bonds to 1.409 Å, causing a more even shielding, revealing just a circular hole in the shielding plot. The consistent negative NICS(0) values: B3LYP (−9.7 ppm), M06 (−10.2 ppm), M06-2X (−10.1 ppm), CAM-B3LYP (−10.2 ppm), HF (−11.7 ppm), and PBE0 (−10.5 ppm). Whilst consistent with the others, MP2 (−10.0 ppm) is less aromatic than the suboptimal geometry, possibly due using the B3LYP optimised geometry instead of one optimised for MP2, or just the problems that MP2 appears to have for triplet states.

Vertical excitation to the lowest energy singlet state produces well shielded C–C bonds in B3LYP, yet the C–H bonds are poorly shielded. The hydrogen constituents are unshielded, and the regions between hydrogen atoms are deshielded significantly. This demonstrates that even simple annulenes are affected by their chemical environments, i.e. despite the enhanced electron delocalisation that this geometry could provide, the weakening of C–H bonds and the lower probability of electrons surrounding hydrogen atoms produces a less stable structure than the ground state geometry. The C–H bonds are important for the molecular geometry and structure. Overall, each model chemistry yields incredibly high magnitude NICS(0): B3LYP (−228.6 ppm), M06 (−246.0 ppm), M06-2X (−147.3 ppm), CAM-B3LYP (−218.9 ppm), PBE0 (−222.3 ppm) suggest strong shielding. HF gives a ridiculously large value of 3703.1 ppm, which has the opposite sign and hence opposite aromatic characterisation to the DFT methods. The MP2 calculation did complete, but no NICS(0) value was displayed in the output file. It is suspected that it was because the value was too large, with too many significant figures, since the NICS(1) values were computed at an unphysical 94144.6 ppm, making this the most extreme value recorded in this thesis.

Overall, both ions follow Baird's rule: $C_7H_7{}^+$ begins antiaromatic and becomes aromatic in the triplet; $C_7H_7{}^-$ follows the reverse trend. There is better consistency between the DFT methods than some of the other annulenes investigated, yet HF and particularly MP2 show poor reliability with extremely large and unphysical magnetic response.

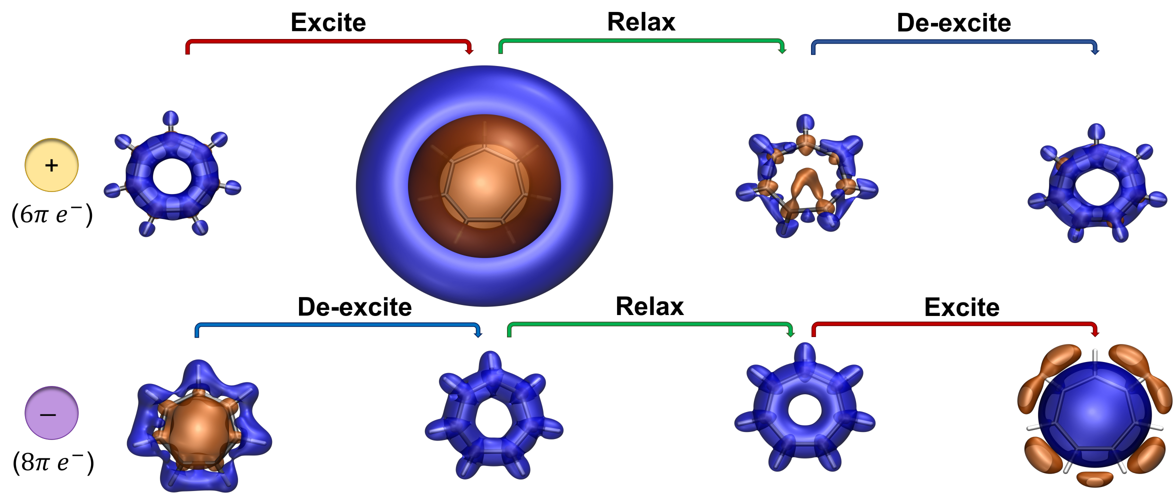

Figure 54: The shielding of $C_7H_7{}^+$ (top) and $C_7H_7{}^-$ (bottom) starting from the $S_0//S_0$ state, vertically exciting to $T_1//S_0$, adiabatically relaxing to $T_1//T_1$ and vertically de-exciting to $S_0//T_1$.

9.9 $n = 8$

Aromatic S_0 $C_8H_8{}^{2+}$ has equal bond lengths of 1.403 Å, with NICS(0): B3LYP (−6.7 ppm), MP2 (−8.2 ppm), M06 (−8.1 ppm), M06-2X (−7.9 ppm), CAM-B3LYP (−6.5 ppm), HF (−7.5 ppm), and PBE0 (−7.9 ppm) suggesting aromaticity, particularly considering the increased ring size. The shielding indicates electron sharing; however, the shielding does not extend far into the centre, suggesting weaker aromaticity than benzene. C–H bonds are not well-shielded, suggesting instability in the structure.

A vertical excitation has deshielding expanding from the centre, emphasizing the 'Baird-style' aromaticity reversal in Figure 55. B3LYP (392.1 ppm), MP2 (555.3 ppm), M06 (577.1 ppm), M06-2X (538.2 ppm), CAM-B3LYP (365.5 ppm), HF (292.5 ppm), and PBE0 (514.5 ppm). NICS(0) values highlight the destabilisation in the molecule. Once again, these values are too large comparatively to be fully meaningful. The B3LYP shielding plot shows C–C bonds are all deshielded, whilst the hydrogen atoms remain well-shielded.

A relaxation reveals this extreme antiaromaticity is due to the D_{2d} geometry, and relaxing to D_2 yields a broadly nonaromatic structure. B3LYP (5.8 ppm), MP2 (3.6 ppm), M06 (3.5 ppm), M06-2X (3.4 ppm), CAM-B3LYP (2.3 ppm), HF (2.6 ppm), and PBE0 (3.1 ppm) are in good agreement, demonstrating that relaxation in the triplet reduces antiaromaticity but does not induce clear aromaticity. The central deshielded region dissipates; some shielding is present around C–C bonds and H atoms are shielded, but C–H bonds are not. Optimised T_1 $C_8H_8{}^{2+}$ C–C bond lengths (1.383, 1.411 and 1.463 Å) show significant variation in size, yet are approximately positioned between delocalised C–C bonds in benzene and a single bond.

A vertical de-excitation remains definitively nonaromatic, but there is a slight shift towards greater shielding. The NICS(0): B3LYP (−1.1 ppm), MP2 (−0.9 ppm), M06 (−0.9 ppm), M06-2X (−1.0 ppm), CAM-B3LYP (−0.7 ppm), HF (−0.8 ppm), and PBE0 (−1.1 ppm) demonstrate this. Although the B3LYP shielding connects all C–C bonds, it is not uniform enough to be considered aromatic, and only relaxation in the ground state produces an aromatic system.

The infamously antiaromatic C_8H_8 has alternating bond lengths to prove it, at 1.334 and 1.467 Å. However, the 'single' C–C bond is considerably shorter than cyclobutadiene (1.567 Å). This could suggest that C_8H_8 is less antiaromatic than C_4H_4, but could also just be a consequence of the greater ring strain in C_4H_4. Unlike C_4H_4, there is no deshielding region visible in Figure 55; NICS(0) and NICS(1) are only 4.7 and 0.8 ppm, respectively. This is supported by previous CASSCF(8,8)-GIAO/6-311 + G*//CASSCF(8,8)-GIAO/6-31G* shielding plots, which revealed almost identical shielding for our D_{2d} geometry.[245] The NICS values at this CASSCF level are nonaromatic, at 1.2 (NICS(0)) and −1.6 ppm (NICS(1)). Our results are closer to previous computed MP2 calculations, 3.1 and −0.5 ppm, respectively.[54] Other methods confirm this minimal deshielding: MP2 (3.9 ppm), M06 (4.6 ppm), M06-2X (5.1 ppm), CAM-B3LYP (4.2 ppm), HF (2.7 ppm), and PBE0 (4.8 ppm), suggesting nonaromatic behaviour. It was also found that restricting the molecule to be planar with D_{8h} with CASSCF(8,8) yielded a far more antiaromatic system, with a large deshielded region expanding above and below the molecular plane. The $\sigma_{iso}(\mathbf{r})$ plot appears similar to our T_1//S_0 $C_9H_9{}^-$ result. The lower energy structure prevents this antiaromaticity as the shielding is localised along all C–C bonds, but not uniformly, as in the case of an aromatic system. Shorter C=C double bonds experience greater shielding than the longer C–C single bonds. Shielding is also present along C–H bonds and hydrogen atoms themselves, suggesting these are stable. The destabilising factor is that carbon–carbon bonds experience greater shielding outside the ring than inside.

To a certain extent, a Baird-style reversal occurs upon a vertical excitation, as shielding around C–C bonds is equal both inside and outside the ring. Shielding is much more abundant everywhere, including C–H bonds and the hydrogen atoms themselves. Nonaromatic NICS(0) shielding is consistent across all model chemistries: B3LYP (−3.2 ppm), MP2 (−3.2 ppm), M06 (−3.3 ppm), M06-2X (−2.4 ppm), CAM-B3LYP (−3.1 ppm), HF (−3.1 ppm), and PBE0 (−3.6 ppm).

Relaxing in the T_1 state yields D_{8h} symmetry with a 1.398 Å C–C bond length. Shielding extends uniformly towards the molecular centre and both NICS(0) and NICS(1) become −10.9 ppm, highlighting the aromaticity of the system. MP2 (−10.7 ppm), M06 (−10.5 ppm), M06-2X (−10.7 ppm), CAM-B3LYP (−10.9 ppm), HF (−12.3 ppm), and PBE0 (−11.1 ppm) all yield similar shieldings. The B3LYP shielding isosurface is almost identical to one generated at the CASSCF(8,8) level previously calculated.[245]

A vertical de-excitation to the ground state changes NICS(0) and NICS(1) to −106.6 and −90.0 ppm, respectively. The shielding could also be mistaken that the molecule is stable and aromatic since shielding encompasses all C–C bonds and extends to the molecular centre. However, the shielding extends above and below the molecular plane by many angstroms, meaning the electrons are not only delocalised within the carbon-ring, but are too delocalised from the molecule itself, increasing nuclear–nuclear repulsion forces. Additionally, lowering the magnitude of the threshold for the isosurface to just 10 ppm reveals deshielding regions outside of the C–C bonds, another destabilising factor. Hence, this molecule is less stable than at the ground state geometry. This once again corresponds to a higher singlet state, confirmed through a negative excitation energy. Other DFT methods yield similar results, with NICS(0) values: M06 (−121.0 ppm), M06-2X (−79.7 ppm), CAM-B3LYP (−98.5 ppm), and PBE0 (−104.6 ppm), but HF (−832.9 ppm) exaggerates this enhanced shielding. MP2 produces an anomalous result of 12434.7 ppm, extreme in magnitude and extremely antiaromatic, is not a trustworthy data point.

The 10 π-electron system $C_8H_8{}^{2-}$is aromatic in the ground state, with equal bond lengths of 1.412 Å. The shielding supports this, with NICS(0) and NICS(1) of −12.0 and −10.7 ppm, respectively. The shielding along C–C bonds is strong and uniform, giving the characteristic 'doughnut-shaped' hole in the shielding. C–H bonds are weakly shielded, along with the H atoms themselves. The greater shielding compared to $C_8H_8{}^{2+}$could be a result of the additional four electrons. This aromatic characterisation is confirmed across all methods: B3LYP (−12.0 ppm), MP2 (−11.8 ppm), M06 (−12.3 ppm), M06-2X (−11.8 ppm), CAM-B3LYP (−11.5 ppm), HF (−13.5 ppm), and PBE0 (−12.9 ppm). These values align closely and strongly support Hückel aromaticity.

After vertical excitation, the molecule undergoes a Baird-style aromatic reversal. The entire molecule is engulfed by deshielding, expanding beyond the molecular plane past the H atoms. There is a shielded region around the outside of the molecule, following the shape of the molecule. NICS(0) and NICS(1) are 90.1 and 74.1 ppm, respectively. This substantial deshielding: B3LYP (90.1 ppm), MP2 (54.4 ppm), M06 (66.5 ppm), M06-2X (54.5 ppm), CAM-B3LYP (84.2 ppm), HF (76.0 ppm), and PBE0 (61.8 ppm). This indicates antiaromatic destabilisation consistent with Baird's rule.

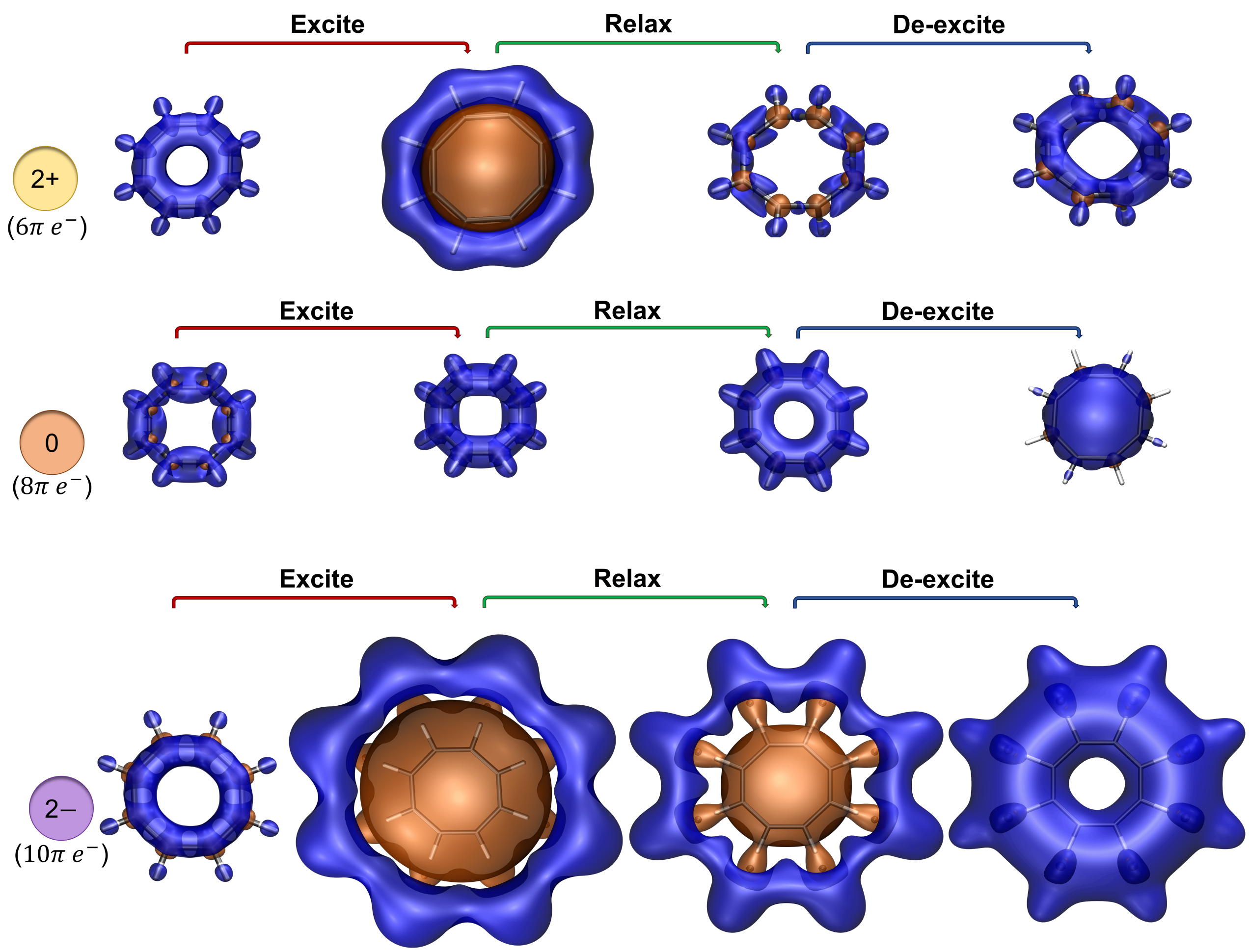

Figure 55: The shielding of $C_8H_8{}^{2+}$ (top), C_8H_8 (middle) and $C_8H_8{}^{2-}$ (bottom) starting from the $S_0//S_0$ state, vertically exciting to $T_1//S_0$, adiabatically relaxing to $T_1//T_1$ and vertically de-exciting to $S_0//T_1$.

Relaxation yields alternating bond lengths of 1.372 and 1.434 Å. Whilst the separation between these bonds is not comparable to cyclobutadiene, the shielding plot does demonstrate the T_1 state is very antiaromatic. The symmetry is only reduced from D_{4d} to D_{4h} and does not change significantly enough to produce a nonaromatic system. NICS(0) and NICS(1) are 32.9 and 26.3 ppm, respectively. Other model chemistries concur with NICS(0) values: MP2 (27.4 ppm), M06 (27.4 ppm), M06-2X (27.4 ppm), CAM-B3LYP (27.2 ppm), HF (25.6 ppm), and PBE0 (30.0 ppm). While these remain positive, they are significantly lower than the vertical excitation values. Shielding remains outside of the molecule, at a similar distance from the molecular centre in the molecular plane. The deshielding also still engulfs all C–C and C–H bonds, along with the area enclosed by the carbon ring. However, deshielding is reduced from the vertical excitation, as there is no deshielded isosurface at -16 ppm between neighbouring H atoms.

Vertical de-excitation removes deshielding along bonds and at the molecular centre. Shielding engulfs all bonds both C–C and C–H bonds, however, the shielding expands beyond the molecule, at a similar radius to the triplet state. There are unshielded ovoids just beyond all H atoms. The NICS(0) and NICS(1) values of -14.3 and -12.0 ppm, respectively are only moderately aromatic compared to the extent of shielding in the plot. The 'doughnut-shaped' hole in the shielding is not completely uniform, resembling more of a heavily-curved square. Despite the more negative NICS values and more abundant shielding regions in the shielding plot than the optimised ground state geometry; the vertical de-excited state is less stable as electrons are delocalised far outside of the molecule. It is assumed other model chemistries would produce similar values, with the NICS(0) values: MP2 (-12.0 ppm), M06 (-12.0 ppm), M06-2X (-12.0 ppm), CAM-B3LYP (-12.4 ppm), HF (-43.5 ppm), and PBE0 (-9.1 ppm), demonstrating robust reestablishment of aromatic ring current despite geometric distortion. HF in particular stands out as having higher magnitude shieldings than at the optimised ground state geometry.

9.10 $\mathrm{n} = 9$

$C_9H_9^+$ has C_2 symmetry, with five symmetry unique C–C bond lengths: 1.377, 1.388, 1.404, 1.412 and 1.419 Å. The bond length variation is moderate, so would traditionally be considered nonaromatic. It has previously been shown using a Heilbronner-style description,[246] that the orientation of the overlapping $2p_z$ rotates around the carbon ring, in such a way that they can be considered to form a Möbius strip. This has been confirmed previously, with both spin-coupled generalized valence bond (SCGVB) and CASSCF(8,9) calculations.[247] The shielding isosurface is therefore different from traditional aromatic systems, by not possessing a symmetrical 'doughnut'-shaped hole in the shielding. H atoms are shielded, but shielding along C–H bonds is weaker and non-uniform. Upon more careful inspection, the absence in shielding is curved near carbon centres, indicating electron sharing. The shielding pattern closely resembles that reported using CASSCF(8,9)-GIAO/6-311+G(d) calculations from ref. 248. This higher-level theory suggests a slightly more aromatic NICS(0) value of -14.1 ppm, than those from B3LYP (-12.0 ppm), MP2 (-12.6 ppm), M06 (-12.1 ppm), M06-2X (-11.7 ppm), CAM-B3LYP (-12.2 ppm), HF (-13.7 ppm), and PBE0 (-12.2 ppm) values computed in this chapter. Nevertheless, all values are very similar and indicate aromaticity.

A vertical excitation yields an antiaromatic molecule. B3LYP, for instance, gives a NICS(0) of 39.2 ppm, and other methods follow this trend: MP2 (20.5 ppm), M06 (37.6 ppm), M06-2X (54.4 ppm), CAM-B3LYP (30.2 ppm), HF (2.6 ppm), and PBE0 (34.0 ppm). These results indicate strong deshielding, consistent with Baird's rule. Higher level NICS(0) calculations at the CASSCF(8,9) level yield similar results at 42.2 ppm,[248] illustrating that this system can be described well in a variety of model chemistries.

Relaxation maintains the C_2 symmetry, but the range of C–C bond lengths is reduced, varying from just 1.395 to 1.402 Å, indicating greater aromatic character and the replacement of a Möbius π system with a traditional one. NICS(0) and NICS(1) transform to −9.5 and −10.1 ppm, respectively. Shielding along C–C bonds is uneven, and from a top view, electrons delocalise across some carbons but not others. However, the C_2 symmetry ensures carbons that appear to have localised bonds from one side of the molecule, have delocalised bonds on the other and vice versa. C–H bonds are not well shielded, reducing the stability of the structure. MP2 (−13.4 ppm), M06 (−9.5 ppm), M06-2X (−9.1 ppm), CAM-B3LYP (−9.4 ppm), HF (−10.0 ppm), and PBE0 (−9.5 ppm) are consistent and reflect enhanced stability through triplet aromaticity and geometric relaxation.

The vertical de-excitation yields an incredibly unstable molecule, with colossal shielding emanating from the centre. B3LYP gives an erratic and extreme value of −2784.9 ppm, with other functionals showing large magnitudes: M06 (−228.0 ppm), M06-2X (−136.5 ppm), CAM-B3LYP (−230.8 ppm), and PBE0 (−2028.0 ppm). These values imply that the $S_0//T_1$ geometry is highly unstable and poorly represented. HF (232.4 ppm) and MP2 (1213.5 ppm) are also large, but indicate strong shielding, suggesting an opposite (and likely incorrect) aromatic characterisation. The shielding plot emphasises that the DFT NICS values are misleading, with an enormous deshielded 'doughnut' region, comparable in thickness to the molecule itself.

$C_9H_9^-$ has equal bond lengths of 1.397 Å, close to those in benzene, highlighting the aromaticity in the symmetrical D_{9h} molecule, as expected by Hückel's rule, since this is a 10 π-electron structure. The H atoms, C–H bonds and C–C bonds are all well shielded. The characteristic 'doughnut'-shaped hole in the shielding is uniform, with highly aromatic and consistently negative NICS(0) values: B3LYP (−13.7 ppm), MP2 (−13.8 ppm), M06 (−13.8 ppm), M06-2X (−13.9 ppm), CAM-B3LYP (−13.8 ppm), HF (−15.1 ppm), and PBE0 (−13.9 ppm) suggesting the electron sharing is possibly greater than that in benzene.

The prominent aromaticity undergoes a Baird-style reversal when excited. The B3LYP deshielding expands from the centre to encompass all C–C bonds, extending many angstroms above and below the molecular plane. Shielding creates a halo in the molecular plane outside the carbon ring, which extends further to encompass H atoms. NICS(0) indicate deshielding across all model chemistries: B3LYP (94.5 ppm), MP2

(35.2 ppm), M06 (72.9 ppm), CAM-B3LYP (42.2 ppm), HF (14.1 ppm), and PBE0 (59.9 ppm). M06-2X predicts an extreme value of 2000.2 ppm, which is clearly unphysical.

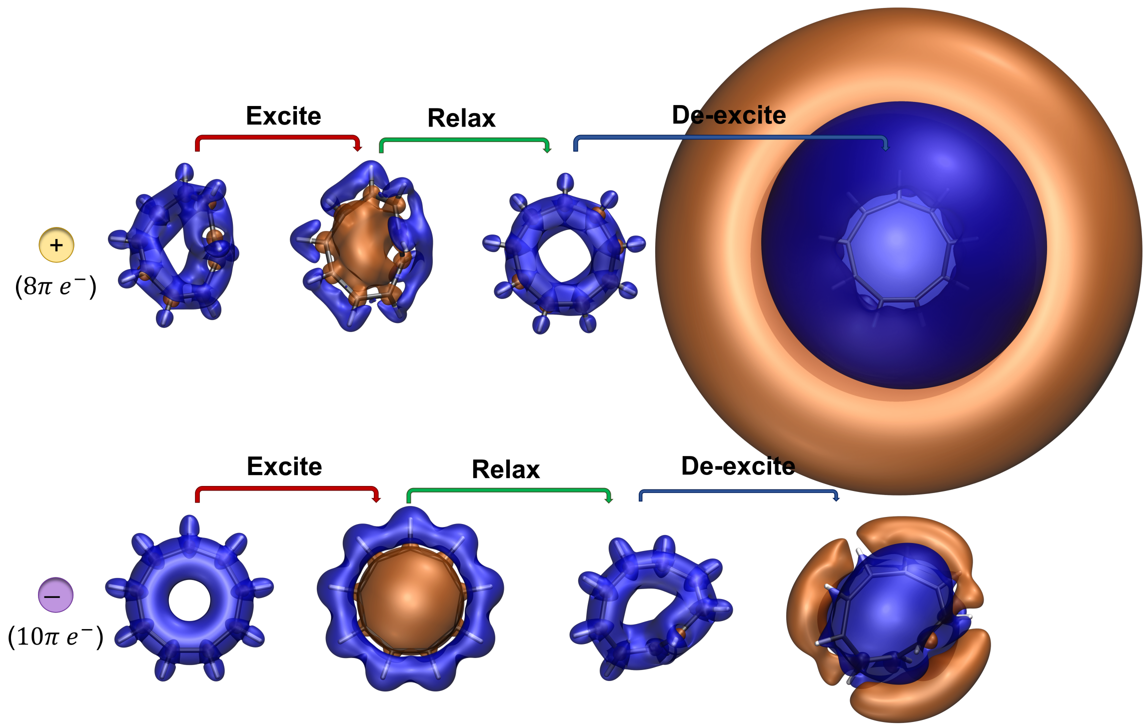

Figure 56: The shielding of $C_9H_9{}^+$ (top) and $C_9H_9{}^-$ (bottom) starting from the $S_0//S_0$ state, vertically exciting to $T_1//S_0$, adiabatically relaxing to $T_1//T_1$ and vertically de-exciting to $S_0//T_1$.

Bond lengths only vary slightly after relaxation, ranging from 1.400 to 1.417 Å, but the ring is very twisted and non-planar. The antiaromaticity is removed by the change in geometry, with localised shielding along C–C bonds. The NICS(0) values are all in good agreement: B3LYP (−11.0 ppm), MP2 (−20.6 ppm), M06 (−11.0 ppm), M06-2X (−10.9 ppm), CAM-B3LYP (−11.1 ppm), HF (−11.7 ppm), and PBE0 (−11.2 ppm). The structure is so twisted that this aromatic characterisation may be because the NICS probes are close to atoms and bonds, however, it is more likely that this is another example of a Möbius annulene.

De-excitation again generates highly variable results, all of extreme magnitude. NICS(0) of CAM-B3LYP (2036.7 ppm), M06 (952.7 ppm), MP2 (201.0 ppm) and HF (72.5 ppm) all suggest high deshielding whilst M06-2X (−579.6 ppm), B3LYP(−206.9) and PBE0 (−204.8 ppm) predict high shielding. However, from inspection of the B3LYP $\sigma_{\mathrm{iso}}(\mathbf{r})$ plot, although there is shielding in the centre, there is significant deshielding around the periphery, suggesting models predicting highly shielded NICS values are actually extremely unstable.

Both the cation and anion of C_9H_9 introduce Möbius aromaticity to the discussion, allowing reasonable aromatic characterisation in states that are not traditionally Hückel or Baird aromatic. Singlet calculations at the T_1 geometry continue to be the most problematic, generating extreme NICS values with differing signs between model chemistries.

9.11 $n = 10$

S_0 $C_{10}H_{10}{}^{2+}$ contains five distinct C–C bond lengths: 1.381, 1.389, 1.400, 1.411 and 1.424 Å. This span indicates a nonaromatic system, with quite a bit of variation in bond lengths preventing aromaticity, yet the bond lengths are significantly shorter than typical single bonds and longer than double bonds, suggesting partial delocalisation. The geometry severely deviates from planarity. In a uniform aromatic annulene, opposite carbons would be separated by an angle of 180° passing through the centre of the molecule. However, in the most extreme case opposite carbons have an angle of 131°. This disrupts the linear combination of π orbitals oriented perpendicular to the molecular plane, necessary to form an aromatic system of delocalised electrons. A ten-carbon arrangement can result in a planar structure, namely naphthalene (albeit with two fewer hydrogen atoms), which also has the advantage of being aromatic in a neutral state. The NICS(0) values are very consistent between model chemistries: B3LYP (-11.5 ppm), M06 (-11.6 ppm), M06-2X (-11.0 ppm), CAM-B3LYP (-11.6 ppm), PBE0 (-11.6 ppm), HF (-12.6 ppm) and MP2 (-12.8 ppm) all suggest aromaticity and coupled with the B3LYP shielding plot in Figure 57 confirm this. Although electrons are localised along C–C bonds, the shielding is very similar to the Möbius annulene $C_9H_9{}^+$ in the ground state. The subsequent excitation, relaxation and de-excitation are also parallel $C_9H_9{}^+$. H atoms themselves experience significant shielding, however, C–H bonds are weaker, suggesting the electrons are pulled into the carbon ring to attempt to stabilise the structure and highlights why the C–C bond lengths are quite short. The relative energy per CH unit of $C_{10}H_{10}{}^{2+}$ is smaller than any of the other dications. This is most probably just a result of the positive charge (or more strictly speaking the lack of negative charge) being spread over more centres than in the smaller dication annulenes. The Hückel 4n π-electron rule also does not hold, owing to the disrupted conjugation and non-planar geometry.

Vertical excitation yields an antiaromatic molecule with NICS(0) values: B3LYP (50.9 ppm), M06 (48.0 ppm), M06-2X (47.2 ppm), CAM-B3LYP (30.6 ppm) and PBE0 (43.6 ppm). No NICS(0) values could be obtained using HF or MP2. DFT methods are supported by the large central deshielded region shown in Figure 57.

The relaxation retains C_2 symmetry, however, the structure becomes more uniform, with bond lengths of 1.402, 1.402, 1.403 and 1.403 Å, which are all extremely close. The non-planarity is a result of ring strain and prevents the system from becoming aromatic. The NICS(0) values are also misleading suggesting greater aromaticity than is revealed in the shielding plot: B3LYP (−6.3 ppm), M06 (−6.5 ppm), M06-2X (−5.8 ppm), CAM-B3LYP (−6.2 ppm), PBE0 (−6.3 ppm), HF (−7.0 ppm), MP2 (−6.2 ppm). The shielding demonstrates the electrons are localised to the C–C bonds.

A vertical de-excitation indicates why the twisted structure of the optimised ground state geometry was necessary. The centre is engulfed in a large deshielded region, destabilising the molecule significantly. The H atoms on the periphery are well shielded, with shielding connecting the H atoms as well. NICS(0) of each method: B3LYP (46.1 ppm), M06 (40.9 ppm), M06-2X (46.8 ppm), CAM-B3LYP (40.0 ppm), PBE0 (48.0 ppm), HF (14.3 ppm) and MP2 (33.1 ppm) are consistent in predicting a reasonable degree of antiaromaticity. Although this final vertical de-excitation is not severely antiaromatic as ${C_9H_9}^+$, the shielding across all four states demonstrates the systems have very similar π-systems and the shielding across all states in consistent across model chemistries.

$C_{10}H_{10}$ shows significant deviation from planarity and despite having a 10-π-electron system, the bond lengths alternate between double and single bonds, with lengths 1.330, 1.337, 1.348, 1.460, 1.467 and 1.476 Å. This may be because this is not the optimal geometry, and the structure is a local minimum. Hückel's rule suggests this system should be aromatic, but ring strain may be overcoming this, with 10-carbon systems such as naphthalene becoming more favourable at this ring size, as two smaller conjoined rings reduce ring strain whilst still maintaining 10 π-electrons. The shielding plot suggests electrons are localised along both C–C and C–H bonds, with little delocalisation. The B3LYP NICS(0) is equally nonaromatic at 2.6 ppm. Whilst M06-2X (−5.8 ppm) and HF (4.8 ppm) also approach a nonaromatic state, MP2 (27.8 ppm), CAM-B3LYP (66.3 ppm) and PBE0 (119.5 ppm) become increasingly antiaromatic. The M06 value failed to compute, but this ground-state structure is surprisingly dependent on the choice of model chemistry. Perhaps the B3LYP-optimised geometry is responsible. Re-optimising the geometry within each model chemistry may yield different shielding results.

A vertical excitation yields little difference to the aromaticity in B3LYP, as the NICS(0) value shifts to B3LYP (−1.6 ppm) and the shielding appears similar. The other model chemistries are in agreement in this case, with NICS(0): M06 (−1.5 ppm), M06-2X (−0.9 ppm), CAM-B3LYP (−0.9 ppm), PBE0 (−1.3 ppm), HF (0.2 ppm) and MP2 (−0.8 ppm).

Relaxation indicates an antiaromatic geometry, with C–C bonds of 1.364, 1.414 and 1.474 Å, yet magnetic shielding remains indicative of a nonaromatic system. NICS(0) and NICS(1) of 0.3 and −2.3 ppm, respectively, support the shielding plot where shielding is localised along C–C bonds. Other model chemistries are consistent: M06 (0.0 ppm), M06-2X (0.5 ppm), CAM-B3LYP (−0.1 ppm), PBE0 (−0.1 ppm), HF (−1.0 ppm), MP2 (−1.2 ppm).

A vertical de-excitation yields NICS(0) values: B3LYP (3.9 ppm), M06 (3.4 ppm), M06-2X (5.5 ppm), CAM-B3LYP (4.1 ppm), PBE0 (4.0 ppm), HF (3.3 ppm) and MP2 (−2.9 ppm) all indicate the molecule remains nonaromatic. Compared to the $S_0//S_0$ calculations, the NICS(0) values in different model chemistries suggest greater stability here, further implying that they predict a significantly different structure. The B3LYP shielding is slightly weaker around the carbon ring with larger non-shielded ovoids around the deshielded ovoids which encompass the carbon centres. Across all four $C_{10}H_{10}$ state and geometry combinations, the molecule remains nonaromatic for B3LYP, and a shared π-system is not formed thus, the similar shielding between different states and geometries indicates the flexibility of the molecule. Model chemistry choice appears to significantly affect the results.

$C_{10}H_{10}{}^{2-}$ is a 12 π-electron system, so would be considered Hückel antiaromatic. However, bond lengths indicate nonaromatic character assuming the values 1.396, 1.405, 1.411, 1.413, 1.413 and 1.434 Å. These are far shorter than single bonds, suggesting some electron sharing, however, the range of 0.038 Å is too large to be considered aromatic. The shielding plot suggests the molecule is non- or weakly-aromatic as supported by NICS(0), NICS(+1) and NICS(−1) which each approach −6.0 ppm for B3LYP. M06-2X (−10.8 ppm), CAM-B3LYP (−10.7 ppm), PBE0 (−8.8 ppm), HF (−10.1 ppm) and MP2 (−7.8 ppm) NICS(0) values all suggest slightly greater aromaticity. No M06 value could be calculated. But with both C–C and C–H bonds well-shielded, the molecule appears to be stable. The energy per CH unit is the lowest for annulene dianion (6.4 kcal mol^{-1}) greater than benzene, but this is most likely because the negative charge is spread across more nuclei, as the energy per CH unit is close to that of $C_8H_8{}^{2-}$(6.6 kcal mol^{-1}) and does not show the same reduction from $C_6H_6{}^{2-}$(13.7 kcal mol^{-1}) and $C_4H_4{}^{2-}$ (26.0 kcal mol^{-1}).

B3LYP suggests that exciting an electron shifts the molecule to antiaromatic, with a deshielded region in the centre of the ring and spanning across all C–C bonds. NICS(0), NICS(+1) and NICS(−1) skyrocket to 161.9, 140.1, 142.6 ppm, respectively. This strongly goes against the other DFT methods which yield NICS(0) values: M06 (2.4 ppm), M06-2X (2.7 ppm), CAM-B3LYP (−2.4 ppm) and PBE0 (2.5 ppm). Once again, no value for HF or MP2 could be computed.

Relaxation using B3LYP produces a smooth structure with D_{5d} symmetry, and ten equal C–C bond lengths of 1.418 Å. Unexpectedly for such a flat and symmetrical optimal structure, magnetic shielding indicates the molecule is antiaromatic. NICS(0) for B3LYP (157.4 ppm) remains extremely antiaromatic and is joined by M06 (133.0 ppm). With the exception of geometrically appearing more aromatic, it is almost impossible to justify from the $\sigma_{iso}(\mathbf{r})$ plots that the relaxation reduces antiaromaticity at all. The characteristic deshielded region expands from the molecular centre to cover all C–C bonds, whilst shielded regions form a 'doughnut-shaped' ring encompassing the hydrogen atoms. Other model chemistries provide the more predictable behaviour from Baird's rule, suggesting NICS(0) values: M06-2X (−15.5 ppm), No CAM-B3LYP value, PBE0 (−16.0 ppm), HF (−17.2 ppm), MP2 (−14.7 ppm). This suggests B3LYP is not describing this system well.

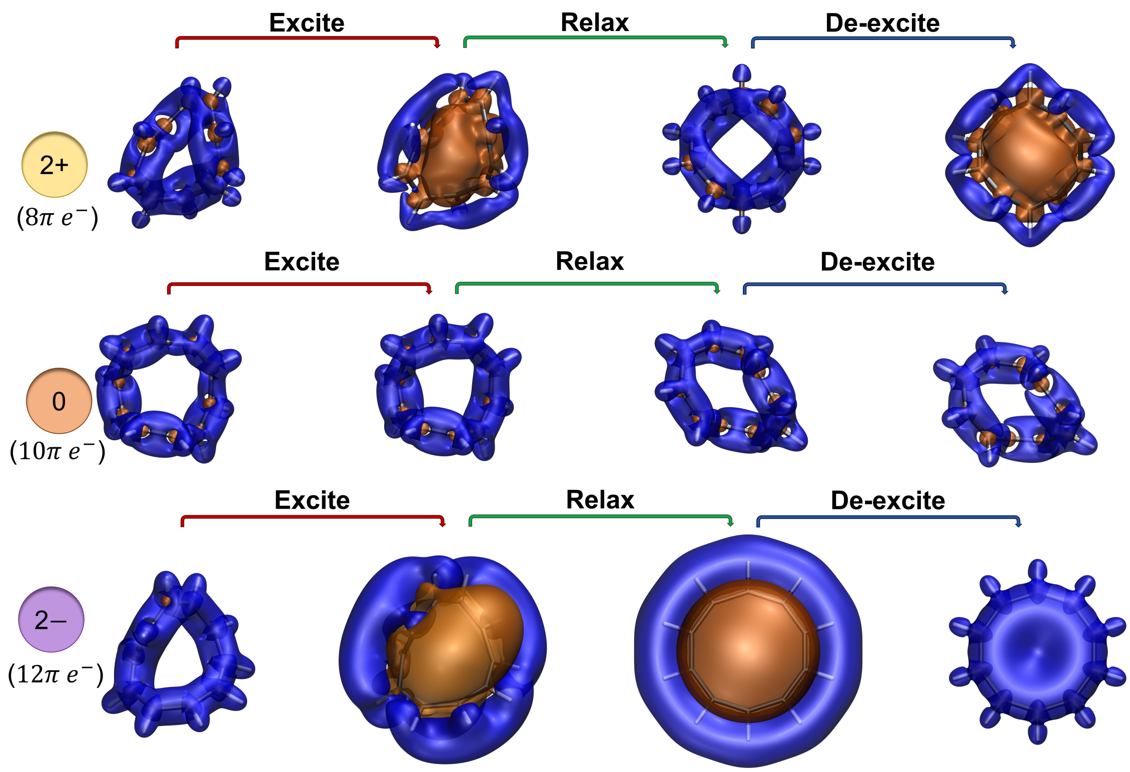

Figure 57: The shielding of ${C_{10}H_{10}}^{2+}$ (top), $C_{10}H_{10}$ (middle) and ${C_{10}H_{10}}^{2-}$ (bottom) starting from the $S_0//S_0$ state, vertically exciting to $T_1//S_0$, adiabatically relaxing to $T_1//T_1$ and vertically de-exciting to $S_0//T_1$.

De-excitation produces a surprisingly aromatic structure for B3LYP. Shielding so large that no characteristic hole appears in the centre of the plot to resemble a 'doughnut' shape. The NICS(0) and NICS(1) values are −16.5 and −15.1 ppm. C–H bonds are shielded to a similar degree as benzene. It is possible the triplet-optimised geometry causes additional ring strain, which is responsible for the structure being more unfavourable than the ground state geometry (1.7 kcal mol^{-1}). The optimal geometry is a consequence of more than just aromaticity. The single C–C bonds and sp^2 hybridisation are also important and often override the aromatic criteria. The triplet geometry is more aromatic than the optimised singlet geometry but is less stable due to other factors and can not be rationalised by aromaticity. Whilst PBE0 (−16.5 ppm) suggests similar aromaticity to B3LYP, NICS(0) values become too extreme in M06 (−221.8 ppm), M06-2X (−231.7 ppm) and CAM-B3LYP (−481.7 ppm) in favour of aromaticity whilst HF (205.8 ppm) and MP2 (909.3 ppm) are unphysically antiaromatic.

The $n = 10$ structures show high model chemistry dependence, with the M06 functional alongside the HF and MP2 methods struggling to finish calculations. Only the optimised T_1 ${C_{10}H_{10}}^{2-}$ is planar and no relaxed state is traditionally Hückel aromatic or antiaromatic, suggesting extending to larger annulenes would predominately show localised shielding around nonaromatic, non-planar and severely twisted structures or Möbius annulenes. The T_1 ${C_{10}H_{10}}^{2-}$ B3LYP shielding highlights that B3LYP cannot accurately describe all states, since it disagrees with Baird's rule.

9.12 Conclusions

This chapter has systematically examined the aromaticity and antiaromaticity of annulenes $C_nH_n^q$ by analysing off-nucleus isotropic magnetic shielding around neutral and charged annulenes, in the ground state; after a vertical excitation; adiabatic relaxation, and vertical de-excitation. It has revealed many changes in geometry are a direct result of aromaticity allowing for a nuanced investigation of vertical excitations, relaxation and de-excitation processes.

It has also been shown that in the ground Hückel's rule is obeyed for annulenes up to $n = 8$, but shielding also identifies Möbius aromaticity in larger annulenes like ${C_9H_9}^+$. Vertical excitations typically obey Baird's rule, showing clear aromatic reversals relative to the ground state. The relaxation increases aromaticity when the triplet state is aromatic, typically by increasing symmetry. Relaxation also greatly reduces antiaromaticity when the vertical excitation is antiaromatic, which has been demonstrated by the reduction of deshielded regions in shielding plots. For ${C_4H_4}^{2-}$ and ${C_5H_5}^-$, the relaxed T_1 state removes antiaromaticity by significant geometrical distortions of the molecule, to such an extent that they can be considered nonaromatic. The most extreme antiaromaticity tends to occur in planar structures.

The analysis was rigorously confined to data derived directly from computations at multiple levels of theory including B3LYP, M06, M06-2X, CAM-B3LYP, HF, PBE0, and MP2. This has highlighted the high method dependence of the magnetic shielding, particularly at sub-optimal, non-relaxed geometries. MP2 yields the most extreme results, often yielding extreme values, most emphasised by $C_7H_7^-$ $S_0//T_1$ which yields a NICS(1) value of 94144.6 ppm, three orders of magnitude beyond values which begin to become questionable and unphysical in their size. MP2 calculations are also the most frequent to fail. HF is significantly better, but disagrees with DFT methods. DFT methods have better agreement with each other than either MP2 or HF, yet still disagree considerably. M06 and M06-2X disagree with aromatic characterisation of B3LYP, CAM-B3LYP and PBE0 for several states. No model chemistry can truly be believed across all states, producing values inconsistent with Hückel, Baird and Möbius aromatic criteria and there is often a different model chemistry which yields more expected values.

The analysis of this chapter shifts from evaluating molecules aromaticity and more to comparing and contrasting the usefulness of different model chemistries for magnetic shielding. It has been highlighted that various model chemistries should be used to evaluate magnetic shielding and serves as a warning to interpreting magnetic shielding without comparisons to bond length alternation or electron counting rules. On the whole, ground state structures at the optimal geometry agree with Hückel and Möbius aromatic criteria in addition to being consistent between models (with the exception of $C_{10}H_{10}$). $T_1//T_1$ shielding is less agreement, but is not as varied as using the sub-optimal geometries.

An interesting finding of this work is that which is revealed by the shielding after a vertical de-excitation. Exactly half of the twenty annulenes studied in this chapter at the B3LYP: $C_3H_3^-$, C_4H_4, $C_5H_5^+$, $C_6H_6^{2+}$, $C_6H_6^{2-}$, $C_7H_7^-$, C_8H_8, $C_8H_8^{2-}$, $C_9H_9^-$ and $C_{10}H_{10}^{2-}$, appear more 'aromatic' in the ground state with the optimised T_1 geometry, than they are with their own optimal ground state geometry. These molecules would be considered aromatic under magnetic criteria as they have large negative NICS values and visible shielding in $\sigma_{\text{iso}}(\mathbf{r})$ plots as evidence for delocalisation. These cases correspond to the diamagnetic term strongly dominating the paramagnetic one, indicating electronic density has a greater impact on the shielding than the ability for the electronic wavefunction to be perturbed. Practically, the following rationale can be used to indicate why the $\sigma_{\text{iso}}(\mathbf{r})$ still accounts for the reason these molecules are not the lowest energy structure, despite the appearance of aromaticity which is usually associated with an energy reduction.

(1) Despite strong shielding within the carbon ring, the C–H bonds are often poorly shielded or not shielded at all. This can sometimes also include the H atoms themselves. The weakening of C–H bonds raises the energy of the structure, making it less stable. Since C–H bonds should have a much lower energy than those in the π-system, weakening these has a greater influence on the molecular energy as a whole, making these geometries less favourable.

(2) Although only visible at -16 ppm on $C_7H_7^-$ and $C_9H_9^-$, at smaller chemical shift thresholds, deshielding is often visible in some form of 'broken halo' structure outside of the ring in the molecular plane. Such regions are not present on ground-state aromatic molecules, as they suggest weaker C–C bonds, as the paramagnetic term dominates, suggesting electrons are easily perturbed by an external magnetic field and hence less restrained by the bonds between nuclei.

(3) The shielding and delocalisation extend excessively in these molecules. The shielding can extend far above and below the molecular plane, suggesting high electron density far away from the nuclei. These bonds are therefore weaker, and the electrons bind to atoms less strongly.

These three indicators will help identify suboptimal structures and unstable states in magnetic shielding studies. However, not all of the unfavourable states exhibit all three indicators. Some cases such as $C_{10}H_{10}{}^{2-}$ experience none to a justifiable extent. It is hoped current density studies may be used to explore this phenomenon further. Crucially, these suboptimal geometries are higher electronic singlet states. S_1 states typically obey Baird's rule; hence it is likely these correspond to the S_2 states. This has been confirmed with TDDFT calculations yielding negative excitation energies. The similarities between the shielding around the de-excited C_8H_8 and previous S_2 C_8H_8 CASSCF calculations are clear. It is assumed that because the T_1 geometry is similar to the S_2 states, the singlet calculations use this higher singlet state as opposed to the ground state for the shielding.

In summary, no model chemistry is without its flaws, and a robust assessment of aromaticity demands careful cross-validation across methods. The findings of this thesis emphasise that NICS results must always be interpreted in the context of molecular charge, electronic state, and structural relaxation. Systems that are antiaromatic in their ground states frequently adopt aromatic character in their triplet states upon relaxation, reinforcing the dynamic and context-dependent nature of aromaticity. Only through analyses of multiple states involving multiple methods can reliable conclusions about aromatic characterisation be drawn.

10 Conclusions

This thesis presents a comprehensive investigation into aromaticity and antiaromaticity through the lens of magnetic shielding, with a particular focus on nucleus-independent chemical shifts (NICS) and three-dimensional shielding volume data. A wide variety of different types of molecule have been used to capture the full scope of aromatic and antiaromatic behaviour in ground and excited electronic states. More concretely, the T_1 excited state aromaticity reversals in condensed heterocyclic systems form the cornerstone of this research. This research has emphasised the role both ring strain and orientation of condensed heterocycles can have on the aromaticity as well as encouraging the proposal of new structures such as sulfinfinitenes. Two more complicated applications of aromaticity including the σ-aromaticity of boron clusters and aromaticity reversals in macrocyclic norcorrole variants with long conjugation pathways demonstrate the wider possibilities for magnetic shielding calculations. By contrast, the extreme model chemistry dependence of the magnetic shielding results for annulenes, particularly when calculated at sub-optimal geometries, serves as a vital warning to always pair conclusions drawn from magnetic shielding with chemical intuition and other criteria to ensure calculations are not grossly misrepresenting the system.

Ethane, ethene, and ethyne demonstrated that one must compare not just the extents of shielding isosurfaces, but also the intensity of the shielding within the shielded region. Otherwise, superposition of shielding due to neighbouring bonds can overemphasize shielding and suggest misleading conclusions. According to the three-dimensional shielding data generated for this thesis, double and triple bonds do not have significantly increased shielding compared to single bonds. Previous work[41,50] has shown that the differences in the three types of bonds are identifiable by inspecting the shielding intensity at specific locations. This should not be as large of a problem for all other molecules in this thesis as they contain delocalised electrons or alternating double and single bonds, so they can readily be compared to each other. Additionally, NICS probes are also reported alongside shielding plots to alleviate concerns of overlapping shielding from neighbouring bonds skewing any interpretation. More crucially for the rest of this thesis, the characteristic deshielded region in the centre of antiaromatic molecules has been shown not to be an electron delocalisation phenomenon intrinsic to antiaromaticity, as the π-systems in T_1 ethyne forms a comparable deshielded region, despite not forming a closed loop.

The geometry of thiophene changes considerably between the S_0 and T_1 states: Not only is its symmetry reduced from C_{2v} to C_s with a loss of planarity but, more importantly, the carbon-carbon 'double' and 'single' bonds in the S_0 state turn into 'single' and 'double' bonds, respectively, in the T_1 state. Looking for thiophene rings with geometries resembling those of a thiophene molecule in its S_0 or T_1 state can help rationalise the levels of antiaromaticity in the T_1 states of some of the compounds with fused thiophene rings. Similar arguments can be made for molecules formulated from condensed furan rings.

A change of basis sets of 6-311++G(2d,2p) and 6-311++G(d,p) in the $T_1//S_0$ state of thiophene used different initial guesses for the Kohn–Sham orbitals and hence the calculations converged to different excited states. This suggests that not only the electronic structure method, but also the basis set can lead to different electronic states when using magnetic shielding to investigate aromaticity; consequently, any analysis should always be paired with chemical intuition.

The geometry relaxation in both the T_1 and T_2 states of thiophene highlights the increased stability compared to retaining the S_0 state geometry. T_2 state of thiophene is the first reported example of 'strongly aromatic' triplet state and the comparison to HOMA values emphasises that aromaticity between the ground and excited state should not be compared directly. What is considered a strong magnetic response in the ground state may not be considered strong in an excited state, even at a similar magnitude.

Off-nucleus isotropic magnetic shielding calculations of heterocycle series, with $4n + 2$ π electron counts of 6, 10 and 14 similar to the hydrocarbon series of benzene, naphthalene, and anthracene, respectively with either an oxygen or sulfur heteroatom have confirmed that the electronic ground states of these molecules are aromatic. However, our electronic ground state NICS results for these two heterocyclic series of compounds do not exhibit trends consistent with the set of disputed predictions made on the basis of the NICS values for benzene, naphthalene, and anthracene[109,110] known as the 'anthracene problem',[57,109,111,112] according to which both rings in naphthalene, as well as the central ring in anthracene should be more aromatic than the benzene ring, and the central ring in anthracene should be more aromatic than the outer rings. Instead, magnetic shielding results suggest that the isolated heterocyclic systems are more aromatic than any condensed rings.

Nineteen of the twenty-four heterocycles investigated experience an overall aromatic reduction when excited to the T_1 state, but this is mainly to a nonaromatic structure. Given the geometry changes, this is expected and does not go against Baird's rule. Only four of the heterocyclic systems experience well-defined Baird-style aromaticity reversals between the S_0 and T_1 states, namely: thieno[2,3-*b*]thiophene, dithieno[3,2-*b*;2′,3′-*d*]thiophene, octathio[8]circulene and dodecafuro[12]circulene.

Condensing thiophene rings into sulflowers and furan rings into oxiflowers yields comparable aromatic trends to condensing benzene rings into coronene and corannulene, circulenes with 6 and 5 benzene rings, respectively. Fusing furan or thiophene rings in such a manner, yields an aromatic molecule in its electronic ground state, despite having a total of 4n π-electrons. In contrast to the hydrocarbon and sulfur containing molecules, the oxygen containing molecules often have far weaker shielding in $\sigma_{\text{iso}}(\mathbf{r})$ plots than the single ring building block (in this case furan), although this is far less detectable in the NICS indices.

Hexathio[6]circulene is relatively weakly aromatic in its electronic ground state but becomes more aromatic in its lowest triplet state. The extents of the changes in aromaticity between the S_0 and T_1 states of the molecules we examined are reduced by the use of geometries optimised separately for the two states: It is well-known that antiaromatic molecules try to 'escape' antiaromaticity through a symmetry reduction, for example, square cyclobutadiene distorts to a rectangular geometry with 'single' and 'double' C–C bonds.

The drive to create interesting structures by fusing aromatic rings has been extended to produce infinitenes.[117] This thesis has used the premise to fuse thiophene rings into sulfinfinitenes. Calculations strongly suggest that [16]sulfinfinitene which can be formally obtained by combining two molecules of the least strained member of the sulflower series, the [8]sulflower (octathio[8]circulene) and should be considered as a promising synthetic target. [18]sulfinfinitene and its precursor, the [9]sulflower (nonathio[9]circulene) show slightly higher strains and slightly lower HOMO–LUMO gaps and could also be of synthetic interest. The aromaticities of these each thiophene ring in the ground state of [14]sulfinfinitene to [20]sulfinfinitene are similar to the aromaticities of other condensed thiophene of between -10.1 and -8.2 ppm. The greater ring strain of [10]sulfinfinitene and [12]sulfinfinitene creates less aromatic rings and even nonaromatic rings, suggesting these will be harder to synthesise.

Examining the magnetic shielding of the S_0 and T_1 electronic states of Ni^{II} norcorrole and norcorrole strongly suggests an aromatic reversal upon the excitation. The strongly deshielded antiaromatic 'internal crosses' spanning 16 atoms and 16 π electrons becomes sufficiently shielded to combine with the peripheral aromatic 'halos' (which do not undergo aromaticity reversals) to produce Baird-aromatic triplet systems with 24 π electrons each. The magnetic shielding studies are validated by the changes in the HOMA values between the optimised geometries of the S_0 and T_1 states of both molecules. Given their close alignment, the optimised geometries of the T_1 and S_1 states of NiNc and H_2Nc and the corresponding HOMA values, it is sensible to suggest that the two molecules undergo similar aromaticity reversals in their S_1 states.

The very low vertical and adiabatic excitation energies of NiNc and H_2Nc from the ground to lowest triplet and singlet state suggest antiaromatic destabilisation of the S_0 states and aromatic stabilisation of the T_1

and S_1 states of the two molecules and indicate that either lower-lying excited state in each molecule could be easily accessed from S_0. The changes in the bowl depths of NiNc and H_2Nc upon excitation could be exploited in the design of new low-amplitude "flapping" fluorophores, similar to those based on π-expanded cyclooctatetraenes and oxepins.[173–175]

The norcorrole variants are interesting molecules whose magnetic shielding provides a picture of bonding which is supported by other computational methods and experimental data. The isosurface plots demonstrate their value in providing a more complete picture. In the ground state, NICS correctly identifies the antiaromatic features of NiNc and H_2Nc, but fails to identify the global networks of conjugation resulting in the aromatic 'halos' surrounding these molecules. This is significantly different from heterocirculenes, such as sulflowers and oxiflowers, where only the local ring aromatic conjugation pathways were at play.

Magnetic shielding has been utilized to study the bonding within aromatic quasi-planar boron clusters, B_n of size $n = 3$–15. σ-aromaticity appears to dominate off-nucleus chemical shifts, rendering π-aromaticity almost undetectable through magnetic shielding in systems with σ-aromaticity. This is even the case for suspected π-antiaromatic clusters (such as B_3^+ or B_{15}^-) where σ-aromaticity dominates to produce high NICS values and well shielded magnetic shielding plots. B_3^+ and B_3^- appear to have almost indistinguishable magnetic shielding, despite the change in π-system character from antiaromatic to aromatic.

Nevertheless, magnetic shielding plots are valuable resources and indicate regions of high electron delocalisation which varies drastically between clusters. In some clusters, the shielding is greatest on either side of the plane, and far weaker within it, even for fully planar structures like B_{13}^+. The aromaticity can cause the greatest shielding to create loops perpendicular to the molecular plane, such as B_{11}^-. Non-planar wheels B_6 and B_7^+, have the greatest shielding above their central atom, whilst the planar wheels B_8^{2-} and B_9^-, have the greatest shielding (and hence electron delocalisation) in a ring within the molecular plane. The cluster's symmetry also has a significant impact on the shielding, with both B_{14} and B_{15}^- isomers having vastly different shielding plots. The more disordered the cluster, the more disordered the shielding isosurface becomes, breaking into multiple isolated regions at high chemical shifts. The reason for these vastly different manifestations requires further investigation.

Visualising magnetic shielding isosurfaces for σ-aromaticity is almost meaningless at ± 16 ppm, where the majority of the molecule appears shielded. Whilst partly due to the close proximity of the atoms, shielding which is not localised on atoms or along two-centre bonds, consistently at $\sigma_{\text{iso}}(\mathbf{r}) \geq 30$ ppm, emphasises the high influence of σ-aromaticity on magnetic shielding and hence bonding.

The stability of boron clusters is theoretically problematic to determine, with no correlation between any HOMO–LUMO gaps, atomisation energies per boron atom, average NICS values, and the number of σ-bonds. It appears that σ-aromaticity must only be compared to traditional π-aromaticity when considering that electrons are delocalised over more than two atoms. Traditional properties of aromaticity such as stabilisation does not extend to σ-aromaticity, and the properties of so-called σ-aromaticity are far closer to being a single bond shared across multiple atoms.

Arguably, the chapter on annulenes reveals the most exciting findings of this thesis. It presents a systematic magnetic shielding analysis of closed shell monocyclic hydrocarbons including dications, neutral species and dianions for even-membered rings, in addition to cations and anions for odd-membered rings, in the range $n = 3$ to 10. Importantly, four geometrical/electronic conditions were evaluated as the system is inspected along a journey starting at the ground state (S_0), after a vertical excitation ($T_1//S_0$), adiabatic relaxation (T_1), and finally a vertical de-excitation ($S_0//T_1$).

The data confirm that Baird aromaticity frequently manifests upon excitation to the T_1 state, especially evident in $C_5H_5{}^+$, $C_6H_6{}^{2+}$ and $C_7H_7{}^-$, whose triplet state Baird aromaticity causes such a stabilisation that these systems are lower in energy than their respective lowest energy singlet states. This means that Baird aromaticity can cause triplet systems to be the ground state.

Notably, shielding anomalies emerge in $S_0//T_1$ configurations, where triplet geometries retain excited-state structure but are evaluated with singlet wavefunctions. These geometries can sometimes reflect S_2-like character, confirmed by negative excitation energies in TDDFT calculations. Three key signs of unphysical shieldings were identified: internal deshielding in planar centres; disjointed halo structures suggesting interrupted delocalisation, and excessive shielding volumes that extend beyond chemically reasonable limits.

Across all systems, model chemistry choice critically impacts the interpretation of magnetic shielding. Whilst B3LYP yields almost identical shielding to CASSCF(8,9) results for $C_9H_9{}^+$ in both the S_0 and T_1 states at the S_0 geometry, it also unfortunately predicts $C_{10}H_{10}{}^{2-}$ is antiaromatic in the T_1 state. The DFT functionals B3LYP, CAM-B3LYP and PBE0 are the most consistent with each other, whilst M06 and M06-2X diverge further. HF can describe some systems better, but is also prone to more extreme values. MP2 breaks frequently and it is strongly advised that this is not to be used for any future excited state or magnetic shielding analysis.

Given the high model chemistry dependence demonstrated within it, the final chapter on annulenes does bring into question the validity of the rest of the work in this thesis. It can be said that if off-nucleus shieldings are calculated at certain non-equilibrium geometries of charged systems, a number of methods including B3LYP-GIAO, can produce unexpected and unphysical results. However, whilst it is not possible to claim 100% certainty in the other results, there are strong reasons to believe the other results are reasonably accurate. Firstly, the other results do not deviate significantly from Hückel's or Baird's rule, beyond what can be attributed to geometry relaxations. Secondly, there are not extreme NICS values reaching triple, quadruple and even quintuple digits that were present in the study of annulenes. Thirdly, no other chapters contain charged systems, it is charged systems which appear to cause more problematic results than neutral ones. Next, some variability in the annulene results could be caused by using the B3LYP optimised geometry, and keeping a consistent model chemistry for both the optimisation and shielding calculations may yield more consistent results. Additionally, no other calculations have negative excitation energies in TDDFT calculations; some annulene values particularly in the $S_0//T_1$ state did, which suggests higher singlet states were computed in the shielding. Finally, the most problematic shieldings which deviated significantly by the selection of model chemistry were those calculated at suboptimal geometries. This means the wavefunctions used in calculations have different symmetries to the nuclear framework. These six criteria separate the annulene study from rest of this thesis.

Aromaticity is not a binary property but a nuanced continuum dependent on electronic configuration and geometry. Ultimately, this work demonstrates that aromaticity, despite its historical elusiveness, can be dissected through magnetic shielding, but only when computational insight is married to chemical judgement can one build a consistent, chemically meaningful picture of aromatic character.

Bibliography

Bibliography

[1] P. B. Karadakov and K. E. Horner, *J. Phys. Chem. A*, 2013, **117**, 518–523.

[2] P. B. Karadakov, *Org. Lett.*, 2020, **22**, 8676–8680.

[3] D. Lloyd, *Non-Benzenoid Conjugated Carbocyclic Compounds*, ELSEVIER, Amsterdam, 1984.

[4] D. Lloyd, *J. Chem. Inf. Comput. Sci.*, 1996, **36**, 442–447.

[5] D. Lewis and D. Peters, *Facts and theories of aromaticity*, Macmillan Press, London, 1975.

[6] P. Muller, *Pure Appl. Chem.*, 1994, **66**, 1077–1184.

[7] N. C. Baird, *J. Am. Chem. Soc.*, 1972, **94**, 4941–4948.

[8] I. Judy, C. Wu, Y. Mo, F. A. Evangelista and P. von Ragué Schleyer, *Chem. Comm.*, 2012, **48**, 8437–8439.

[9] M. J. S. Dewar, *The Molecular Orbital Theory of Organic Chemistry*, McGraw-Hill, New York, 1969.

[10] W. Kohn and L. J. Sham, *Phys. Rev.*, 1965, **140**, A1133.

[11] E. Runge and E. K. U. Gross, *Phys. Rev. Lett.*, 1984, **52**, 997–1000.

[12] R. O. Jones and O. Gunnarsson, *Rev. Mod. Phys.*, 1989, **61**, 689–707.

[13] P. Hohenberg and W. Kohn, *Phys. Rev*, 1964, **136**, B864–B871.

[14] J. P. Perdew, J. Chevary, S. Vosko, K. A. Jackson, M. R. Pederson, D. J. Singh and C. Fiolhais, *Phys. Rev. B*, 1993, **48**, 6671–6687.

[15] A. D. Becke, *Phys. Rev. A*, 1988, **38**, 3098–3100.

[16] S. H. Vosko, L. Wilk and M. Nusair, *Can. J. Phys.*, 1980, **58**, 1200–1211.

[17] C. Lee, W. Yang and R. G. Parr, *Phys. Rev. B*, 1988, **37**, 785–789.

[18] C. Møller and M. S. Plesset, *Phys. Rev.*, 1934, **46**, 618–622.

[19] P. Siegbahn, A. Heiberg, B. Roos and B. Levy, *Phys. Scr.*, 1980, **21**, 323.

[20] B. O. Roos, *Int. J. Quantum Chem.*, 1980, **18**, 175–189.

[21] P. E. Siegbahn, J. Almlöf, A. Heiberg and B. O. Roos, *J. Chem. Phys.*, 1981, **74**, 2384–2396.

[22] B. O. Roos, P. R. Taylor and P. E. Sigbahn, *Chem. Phys.*, 1980, **48**, 157–173.

[23] D. S. Levine, D. Hait, N. M. Tubman, S. Lehtola, K. B. Whaley and M. Head-Gordon, *J. Chem. Theory Comput.*, 2020, **16**, 2340–2354.

[24] S. Grimme, J. Antony, S. Ehrlich and H. Krieg, *J. Chem. Phys.*, 2010, **132**, 154104.

[25] E. M. Arpa, S. Stafström and B. Durbeej, *J. Org. Chem.*, 2025, **90**, 1297–1308.

[26] E. D. Raczyńska, M. Hallman, K. Kolczyńska and T. M. Stepniewski, *Symmetry*, 2010, **2**, 1485–1509.

[27] E. M. Arpa and B. Durbeej, *Phys. Chem. Chem. Phys.*, 2023, **25**, 16763–16771.

[28] A. Mischie, A. M. Toader, M. C. Buta and F. Cimpoesu, *Comput. Theor. Chem.*, 2023, **1230**, 114370.

[29] T. Lu and F. Chen, *J. Comp. Chem.*, 2012, **33**, 580–592.

[30] J. Jusélius, D. Sundholm and J. Gauss, *J. Chem. Phys.*, 2004, **121**, 3952–3963.

[31] H. M. McConnell and R. E. Robertson, *J. Chem. Phys.*, 1958, **29**, 1361–1365.

[32] N. F. Ramsey, *Phys. Rev.*, 1950, **78**, 699.

[33] W. Van den Heuvel and A. Soncini, *J. Chem. Phys.*, 2013, **138**, 054113.

[34] V. Gogonea, P. v. R. Schleyer and P. R. Schreiner, *Angew. Chem. Int. Ed.*, 1998, **37**, 1945–1948.

[35] P. Fowler, E. Steiner and L. Jenneskens, *Chem. Phys. Lett.*, 2003, **371**, 719–723.

[36] Z. Rinkevicius, J. Vaara, L. Telyatnyk and O. Vahtras, *J. Chem. Phys.*, 2003, **118**, 2550–2561.

[37] J. Vaara, *Phys. Chem. Chem. Phys.*, 2007, **9**, 5399–5418.

[38] P. V. R. Schleyer, C. Maerker, A. Dransfeld, H. Jiao and N. J. R. Van Eikema Hommes, *J. Am. Chem. Soc.*, 1996, **118**, 6317 – 6318.

[39] M. Bühl and C. van Wüllen, *Chem. Phys. Lett.*, 1995, **247**, 63–68.

[40] R. G.-P. I.Fernandez and A. Stanger, *Aromaticity: Modern Computational Methods and Applications*, Elsevier, 2021, pp. 99–153.

[41] K. E. Horner, *Ph.D. thesis*, University of York, 2014.

[42] M. A. A.-B. H. Al-Yassiri, *Ph.D. thesis*, University of York, 2019.

[43] S. Klod and E. Kleinpeter, *J. Chem. Soc.*, 2001, 1893–1898.

[44] E. Kleinpeter and A. Koch, *Magn. Reson. Chem.*, 2024, **62**, 686–693.

[45] M. J. Frisch, G. W. Trucks, H. B. Schlegel, G. E. Scuseria, M. A. Robb, J. R. Cheeseman, G. Scalmani, V. Barone, G. A. Petersson, H. Nakatsuji, X. Li, M. Caricato, A. V. Marenich, J. Bloino, B. G. Janesko, R. Gomperts, B. Mennucci, H. P. Hratchian, J. V. Ortiz, A. F. Izmaylov, J. L. Sonnenberg, D. Williams-Young, F. Ding, F. Lipparini, F. Egidi, J. Goings, B. Peng, A. Petrone, T. Henderson, D. Ranasinghe, V. G. Zakrzewski, J. Gao, N. Rega, G. Zheng, W. Liang, M. Hada, M. Ehara, K. Toyota, R. Fukuda, J. Hasegawa, M. Ishida, T. Nakajima, Y. Honda, O. Kitao, H. Nakai, T. Vreven, K. Throssell, J. A. Montgomery, Jr., J. E. Peralta, F. Ogliaro, M. J. Bearpark, J. J. Heyd, E. N. Brothers, K. N. Kudin, V. N. Staroverov, T. A. Keith, R. Kobayashi, J. Normand, K. Raghavachari, A. P. Rendell, J. C. Burant, S. S. Iyengar, J. Tomasi, M. Cossi, J. M. Millam, M. Klene, C. Adamo, R. Cammi, J. W. Ochterski, R. L. Martin, K. Morokuma, O. Farkas, J. B. Foresman and D. J. Fox, *Gaussian˜16 Revision C.01*, 2016, Gaussian Inc. Wallingford CT.

[46] W. Humphrey, A. Dalke and K. Schulten, *J. Mol. Graph.*, 1996, **14**, 33–38.

[47] P. B. Karadakov, *ChemPhysChem*, 2023, **24**, e202300038.

[48] P. B. Karadakov, P. Hearnshaw and K. E. Horner, *J. Org. Chem.*, 2016, **81**, 11346–11352.

[49] K. E. Horner and P. B. Karadakov, *J. Org. Chem.*, 2013, **78**, 8037–8043.

[50] P. B. Karadakov and K. E. Horner, *J. Chem. Theory Comput.*, 2016, **12**, 558–563.

[51] P. B. Karadakov and J. Kirsopp, *Chem. Eur. J.*, 2017, **23**, 12949–12954.

[52] M. Kataoka, *J. Chem. Res.*, 2004, 573–574.

[53] P. B. Karadakov, *J. Phys. Chem. A*, 2008, **112**, 7303–7309.

[54] P. B. Karadakov, *J. Phys. Chem. A*, 2008, **112**, 12707–12713.

[55] P. v. R. Schleyer, H. Jiao, N. J. R. v. E. Hommes, V. G. Malkin and O. Malkina, *J. Am. Chem. Soc.*, 1997, **119**, 12669–12670.

[56] H. Fallah-Bagher-Shaidaei, C. S. Wannere, C. Corminboeuf, R. Puchta and P. V. R. Schleyer, *Org. Lett.*, 2006, **8**, 863–866.

[57] P. B. Karadakov and M. A. Al-Yassiri, *J. Phys. Chem. A*, 2023, **127**, 3148–3162.

[58] B. P. Pritchard, D. Altarawy, B. Didier, T. D. Gibson and T. L. Windus, *J. Chem. Inf. Model.*, 2019, **59**, 4814–4820.

[59] V. L. Orr, Y. Ichikawa, A. R. Patel, S. M. Kougias, K. Kobayashi, J. F. Stanton, B. J. Esselman, R. C. Woods and R. J. McMahon, *J. Chem. Phys.*, 2021, **154**, 244310.

[60] L. Serrano-Andrés, M. Merchán, M. Fülscher and B. O. Roos, *Chem. Phys. Lett.*, 1993, **211**, 125–134.

[61] S. Salzmann, M. Kleinschmidt, J. Tatchen, R. Weinkauf and C. M. Marian, *Phys. Chem. Chem. Phys.*, 2008, **10**, 380–392.

[62] E. Van Veen, *Chem. Phys. Lett.*, 1976, **41**, 535–539.

[63] W. M. Flicker, O. A. Mosher and A. Kuppermann, *J. Chem. Phys.*, 1976, **64**, 1315–1321.

[64] M. H. Palmer, I. C. Walker and M. F. Guest, *Chem. Phys.*, 1999, **241**, 275–296.

[65] H. Haberkern, K. R. Asmis, M. Allan and P. Swiderek, *Phys. Chem. Chem. Phys.*, 2003, **5**, 827–833.

[66] T. Kupka, R. Wrzalik, G. Pasterna and K. Pasterny, *J. Mol. Struct.*, 2002, **616**, 17–32.

[67] E. Cummings and P. B. Karadakov, *Chem.-Eur. J.*, 2023, e202303724.

[68] N. Sakai, G. K. Prasad, Y. Ebina, K. Takada and T. Sasaki, *Chem. Mater.*, 2006, **18**, 3596–3598.

[69] G. Dai, J. Chang, X. Shi, W. Zhang, B. Zheng, K.-W. Huang and C. Chi, *Chem. Eur. J.*, 2015, **21**, 2019–2028.

[70] M. Hermann, R. Wu, D. C. Grenz, D. Kratzert, H. Li and B. Esser, *J. Mater. Chem. C*, 2018, **6**, 5420–5426.

[71] C. Liu, S. Xu, W. Zhu, X. Zhu, W. Hu, Z. Li and Z. Wang, *Chem. Eur. J.*, 2015, **21**, 17016–17022.

[72] C. Zhang and X. Zhu, *Acc. Chem. Res.*, 2017, **50**, 1342–1350.

[73] J. L. Eigenbrode, R. E. Summons, A. Steele, C. Freissinet, M. Millan, R. Navarro-González, B. Sutter, A. C. McAdam, H. B. Franz, D. P. Glavin, P. D. Archer, P. R. Mahaffy, P. G. Conrad, J. A. Hurowitz, J. P. Grotzinger, S. Gupta, D. W. Ming, D. Y. Sumner, C. Szopa, C. Malespin, A. Buch and P. Coll, *Science*, 2018, **360**, 1096–1101.

[74] J. Heinz and D. Schulze-Makuch, *Astrobiology*, 2020, **20**, 552–561.

[75] M. Millan, A. J. Williams, A. C. McAdam, J. L. Eigenbrode, A. Steele, C. Freissinet, D. P. Glavin, C. Szopa, A. Buch, R. E. Summons, J. M. T. Lewis, G. M. Wong, C. H. House, B. Sutter, O. McIntosh, A. B. Bryk, H. B. Franz, C. Pozarycki, J. C. Stern, R. Navarro-Gonzalez, D. P. Archer, V. Fox, K. Bennett, S. Teinturier, C. Malespin, S. S. Johnson and P. R. Mahaffy, *J. Geophys. Res. Planets*, 2022, **127**, e2021JE007107.

[76] R. Casares, Á. Martínez-Pinel, S. Rodríguez-González, I. R. Márquez, L. Lezama, M. T. González, E. Leary, V. Blanco, J. G. Fallaque, C. Díaz *et al.*, *J. Mater. Chem. C*, 2022, **10**, 11775–11782.

[77] H. K. Saha, D. Mallick and S. Das, *Chem. Commun.*, 2022, **58**, 8492–8495.

[78] J. Usuba, M. Hayakawa, S. Yamaguchi and A. Fukazawa, *Chem. Eur. J.*, 2021, **27**, 1638–1647.

[79] J. Wirz, A. Krebs, H. Schmalstieg and H. Angliker, *Angew. Chem. Int. Ed. Engl.*, 1981, **20**, 192–193.

[80] M. E. Cinar and T. Ozturk, *Chem. Rev.*, 2015, **115**, 3036–3140.

[81] G. A. Sotzing, M. A. Invernale and Y. Ding, *Electrochromic devices prepared from the in situ formation of conjugated polymers*, 2013, US Patent App. 13/606,829.

[82] R. Inoue, M. Hasegawa, T. Nishinaga, K. Yoza and Y. Mazaki, *Angew. Chem. Int. Ed.*, 2015, **54**, 2734–2738.

[83] Ambeed, *Dithieno-thiophene*, 2023, `https://www.ambeed.com/products/3593-75-7.html`, 02,14, 2023.

[84] P. B. Karadakov and T. Riley, *Chem. Eur. J.*, 2023, **29**, e202203400.

[85] K. Y. Chernichenko, V. V. Sumerin, R. V. Shpanchenko, E. S. Balenkova and V. G. Nenajdenko, *Angew. Chem. Int. Ed.*, 2006, **45**, 7367–7370.

[86] N. N. Karaush-Karmazin, G. V. Baryshnikov, L. I. Valiulina, R. Valiev, H. Ågren and B. F. Minaev, *New J. Chem.*, 2019, **43**, 12178–12190.

[87] S. Hashimoto, R. Kishi and K. Tahara, *New J. Chem.*, 2022, **46**, 22703–22714.

[88] G. V. Baryshnikov, R. R. Valiev, N. N. Karaush and B. F. Minaev, *Phys. Chem. Chem. Phys.*, 2014, **16**, 15367–15374.

[89] Y. Yang, S. Helili and A. Kerim, *Mol. Phys.*, 2022, **120**, e2060146.

[90] L. H. Nguyen, *ACS Omega*, 2021, **6**, 30085–30092.

[91] B. Lousen, S. K. Pedersen, P. Bols, K. H. Hansen, M. R. Pedersen, O. Hammerich, S. Bondarchuk, B. Minaev, G. V. Baryshnikov, H. Ågren and M. Pittelkow, *Chem. Eur. J.*, 2020, **26**, 4935–4940.

[92] C. B. Nielsen, T. Brock-Nannestad, P. Hammershøj, T. K. Reenberg, M. Schau-Magnussen, D. Trpcevski, T. Hensel, R. Salcedo, G. V. Baryshnikov, B. F. Minaev and M. Pittelkow, *Chem. Eur. J.*, 2013, **19**, 3898–3904.

[93] M. Plesner, T. Hensel, B. E. Nielsen, F. S. Kamounah, T. Brock-Nannestad, C. B. Nielsen, C. G. Tortzen, O. Hammerich and M. Pittelkow, *Org. Biomol. Chem.*, 2015, **13**, 5937—5943.

[94] Y. Nagata, S. Kato, Y. Miyake and H. Shinokubo, *Org. Lett.*, 2017, **19**, 2718–2721.

[95] R. G. Lawton and W. E. Barth, *J. Am. Chem. Soc.*, 1971, **93**, 1730–1745.

[96] E. Steiner, P. W. Fowler and L. W. Jenneskens, *Angew. Chem., Int. Ed. Engl.*, 2001, **40**, 362–366.

[97] W. Winter and H. Straub, *Angew. Chem. Int. Ed. Engl.*, 1978, **17**, 127–128.

[98] P. B. Karadakov, J. Gerratt, D. L. Cooper, M. Raimondi and M. Sironi, *Int. J. Quantum Chem.*, 1996, **60**, 545–552.

[99] M. L. McKee, M. Balci, H. Kilic and E. Yurtsever, *J. Phys. Chem. A*, 1998, **102**, 2351–2356.

[100] M. Ø. Jensen, T. Thorsteinsson and A. E. Hansen, *Int. J. Quantum Chem.*, 2002, **90**, 616–628.

[101] J. K. Pagano, J. Xie, K. A. Erickson, S. K. Cope, B. L. Scott, R. Wu, R. Waterman, D. E. Morris, P. Yang, L. Gagliardi *et al.*, *Nature*, 2020, **578**, 563–567.

[102] M. Gantenbein, X. Li, S. Sangtarash, J. Bai, G. Olsen, A. Alqorashi, W. Hong, C. J. Lambert and M. R. Bryce, *Nanoscale*, 2019, **11**, 20659–20666.

[103] W. Zeng, O. El Bakouri, D. W. Szczepanik, H. Bronstein and H. Ottosson, *Chem. Sci. J.*, 2021, **12**, 6159–6171.

[104] S. Escayola, C. Tonnelé, E. Matito, A. Poater, H. Ottosson, M. Solà and D. Casanova, *Angew. Chem. Int. Ed.*, 2021, **60**, 10255–10265.

[105] O. Ivasenko, J. M. MacLeod, K. Y. Chernichenko, E. S. Balenkova, R. V. Shpanchenko, V. G. Nenajdenko, F. Rosei and D. F. Perepichka, *Chem. Commun.*, 2009, 1192–1194.

[106] Z. Chen, C. S. Wannere, C. Corminboeuf, R. Puchta and P. v. R. Schleyer, *Chem. Rev.*, 2005, **105**, 3842–3888.

[107] S. Pelloni, A. Ligabue and P. Lazzeretti, *Org. Lett.*, 2004, **6**, 4451–4454.

[108] P. B. Karadakov, *Chemistry*, 2021, **3**, 861–872.

[109] P. v. R. Schleyer, M. Manoharan, H. Jiao and F. Stahl, *Org. Lett.*, 2001, **3**, 3643–3646.

[110] G. Portella, J. Poater, J. M. Bofill, P. Alemany and M. Sola, *J. Org. Chem.*, 2005, **70**, 2509–2521.

[111] P. Bultinck, *Faraday Discuss.*, 2007, **135**, 347–365.

[112] P. W. Fowler and W. Myrvold, *J. Phys. Chem. A*, 2011, **115**, 13191–13200.

[113] C.-H. Wu, L. J. Karas, H. Ottosson and J. I.-C. Wu, *Proc. Natl. Acad. Sci.*, 2019, **116**, 20303–20308.

[114] E. Osawa, *Kagaku*, 1970, **25**, 854–863.

[115] E. Osawa, *Philos. Trans. R. Soc. London, Ser. A*, 1993, **343**, 1–8.

[116] D. E. H. . Jones, *New Sci.*, 1966, **32**, 245.

[117] M. Krzeszewski, H. Ito and K. Itami, *J. Am. Chem. Soc.*, 2021, **144**, 862–871.

[118] C. H. Arnaud, *Check out the molecules of the year*, 2021, `https://cen.acs.org/content/cen/articles/99/i45/CENs-Year-Chemistry-2021.html`, Accessed: 12 March 2025.

[119] H. Rzepa, *Blog Post*, 2021, `https://www.ch.imperial.ac.uk/rzepa/blog/?p=24503`, Accessed: 12 March 2025.

[120] H. Christoph, J. Grunenberg, H. Hopf, I. Dix, P. G. Jones, M. Scholtissek and G. Maier, *Chem. -Eur. J.*, 2008, **14**, 5604–5616.

[121] R. Bhola, T. Bally, A. Valente, M. K. Cyrański, Ł. Dobrzycki, S. M. Spain, P. Rempała, M. R. Chin, B. T. King *et al.*, *Angew. Chem. Int. Ed.*, 2009, **49**, 399–402.

[122] K. Yamamoto, T. Harada, Y. Okamoto, H. Chikamatsu, M. Nakazaki, Y. Kai, T. Nakao, M. Tanaka, S. Harada and N. Kasai, *J. Am. Chem. Soc.*, 1988, **110**, 3578–3584.

[123] K. Yamamoto, H. Sonobe, H. Matsubara, M. Sato, S. Okamoto and K. Kitaura, *Angew. Chem. Int. Ed. Engl.*, 1996, **35**, 69–70.

[124] K. Yamamoto, T. Harada, M. Nakazaki, T. Naka, Y. Kai, S. Harada and N. Kasai, *J. Am. Chem. Soc.*, 1983, **105**, 7171–7172.

[125] C.-N. Feng, M.-Y. Kuo and Y.-T. Wu, *Angew. Chem.*, 2013, **125**, 7945–7948.

[126] H. A. Staab and F. Diederich, *Chem. Ber.*, 1983, **116**, 3487–3503.

[127] H. A. Staab, F. Diederich, C. Krieger and D. Schweitzer, *Chem. Ber.*, 1983, **116**, 3504–3512.

[128] K. Du and Y. Wang, *J. Am. Chem. Soc.*, 2023, **145**, 10763–10778.

[129] S. M. Bachrach, *J. Org. Chem.*, 2023, **88**, 7962–7976.

[130] S. Cross, M. M. Kuttel, J. E. Stone and J. E. Gain, *J. Mol. Graphics Modell.*, 2009, **28**, 131–139.

[131] P. B. Karadakov and E. Cummings, *Chem. Comm.*, 2024, **60**, 14633–14636.

[132] M. Alizadeh, M. Jalal, K. Hamed, A. Saber, S. Kheirouri, F. Pourteymour Fard Tabrizi and N. Kamari, *J. Inflamm. Res.*, 2020, **13**, 451–463.

[133] F. Dumur, *Catalysts*, 2023, **13**, 493.

[134] T. Luo, Y. Wang, J. Hao, P.-A. Chen, Y. Hu, B. Chen, J. Zhang, K. Yang and Z. Zeng, *Angew. Chem.*, 2023, **135**, e202214653.

[135] R. Bielski and G. Grynkiewicz, *Green Chem.*, 2021, **23**, 7458–7487.

[136] E. Hückel, *Z. physik*, 1931, **70**, 204–286.

[137] E. Hückel, *Z Phys Chem (N F)*, 1932, **76**, 628–648.

[138] W. von E. Doering and F. L. Detert, *J. Am. Chem. Soc.*, 1951, **73**, 876–877.

[139] N. C. Baird, *J. Am. Chem. Soc.*, 1972, **94**, 4941–4948.

[140] W. E. Barth and R. G. Lawton, *J. Am. Chem. Soc.*, 1966, **88**, 380–381.

[141] E. Cummings and P. B. Karadakov, *ChemPhysChem*, 2024, e202400758.

[142] N. N. Karaush-Karmazin, G. V. Baryshnikov and B. F. Minaev, *Chem.*, 2021, **3**, 1411–1436.

[143] A. D. Becke, *J. Chem. Phys.*, 1993, **98**, 5648–5652.

[144] P. J. Stephens, F. J. Devlin, C. F. Chabalowski and M. J. Frisch, *J. Phys. Chem.*, 1994, **98**, 11623–11627.

[145] S. Grimme, S. Ehrlich and L. Goerigk, *J. Comp. Chem.*, 2011, **32**, 1456–1465.

[146] F. Weigend and R. Ahlrichs, *Phys. Chem. Chem. Phys.*, 2005, **7**, 3297–3305.

[147] K. Xiao, Y. Liu, T. Qi, W. Zhang, F. Wang, J. Gao, W. Qiu, Y. Ma, G. Cui, S. Chen *et al.*, *J. Am. Chem. Soc.*, 2005, **127**, 13281–13286.

[148] R. Pino-Rios, R. Báez-Grez and M. Sola, *Phys. Chem. Chem. Phys.*, 2021, **23**, 13574–13582.

[149] W. D. A. Ghosh, I. H. Wasbotten and J. C. Swarts, *Eur. J. Inorg. Chem.*, 2005, 4479–4485.

[150] S. K. M. Bröring and C. Kleeberg, *Angew. Chem., Int. Ed.*, 2008, **47**, 5658–5660.

[151] T. Ito, Y. Hayashi, S. Shimizu, J.-Y. Shin, N. Kobayashi and H. Shinokubo, *Angew. Chem., Int. Ed.*, 2012, **51**, 8542–8545.

[152] R. Nozawa, H. Tanaka, W.-Y. Cha, Y. Hong, I. Hisaki, S. Shimizu, J.-Y. Shin, T. Kowalczyk, S. Irle, D. Kim and H. Shinokubo, *Nat. Commun.*, 2016, **7**, 13620.

[153] T. Yonezawa, S. A. Shafie, S. Hiroto and H. Shinokubo, *Angew. Chem., Int. Ed.*, 2017, **56**, 11822–11825.

[154] M. J. W. M. J. G. Peach and D. J. Tozer, *J. Chem. Theory Comput.*, 2011, **7**, 3578–3585.

[155] C. A. A. Chantzis, A. D. Laurent and D. Jacquemin, *J. Chem. Theory Comput.*, 2013, **9**, 4517–4525.

[156] T. Lu and F. Chen, *J. Comput. Chem.*, 2012, **33**, 580–592.

[157] C. Adamo and V. Barone, *J. Chem. Phys.*, 1999, **110**, 6158–6170.

[158] J.-D. Chai and M. Head-Gordon, *J. Chem. Phys.*, 2008, **128**, 084106.

[159] K. Aidas, C. Angeli, K. L. Bak, V. Bakken, R. Bast, L. Boman, O. Christiansen, R. Cimiraglia, S. Coriani, P. Dahle, E. K. Dalskov, U. Ekström, T. Enevoldsen, J. J. Eriksen, P. Ettenhuber, B. Fernández, L. Ferrighi, H. Fliegl, L. Frediani, K. Hald, A. Halkier, C. Hättig, H. Heiberg, T. Helgaker, A. C. Hennum, H. Hettema, R. Hjerteæs, S. Höst, I.-M. Höyvik, M. F. Iozzi, B. Jansík, H. J. A. Jensen, D. Jonsson, P. Jörgensen, J. Kauczor, S. Kirpekar, T. Kjærgaard, W. Klopper, S. Knecht, R. Kobayashi, H. Koch, J. Kongsted, A. Krapp, K. Kristensen, A. Ligabue, O. B. Lutnæs, J. I. Melo, K. V. Mikkelsen, R. H. Myhre, C. Neiss, C. B. Nielsen, P. Norman, J. Olsen, J. M. H. Olsen, A. Osted, M. J. Packer, F. Pawlowski, T. B. Pedersen, P. F. Provasi, S. Reine, Z. Rinkevicius, T. A. Ruden, K. Ruud, V. V. Rybkin, P. Sałek, C. C. M. Samson, A. S. de Merás, T. Saue, S. P. A. Sauer, B. Schimmelpfennig, K. Sneskov, A. H. Steindal, K. O. Sylvester-Hvid, P. R. Taylor, A. M. Teale, E. I. Tellgren, D. P. Tew, A. J. Thorvaldsen, L. Thøgersen, O. Vahtras, M. A. Watson, D. J. D. Wilson, M. Ziolkowski and H. Ågren, *Wiley Interdiscip. Rev.: Comput. Mol. Sci.*, 2014, **4**, 269–284.

[160] P. B. Karadakov and S. Saito, *Angew. Chem., Int. Ed.*, 2020, **59**, 9228–9230.

[161] P. B. Karadakov and E. Cummings, *Phys. Chem. Chem. Phys.*, 2024, **26**, 25385–25392.

[162] J. Conradie, C. Foroutan-Nejad and A. Ghosh, *Sci. Rep.*, 2019, **9**, 4852.

[163] H. Fliegl, R. Valiev, F. Pichierri and D. Sundholm, *Chem. Modell.*, 2018, **14**, 1–42.

[164] R. Nozawa, K. Yamamoto, I. Hisaki, J.-Y. Shin and H. Shinokubo, *Chem. Commun.*, 2016, **52**, 7106–7109.

[165] T. Yoshida, K. Takahashi, Y. Ide, R. Kishi, J.-Y. Fujiyoshi, S. Lee, Y. Hiraoka, D. Kim, M. Nakano, T. Ikeue, H. Yamada and H. Shinokubo, *Angew. Chem., Int. Ed.*, 2018, **57**, 2209–2213.

[166] H. Fliegl, S. Taubert, O. Lehtonen and D. Sundholm, *Phys. Chem. Chem. Phys.*, 2011, **13**, 20500–20518.

[167] H. Fliegl, F. Pichierri and D. Sundholm, *J. Phys. Chem. A*, 2015, **119**, 2344–2350.

[168] R. Nozawa, J. Kim, J. Oh, A. Lamping, Y. Wang, S. Shimizu, I. Hisaki, T. Kowalczyk, H. Fliegl, D. Kim and H. Shinokubo, *Nat. Commun.*, 2019, **10**, 3576.

[169] P. B. Karadakov and D. L. Cooper, *J. Phys. Chem. A*, 2016, **120**, 8769–8779.

[170] H. Fliegl, D. Sundholm, S. Taubert, J. Jusélius and W. Klopper, *J. Phys. Chem. A*, 2009, **113**, 8668–8676.

[171] R. V. Williams, *Chem. Rev.*, 2001, **101**, 1185–1204.

[172] T. Ito, Y. Hayashi, S. Shimizu, J.-I. Shin, N. Kobayashi and H. Shinokubo, *Angew. Chem., Int. Ed.*, 2012, **51**, 8542–8545.

[173] T. Yamakado, S. Takahashi, K. Watanabe, Y. Matsumoto, A. Osuka and S. Saito, *Angew. Chem., Int. Ed.*, 2018, **57**, 5438–5443.

[174] R. Kimura, H. Kuramochi, P. Liu, T. Yamakado, A. Osuka, T. Tahara and S. Saito, *Angew. Chem., Int. Ed.*, 2020, **59**, 16430–16435.

[175] R. Kotani, L. Liu, P. Kumar, H. Kuramochi, T. Tahara, P. Liu, A. Osuka, P. B. Karadakov and S. Saito, *J. Am. Chem. Soc.*, 2020, **142**, 14985–14992.

[176] J. Pang, S. Peng, C. Hou, H. Zhao, Y. Fan, C. Ye, N. Zhang, T. Wang, Y. Cao, W. Zhou *et al.*, *ACS sensors*, 2023, **8**, 482–514.

[177] C. Cheng, Q. Liang, M. Yan, Z. Liu, Q. He, T. Wu, S. Luo, Y. Pan, C. Zhao and Y. Liu, *J. Hazard. Mater.*, 2022, **424**, 127721.

[178] A. Jiříčková, O. Jankovsky, Z. Sofer and D. Sedmidubsky, *Mater.*, 2022, **15**, 920.

[179] A. F. Carvalho, B. Kulyk, A. J. Fernandes, E. Fortunato and F. M. Costa, *Adv. Mater.*, 2022, **34**, 2101326.

[180] J. Liu, S. Bao and X. Wang, *Micromachines*, 2022, **13**, 184.

[181] A. J. Mannix, B. Kiraly, M. C. Hersam and N. P. Guisinger, *Nat. Rev. Chem.*, 2017, **1**, 0014.

[182] A. R. Pitochelli and F. M. Hawthorne, *J. Am. Chem. Soc.*, 1960, **82**, 3228–3229.

[183] M. F. Hawthorne, D. C. Young and P. A. Wegner, *J. Am. Chem. Soc.*, 1965, **87**, 1818–1819.

[184] J. L. Gay-Lussac and L. J. Thénard, *Ann. Chim. Phys*, 1808, **68**, 169–174.

[185] H. Davy, *Philos. Trans. Royal Soc. A PHILOS T R SOC A*, 1808, 333–370.

[186] D. E. Sands and J. Hoard, *J. Am. Chem. Soc.*, 1957, **79**, 5582–5583.

[187] A. R. Oganov, J. Chen, C. Gatti, Y. Ma, Y. Ma, C. W. Glass, Z. Liu, T. Yu, O. O. Kurakevych and V. L. Solozhenko, *Nature*, 2009, **457**, 863–867.

[188] Z. Zhang, E. S. Penev and B. I. Yakobson, *Chem. Soc. Rev.*, 2017, **46**, 6746–6763.

[189] A. J. Mannix, Z. Zhang, N. P. Guisinger, B. I. Yakobson and M. C. Hersam, *Nat. Nanotechnol.*, 2018, **13**, 444–450.

[190] A. Oganov and V. Solozhenko, *J. Superhard Mater.*, 2009, **31**, 285–291.

[191] L. Bolaños, K. Lukaszewski, I. Bonilla and D. Blevins, *Plant Physiol. Biochem.*, 2004, **42**, 907–912.

[192] S. Meng, Q. Chen, H. Lin, F. Zhou, Y. Gong, C. Pan and S. Lu, *Nanomaterials*, 2021, **11**, 687.

[193] S. Krishnan and K. Senthilkumar, *Chem. Phys. Lett.*, 2022, **804**, 139914.

[194] S. Wang, Y. Ren, Z. Wang, X. Jiang, S. Xu, X. Zhang, S. Zhao, W. A. Zalloum, X. Liu and P. Zhan, *Expert Opin Drug Discov.*, 2022, **17**, 1329–1340.

[195] Z. J. Leśnikowski, *Expert Opin Drug Discov.*, 2021, **16**, 481–483.

[196] H. F. Schaefer III and F. E. Harris, *Phys. Rev.*, 1968, **167**, 67.

[197] M. J. Dewar, *J. Am. Chem. Soc.*, 1984, **106**, 669–682.

[198] D. Cremer and J. Gauss, *J. Am. Chem. Soc*, 1986, **108**, 7467–7477.

[199] D. Cremer and E. Kraka, *J. Am. Chem. Soc*, 1985, **107**, 3800–3810.

[200] D. Cremer and E. Kraka, *J. Am. Chem. Soc*, 1985, **107**, 3811–3819.

[201] M. Dewar and M. McKee, *Pure Appl. Chem.*, 1980, **52**, 1431–1441.

[202] M. J. Dewar, *Bull. Soc. Chim. Belg.*, 1979, **88**, 957–967.

[203] L. Rincon, R. Almeida, J. E. Alvarellos, D. Garcia-Aldea, A. Hasmy and C. Gonzalez, *Dalton Trans.*, 2009, **17**, 3328–3333.

[204] G. Wei, Z. Pu, R. Zou, G. Li and Q. Luo, *Sci. China Chem.*, 2010, **53**, 202–209.

[205] B. Kiran, S. Bulusu, H.-J. Zhai, S. Yoo, X. C. Zeng and L.-S. Wang, *PNAS*, 2005, **102**, 961–964.

[206] D. E. Bean and P. W. Fowler, *J. Phys. Chem. C*, 2009, **113**, 15569–15575.

[207] F. A. Cotton, G. Wilkinson, C. A. Murillo and M. Bochmann, *Advanced inorganic chemistry*, John Wiley and Sons, Inc., 1999.

[208] C. L. Perkins, M. Trenary and T. Tanaka, *Phys. rev. lett.*, 1996, **77**, 4772.

[209] H. Hubert, B. Devouard, L. A. Garvie, M. O'Keeffe, P. R. Buseck, W. T. Petuskey and P. F. McMillan, *Nature*, 1998, **391**, 376–378.

[210] I. Boustani, *Int. J. Quantum Chem.*, 1994, **52**, 1081–1111.

[211] A. Ricca and C. W. Bauschlicher Jr, *Chem. phys.*, 1996, **208**, 233–242.

[212] I. Boustani, *Phys. Rev. B*, 1997, **55**, 16426.

[213] H.-J. Zhai, B. Kiran, J. Li and L.-S. Wang, *Nat. mater.*, 2003, **2**, 827–833.

[214] L.-S. Wang, H.-S. Cheng and J. Fan, *J. Chem. Phys.*, 1995, **102**, 9480–9493.

[215] K.-M. Ho, A. A. Shvartsburg, B. Pan, Z.-Y. Lu, C.-Z. Wang, J. G. Wacker, J. L. Fye and M. F. Jarrold, *Nature*, 1998, **392**, 582–585.

[216] R. B. King, *J. Phys. Chem. A*, 2022, **126**, 901–909.

[217] L. Hanley, J. L. Whitten and S. L. Anderson, *J. Phys. Chem.*, 1988, **92**, 5803–5812.

[218] L. Hanley and S. L. Anderson, *J. Chem. Phys.*, 1988, **89**, 2848–2860.

[219] H. Prinzbach, A. Weiler, P. Landenberger, F. Wahl, J. Wörth, L. T. Scott, M. Gelmont, D. Olevano and B. v. Issendorff, *Nature*, 2000, **407**, 60–63.

[220] L. Chkhartishvili, 2017 IEEE 7th International Conference Nanomaterials: Application & Properties (NAP), 2017, pp. 04NESP10–1–04NESP10–5.

[221] M. Monajjemi, Y. Rafiee, F. Mollaamin and S. Shahriari, *Russ. J. Phys. Chem.*, 2023, **97**, 151–167.

[222] H.-J. Zhai, L.-S. Wang, A. N. Alexandrova, A. I. Boldyrev and V. G. Zakrzewski, *J. Phys. Chem. A*, 2003, **107**, 9319–9328.

[223] K. E. Horner and P. B. Karadakov, *J. Org. Chem.*, 2015, **80**, 7150–7157.

[224] Q. S. Li and H. W. Jin, *J. Phys. Chem. A*, 2002, **106**, 7042–7047.

[225] R. Islas, T. Heine and G. Merino, *Acc. Chem. Res.*, 2012, **45**, 215–228.

[226] L. V. Duong, D. T. T. Mai, M. P. Pham-Ho and M. T. Nguyen, *Phys. Chem. Chem. Phys.*, 2019, **21**, 13030–13039.

[227] A. G. Arvanitidis, K. Z. Lim, R. W. A. Havenith and A. Ceulemans, *Int. J. Quantum Chem.*, 2018, **118**, e25575.

[228] M. Atiş, C. Özdoşan and Z. B. Güvenç, *Chinese J. Chem. Phys.*, 2009, **22**, 380.

[229] J. Yan, T. Slanina, J. Bergman and H. Ottosson, *Chem. A Eur. J.*, 2023, **29**, e202203748.

[230] H. Kim, W. Park, Y. Kim, M. Filatov, C. H. Choi and D. Lee, *Nat. Commun*, 2021, **12**, 5409.

[231] B. Durbeej, J. Wang and B. Oruganti, *ChemPlusChem*, 2018, **83**, 958–967.

[232] A. B. Skov, N. Ree, A. S. Gertsen, P. Chabera, J. Uhlig, J. S. Lissau, L. Nucci, T. Pullerits, K. V. Mikkelsen, M. Brøndsted Nielsen *et al.*, *ChemPhotoChem*, 2019, **3**, 619–629.

[233] B. Oruganti, J. Wang and B. Durbeej, *Org. Lett.*, 2017, **19**, 4818–4821.

[234] J. Wang, B. Oruganti and B. Durbeej, *ChemPhotoChem*, 2019, **3**, 450–460.

[235] B. Oruganti, P. Pál Kalapos, V. Bhargav, G. London and B. Durbeej, *J. Am. Chem. Soc.*, 2020, **142**, 13941–13953.

[236] B. J. Lampkin, Y. H. Nguyen, P. B. Karadakov and B. VanVeller, *Phys.Chem. Chem. Phys.*, 2019, **21**, 11608–11614.

[237] L. J. Karas, C.-H. Wu, H. Ottosson and J. I. Wu, *Chem. Sci.*, 2020, **11**, 10071–10077.

[238] Y. Zhao and D. G. Truhlar, *Theor. Chem. Acc.*, 2008, **120**, 215–241.

[239] T. Yanai, D. P. Tew and N. C. Handy, *Chem. Phys. Lett.*, 2004, **393**, 51–57.

[240] V. Fock, *Phys. Rev.*, 1951, **84**, 226–232.

[241] C. C. J. Roothaan, *Rev. Mod. Phys.*, 1951, **23**, 69–89.

[242] D. Zhao, K. D. Doney and H. Linnartz, *ApJ*, 2014, **791**, L28.

[243] T. M. Krygowski and M. K. Cyrański, *Tetrahedron*, 1999, **55**, 11143–11148.

[244] P. W. Fowler and E. Steiner, *J. Phys. Chem. A*, 1997, **101**, 1409–1413.

[245] P. B. Karadakov and N. Preston, *Phys. Chem. Chem. Phys.*, 2021, **23**, 24750–24756.

[246] E. Heilbronner, *Tetrahedron Letts*, 1964, **5**, 1923–1928.

[247] P. B. Karadakov and D. L. Cooper, *Chem. Phys. Chem.*, 2018, **19**, 3186–3190.

[248] P. B. Karadakov, M. Di and D. L. Cooper, *J. Phys. Chem. A*, 2020, **124**, 9611–9616.

Abbreviations

Abbreviation	Definition
B3LYP	Becke, 3-parameter, Lee–Yang–Parr hybrid functional
CAM-B3LYP	Coulomb-attenuating method B3LYP
DFT	Density Functional Theory
DFT-D3(BJ)	DFT with Grimme's D3 dispersion correction and Becke–Johnson damping
GIAO	Gauge-Including Atomic Orbitals
HF	Hartree–Fock
HOMA	Harmonic Oscillator Model of Aromaticity
HOMER	Harmonic Oscillator Model of Excited-State Aromaticity/Antiaromaticity
M06	Minnesota 2006 density functional
M06-2X	Minnesota 2006 double hybrid with 54% HF exchange
MP2	Second-order Møller–Plesset perturbation theory
NICS	Nucleus-independent chemical shift
PBE0	Perdew–Burke–Ernzerhof hybrid functional
RB3LYP	Restricted B3LYP (same spatial orbitals for α and β spins)
SCF	Self-consistent field
S_0	Singlet ground electronic state
T_1	First triplet excited state
T_2	Second triplet excited state
TDDFT	Time-Dependent Density Functional Theory
TDA	Tamm–Dancoff Approximation
TZVP	Triple-zeta valence with polarisation basis set
TZVPPD	Triple-zeta valence with double polarisation and diffuse functions
UB3LYP	Unrestricted B3LYP (separate orbitals for α and β spins)
VTZ	Valence triple-zeta basis set
ωB97X	Range-separated hybrid functional with long-range correction

Appendix

Table 14: B3LYP-GIAO/6-311++(2d,2p)//B3LYP/def2-TZVP NICS calculations of annulenes.

	State: S_0, Geometry: S_0			State: T_1, Geometry: S_0			State: T_1, Geometry: T_1			State: S_0, Geometry: T_1		
NICS	(0)	(+1)	(−1))	(0)	(+1)	(−1))	(0)	(+1)	(−1))	(0)	(+1)	(−1))
$C_3H_3^+$	−22.9	−14.8	−14.8	1125.7	152.2	152.2	−85.5	−25.4	−25.4	−38.1	−14.7	−14.7
$C_3H_3^-$	−12.1	3.3	7.7	−19.9	−10.4	−6.6	−31.9	−9.9	−6.6	−64.0	−43.2	−25.4
$C_4H_4^{2+}$	−7.0	−14.8	−14.8	265.2	308.1	308.1	−2.1	−1.9	−1.9	129.0	18.0	18.0
C_4H_4	27.2	17.8	17.8	2.1	−5.0	−5.0	−1.5	−6.5	−6.5	−344.4	−303.8	−303.8
$C_4H_4^{2-}$	−58.8	−27.5	−27.5	28.0	22.7	22.7	−4.6	−7.3	2.1	10.6	3.8	11.3
$C_5H_5^+$	87.2	66.5	66.5	−1.6	−9.3	−9.3	−2.1	−9.9	−9.9	−63.1	−63.8	−63.8
$C_5H_5^-$	−12.0	−9.4	−9.4	92.3	76.7	76.7	3.8	−0.1	−0.1	−5.4	−8.2	−6.2
$C_6H_6^{2+}$	10.9	6.8	6.8	−2.0	−8.5	−8.5	−1.3	−8.6	−8.6	−47.7	−49.5	−49.5
C_6H_6	−7.6	−9.9	−9.9	107.1	84.0	84.0	31.1	22.5	22.5	−7.4	−9.6	−9.6
$C_6H_6^{2-}$	−4.1	−10.0	−4.7	−0.9	−5.5	−0.5	7.4	−1.6	−0.2	−10.7	−13.9	−12.1
$C_7H_7^+$	−6.0	−9.4	−9.4	946.8	793.2	793.2	17.2	11.0	11.0	−3.2	−7.5	−7.5
$C_7H_7^-$	156.5	126.8	126.8	−4.4	−5.5	−5.5	−9.7	−9.5	−9.5	−228.6	−189.2	−189.2
$C_8H_8^{2+}$	−6.7	−9.0	−9.0	392.1	327.4	327.4	5.8	1.1	1.1	−1.1	−6.1	−6.1
C_8H_8	4.7	0.8	0.8	−3.2	−6.0	−6.0	−10.9	−10.9	−10.9	−106.6	−90.0	−90.0
$C_8H_8^{2-}$	−12.0	−10.7	−10.7	90.1	74.1	74.1	32.9	26.3	26.3	−14.3	−12.0	−12.0
$C_9H_9^+$	−12.0	−12.6	−12.6	39.2	32.2	32.2	−9.5	−10.1	−10.1	−2784.9	−2336.6	−2336.4
$C_9H_9^-$	−13.7	−12.3	−12.3	94.5	78.6	78.6	−11.0	−10.0	−10.0	−206.9	−177.0	−177.0
$C_{10}H_{10}^{2+}$	−11.5	−17.5	−12.1	50.9	39.5	46.6	−6.3	−8.7	−8.7	46.1	38.0	38.0
$C_{10}H_{10}$	2.6	0.1	0.0	−1.6	−3.7	−3.7	0.3	−2.3	−2.3	3.9	−5.1	−5.1
$C_{10}H_{10}^{2-}$	−6.0	−6.0	−6.0	161.9	140.1	142.6	157.4	133.7	133.7	−16.5	−15.1	−15.1

Table 15: CAM-B3LYP-GIAO/6-311++(2d,2p)//B3LYP/def2-TZVP NICS calculations of annulenes.

	State: S_0, Geometry: S_0			State: T_1, Geometry: S_0			State: T_1, Geometry: T_1			State: S_0, Geometry: T_1		
NICS	(0)	(+1)	(−1))	(0)	(+1)	(−1))	(0)	(+1)	(−1))	(0)	(+1)	(−1))
$C_3H_3^+$	−23.1	−15.0	−15.0	3.1	109.1	109.1	−32.1	−5.9	−5.6	−4.9	−18.6	−19.6
$C_3H_3^-$	−13.3	2.4	7.1	−24.6	4.2	−4.8	−32.7	−10.2	−6.8	−72.7	−50.6	−29.9
$C_4H_4^{2+}$	−6.7	−15.0	−15.0	327.3	377.0	377.0	−2.0	−1.9	−1.9	−129.1	−34.1	−34.1
C_4H_4	27.7	18.0	18.0	2.4	−5.0	−5.0	−1.3	−6.6	−6.6	−295.1	−262.7	−262.7
$C_4H_4^{2-}$	−53.0	−34.9	−34.9	28.9	23.5	23.5	−7.0	−3.1	1.7	9.0	14.9	20.1
$C_5H_5^+$	87.4	67.0	67.0	−9.4	−1.3	−1.3	−9.9	−2.0	−2.0	−61.9	−60.1	−60.1
$C_5H_5^-$	−11.7	−9.3	−9.3	72.8	60.1	60.1	3.5	−0.3	0.0	−8.1	−6.2	−5.1
$C_6H_6^{2+}$	11.5	7.0	7.0	−1.5	−8.5	−8.5	−1.0	−8.6	−8.6	−44.9	−47.8	−47.8
C_6H_6	−7.5	−10.0	−10.0	90.4	70.2	70.2	27.2	19.2	19.2	−7.4	−9.7	−9.7
$C_6H_6^{2-}$	−9.6	−4.5	−3.8	−6.3	−1.5	0.0	−8.9	−11.4	−10.6	−18.2	−17.4	−17.3
$C_7H_7^+$	−9.4	−5.9	−5.9	365.5	296.7	296.7	16.1	9.8	9.8	−3.1	−7.5	−7.5
$C_7H_7^-$	52.7	40.6	40.7	−6.0	−6.9	−6.9	−10.2	−10.0	−10.0	−218.9	−181.1	−181.1
$C_8H_8^{2+}$	−6.5	−8.9	−8.9	91.2	72.5	72.5	5.3	0.5	0.5	−1.1	−6.2	−6.2
C_8H_8	4.2	0.5	0.5	−3.1	−5.9	−5.9	−10.9	−10.9	−10.9	−98.5	−83.5	−83.5
$C_8H_8^{2-}$	−12.9	−11.2	−11.2	55.3	45.0	45.1	24.8	19.6	19.6	−12.6	−11.0	−11.0
$C_9H_9^+$	−12.2	−12.8	−12.8	30.2	24.3	24.3	−9.4	−10.1	−10.1	−230.8	−197.6	−197.6
$C_9H_9^-$	−13.8	−12.4	−12.4	42.2	34.3	34.3	−11.1	−10.4	−10.4	2036.7	1704.4	1704.4
$C_{10}H_{10}^{2+}$	−11.6	−17.7	−12.3	30.6	20.8	28.3	−6.2	−8.7	−8.7	40.0	32.3	32.3
$C_{10}H_{10}$	66.3	56.6	57.7	−0.9	−3.1	−3.1	−0.1	−2.7	−2.7	4.1	−5.2	−5.2
$C_{10}H_{10}^{2-}$	−10.7	−10.2	−10.1	2.4	−0.1	−0.1	DF	DF	DF	−481.7	−413.3	−413.3

Table 16: HF-GIAO/6-311++(2d,2p)//B3LYP/def2-TZVP NICS calculations of annulenes.

	State: S_0, Geometry: S_0			State: T_1, Geometry: S_0			State: T_1, Geometry: T_1			State: S_0, Geometry: T_1		
NICS	(0)	(+1)	(−1))	(0)	(+1)	(−1))	(0)	(+1)	(−1))	(0)	(+1)	(−1))
$C_3H_3^+$	−28.1	−16.0	−16.0	−159.6	15.4	15.4	−37.6	−6.9	−6.5	−75.9	61.0	114.0
$C_3H_3^-$	−16.4	−0.6	4.9	−27.1	−12.7	−8.8	−37.0	−11.9	−8.5	−344.4	−290.5	−202.4
$C_4H_4^{2+}$	−8.9	−15.9	−15.9	160.5	161.3	161.3	−2.7	−2.6	−2.6	−9.0	−9.4	−9.4
C_4H_4	27.0	18.8	18.8	−1.9	−6.4	−6.4	−5.4	−7.9	−7.9	−418.7	−371.6	−371.6
$C_4H_4^{2-}$	−31.8	−22.8	−22.8	20.9	19.3	19.3	−7.2	−4.5	2.0	9.1	35.3	29.8
$C_5H_5^+$	47.2	33.4	33.4	−10.2	−4.1	−4.1	−10.0	−2.0	−2.0	−148.9	−159.1	−159.1
$C_5H_5^-$	−13.6	−9.9	−9.9	−5.0	−11.0	−11.0	−1.1	−5.7	−4.0	−8.3	−6.5	−6.1
$C_6H_6^{2+}$	11.1	5.7	5.7	−1.8	−8.9	−8.9	−2.1	−9.3	−9.3	−153.0	−145.2	−145.2
C_6H_6	−9.3	−10.8	−10.8	38.4	28.1	28.1	11.7	7.1	7.1	−9.1	−10.6	−10.6
$C_6H_6^{2-}$	−14.1	−7.3	−7.5	0.1	5.4	0.0	−10.9	−12.5	−11.6	−19.0	−18.5	−17.6
$C_7H_7^+$	−10.3	−7.4	−7.4	DF	DF	DF	8.6	3.4	3.4	−4.0	−8.1	−8.1
$C_7H_7^-$	36.0	27.5	27.6	−3.6	−4.5	−4.5	−11.7	−10.9	−10.9	3703.1	3047.1	3047.1
$C_8H_8^{2+}$	−7.5	−9.7	−9.7	12.1	7.2	7.2	3.6	−0.9	−0.9	−1.6	−6.8	−6.8
C_8H_8	2.7	−0.9	−0.9	−3.1	−5.9	−5.9	−12.3	−11.9	−11.9	−832.9	−693.8	−693.8
$C_8H_8^{2-}$	−13.7	−11.8	−11.8	19.5	15.7	15.8	28.9	23.3	23.3	−43.5	−31.3	−31.3
$C_9H_9^+$	−13.7	−13.9	−13.9	2.6	0.3	0.3	−10.0	−10.5	−10.5	232.4	196.2	196.2
$C_9H_9^-$	−15.1	−13.4	−13.4	14.1	11.1	11.1	−11.7	−10.5	−10.5	72.5	58.8	58.8
$C_{10}H_{10}^{2+}$	−12.6	−18.3	−13.0	DF	DF	DF	−7.0	−9.4	−9.4	14.3	9.7	9.7
$C_{10}H_{10}$	4.8	5.0	−2.9	0.2	−2.0	−2.0	−1.0	−3.6	−3.6	3.3	−6.2	−6.2
$C_{10}H_{10}^{2-}$	−10.1	−9.7	−9.6	DF	DF	DF	−17.2	−14.8	−14.8	205.8	176.7	176.7

Table 17: PBE0-GIAO/6-311++(2d,2p)//B3LYP/def2-TZVP NICS calculations of annulenes.

	State: S_0, Geometry: S_0			State: T_1, Geometry: S_0			State: T_1, Geometry: T_1			State: S_0, Geometry: T_1		
NICS	(0)	(+1)	(−1))	(0)	(+1)	(−1))	(0)	(+1)	(−1))	(0)	(+1)	(−1))
$C_3H_3^+$	−23.1	−14.8	−14.8	−31.5	97.0	97.0	−33.4	−6.2	−5.8	−5.9	−17.3	−16.8
$C_3H_3^-$	−12.9	3.1	7.6	−22.1	−11.2	−7.3	−33.3	−10.1	−6.9	−66.1	−45.2	−26.7
$C_4H_4^{2+}$	−7.2	−15.0	−15.0	251.3	291.5	291.5	−2.1	−1.8	−1.8	−670.9	−142.4	−142.4
C_4H_4	27.4	18.1	18.1	1.6	−5.0	−5.0	−2.0	−6.6	−6.6	−346.7	−305.8	−305.8
$C_4H_4^{2-}$	−20.5	−9.5	−9.5	27.2	22.1	22.1	−7.3	−4.6	1.8	4.5	11.5	11.7
$C_5H_5^+$	86.6	65.9	65.9	−9.4	−1.8	−1.8	−10.0	−2.4	−2.4	−64.4	−63.7	−63.7
$C_5H_5^-$	−12.4	−9.6	−9.6	57.6	46.6	46.6	2.2	−1.5	−1.0	−8.4	−6.4	−5.7
$C_6H_6^{2+}$	10.8	6.8	6.8	−1.9	−8.6	−8.6	−1.2	−8.7	−8.7	−48.3	−50.2	−50.2
C_6H_6	−7.7	−10.1	−10.1	92.6	71.9	71.9	28.1	20.0	20.0	−7.5	−9.8	−9.8
$C_6H_6^{2-}$	−10.5	−4.8	−4.4	−6.0	−1.6	0.0	5.2	−2.8	−1.4	−10.9	−14.1	−12.2
$C_7H_7^+$	−9.4	−5.9	−5.9	411.1	332.5	332.5	16.7	10.4	10.4	−3.1	−7.6	−7.6
$C_7H_7^-$	56.0	43.3	43.5	−5.7	−6.6	−6.6	−10.5	−10.2	−10.2	−222.3	−183.9	−183.9
$C_8H_8^{2+}$	−6.6	−9.0	−9.0	109.0	87.2	87.2	5.7	0.9	0.9	−1.1	−6.2	−6.2
C_8H_8	4.8	0.9	0.9	−3.6	−6.3	−6.3	−11.1	−11.0	−11.0	−104.6	−88.4	−88.4
$C_8H_8^{2-}$	−12.9	−11.3	−11.3	61.8	50.3	50.4	30.0	23.9	23.9	−9.1	−9.2	−9.2
$C_9H_9^+$	−12.2	−12.8	−12.8	34.0	27.6	27.6	−9.5	−10.2	−10.2	−2028.0	−1700.4	−1700.4
$C_9H_9^-$	−13.9	−12.5	−12.5	59.9	49.0	49.0	−11.2	−10.5	−10.5	−204.8	−175.3	−175.3
$C_{10}H_{10}^{2+}$	−11.6	−17.7	−12.3	43.6	32.7	40.0	−6.3	−8.8	−8.8	48.0	39.5	39.5
$C_{10}H_{10}$	119.5	103.0	104.9	−1.3	−3.5	−3.4	−0.1	−2.7	−2.7	4.0	−5.2	−5.2
$C_{10}H_{10}^{2-}$	−8.8	−8.4	−8.3	2.5	0.0	0.0	−16.0	−13.8	−13.8	−16.5	−15.2	−15.2

Table 18: M06-GIAO/6-311++(2d,2p)//B3LYP/def2-TZVP NICS calculations of annulenes.

	State: S_0, Geometry: S_0			State: T_1, Geometry: S_0			State: T_1, Geometry: T_1			State: S_0, Geometry: T_1		
NICS	(0)	(+1)	(−1))	(0)	(+1)	(−1))	(0)	(+1)	(−1))	(0)	(+1)	(−1))
$C_3H_3^+$	−24.6	−15.0	−15.0	2949.1	−522.2	−522.2	−32.1	−6.0	−5.7	−6.7	−17.0	−21.9
$C_3H_3^-$	−10.4	5.9	7.9	−18.1	−10.0	−5.1	−32.3	−9.9	−6.3	−105.9	−48.2	−63.0
$C_4H_4^{2+}$	−7.8	−15.1	−15.1	919.2	1070.5	1070.5	−1.0	−1.7	−1.7	102.9	13.6	13.6
C_4H_4	26.8	17.2	17.2	2.1	−5.0	−5.0	−1.6	−6.6	−6.6	−467.7	−409.4	−409.4
$C_4H_4^{2-}$	−12.7	−10.7	−10.7	31.8	25.8	25.8	−6.4	−3.4	2.0	87.9	353.8	156.5
$C_5H_5^+$	74.5	55.3	55.3	−9.4	−1.6	−1.6	−10.0	−2.2	−2.2	−70.2	−70.3	−70.3
$C_5H_5^-$	−12.1	−9.4	−9.4	77.2	63.7	63.7	3.8	0.9	0.7	−8.1	−6.2	−5.3
$C_6H_6^{2+}$	10.9	6.5	6.5	−1.8	−8.6	−8.6	−1.3	−8.8	−8.8	−58.2	−59.0	−59.0
C_6H_6	−7.6	−10.0	−10.0	111.1	86.7	86.7	31.4	22.6	22.6	−7.3	−9.7	−9.7
$C_6H_6^{2-}$	−9.0	−4.2	−2.8	−1.9	3.5	0.0	−16.8	−17.9	−16.2	−10.6	−14.0	−12.3
$C_7H_7^+$	−9.4	−5.8	−5.8	577.1	472.9	472.9	17.2	10.8	10.8	−3.0	−7.6	−7.6
$C_7H_7^-$	52.4	40.3	40.5	−9.0	−9.4	−9.4	−10.2	−10.0	−10.0	−246.0	−202.9	−202.9
$C_8H_8^{2+}$	−6.6	−9.0	−9.0	129.3	104.5	104.5	5.7	0.9	0.9	−1.1	−6.3	−6.3
C_8H_8	4.6	0.9	0.9	−3.3	−6.1	−6.1	−10.9	−10.9	−10.9	−121.0	−102.0	−102.0
$C_8H_8^{2-}$	−12.3	−11.8	−11.8	66.5	54.4	54.5	34.1	27.4	27.4	DF	DF	DF
$C_9H_9^+$	−12.1	−12.9	−12.9	37.6	30.7	30.7	−9.5	−10.2	−10.2	−228.0	−194.9	−194.9
$C_9H_9^-$	−13.8	−12.4	−12.4	72.9	60.1	60.1	−11.0	−10.4	−10.4	952.7	796.4	796.4
$C_{10}H_{10}^{2+}$	−11.6	−17.8	−12.3	48.0	36.8	44.1	−6.5	−8.9	−8.9	40.9	33.3	33.3
$C_{10}H_{10}$	DF	DF	DF	−1.5	−3.7	−3.7	0.0	−2.7	−2.7	3.4	−5.4	−5.4
$C_{10}H_{10}^{2-}$	DF	DF	DF	2.4	−0.2	−0.2	133.0	112.8	112.8	−221.8	−190.3	−190.3

Table 19: M06−2X-GIAO/6-311++(2d,2p)//B3LYP/def2-TZVP NICS calculations of annulenes.

	State: S_0, Geometry: S_0			State: T_1, Geometry: S_0			State: T_1, Geometry: T_1			State: S_0, Geometry: T_1		
NICS	(0)	(+1)	(−1))	(0)	(+1)	(−1))	(0)	(+1)	(−1))	(0)	(+1)	(−1))
$C_3H_3^+$	−20.8	−15.4	−15.4	212.7	59.1	59.1	−25.6	−4.2	−4.2	150.9	−157.3	45.1
$C_3H_3^-$	−11.1	2.8	8.1	−52.3	−47.3	1.1	−31.1	−10.8	−6.2	−61.9	−44.1	−24.3
$C_4H_4^{2+}$	−5.1	−15.5	−15.5	−99.4	−129.8	−129.8	0.4	−1.1	−1.1	14.0	−5.4	−5.4
C_4H_4	31.9	20.4	20.4	4.5	−4.8	−4.8	0.4	−6.5	−6.5	−172.6	−156.7	−156.7
$C_4H_4^{2-}$	−12.7	−6.0	−6.0	55.0	45.8	45.8	−4.8	−1.6	2.4	3.2	20.9	11.8
$C_5H_5^+$	100.3	75.9	75.9	−9.5	0.1	0.1	−10.0	−0.7	−0.7	−58.5	−54.1	−54.1
$C_5H_5^-$	−12.0	−9.6	−9.6	156.8	132.7	132.7	3.8	−0.7	0.0	−8.4	−6.2	−4.9
$C_6H_6^{2+}$	13.1	7.9	7.9	−0.3	−8.5	−8.5	0.2	−8.7	−8.7	−46.7	−51.0	−51.0
C_6H_6	−7.0	−10.1	−10.1	127.5	98.0	98.0	36.6	26.1	26.1	−6.8	−9.8	−9.8
$C_6H_6^{2-}$	−10.4	−4.9	−3.9	−5.6	−0.5	0.0	−7.0	−10.2	−9.4	−17.7	−18.5	−16.9
$C_7H_7^+$	−9.2	−5.0	−5.0	−242.0	−194.7	−194.7	20.0	12.4	12.4	−2.1	−7.4	−7.4
$C_7H_7^-$	67.6	52.3	52.5	−4.8	−6.2	−6.2	−10.1	−10.1	−10.1	−147.3	−122.6	−122.6
$C_8H_8^{2+}$	−5.7	−8.8	−8.8	833.6	676.7	676.7	6.2	0.8	0.8	0.0	−6.0	−6.0
C_8H_8	5.1	0.8	0.8	−2.4	−5.7	−5.7	−10.7	−11.0	−11.0	−79.7	−68.1	−68.1
$C_8H_8^{2-}$	−13.1	−11.5	−11.5	1105.1	921.4	920.9	33.6	26.7	26.7	−14.4	−12.2	−12.2
$C_9H_9^+$	−11.7	−12.8	−12.8	54.4	44.7	44.7	−9.1	−10.1	−10.1	−136.5	−117.8	−117.8
$C_9H_9^-$	−13.9	−12.6	−12.6	2000.2	1672.2	1672.2	−10.9	−10.5	−10.5	−579.6	−487.2	−487.2
$C_{10}H_{10}^{2+}$	−11.0	−17.8	−12.2	47.2	35.2	42.9	−5.8	−8.6	−8.6	46.8	37.9	37.9
$C_{10}H_{10}$	−5.8	−8.6	−8.6	−0.9	−3.4	−3.4	0.5	−2.5	−2.5	5.5	−4.9	−4.9
$C_{10}H_{10}^{2-}$	−10.8	−10.4	−10.3	2.7	0.0	−0.1	−15.5	−13.5	−13.5	−231.7	−198.9	−198.9

Table 20: MP2-GIAO/6-311++(2d,2p)//B3LYP/def2-TZVP NICS calculations of annulenes.

	State: S_0, Geometry: S_0			State: T_1, Geometry: S_0			State: T_1, Geometry: T_1			State: S_0, Geometry: T_1		
NICS	(0)	(+1)	(−1))	(0)	(+1)	(−1))	(0)	(+1)	(−1))	(0)	(+1)	(−1))
$C_3H_3^+$	−23.4	−15.0	−15.0	−329.9	28.9	28.9	−29.7	−5.7	−5.4	−1372.1	1566.2	2678.6
$C_3H_3^-$	−14.9	2.3	6.4	−23.7	−12.4	−7.5	−33.0	−10.2	−6.7	682.1	625.8	458.1
$C_4H_4^{2+}$	−6.5	−15.0	−15.0	363.5	401.3	401.3	0.3	−0.8	−0.8	−115.1	−26.4	−26.4
C_4H_4	26.9	17.1	17.1	3.1	−4.6	−4.6	−0.6	−6.2	−6.2	−1398.7	−1213.7	−1213.7
$C_4H_4^{2-}$	31.2	33.2	33.2	35.8	30.3	30.3	DF	DF	DF	−44.6	−68.3	−65.1
$C_5H_5^+$	72.6	54.3	54.3	−9.9	−1.9	−1.9	DF	DF	DF	36.9	47.1	47.1
$C_5H_5^-$	−12.2	−9.4	−9.4	DF	DF	DF	−0.3	−4.8	−3.8	−8.6	−6.5	−6.1
$C_6H_6^{2+}$	12.3	7.8	7.8	−0.7	−8.1	−8.1	−0.2	−8.2	−8.2	166.6	144.6	144.6
C_6H_6	−7.6	−10.0	−10.0	65.6	49.7	49.7	24.7	17.0	17.0	−7.4	−9.7	−9.7
$C_6H_6^{2-}$	−10.6	−5.6	−5.0	5.4	13.3	0.0	−9.0	−11.3	−10.5	−28.8	−25.8	−24.9
$C_7H_7^+$	−9.4	−6.0	−6.0	DF	DF	DF	17.1	10.5	10.5	−3.6	−8.0	−8.0
$C_7H_7^-$	56.6	43.7	43.9	−14.8	−14.7	−14.7	−10.0	−9.9	−9.9	DF	94144.6	94144.6
$C_8H_8^{2+}$	−6.7	−9.0	−9.0	31.6	23.1	23.1	5.7	0.6	0.6	−1.3	−6.4	−6.4
C_8H_8	3.9	0.6	0.6	−3.2	−6.1	−6.1	−11.0	−11.0	−11.0	12434.7	10331.1	10331.1
$C_8H_8^{2-}$	−12.2	−10.9	−10.9	58.0	47.3	46.4	72.1	58.1	58.1	231.3	144.1	144.1
$C_9H_9^+$	−12.6	−13.0	−13.0	20.5	15.7	15.7	−13.4	−13.5	−13.5	1213.5	1031.4	1031.4
$C_9H_9^-$	−13.8	−12.4	−12.4	35.2	28.1	28.1	−20.6	−19.9	−19.9	201.0	166.4	166.4
$C_{10}H_{10}^{2+}$	−12.8	−18.8	−13.1	DF	DF	DF	−6.2	−8.8	−8.8	33.1	26.1	26.1
$C_{10}H_{10}$	27.8	25.1	17.5	−0.8	−3.4	−3.3	−1.2	−4.0	−4.0	2.9	−5.4	−5.4
$C_{10}H_{10}^{2-}$	−7.8	−7.6	−7.5	DF	DF	DF	−14.7	−12.8	−12.8	909.3	781.8	781.8